The Fundamental Plane and Peculiar Velocities from the 6dF Galaxy Survey

---

Submitted in Total Fulfillment
of the Requirements of the Degree of
Doctor of Philosophy

School of Physics
The University of Melbourne

Christina Magoulas

November 2012

Abstract

Early-type galaxies (ellipticals and lenticulars) are observed to populate the relation known as the Fundamental Plane that links their effective radius, R_e, stellar velocity dispersion, σ, and mean surface brightness, I_e. We have measured Fundamental Plane parameters in the near-infrared J, H and K passbands for $\sim 10^4$ of the brightest early-type galaxies in the 6dF Galaxy Survey (6dFGS). We improve upon previous regression techniques used to derive the Fundamental Plane by developing a robust maximum likelihood algorithm for fitting the galaxy distribution in Fundamental Plane space with a 3D Gaussian model.

We exploit this large near-infrared-selected sample of galaxies to investigate trends in the Fundamental Plane with stellar population, morphology and environment. The 6dFGS galaxies exhibit clear stellar population trends in Fundamental Plane space, with age varying most strongly orthogonal to the plane. Remarkably, none of the stellar population parameters vary along the long axis of the plane, which corresponds to luminosity density. The Fundamental Plane slopes show little variation with either morphology or environment, but the Fundamental Plane size zeropoint is systematically larger for galaxies in lower density environments and for early-type spiral bulges. We speculate that age drives all the trends with residuals about the plane through its correlation with environment, morphology and metallicity.

Using the Fundamental Plane, we measure distances and peculiar velocities for $\sim 10^4$ 6dFGS galaxies to form the largest and most homogeneous peculiar velocity sample to date. Using a maximum-likelihood approach, we measure the overall bulk galaxy motions from the 6dFGS velocity field for the local volume of the universe, finding broad agreement with the predicted velocity field constructed from the 2MASS Redshift Survey. The local volume out to 16 120 km s^{-1} is found to have a bulk motion of 337 km s^{-1} in the direction $(l, b) = (313^\circ \pm 9^\circ, 14^\circ \pm 10^\circ)$, in good agreement with the results of other recent studies. A comparison of the observed and predicted fields is used to constrain parameters relating the distribution of galaxies and matter. We obtain a redshift-space distortion parameter $\beta = 0.29 \pm 0.06$ and a bias parameter for the 6dFGS velocity sample of $b = 1.69 \pm 0.36$.

The 6dFGS velocity field provides an independent probe of cosmological parameters defining models of large-scale structure formation. Next steps include: (i) combining the 6dFGS sample in the south with the SDSS sample in the north to obtain an all-sky velocity field; (ii) deriving additional constraints on cosmological parameters from the velocity power spectrum analysis; and (iii) comparing the Fundamental Plane distances and velocities for early-type galaxies with the Tully-Fisher distances and velocities for spiral galaxies that will be obtained with the WALLABY survey on the Australian SKA Pathfinder.

Declaration

This is to certify that:

(i) This thesis entitled "The Fundamental Plane and Peculiar Velocities from the 6dF Galaxy Survey" comprises only my original work towards the PhD, except where indicated in the Preface,

(ii) due acknowledgement has been made in the text to all other material used,

(iii) the thesis is less than 100,000 words in length, exclusive of tables, maps, bibliographies and appendices.

.....

Christina Magoulas

Preface

While the work presented herein is essentially my own, there are some elements that are the result of collaboration or the work of others. Any such data or results are acknowledged explicitly in the text, and are summarised here:

- Chapter 1 is a review of the literature of early-type galaxies, the Fundamental Plane, galaxy distances and peculiar velocities and is my own work. References are quoted in the text.

- Chapter 2 is my own work aside from the following exceptions where I have summarised and reworded the contribution from collaborators in the following sections. The derivation of spectroscopic (§2.3) and photometric (§2.4) measurements for a sample of 6dFGS galaxies are the work of Lachlan Campbell and are being prepared for journal submission in the near future. The morphological classification in §2.5 was undertaken by several experienced astronomers. In §2.8.1 the 6dFGS group catalogue was provided by Alex Merson (which is being prepared for journal submission) and the measurements of local environment parameters by Sarah Brough. The stellar population measurements in §2.8.2 are the work of Rob Proctor using the method of Proctor & Sansom (2002) and are being prepared for journal submission.

- Chapter 3 is based very closely on the following publication of original research:

  Magoulas C., Springob C. M., Colless M., Jones D. H., Campbell L. A., Lucey J. R., Mould J., Jarrett T., 2012, *The 6dF Galaxy Survey: The Near-Infrared Fundamental Plane of Early-Type Galaxies*, MNRAS, 427, 245

  The development and testing of the maximum likelihood Fundamental Plane fitting routine (including the modelling of several selection criteria and also extensions to the 3D Gaussian model outlined in §3.7) is my own work. The mock generation code used to create simulations of mock Fundamental Plane galaxy samples is also my own work.

- Chapter 4 is based very closely on the following publication of original research:

  Magoulas C., Springob C. M., Colless M., Jones D. H., Campbell L. A., Lucey J. R., Mould J., Jarrett T., 2012, *The 6dF Galaxy Survey: The Near-Infrared Fundamental Plane of Early-Type Galaxies*, MNRAS, 427, 245

  All Fundamental Plane fitting in Chapter 4 is entirely my work, and is used to analyse the 6dFGS Fundamental Plane trends with waveband, environment and morphology. The analysis of the Fundamental Plane in κ-space and the dependence of Fundamental Plane scatter on velocity dispersion error is also my own work. Supplementary data that is provided by collaborators is cited accordingly in the text, as per Chapter 2.

- Chapter 5 is based very closely, in §5.2 and §5.3, on the following publication of original research, which I have summarised and reworded:

  Springob C. M., Magoulas C., Proctor R., Colless M., Jones D. H., Kobayashi C., Campbell L., Lucey J. R., Mould J., 2012, *The 6dF Galaxy Survey: stellar population trends across and through the Fundamental Plane*, MNRAS, 420, 2773

  I provided the best-fit Fundamental Plane definition used in the analysis of the stellar population trends in §5.2 and §5.3. §5.4 and §5.5 are my own work, for which I have written the maximum likelihood Fundamental Plane fitting code (including the extension of the 4D Gaussian age model), and have not been published elsewhere.

- Chapter 6 is being prepared for journal submission in the near future. This is my own original work, with the exception of the model of the 2MRS predicted density and velocity fields, which is from Erdoğdu et al. (2012, submitted) following the method of Erdoğdu et al. (2006).

Acknowledgements

At the time, the decision to begin a PhD with supervisors who I barely knew, at a different institution from mine, into research I knew almost nothing about (I didn't even know what the Fundamental Plane was!) was a particularly nerve-racking one. I am therefore grateful to Rachel Webster for the initial 'nudge' in the right direction and for introducing me to the research projects available at the AAO and (as it turns out, correctly) mentioning which one was the most interesting.

Any fear and doubt I had at the start was immediately alleviated from the moment I began working with my supervisors at the AAO who have made this such a rewarding experience. I am indebted to my supervisor Matthew Colless for his invaluable guidance and support throughout this entire process. I am fortunate to have had such a generous mentor whose 'metaphorical' door (email) was always open. Without his careful and considered advice and motivation, this thesis would not have become what it is.

I would also like to thank Heath Jones for his continued encouragement since the first day of this PhD, and for always being willing to provide insightful feedback on all manner of papers, talks, reports, (this thesis!) etc... whenever it was needed.

This thesis has benefited from the wisdom and guidance of Jeremy Mould and also John Lucey - both of whom have been more than willing to share their exhaustive knowledge on anything and everything. And a special thanks to Chris Springob with whom I have worked so closely and who has patiently answered every question I have thrown at him, no matter how inane. Now I finally have time to watch all those sci-fi movies you frequently recommended.

I acknowledge the hard work and efforts, that this work draws upon, of Lachlan Campbell in the derivation of the Fundamental Plane parameters and also by the 6dFGS team in the original acquisition of the data. I am also grateful for the help of Chris Fluke in creating the stunning 3D visualisations of our Fundamental Plane and the expertise in NIR photometry shared by Tom Jarrett.

I would like to thank all the friendly astronomers/staff and visiting summer students at the AAO (too many to name!) who made my trips to Sydney all the more pleasant, and who were only too happy to share a cup of tea and some sage

advice, and to partake in discussions on all things PhD related and otherwise.

Of course a special thanks to Mum and Dad who have always been part of my scientific endeavours all the way from the glittery solar system posters in primary school, to my first powerpoint presentation on black holes in high school, until now with the completion of this thesis. And to my sisters - Lisa, De and Jen - who may not fully understand what I do or why it takes so long to do it, but who have always been supportive nonetheless (even attending some of my talks!)

I would like to thank my friends Rebekah, Nis and Allen for their patience and support, even when they were ignored because I was too busy with the demands of PhD research :)

Whilst at the University of Melbourne, I have been fortunate to meet several people who have made this journey a memorable one. I am glad to have shared this experience with my fellow astros (Steve, Bennett and Dre) who have been around since the early days in 359 (we've all come a long way since then!) and those current PhD students (Madusha, Letizia, T'Mir, Tony) and past/current Masters students who I was lucky enough to meet along the way. Thanks also to those former PhD graduates (Ned, Ave, Sal) who have kindly shared their previous experiences - especially Ned, through our many animated and passionate discussions on all things galaxies, and the insightful points of view on the life of a PhD student. Thanks to all of you for your friendly advice, inspiration and, most of all, enjoyable company.

The sufferance and forbearance, on a daily basis, of my officemate Loren, does not go unnoticed. I am grateful for the unexpected but lasting friendship between us that has been forged by the trials and tribulations of PhD research. Our friendship will continue to be one of the fondest memories from this experience. I will miss our daily venture to acquire coffee which was really just an excuse to get out of the office.

And finally, for Brad - someone who I have relied heavily upon, particularly in the past few months, I offer my feeble thanks and appreciation. You have kept me grounded in moments of utter chaos and for that, and much more, I am deeply grateful.

Contents

List of Tables

List of Figures

Chapter 1

Introduction

1.1 Overview

The rapid development in the late 1990s in our understanding of the origin of the universe and the formation of structure on the largest scales was driven by major advances in telescope technology. Observational cosmology emerged as a precision science with the mapping of radiation from the cosmic microwave background (CMB) of the universe by the COsmic Background Explorer (COBE) satellite. For the first time, the anisotropy of the fluctuations in the CMB (i.e. the remnant from the Big Bang) was measured by COBE (Smoot et al., 1992) to better than 1 part in 100,000 suggesting these fluctuations are the primordial seeds of structure formation.

The large-scale structure of the nearby universe was revealed in greater detail and depth as a result of two major redshift surveys - the Two-degree Field Galaxy Redshift Survey (2dFGRS; Colless et al., 2001a) and the Sloan Digital Sky Survey (SDSS; York et al., 2000). Utilising technological developments in spectroscopy, these surveys measured the position and redshift of hundreds of thousands of galaxies, improving upon previous surveys by an order of magnitude and remaining the largest of their kind still to this day. The filamentary structure evident in the detailed maps of the distribution and clustering of galaxies from these surveys appeared to agree with a cosmological model in which large-scale structure is formed from primordial density fluctuations that collapse via gravitational instability in a dark-matter dominated universe, known as the Λ-Cold Dark Matter model (ΛCDM).

In the last decade, observational evidence has mounted for ΛCDM as the standard model of cosmology describing the observable universe. The strongest and most detailed support for this model comes from the measurements made with the Wilkinson Microwave Anisotropy Probe (WMAP; Bennett et al., 2003). As a successor to COBE, WMAP mapped the CMB temperature fluctuations with even greater precision and on smaller scales. Together with supernova distance measurements from the High-z Supernova Search Team (HIZ; Riess et al., 1998) and the Supernova Cosmology Project (SCP; Perlmutter et al., 1999) that provided the first evidence for the accelerating expansion of the universe (as suggested by a non-zero cosmological constant, Λ) and local large-scale structure redshift surveys (SDSS and 2dFGRS), WMAP established ΛCDM as the dominant cosmological paradigm.

However, further refinement of ΛCDM or other theoretical cosmological models is limited by the precision of cosmological distance measures. The difficulty lies, in part, in the fact that the associated error in these measurements typically grows linearly with distance. This work presents a detailed study of one such measure – the Fundamental Plane – which uses a tight correlation between the galaxy properties of early-type galaxies to determine their distances using observations from the 6dF Galaxy Survey.

In this chapter, Section 1.2 gives a description of the properties of early-type galaxies and, in Section 1.3, a summary of the scaling relations they obey, such as the Fundamental Plane. In Section 1.4 we discuss the physical origin of the Fundamental Plane and its implications for the structure and formation of early-type galaxies. We then focus, in Section 1.5, on how the Fundamental Plane can be used to measure distances and hence peculiar velocities, and discuss how peculiar velocities are a valuable probe of the matter distribution in the nearby universe. Finally, in Section 1.6, we outline the structure of the thesis.

1.2 Structure of Early-Type Galaxies

There are four principal morphological classes of large galaxies: ellipticals, lenticulars, spirals and irregulars. Elliptical galaxies are distinguished from other galaxies by their featureless round or elliptical appearance and are comprised of a spheroidal bulge of stars with predominantly old stellar populations and very little gas. Spiral galaxies are characterised by a flat, rotating disk consisting of young, active stellar populations and cold gas gathered in the spiral arms for which they are named. Lenticular (or S0) galaxies are intermediate between ellipticals and spirals: they contain a disk component (like spiral galaxies) but are not actively forming stars and hence contain older stellar populations (like elliptical galaxies). Even though lenticulars possess a disk component, they are structurally more similar to elliptical galaxies and the two are often collectively referred to as 'early-types'. Irregular galaxies are named for their peculiar shape or appearance as a result of galaxy mergers or other violent interactions. Spiral and irregular galaxies are referred to as 'late-types'. The sequence from elliptical, lenticular, spiral, irregular is essentially related to the galaxies' disk-to-bulge ratio, with ellipticals being all bulge, lenticulars and 'early-type spirals' having large bulges as well as disks, and 'late-type spirals' and the less peculiar irregulars being (almost) all disk.[1] Most galaxies in the universe can be classified into one of these four common groups, although there do exist sub-groups and individual galaxies that do not fit into this sequence.

[1]The early- and late-type nomenclature was first used in Hubble (1926) to refer to an evolution in complexity between types (rather than galaxy evolution itself). Therefore these definitions are used here with the understanding that the term early-type refers to 'bulge-dominated' galaxies only.

Current theories of galaxy formation suggest elliptical galaxies are formed through mergers of smaller galaxies (Kormendy et al., 2009, and references therein). Consequently they are preferentially found in dense environments and are amongst the most dynamically evolved systems in the universe. Elliptical galaxies can be recognised by their smooth brightness profiles. Their homogeneity as a galaxy population and seemingly simple structure (as compared to spiral galaxies) imply a similarity in their formation mechanisms and evolution and a physical connection between the galaxy properties.

The surface brightness profile of elliptical galaxies are well represented by a Sérsic model (Sérsic, 1963)

$$I(R) = I_e \exp\left\{-b_n\left[\left(\frac{R}{R_e}\right)^{1/n} - 1\right]\right\} . \tag{1.1}$$

Here R_e is the half-light radius of the galaxy, I_e is the intensity at R_e, the Sérsic index n defines the profile shape, and b_n is a constant that depends on n. For disks, $n \approx 1$ (the exponential case) while for bulges and ellipticals $n \approx 4$ (referred to as a de Vaucouleurs profile).

1.3 Galaxy Scaling Relations

Galaxies are observed to exhibit strong trends between their physical properties, known as scaling relations. Scaling relations between the structural parameters of galaxies are crucial tools that inform our understanding of the formation processes of galaxies, and by extension the regularity among differing galaxy populations. They are also important in providing the motivating observations that theories of galaxy formation must explain and reproduce.

1.3.1 Faber-Jackson and Kormendy Relations

One of the first early-type galaxy scaling relations was recognised by Faber & Jackson (1976), and connects galaxy luminosity, L, and stellar velocity dispersion, σ, as shown in Figure 1.1. The stellar velocity dispersion is a measure of the kinematic motions of the stars in a (pressure supported) elliptical galaxy and is analogous to the rotation velocity for a (rotationally supported) disk galaxy. The Faber-Jackson (FJ) relation has the form of a power law, $L \propto \sigma^{\gamma}$, where γ is usually observed to be in the range 3 to 5 (Bernardi et al., 2003a; Desroches et al., 2007; La Barbera et al., 2010a; Falcón-Barroso et al., 2011). The FJ slope depends to some extent on luminosity and, for the largest galaxy samples (La Barbera et al., 2010a; Bernardi et al., 2003a), this appears as 'curvature' in the FJ relation towards low L and σ values, or as a deviation from a strict power law at low masses.

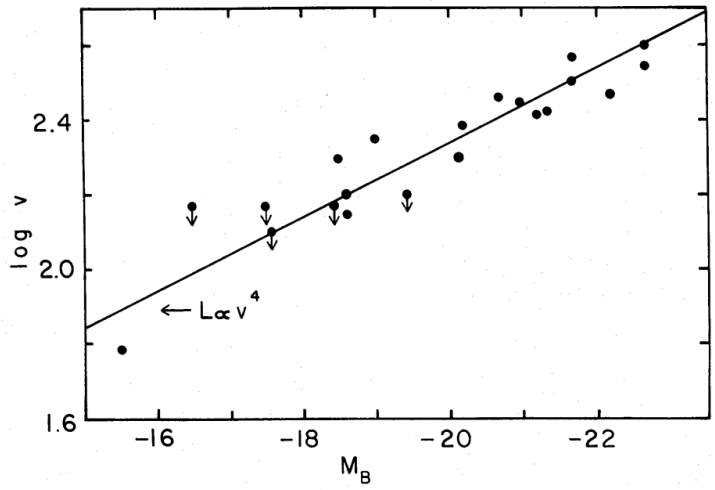

Figure 1.1: The Faber-Jackson relation; an empirical correlation between the stellar velocity dispersion and absolute magnitude (or luminosity) of early-type galaxies. (Figure 16 from Faber & Jackson 1976).

A similar relation between galaxy luminosity (or absolute magnitude) and effective radius, R_e, was derived around the same time (Kormendy, 1977). The Kormendy relation also has power-law form, $L \propto R_e^{\epsilon}$, (although the relation of surface brightness with size has also been referred to as the Kormendy relation) with ϵ usually found to be in the range -1 to -2 (Bernardi et al., 2003a; Desroches et al., 2007; La Barbera et al., 2010a; Falcón-Barroso et al., 2011). The recent study of La Barbera et al. (2010a) observed that the slope of the Kormendy relation was steeper towards longer wavelengths, suggesting that smaller early-type galaxies have a higher ratio of optical-to-near-infrared radii compared to larger galaxies.

Both relations show a wide range of slopes depending on the properties of the sample under consideration (e.g. absolute magnitude and morphological type) and substantial intrinsic scatter, in the range 0.2–0.5 dex (e.g. Desroches et al., 2007; Nigoche-Netro, Ruelas-Mayorga & Franco-Balderas, 2008; Nigoche-Netro et al., 2010; La Barbera et al., 2010a).

1.4 The Fundamental Plane

1.4.1 History of the Fundamental Plane

The apparently large intrinsic scatter in the Faber-Jackson relation (after accounting for observational errors) prompted a search for a third 'hidden' parameter. Two teams, Djorgovski & Davis (1987) and Dressler et al. (1987b, a team known as the Seven Samurai or 7S) found simultaneously and independently that, in the three-dimensional space of size, surface brightness and velocity dispersion, early-type galaxies populate a more tightly correlated two-dimensional plane, called the

Fundamental Plane (FP), that has significantly lower intrinsic scatter than the FJ relation. The previously established Faber-Jackson and Kormendy relations could then be understood as projections of the Fundamental Plane. The fact that the FP links distance-independent quantities (velocity dispersion and surface brightness) with a distance-dependent quantity (angular size), together with its relatively small intrinsic scatter, meant that it was immediately adopted as a new method for measuring galaxy distances.

The FP was originally formulated as a two-dimensional correlation, the D_n–σ relation (Burstein et al., 1986; Dressler et al., 1987b), between velocity dispersion and the photometric parameter D_n, defined as the diameter enclosing a mean surface brightness. D_n turns out to combine effective radius and surface brightness in such a way that the D_n–σ relation is a reasonable approximation to the edge-on view of the FP. However, it was realised that D_n–σ is in fact a tilted projection of the FP (Lucey, Bower & Ellis, 1991; Jorgensen, Franx & Kjaergaard, 1993), which induces a systematic error and increases the scatter, making D_n–σ a less reliable indicator of distance. In consequence the FP has become widely accepted as the preferred distance indicator.

The Fundamental Plane has the familiar power-law form of galaxy scaling relations, $R_e \propto \sigma_0^a \langle I_e \rangle^b$, and connects the structural and kinematic properties of early-type galaxies. In this relation, R_e is the effective radius containing half the galaxy's light (also called the half-light radius); $\langle I_e \rangle$ is the mean surface brightness within R_e (in flux units), and σ_0 is the central stellar velocity dispersion.

1.4.2 Fundamental Plane Theory

Since the original formulation of the FP relation, the size and quality of early-type galaxy samples have been steadily improved (e.g. Bernardi et al., 2003b; D'Onofrio et al., 2008; La Barbera et al., 2008; Hyde & Bernardi, 2009; Gargiulo et al., 2009; La Barbera et al., 2010b; Graves, Faber & Schiavon, 2010) in an effort to explain important properties such as the observed orientation (or *tilt*) of the FP and its intrinsic scatter (or *thickness*).

The *tilt* of the FP is the difference between the observed coefficients of the plane, a (for $\log \sigma_0$) and b (for $\log \langle I_e \rangle$), and the values $a = 2$ and $b = -1$ that would follow if galaxies were dynamical systems that were all homologous (i.e. possessed the same structural and kinematic distributions), virialised (i.e. dynamically relaxed), and had the same fixed mass-to-light ratio.

These so-called 'virial' FP coefficients are derived by first assuming the virial theorem applies, so that

$$\frac{2\langle V^2 \rangle}{2} = \frac{GM}{\langle R \rangle} \ . \tag{1.2}$$

The physical quantities of average velocity ($\langle V \rangle$), radius ($\langle R \rangle$) and luminosity (L) can be related to the observable FP parameters ($\log R_e$, $\log \sigma_0$ and $\log \langle I_e \rangle$) by the relevant structure constants k_R, k_V and k_L:

$$\begin{aligned} R_e &= k_r \langle R \rangle, \\ \sigma^2 &= k_V \langle V^2 \rangle, \\ L &= k_L I_e R_e^2 \ . \end{aligned} \tag{1.3}$$

Substituting equation 1.3 into equation 1.2 provides an expression for R_e :

$$R_e = c_0^{-1} (M/L)^{-1} \sigma^2 I_e^{-1} \ . \tag{1.4}$$

where M/L is mass-to-light ratio and $c_0 = G k_V k_R k_L$. Assuming the galaxies are homologous systems with constant mass-to-light ratio (so that the structure constants and M/L are fixed), equation 1.4 reduces to the 'virial' Fundamental Plane, $R_e \propto \sigma^2 I_e^{-1}$.

The physical origin of the tilt of the observed FP (relative to the virial FP) is usually interpreted as being due to some combination of systematic deviations from either dynamical homology (i.e. differences in density profile or orbital structure) or fixed mass-to-light ratio (i.e. differences in stellar population or the ratio of baryonic matter to dark matter); see, e.g., Ciotti, Lanzoni & Renzini (1996); Busarello et al. (1997); Graham & Colless (1997); Trujillo, Burkert & Bell (2004); Cappellari et al. (2006); Bolton et al. (2007). Variations in M/L from stellar population effects usually contribute no more than 50% to the tilt of the FP (Pahre, de Carvalho & Djorgovski, 1998; Prugniel & Simien, 1997; Proctor et al., 2008; Hyde & Bernardi, 2009). Similarly, departures from structural homology can enter the FP in differences in the light profiles (e.g. allowing n to vary in equation 1.1), but are not able to explain the entirety of the observed tilt while also maintaining the thinness of the FP (Ciotti, Lanzoni & Renzini, 1996; Graham & Colless, 1997; Prugniel & Simien, 1997; Bertin, Ciotti & Del Principe, 2002). The conclusion is that some combination of these effects is required to explain the tilt of the FP.

FP samples are only now reaching the size and measurement quality required to be able to measure (and hopefully disentangle) these effects more precisely, as with the early-type galaxy study of Graves & Faber (2010). Using a sample of ∼16 000 quiescent galaxies from SDSS, Graves et al. observed that variations in both stellar population and dark matter content (which rotate the FP in different axes in three-dimensional space) are required to explain the observed tilt. Even so, a consistent model is yet to emerge that explains the entirety of the observed FP tilt, leaving its origin an open and much-debated question.

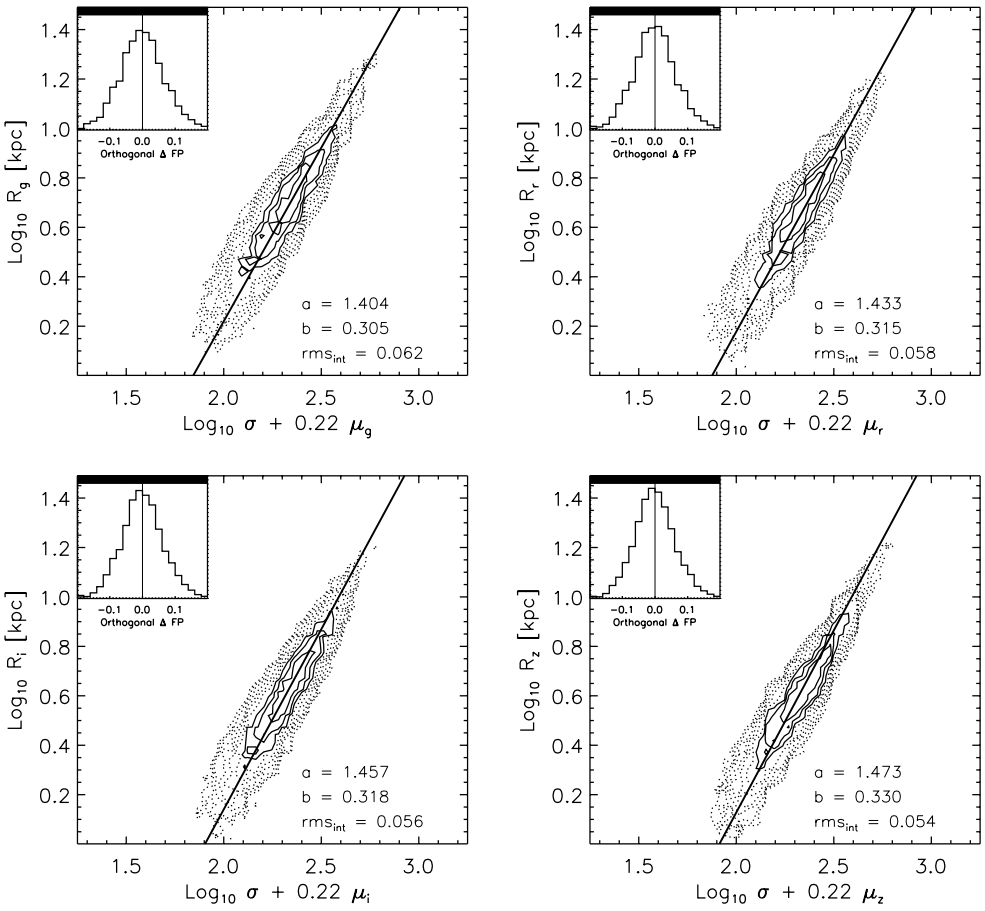

Figure 1.2: The edge-on projection of the SDSS Fundamental Plane in the g, r, i and z bands. The FP slope in velocity dispersion, a, is found to increase from the g to the z bands. (Figure 3 from Hyde & Bernardi 2009).

1.4.3 Waveband Dependence and the FP

Several authors (Scodeggio et al., 1998; Bernardi et al., 2003b; Hyde & Bernardi, 2009; La Barbera et al., 2010a) have detected a slight steepening of the slope in $\log \sigma_0$ (i.e. an increase in a) going from bluer to redder passbands. This wavelength variation has also been extended to near-infrared (NIR) FP samples (e.g. Pahre, Djorgovski & de Carvalho, 1998; Jun & Im, 2008). This trend suggests a variation of stellar content (and M/L) along the FP. In contrast, the slope in $\log\langle I_e \rangle$, (i.e. b), is found to be largely independent of wavelength (Bernardi et al., 2003b; Hyde & Bernardi, 2009; La Barbera et al., 2010a).

The analysis of multi-wavelength SDSS data for a large sample of early-type galaxies by Hyde & Bernardi (2009) identified this steepening across the optical to near-infrared bands as shown in Figure 1.2. This suggests that the NIR Fundamental Plane is closer to the virial plane, as the stellar population effects (responsible for

the waveband dependence of the slopes) are negligible, assuming NIR-light traces the stellar mass in galaxies closely (Pahre, Djorgovski & de Carvalho, 1998; Pahre, de Carvalho & Djorgovski, 1998; Proctor et al., 2008). However, while optical FP data for large (i.e. $N_g > 10\,000$) galaxy samples is abundant, the NIR FP data, required to detect these effects, is still limited to samples of ∼5000 galaxies.

1.4.4 Universality of the Fundamental Plane

The Fundamental Plane relation is often claimed to be 'universal', in the sense that the coefficients are similar for galaxies across environments ranging from the low-density field to high-density clusters (e.g. Jorgensen, Franx & Kjaergaard, 1996; Pahre, de Carvalho & Djorgovski, 1998; Kochanek et al., 2000; Colless et al., 2001b; Reda, Forbes & Hau, 2005). However there are also apparently contrary suggestions in the literature that there are mild, but statistically significant, environmental variations (e.g. Lucey, Bower & Ellis, 1991; de Carvalho & Djorgovski, 1992; Bernardi et al., 2003b; D'Onofrio et al., 2008; La Barbera et al., 2010c).

To address the questions of universality at low redshift, D'Onofrio et al. (2008) used combined FP data for galaxies in and around massive nearby clusters to derive the Fundamental Plane for galaxies in a wide range of environments. They found no dependence in the FP coefficients for global cluster properties (such as cluster velocity dispersion, cluster radius and cluster richness), but did find the FP coefficients were correlated with proxies for *local* environment such as cluster-centric distance and local density (D'Onofrio et al., 2008).

La Barbera et al. (2010c) analysed the environmental dependence of the FP using a much larger sample of the local galaxy population than D'Onofrio et al. (2008) (without the selection in clusters) and also studying the additional dependence with waveband. La Barbera et al. (2010c) detect a systematic difference in the FP offset and surface brightness slope b with global group properties (in particular parent group mass), although they suggest the dependence is driven by a strong trend in the FP offset with local density. This is consistent with D'Onofrio et al. (2008), although their variation in b is stronger than in La Barbera et al. (2010c), which can be attributed to the different mass range of the two samples.

Any variation in the FP between field and cluster galaxies, or between galaxies in clusters of different richness, is interesting from the point of view of the formation of early-type galaxies. However, any significant environmental variation in the FP complicates the use of the FP as a distance indicator, as a *global* FP that is relevant for all galaxies, whether in the field or in a cluster, could not be used to establish consistent distance measurements.

1.4.5 Galaxy Morphology and the Fundamental Plane

The structural similarity of elliptical (E) galaxies and the bulges of lenticular (S0) and early-type spiral (Sp) galaxies suggests that the latter classes of object may also populate the FP (Dressler et al., 1987b), and indeed Jorgensen, Franx & Kjaergaard (1996) found that the FPs for E and S0 galaxies were consistent. In contrast, galaxies with both bulge *and* disk components have been observed to be offset from ellipticals on the FP (Bender, Burstein & Faber, 1992; Saglia, Bender & Dressler, 1993; Falcón-Barroso, Peletier & Balcells, 2002).

However the FP is usually defined by measurements of a *central* velocity dispersion, σ_0, that can be influenced by the presence of a disk component in a galaxy. The effect of a disk component is lessened when using the *effective* velocity dispersion averaged within an effective radius (instead of σ_0), which can only be measured by integral-field spectroscopy (Falcón-Barroso et al., 2011). This could account for the apparent offset of bulge-dominated galaxies, and confirm that bulges are indeed structurally homologous with, and share a similar formation epoch to, ellipticals.

It is therefore important to examine whether there are morphological variations in the observed FP, and (if so) whether these are due to intrinsic differences between E's and the bulges of S0's and early-type Sp's, or to observational contamination of the bulge parameters by the disk for the latter classes of galaxy. If such morphological variation exists, for either reason, it would result at some level in offsets and increased scatter of the FP, and increase the systematic and random errors (respectively) in the estimated distances and peculiar velocities.

1.4.6 Stellar Populations and the Fundamental Plane

The physical origins of the Fundamental Plane provide constraints on theories of galaxy formation and evolution and are therefore intimately tied to the stellar population properties of early-type galaxies. The variation of stellar populations along the sequence of early-type galaxies provides clues to the connection between galaxy structure and mass assembly histories and galaxy star formation histories.

Most previous studies have only examined pairwise correlations between FP quantities and stellar population parameters. For example, the pairwise correlations of stellar population parameters (in particular age) with velocity dispersion are well established (Nelan et al., 2005; Thomas et al., 2005; Smith, Lucey & Hudson, 2007). And the correlation of the residuals of the Fundamental Plane with age (Forbes, Ponman & Brown, 1998; Reda, Forbes & Hau, 2005; Gargiulo et al., 2009) has important implications for the origin of scatter about the plane, as it suggests the FP thickness can be understood as an age sequence.

The study of Graves, Faber & Schiavon (2009a,b) was able to extend the analysis of the variation of stellar populations throughout the Fundamental Plane by inves-

tigating trends of age, metallicity and abundance ratios with all the FP parameters in three dimensions. In Graves, Faber & Schiavon (2009b), the most striking trends in the three-dimensional FP space were that all stellar population parameters were found to increase with increasing velocity dispersion while little stellar population variation was found with effective radius and surface brightness. However, the surface brightness residuals of the Fundamental Plane were observed to correlate with stellar populations, suggesting that the thickness of the plane is driven by age (consistent with Forbes, Ponman & Brown 1998), in the expected sense that galaxies above the plane (with higher surface brightness) are younger than those below the plane (with lower surface brightness); see Graves, Faber & Schiavon (2009b).

1.5 Galaxy Distances and Peculiar Velocities

A notable property of the Fundamental Plane is its remarkably small intrinsic scatter or *thickness*, which has enabled its use as a distance indicator for early-type galaxies. The intrinsic scatter in the distance-dependent quantity, R_e, is measured to be as small as 10–15%, although the effective precision of the distance estimator, including observational errors, is typically 20–30% (see summary in Table 5 of Colless et al., 2001b) .

The Fundamental Plane relation of early-type galaxies is a tool with two primary uses—the first, understanding galaxy formation and evolution processes and interpreting the physical origins of the FP (see above), and the second, measuring galaxy distances. This second application is crucial in mapping large-scale motions of galaxies in the local universe, as discussed below.

1.5.1 Fundamental Plane Distances

The substantial scatter in the Faber-Jackson relation meant it was not suitable for determining accurate distances to galaxies in the local universe. However, with the introduction of the Fundamental Plane (Dressler et al., 1987b; Djorgovski & Davis, 1987), a relation now existed with the demonstrated ability to measure the distance of early-type galaxies with an uncertainty of 20–30% and the potential to do significantly better, since the apparent intrinsic scatter in the relation appears to be as low as 10–15%.

The Fundamental Plane can be used as a measure of relative galaxy distance in a similar manner to the Tully-Fisher (TF) relation for star-forming spiral galaxies (Tully & Fisher, 1977), because of the distance dependence of galaxy size (i.e. the effective radius of the galaxy). Through the Fundamental Plane (FP), effective radius is linearly related to the two distance-independent quantities I_e and σ_0:

$$\log R_e = a \log \sigma_0 + b \log I_e + c \ . \tag{1.5}$$

Once the coefficients of the FP have been established, the $\log R_e$ offset of a galaxy from the plane in FP space can be used as a measure of that galaxy's distance.

Given the large number of objects for which FP and TF parameters can be easily observed, both relations have flourished as workhorses of distance (and hence peculiar velocity) measurement for, respectively, early-type and spiral galaxies (see Strauss & Willick 1995 and references therein). Other distance indicators with better precision for individual measurements (<10%) are limited in various ways; for example, Type Ia supernovae are limited (at least to date) by the relatively small numbers of objects for which distances can be measured (Riess et al., 1997), while surface brightness fluctuations are observationally expensive, limiting the volume over which they are used (Blakeslee et al., 1999). The Fundamental Plane as a distance indicator has the distinct advantage of sampling a relatively abundant population of distance tracers (early-type galaxies) and being applicable over a relatively wide range in redshift (albeit with decreasing absolute precision at greater distances).

1.5.2 Peculiar Velocities

The deviations from a smooth Hubble Flow that are present in the motions of galaxies are known as peculiar velocities. These deviations are gravitationally induced by inhomogeneities in the distribution of matter that result in the motion of galaxies towards over-dense regions and away from under-dense regions in the large-scale matter structure. The peculiar velocity, v_p, of a galaxy is (at low redshifts) given by the difference between its recession velocity due to the Hubble flow, cz, and the distance, d, measured by a redshift-independent distance indicator (such as the Fundamental Plane):

$$v_p = cz - H_0 d \ . \tag{1.6}$$

As peculiar velocities are regulated by the scale and amplitude of fluctuations in the density field, they are a direct tracer of the underlying distribution of mass in the universe. The peculiar velocity field of galaxies is therefore a powerful cosmological probe that can provide independent constraints on the parameters defining models of large-scale structure formation. It is sensitive to mass fluctuations on scales up to $\sim 100\, h^{-1}$ Mpc and remains the only such probe in the low-redshift universe.

The relationship between the peculiar velocity field and the density field can be expressed in terms of gravitational instability theory. Defining the density fluctuation field, δ_m, as

$$\delta_m(\boldsymbol{r}) = \frac{\rho(\boldsymbol{r}) - \langle\rho\rangle}{\langle\rho\rangle} \ , \tag{1.7}$$

then in the regime where perturbations are linear (i.e. small mass density fluctuations relative to the mean density of the universe, $\delta_m \ll 1$) the velocity field, $\boldsymbol{v}(\boldsymbol{r})$, is given

(Peebles, 1993) by

$$\boldsymbol{v}(\boldsymbol{r}) = \frac{f}{4\pi} \int d^3\boldsymbol{r}' \frac{\boldsymbol{r}' - \boldsymbol{r}}{|\boldsymbol{r}' - \boldsymbol{r}|^3} \delta_m(\boldsymbol{r}') \ , \tag{1.8}$$

where f describes the rate of growth of structure and is approximately equal to $\Omega_m^{0.6}$ (Peebles, 1980) in a flat ΛCDM universe.

The galaxy distribution in redshift space is distorted from its real-space distribution by the peculiar velocity field. If we make the assumption that the galaxy density and matter density fluctuations are related by a linear bias parameter, b, such that

$$b = \delta_g / \delta_m \ , \tag{1.9}$$

then the form of this distortion can be characterised by the linear redshift distortion parameter, $\beta = \Omega_m^{0.6}/b$. In the linear regime, therefore, Equation 1.8 becomes

$$\boldsymbol{v}(\boldsymbol{r}) = \frac{\beta}{4\pi} \int d^3\boldsymbol{r}' \frac{\boldsymbol{r}' - \boldsymbol{r}}{|\boldsymbol{r}' - \boldsymbol{r}|^3} \delta_g(\boldsymbol{r}') \ . \tag{1.10}$$

This linear theory has been effective in generating predictive models linking velocity and density fields that aid in our interpretation of the observed velocities and the mass distributions responsible for them. Simple parametric models for the large-scale structure were the first to be developed, and included infall onto one or more 'Virgo-like' overdensities (Lynden-Bell et al., 1988; Han & Mould, 1990), reflecting the understanding of the nearby universe at the time. With the advent of redshift surveys that covered most of the sky, it became plausible to predict peculiar velocities directly, by making an assumption about how matter traces the distribution of galaxies (encompassed in the value for β). These so-called 'non-parametric' models are able to reconstruct the three-dimensional density and velocity fields from galaxy redshift catalogues, and allow comparison with the observed velocity data to estimate the β parameter (Branchini et al., 1999; Erdoğdu et al., 2006).

1.5.3 The Local Peculiar Velocity Field

The discovery of the Fundamental Plane as a new method for estimating redshift-independent distances by the 7S team (Dressler et al., 1987b) led to a surprising result. Using the FP to determine distances and peculiar velocities for a sample of 400 elliptical galaxies, they discovered a large-scale coherent motion deviating from Hubble flow with respect to the CMB rest frame (Dressler et al., 1987a). This motion was found to be consistent with a flow model that allowed for a streaming motion towards a 'Great Attractor' in the direction of, but beyond ($cz \sim 4500\,\mathrm{km\ s^{-1}}$), the Hydra-Centaurus (HC) Supercluster (Lynden-Bell et al., 1988).

An accurate determination of the average streaming motion or 'bulk flow' in the nearby universe then became a key focus of subsequent peculiar velocity surveys,

along with accounting for the ∼600 km s^{-1} dipole motion of the Local Group with respect to the CMB (Kogut et al., 1993). When averaged over a large enough volume, cosmological models predict that the bulk flow should approach the Hubble flow, commonly measured as a convergence to the CMB rest frame. There is now consensus in the direction of the bulk flow found by multiple studies, however some inconsistencies in the observed amplitude and scale still remain.

For peculiar velocity studies within a redshift distance of 6000 km s^{-1} there is general agreement between models of the velocity features and the direction and magnitude of the dipole. The ENEAR survey measured FP distances and peculiar velocities for 1145 early-type galaxies detecting a bulk flow of 220 ± 60 km s^{-1} out to a depth $cz < 6000$ km s^{-1} (da Costa et al., 2000a). This is consistent with the 200 ± 65 km s^{-1} within 6500 km s^{-1} found in the I band Tully Fisher survey of field spiral galaxies (SFI; Giovanelli et al., 1998). These results suggest most of the Local Group motion is accounted for in mass concentrations within 6000 km s^{-1}.

However, beyond 6000 km s^{-1}, large-scale flows of different amplitude and direction have been found. Large bulk motions (in excess of 600 km s^{-1}) have been claimed by Lauer & Postman (1994), using a photometric relation between brightest cluster galaxies in 119 Abell clusters, and, towards a different direction, by the Streaming Motions of Abell Clusters (SMAC) survey of Hudson et al. (2004), using the Fundamental Plane. In contrast, the EFAR Fundamental Plane survey found flows consistent with zero at these same large distances (Colless et al., 2001b). The large-scale results are naively inconsistent between surveys due to sparse sampling of the complex peculiar velocity field, although the discrepancies are largely a result of the significant random error in velocity measurements at these scales as well as selection bias (Hudson et al., 2004).

The most recent peculiar velocity studies consist of samples containing a large number of measurements (on the order of ∼5000) to reach a consensus on the scale of these flows and also establish whether they are consistent with the predictions of ΛCDM cosmology. The SFI++ survey is the largest of these, and is based on a homogeneous catalogue of Tully-Fisher measurements for ∼5000 spiral galaxies (Masters et al., 2006; Springob et al., 2007). The data from SFI++ makes up a large part of the ∼5000 peculiar velocity measurements of the concatenated COMPOSITE sample of Watkins, Feldman & Hudson (2009). The bulk flow, as measured by Watkins, Feldman & Hudson (2009) in shells of radius R_I, is shown in Figure 1.3. The magnitude of the bulk flow from the COMPOSITE sample is 407 ± 81 km s^{-1} within a radius of $50\,h^{-1}$ Mpc, and is due to mass outside the sample (Watkins, Feldman & Hudson, 2009). This result is inconsistent with ΛCDM and the Five-Year WMAP constraints (Dunkley et al., 2009) at the 98% level, and may indicate a possible departure from the standard cosmological paradigm. However, much of the

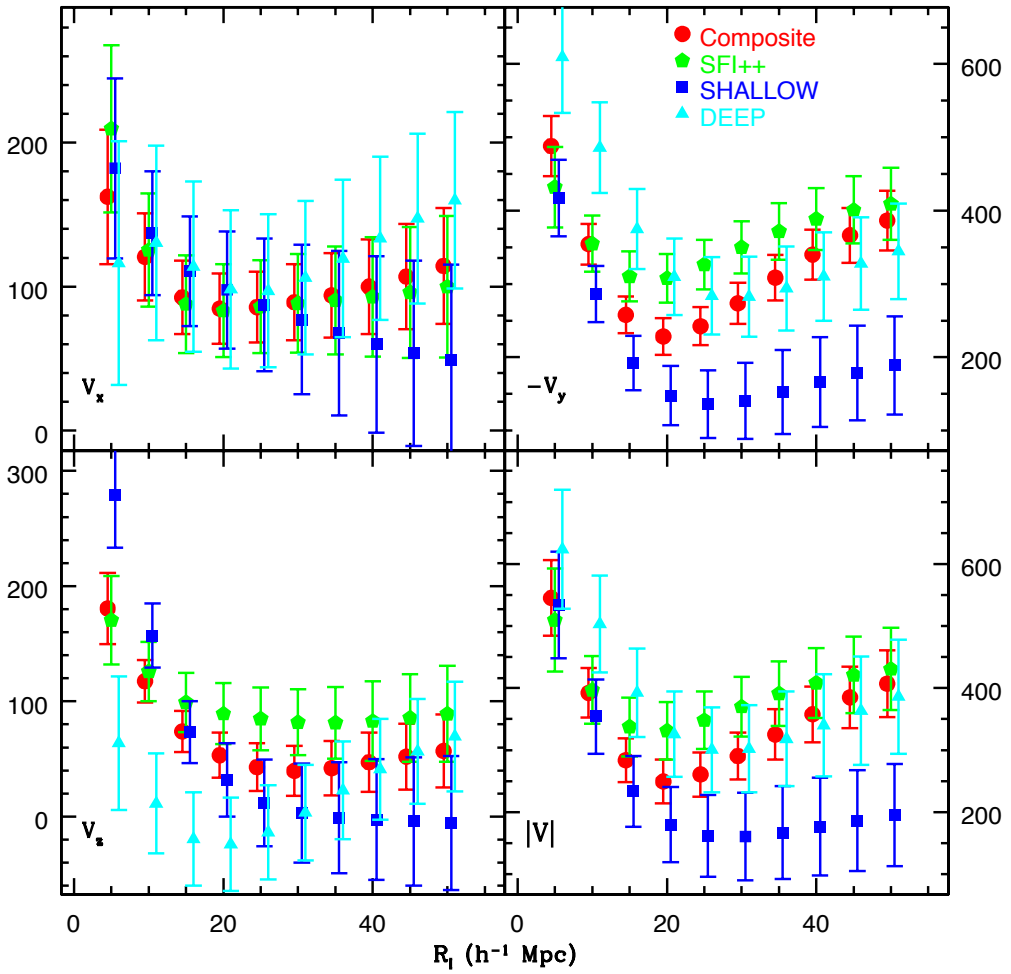

Figure 1.3: The bulk flow (x, y and z Cartesian components and magnitude $|V|$) as a function of survey volume radius R_I of the COMPOSITE survey (red) as compared to the bulk flow from the SFI++ sample (green) and the COMPOSITE sample divided into a SHALLOW (dark blue) and DEEP (light blue) subsample. (Figure 5 from Watkins, Feldman & Hudson 2009).

same data was re-analysed by Nusser & Davis (2011) using a different method, who found a bulk flow consistent with ΛCDM. Thus the question of the convergence of the bulk flow currently remains open-ended.

1.5.4 Cosmological Constraints from Peculiar Velocities

On scales of $100\,h^{-1}$ Mpc the peculiar velocity field of galaxies is an effective probe of mass fluctuations and hence is sensitive to the matter power spectrum. The power spectrum is often expressed as a two-parameter model defined by the shape of the spectrum, Γ, and the normalisation, σ_8 (the amplitude of fluctuations on a scale of $8\,h^{-1}$ Mpc). Sophisticated methods have been developed to constrain these parameters, including likelihood analysis of the covariance matrix averaged in cells

(Abate & Erdoğdu, 2009) and principal component analysis using optimal minimum-variance weighting (Watkins, Feldman & Hudson, 2009).

The observed peculiar velocity and density fields in the local volume can also be used to constrain cosmological parameters, and in particular the redshift-space distortion parameter β and linear bias parameter b (e.g. Davis et al., 2011; Bilicki et al., 2011; Turnbull et al., 2012).

Using a Fisher information matrix analysis, Burkey & Taylor (2004) found that a data set that coupled redshift and peculiar velocity information can tightly constrain a number of cosmological parameters such as the amplitude of galaxy power spectrum A_g and the shape parameter of the matter power spectrum Γ. In particular, the redshift distortion parameter β and the correlation between luminous and dark matter can be constrained to significantly better accuracy when peculiar velocity information is combined with redshift measurements.

1.6 Thesis Motivation and Outline

This thesis uses new improved methods and the largest homogeneous sample to date to determine the near-infrared Fundamental Plane. This Fundamental Plane survey provides the means to derive individual galaxy motions, and forms the largest and most far-reaching peculiar velocity sample to date. The specific objectives of this thesis are:

1. to derive the most accurate near-infrared Fundamental Plane to date, using the largest and most homogeneous near-infrared-selected sample of galaxies;

2. to develop a robust technique for fitting the FP, properly accounting for the observational errors and selection biases in the sample;

3. to investigate the physical origins of the FP and its implications for galaxy formation and evolution, by exploring the variations with a range of galaxy and environmental properties;

4. to compile the largest peculiar velocity catalogue to date and recover the overall bulk galaxy motions in the nearby universe from the 6dFGS velocity field; and

5. to compare the galaxy density and peculiar velocity fields to establish the distribution of dark and luminous matter and better constrain key cosmological parameters.

This thesis is organised as follows: Chapter 2 describes the properties of the 6dF Galaxy Survey in detail and outlines the measurement of the Fundamental Plane parameters. A key aspect of Chapter 2 is the specification of the selection criteria of the final 6dFGS FP sample. The development of a maximum likelihood method for

fitting the Fundamental Plane is presented in Chapter 3, together with comprehensive simulations and tests of the methodology. Chapter 4 presents the results of fitting the 6dFGS Fundamental Plane sample as a function of waveband, environment and morphology, and examines the implications for the structure and formation of early-type galaxies. Chapter 5 is devoted to exploration and discussion of the correlations of stellar populations with Fundamental Plane parameters. Chapter 6 describes the derivation of Bayesian FP distances and peculiar velocities for the 6dFGS galaxies, presents a cosmographic description of the local peculiar velocity field, and uses peculiar velocity measurements to put new constraints on the bulk flow and other cosmological parameters. The thesis concludes with a final summary in Chapter 7 of the research presented in the preceding chapters, and with an indication of the development of future work. In the digital version of this thesis, there are several figures in these chapters that can be viewed as interactive 3D visualisations. In Appendix A we outline the method used to create these 3D visualisation with custom C-code and the S2PLOT graphics library (Barnes et al., 2006) using the approach described in Barnes & Fluke 2008.

Chapter 2

6dFGS Fundamental Plane Data

2.1 Introduction

The Fundamental Plane is arguably the single most significant insight into the nature of early-type galaxies made over the past three decades. Foremost, it provides a direct link between the structural and kinematic properties of these galaxies over several orders of magnitude in mass. However, this strength is also its chief difficulty: a proper interpretation of the interdependencies between its parameters demands a careful and systematic treatment of data selection, incompleteness and observational errors, over multi-dimensional space. Without this attention to detail, conclusions about the nature of the Fundamental Plane (and the galaxies populating it) can be subtly misguided, or completely wrong.

The 6dFGS Fundamental Plane data used in this thesis are derived from two sources: (i) measurements of high signal-to-noise spectra from the 6dF spectrograph itself, and (ii) near-infrared photometry (and related size information) from the Two-Micron All-Sky Survey. Additional tabulations of galaxy morphology and spectral features were made by eye and included in the final sample, as well as used for further trimming. The final selection (of what we will call *The 6dF Galaxy Survey Velocity Sample, 6dFGSv*) was made by imposing limits in the following parameters:

(i) velocity dispersion (σ_0),

(ii) redshift (cz),

(iii) morphology,

(iv) apparent magnitude (m), and

(v) selection probability (S) and χ^2 (as defined by interim fits to the FP).

In this chapter we describe the nature and selection of the data that make up the 6dFGS Fundamental Plane (FP) sample. In Sections 2.3 and 2.4 we focus on the derivation of the chief parameters that define the FP, $R_e \propto \sigma_0^a \langle I_e \rangle^b$, where σ_0 is the velocity dispersion, R_e is the effective radius and I_e is the surface brightness. We adopt an abbreviated notation for these parameters where $r \equiv \log R_e$, $s \equiv \log \sigma_0$ and $i \equiv \log\langle I_e \rangle$. We derive FP parameters for approximately 10^4 of the brightest

galaxies in 6dFGS that are representative of an early-type galaxy population. The morphologies and spectra of all the galaxies in the FP sample were classified by eye, as outlined in Section 2.5. These data were used for the dual purposes of galaxy rejection as well galaxy classification. Those galaxies removed were rejected via several criteria: non-early morphological type, contamination of their fibre spectrum by an obvious disk, the real (or apparent) merger of their image with field stars or galaxies, or the presence of strong emission line features in their spectra. We then describe a selection function that accounts for the unavoidable censoring of some observables (Section 2.6). We derive the uncertainties on the Fundamental Plane parameters from measurement error in Section 2.7.

In Section 2.8 we further characterise the galaxies in the 6dFGSv sample according to (i) local environment (in terms of both cluster richness and projected density), and (ii) stellar content (including galaxy ages and metallicities). We conclude the chapter with an overview of the final catalogue for the 6dFGS Fundamental Plane sample, as employed throughout the remainder of the thesis.

2.2 The 6dF Galaxy Survey (6dFGS)

Galaxy redshift surveys have provided a greater understanding of the galaxy distribution and large-scale structure in the universe. The Six-degree Field Galaxy Survey (6dFGS) was devised to extend the existing knowledge of the local galaxy population by combining measurements of both redshifts and peculiar velocities (Jones et al., 2004, 2005, 2009). 6dFGS is a comprehensive census of galaxy spectroscopy and redshifts in the southern hemisphere. Observations were undertaken with the Six degree Field (6dF) multi-object spectrograph (Watson, Parker & Miziarski, 1998), from which the survey name derives. The survey itself was carried out over six years on the United Kingdom Schmidt Telescope (UKST) operated by the Australian Astronomical Observatory (AAO). The primary redshift survey contains measurements of more than 125 000 redshifts and has a median redshift of 0.053 ($cz_{helio} \sim 15\,900$ km s^{-1}). The redshift maps produced from this survey reveal detailed traces of the large-scale structure, as shown in Jones et al. (2009) – see Figure 2.1.

Primary targets were selected from total K band magnitudes from the Two-Micron All-Sky Survey (2MASS) Extended Source Catalog (XSC; Jarrett et al., 2000), an imaging survey of the entire sky in the near-infrared J (1.2 μm), H (1.6 μm) and K_s (2.2 μm) bands (Jarrett et al., 2000). The XSC consists of 1.6 million resolved galaxies and covers >99% of the sky to limits of $J = 15.5$, $H = 14.8$ and $K_s = 13.5$. 2MASS provides the complementary near-infrared photometry and imaging for the 6dF spectroscopy of galaxies in the local universe. Secondary 6dFGS samples were selected to approximately equivalent limits in the 2MASS J and H bands as well as the SuperCOSMOS (Hambly et al., 2001) $r_{\rm F}$ and $b_{\rm J}$ bands. The total apparent mag-

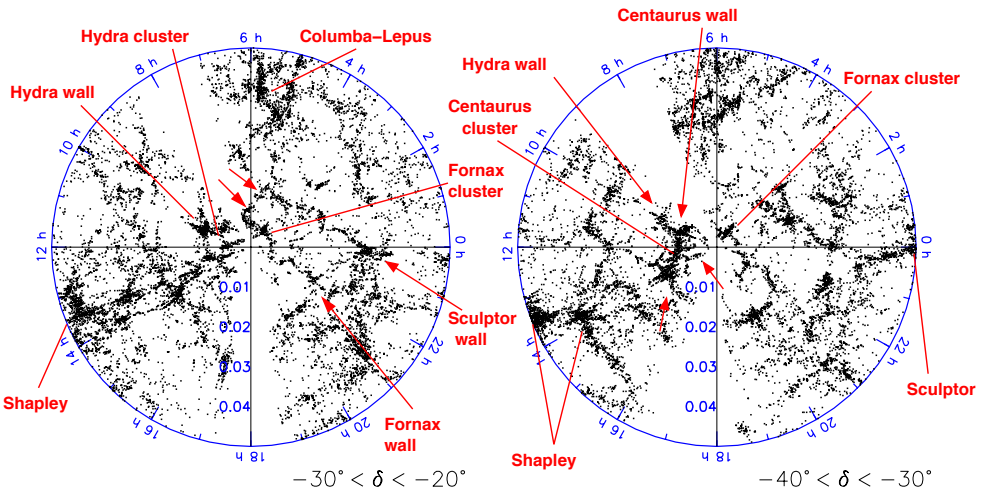

Figure 2.1: 6dFGSz radial redshift map out to $z_{helio} = 0.05$ in a declination slice of $-30° < \delta < -20°$ (*left*) and $-40° < \delta < -30°$ (*right*). Some large structures are indicated with red arrows. (Figure 8 from Jones et al. 2009).

nitude limits of the 6dFGS are $(K, H, J, r_{\rm F}, b_{\rm J}) \leq (12.65, 12.95, 13.75, 15.60, 16.75)$ which are ∼1.5 magnitudes brighter than the regime where 2MASS XSC begins to suffer incompleteness.

The 6dFGS extends across 17 000 deg^2 of the southern sky, avoiding a 10 degree-strip either side of the Galactic Plane. In this way, its JHK near-infrared selection ensures good coverage close to the Galactic Plane. In the case of the $b_{\rm J}$ and $r_{\rm F}$ samples, the survey reaches to within 20 degrees. Compared to the 2dF Galaxy Redshift Survey (2dFGRS; Colless et al., 2001b) and Sloan Digital Sky Survey (SDSS DR7; Abazajian et al., 2009) – two of the largest redshift surveys of their kind – 6dFGS is ten times the area of the 2dFGS and has twice that of SDSS. The fibre aperture size of 6dFGS is 6.7 arcsec and so the projected distance of a galaxy at the median redshift of the sample ($z_{helio} = 0.053$) is $4.8\,h^{-1}$ kpc. In terms of individual galaxy coverage, 6dFGS covers a 40% greater aperture area across each galaxy than does SDSS, and more than three times the area of 2dFGS (at their respective median redshifts).

The 6dFGS spectra and redshifts, along with the 2MASS images and photometry and a variety of associated parameters, can be accessed from the 6dFGS database at `www-wfau.roe.ac.uk/6dfgs`. This near-infrared selection is a unique feature of the 6dF Galaxy Survey and is advantageous in many respects. Near-infrared passbands are less sensitive to dust extinction, allowing measurements closer to the Galactic Plane, and are also more strongly correlated with stellar mass than bluer passbands. The consequent preference for redder, older stellar populations has the advantage of favouring early-type galaxies over star-forming late-type galaxies, and is therefore

ideal for Fundamental Plane studies.

The wide sky coverage of 6dFGS galaxies affords a detailed mapping of large-scale galaxy structures across the southern sky. These distributions (projected in Galactic coordinates) are shown for the southern (Figure 2.2) and northern galactic skies (Figure 2.3) out to a redshift of $z_{helio} \sim 0.2$. Galaxies are colour-coded by redshift and large local structures such as the Horologium-Reticulum and Shapley Supercluster are obvious.

The 6dFGS was designed as a *combined* redshift and peculiar velocity survey of galaxies (Jones et al., 2004, 2005, 2009). The chief advantage of such a combined survey is homogeneous sampling of the galaxy population over a large volume of the local universe. The 6dFGS Fundamental Plane sample is selected from the brightest (highest S/N) ellipticals, lenticulars and early-type spiral bulges in the primary sample volume out to $\sim$16 500 km s^{-1}. This sample forms the basis of the 6dFGS peculiar velocity survey (6dFGSv), which has the broad aims of mapping out the large-scale velocity field in the nearby Universe and providing tighter constraints on a range of cosmological parameters (Colless et al., 2005).

The 6dFGS peculiar velocity survey will provide the largest homogeneous peculiar velocity sample to date, leading to improved measurements of the motions in the local universe due to its wide coverage. Substantial improvement in the precision of bulk flow measurements and cosmographic description of the nearby universe will be gained from such densely distributed and deep surveys.

2.3 6dFGS Spectroscopy

2.3.1 Preselection of Spectra

We initially select galaxies for the 6dFGS Fundamental Plane sample by taking those objects from the main redshift survey with reliable redshifts less than 16 500 km s^{-1} (i.e. $z_{helio} < 0.055$). By *reliable*, we mean those galaxies whose heliocentric redshifts are beyond doubt, as reflected in their redshift quality value ($Q = 3 - 5$, as defined in Jones et al. 2004). The redshift limit occurs because the key spectral features used to measure $\log \sigma_0$ are redshifted beyond the red wavelength cut-off of the high resolution 6dF spectra used (Campbell, 2009). At higher redshifts crucial spectral features such as Fe 5270 Å, Mg b 5174 Å and Hβ 4861 Å begin to move out of the V band spectra and into the lower resolution R band spectra.[1] These criteria select around 43 000 of the available $\sim$125 000 galaxies in the full 6dFGS redshift survey.

For the 6dFGS Fundamental Plane sample we in fact impose a stricter upper redshift limit (in the CMB frame) of $cz \leq cz_{\max} = 16\,120$ km s^{-1} (Figure 2.4, in red).

[1]The *V band* and *R band* terms that we refer to here are not related to the standard Johnson *VR* broadband photometric bandpasses. Rather, they refer to *visual-* and *red-wavelength* regions of the 6dF spectrograph.

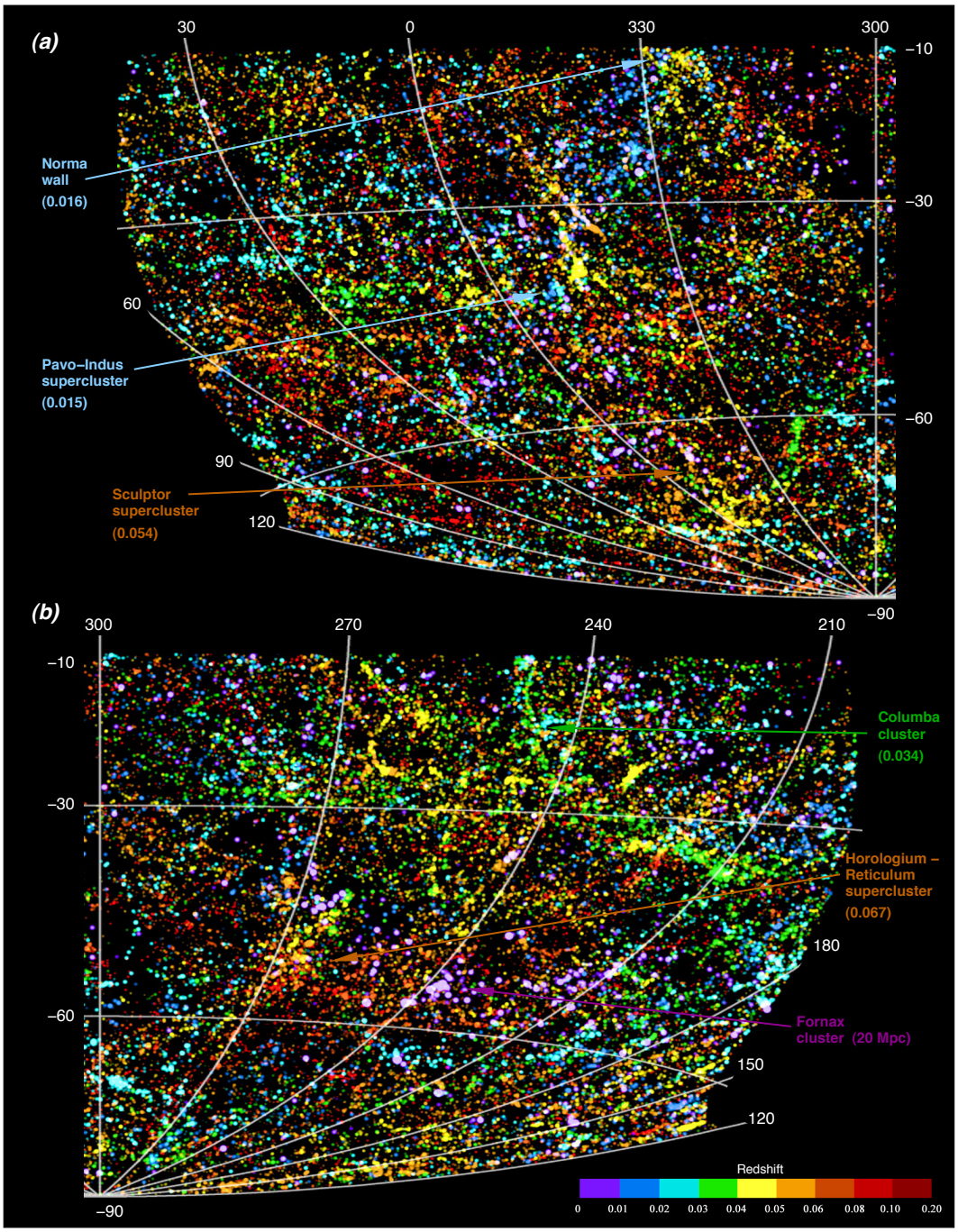

Figure 2.2: Aitoff projection of the distribution of the 6dFGS galaxies in the south, coloured by redshift from low ($z_{helio} < 0.02$) to high ($z_{helio} > 0.1$) redshift. (Figure 6 from Jones et al. 2009).

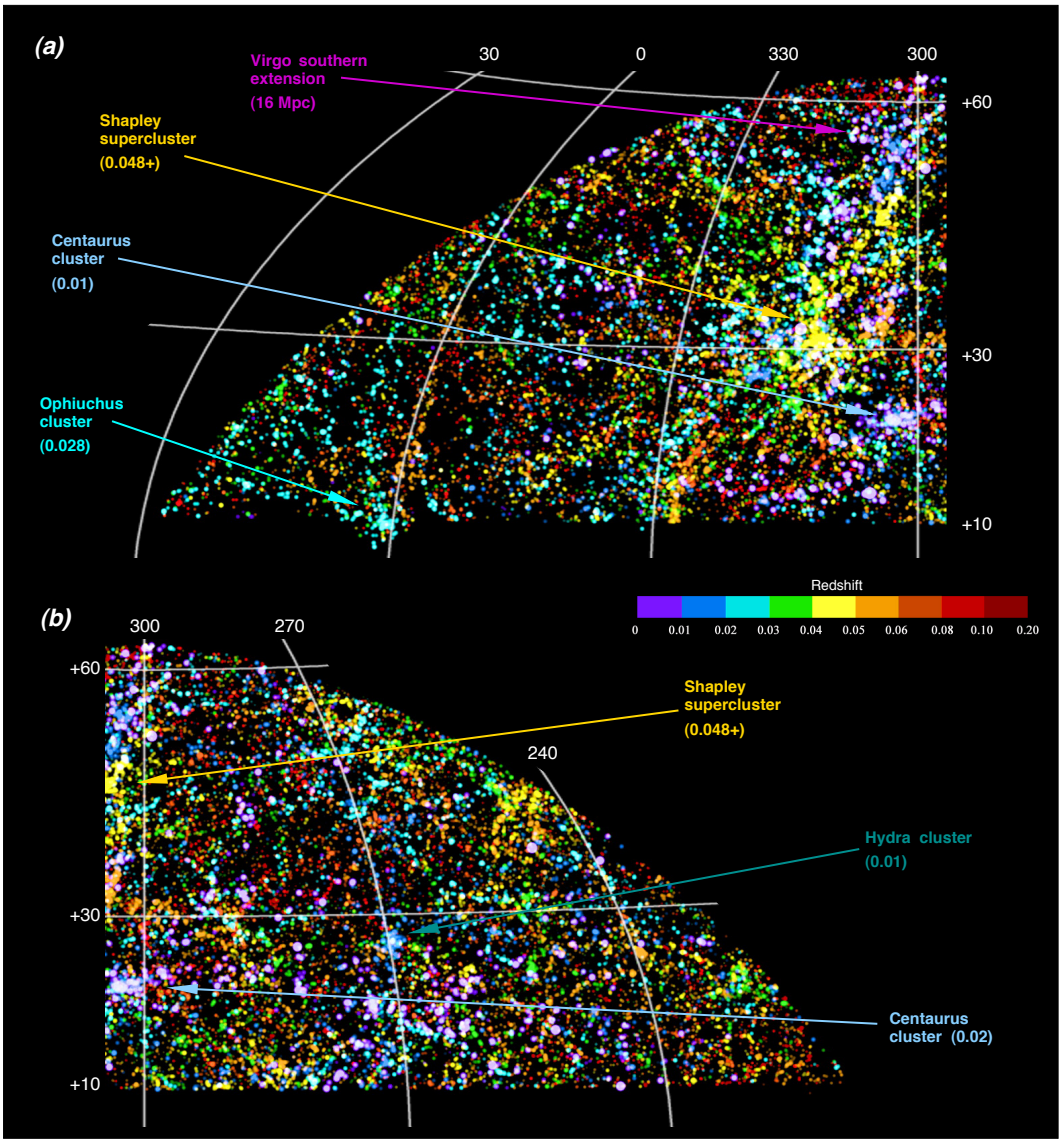

Figure 2.3: Same as for Figure 2.2 the 6dFGS galaxies in the north, coloured by redshift from low ($z_{helio} < 0.02$) to high ($z_{helio} > 0.1$). (Figure 7 from Jones et al. 2009).

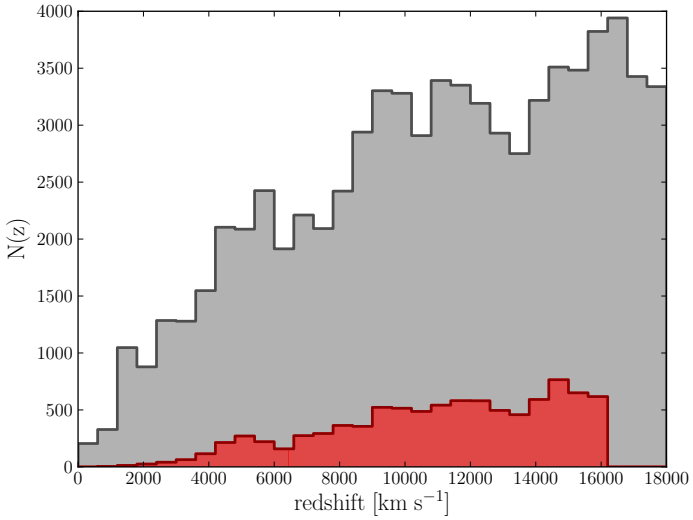

Figure 2.4: Redshift distribution of the 6dFGSv FP sample (red; $N_g = 8901$) with maximum redshift $cz_{max} = 16\,120$ km s^{-1} compared to the full 6dFGS redshift sample (grey; $N_g = 124\,646$).

This is used in order to avoid an asymmetry on the sky when redshifts are converted from the heliocentric frame to the CMB frame (which we use for the peculiar velocities), and excludes 750 galaxies. We also only include galaxies with CMB-frame redshifts high enough ($cz \geq cz_{min} = 3000$ km s^{-1}) that their peculiar velocities are not significant relative to their recession velocities and so do not appreciably increase the scatter about the FP. This removes a further 92 low-redshift galaxies from the sample. However, unlike other selection criteria, galaxies excluded from the FP fitting by these upper and lower redshift limits are re-instated in the sample when deriving Fundamental Plane distances and peculiar velocities. The maximum redshift used for the FP sample ($cz_{max} = 16\,120$ km s^{-1}) is around the median redshift of the full 6dFGS redshift sample (Figure 2.4, in grey).

The spectra of these galaxies were then cross-correlated with a range of stellar and galaxy spectral templates (see Zaritsky, Zabludoff & Willick 1995) to identify likely early-type galaxies. Only those galaxy spectra matching the templates for early-type galaxies or K-giant stars were retained as suitable spectra for the measurement of velocity dispersion.

2.3.2 Velocity Dispersions

The stellar velocity dispersion of an early-type galaxy (or spiral bulge) measures the spread in velocities of stars along a line of sight through its centre. The velocities of the stars are isotropic and are in fact the fundamental mechanism supporting early-types and spiral bulges against gravitational collapse. As such, the velocity dispersion is a kinematic measure of the total stellar mass, since galaxies of larger mass can

support a larger range of stellar orbital velocities. In practice, velocity dispersion is determined by measuring the broadening of absorption lines in the spectrum of the galaxy, where this broadening is a consequence of random stellar motions and their Doppler shift.

Central velocity dispersions were derived for the apparent early-type galaxies using the Fourier cross-correlation method of Tonry & Davis (1979). In this method, each galaxy spectrum was convolved with a range of high signal-to-noise stellar templates (also observed with the 6dF spectrograph). Stars were used as templates because of their higher-quality spectra and the fact that they have many absorption lines in common with those found in the selected galaxies. The stellar templates ranged from G8 to K3 giants. Each resultant cross-correlation spectrum had a second-order polynomial fit to its strongest peak (approximating a Gaussian broadening function). The velocity dispersion is then measured from the full width at half maximum (FWHM) of the Gaussian function for each of the templates, weighted by the magnitude of the cross-correlation.

The observed dispersions depend on the physical projected size of the measurement aperture. This varies with distance to the galaxy and so needs to be corrected on an individual galaxy basis. The velocity dispersion, σ_{ap}, measured through an aperture of size (in arcseconds), R_{ap}, was corrected to a standard circular $\log R_e/8$ aperture, where R_e is the R band effective radius of the galaxy. The effective (or half-light) radius is the scale length of the $r^{1/4}$ light profile that is found to be an excellent fit to E/S0 galaxies (de Vaucouleurs, 1948). The formal derivation of R_e is described in Section 2.4.

We correct R_{ap} to $R_e/8$ following the empirically-derived formula of Jorgensen, Franx & Kjaergaard (1995),

$$\frac{\sigma_{e8}}{\sigma_{ap}} = \left(\frac{R_e/8}{R_{ap}}\right)^{0.04} \quad . \tag{2.1}$$

The size of the 6dF fibre is 6.7 arcseconds and so $R_{ap} = 6.7/2 = 3.35$ arcseconds. (see below) . Our measurements of effective radius in the JHK near-infrared bands (also in units of arcseconds) are converted to R band radii according to

$$\begin{aligned} \log R_R &= 1.029 \log R_J + 0.140 \\ \log R_R &= 1.036 \log R_H + 0.150 \\ \log R_R &= 1.000 \log R_K + 0.190 \ . \end{aligned} \tag{2.2}$$

These were derived using a sample of 6dFGS galaxies with R band effective radii measured from the ENEAR survey (da Costa et al., 2000b). Hereafter, we refer to the aperture-corrected velocity dispersion, σ_{e8}, as simply the central velocity dispersion, σ_0.

The 6dFGS FP sample of 11 287 galaxies (Campbell, 2009) has a velocity dispersion limit ($s \geq 2.05$) that is set by the instrumental resolution of the V band 6dFGS spectra (as explained in Section 2.3.1). This limit is only achieved for galaxies with observed redshifts $cz_{helio} < 16\,500\,\mathrm{km\ s^{-1}}$,

This initial selection of galaxies furnishes a potential FP sample of galaxies with

1. early-type spectra (matched through the spectral templates),
2. sufficiently high signal-to-noise ratio ($S/N > 5\,\mathrm{\AA}^{-1}$) for reliable velocity dispersion measurements, and
3. velocity dispersions greater than the instrumental resolution limit ($\sigma_0 > 112\,\mathrm{km\ s^{-1}}$),

The velocity dispersion errors, ϵ_s, are based on the Tonry & Davis (1979) formulation derived from their Fourier cross-correlation analysis. The errors depend on the signal-to-noise measured in the cross-correlation peak but are validated by the large number of repeat velocity dispersion measurements in the 6dFGS sample. The reliability of the velocity dispersion measurements was tested through an external comparison with other surveys (Campbell, 2009). The 6dFGS velocity dispersion measurements of 744 galaxies in common with four other galaxy surveys had an average external error of ∼10%, and were free of any systematic bias.

2.4 2MASS Imaging and Photometry

The two photometric parameters of the Fundamental Plane, effective radius (R_e) and surface brightness ($\langle\mu_e\rangle$), were derived from our own measurements of the 2MASS XSC data. The relatively large point-spread function (PSF) of 2MASS (FWHM ∼ 3.2″) necessitated a PSF correction to be applied throughout. 2MASS extrapolated magnitudes (i.e. `j_m_ext`, `h_m_ext`, `k_m_ext`) were used to determine the circular apparent half-light radius ($\mathrm{r_{APP}}$) of each galaxy.

2.4.1 Effective (Half-light) Radii

The half-light radius of a galaxy, R_e, is defined as the scale length of the light distribution modelled by an $r^{1/4}$ profile (de Vaucouleurs, 1948). The $r^{1/4}$ profile is a special case (i.e. $n = 4$) of the generalised Sérsic model (Sérsic, 1963), which has the intensity profile

$$I(R) = I_e \exp\left\{-b_n\left[\left(\frac{R}{R_e}\right)^{1/n} - 1\right]\right\}\ . \tag{2.3}$$

Here, I_e is the intensity at R_e, n defines the profile shape, and b_n is a constant defined by n. de Vaucouleurs (1948) has shown the $r^{1/4}$ profile to be a good approximation

of the light distribution of early-type galaxies and the bulges of spirals.

Effective radius is measured in angular units of arcseconds, R_e^θ, and subsequently converted to physical units (h^{-1} kpc) using the angular diameter distance, D_A, where

$$\log R_e = \log R_e^\theta + \log D_A \ . \tag{2.4}$$

For a flat cosmology (with $\Omega_m = 0.3$, $\Omega_\Lambda = 0.7$, and $H_0 = 100\,h\,\mathrm{km\ s^{-1}\,Mpc^{-1}}$), angular diameter distance is defined as

$$D_A(z) = \frac{c}{1+z}\int_0^{z_0} \frac{dz'}{H_o\sqrt{\Omega_m(1+z')^3+\Omega_\Lambda}} \ . \tag{2.5}$$

The galaxies in our FP sample are sufficiently small in apparent size that the effect of atmospheric seeing must be taken into account in measurements of half-light radius. The basis for this correction was a model 2D Gaussian PSF image derived from stars in the original 2MASS images. GALFIT (Peng et al., 2002) was run with both the galaxy image and model PSF image as inputs to find the best-fit 2D Sérsic model to the galaxy. The half-light radius was determined both before and after convolution with the PSF ($\mathrm{r_{MODEL}}$ and $\mathrm{r_{SMODEL}}$). The difference $\mathrm{r_{SMODEL}}-\mathrm{r_{MODEL}}$ was then subtracted from $\mathrm{r_{APP}}$ to derive the desired PSF-corrected half-light radius (i.e. the R_e).

2.4.2 Surface Brightnesses

The effective surface brightness ($\langle\mu_e\rangle$) is the flux per unit area, averaged over the central region of the galaxy. It relates to both apparent magnitude and effective radius through the expression

$$\langle\mu_e\rangle = m + 2.5\log(2\pi R_e^2) \tag{2.6}$$

where m is any one of the 2MASS-derived apparent magnitudes (in JHK) and R_e is the effective radius (as defined above). Corrections to surface brightness are required for Galactic extinction, and the cosmological effects of surface brightness dimming and K-corrections. The correction for Galactic extinction, A_λ, is dependent on sky position. We derive our values from the all-sky maps of infrared dust emission of Schlegel, Finkbeiner & Davis (1998). Cosmological surface brightness dimming goes as the inverse fourth power of redshift, a correction of $2.5\log[(1+z)^{-4}]$ magnitudes from the equivalent surface brightness at zero redshift ($z = 0$). Cosmological K-corrections account for the effect of redshift on galaxy colours as seen through fixed passbands in the observer's frame of rest. They depend on the shape of the galaxy spectral energy distribution and so differ across galaxy type. The 2MASS galaxy photometry uses the following K-corrections for early-type galaxies (based on the

stellar population models of McLeod & Rieke 1995), $k_J = 0.7z$, $k_H = 0.2z$, and $k_K = -3.3z$.

Adjusting for all three effects gives a fully-corrected surface brightness of

$$\langle\mu_e\rangle_c = \langle\mu_e\rangle - 2.5\log(1+z)^4 - k_{cor}(\lambda) - A_\lambda \ . \tag{2.7}$$

Ultimately we want to use logarithmic units for all FP parameters. In the case of surface brightness, this means converting from magnitudes (i.e. $\langle\mu_e\rangle$ in mag arcsec^{-2}) to log-luminosity (i.e. $\log\langle I_e\rangle$ in $\mathrm{L}_\odot\,\mathrm{pc}^{-2}$), via

$$\log\langle I_e\rangle = 0.4M_{JHK,\odot} - 0.4\langle\mu_e\rangle + 8.629 \ , \tag{2.8}$$

where $M_\odot$ is the absolute magnitude of the Sun, ($M_{JHK,\odot} = 3.67$, 3.33, and 3.29 in JHK, respectively[2]).

There are 500 galaxies in the 6dFGS FP sample that are in common with three surveys that can be used as an independent check on the $\log R_e$ and $\log\langle I_e\rangle$ values we have measured. If we define a parameter, $X_{\rm FP}$, defined in terms of both radius and surface brightness,

$$X_{\rm FP} = \log R_e - b\log\langle I_e\rangle \ , \tag{2.9}$$

then we have convenient way of measuring of the robustness of the quantities derived from our photometry. This is due to the fact that the combination of photometric quantities entering the $X_{\rm FP}$ parameter serve to minimise the systematic errors. Campbell (2009) compared $X_{\rm FP}$ values from 6dFGS to literature values for the galaxies in common and found no systemic bias, and an external error of $4-10\%$. This comparison was done with photometry in the visible R band as a large sample of homogenous NIR photometry was not available at that time, effectively offsetting the radii due to galaxy colour gradients.

2.5 6dFGS Morphological Classification

Classifying galaxy morphological type in the 6dFGS Fundamental Plane sample is of paramount importance to its integrity for two reasons. First, it allows us to confirm that our spectral pre-selection has provided a sample of early-types appropriate to the task, with problem galaxies removed. Problem galaxies might be those whose photometry is compromised by a nearby object or whose spectroscopy is affected by significant light from a disk. The second advantage of morphological classification is that during eventual fitting of the FP, we can examine how that fit changes for different galaxy types. The three types we consider in this context are ellipticals, lenticulars and spiral bulges.

[2] `http://mips.as.arizona.edu/~cnaw/sun.html`

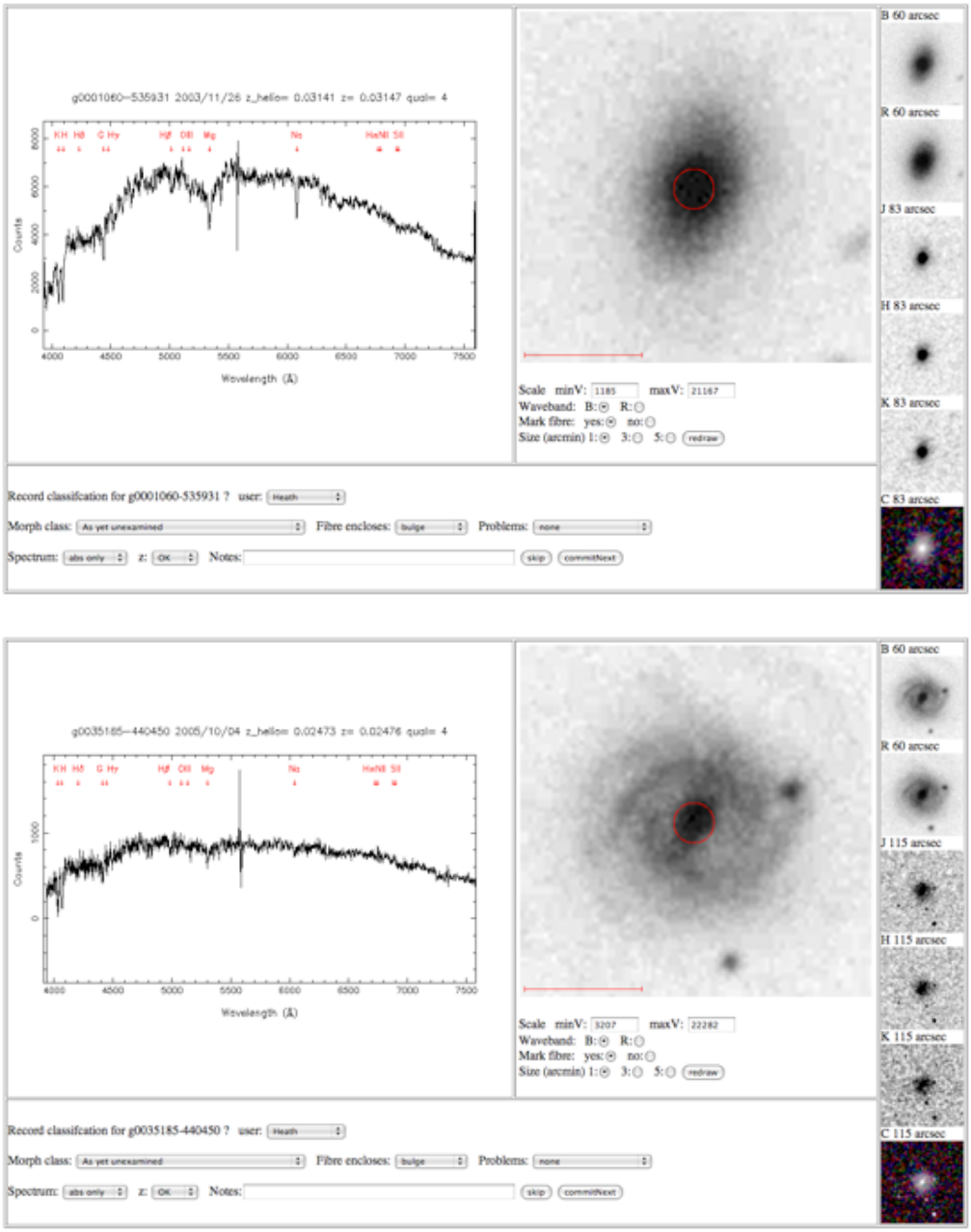

Figure 2.5: Example output used for visual classification of galaxy morphology including 2MASS and SuperCOSMOS images (right) and 6dF spectra (left). *Above:* example elliptical galaxy in 6dFGS; *below:* example spiral galaxy in 6dFGS.

All 11 287 galaxies in the preliminary 6dFGS FP sample were visually inspected to provide morphological classifications. Each galaxy was examined by up to four experienced astronomers, and on average classified twice. This was done to determine and flag any galaxies without dominant bulges that might bias, or add scatter to, the FP fits, and also to allow us to test whether ellipticals, lenticulars and spiral bulges have different FP distributions.

All of the galaxies were visually inspected using the 2MASS J, H and K band images and also the higher-resolution SuperCOSMOS images in the b_J and r_F (Figure 2.5). The galaxies were classified into the standard morphological types: elliptical (E), lenticular (S0), spiral (Sp) and irregular or amorphous (Irr), plus the transition cases E/S0, S0/Sp and Sp/Irr. Each classification was allocated a galaxy m-type (integer ranging from -4 to $+6$) such that $|m|$ preserved the basic morphological typing of galaxies without regard for whether the system was edge-on. The m-type scheme is summarised in Table 2.1.

The visual inspection process was also used to tag other galaxy attributes that could potentially influence the use of the spectral data for the FP analysis. The presence of dust lanes was flagged for this very reason. Furthermore, galaxy images had 6.7 arcsec diameter circles superimposed in order to determine whether the 6dF fibre enclosed only bulge light or whether there was significant contamination by light from the disks of S0 and Sp galaxies. At the same time, the 6dFGS spectra were scrutinised for any discernible emission features.

From this sample there were 429 galaxies excluded on the basis of one or more of the criteria defined below. If any one of these criteria was flagged by two or more classifiers, or flagged by the single classifier in cases where a galaxy was only classified once, then the galaxy was excluded as not being bulge-dominated or as problematic in some other respect. The exclusion criteria were defined as:

(i) galaxy morphology classified as irregular or amorphous;

(ii) galaxy identified as edge-on with a full dust lane;

(iii) significant fraction of light in fibre is from a disk;

(iv) light in fibre contaminated by nearby star, galaxy or defect.

We compared our classifications with 281 6dFGS galaxies in common with Galaxy Zoo (Lintott et al., 2011). The Galaxy Zoo project employed countless thousands of volunteers from the general public to inspect and assign basic galaxy types (elliptical or spiral) to the nearest galaxies in the Sloan Digital Sky Survey. For this exercise, we mapped the mean Galaxy Zoo types to a discrete scale matching our m-type parameter, where E=0 and Sp=4 (and similar for the intermediate cases in between).

Table 2.1: Morphological classification of the 6dFGSv

Morphology	m-type	Description
Edge-on disk galaxy with full-length dust lane	-4	— are most likely to be spirals, but are classified separately due to their orientation.
Edge-on disk galaxy with partial or no dust lane	-2	Probably S0s which often have dust lanes confined to their central regions. (Orientation forces us to create a separate category.)
Elliptical	0	— (including D and cD galaxies), have smooth radial profiles with no intensity discontinuities.
Transition case: Elliptical – S0	$+1$	Those instances in which it is difficult to distinguish between a cD galaxy and its halo, and the bulge of an S0 and its disk. Usually the S0 bulge will cut-off more sharply than the cD. This category is meant for such ambiguous classifications, although there are likely also to be genuine transition types.
S0 (inclined/face-on)	$+2$	Disk galaxies that can only be unambiguously classified if tilted or facing the observer. They have a clearly recognisable non-spheroidal (i.e. disk or lens) component. and are distinguishable from Es by an intensity discontinuity between bulge and disk.
Transition case: S0 – Spiral	$+3$	If the spiral structure is faint and uncertain, or in edge-on cases, shows a very faint dusty disk.
Spiral (inclined/face-on)	$+4$	Disk galaxies that can only be unambiguously classified if tilted or facing the observer. They show a clear spiral (or outer ring).
Transition case: Spiral – Amorphous	$+5$	intended for chaotic dust patterns with marginal spiral structure.
Irregular or Amorphous	$+6$	Dusty galaxies with no axial symmetry in their structure, (e.g. Magellanic Cloud types, but which are not peculiar nor cases of merging.)
Unclassifiable	*999*	Perhaps because it is a peculiar galaxy, or unable to be classified due to a problem with the image.

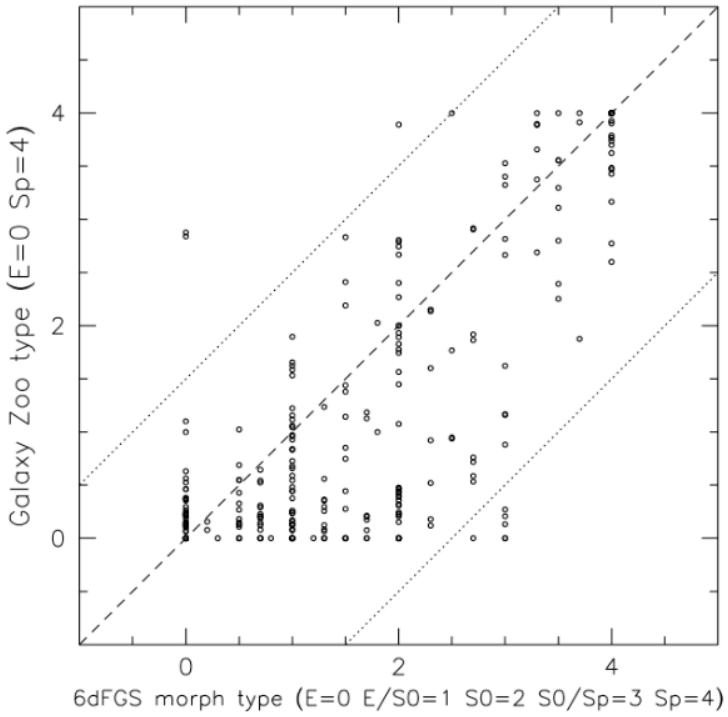

Figure 2.6: Comparison of 6dFGS galaxy morphologies and Galaxy Zoo classifications. Mean galaxy types are mapped to E=0 and Sp=4.

All problem cases (as defined above) and edge-on galaxies (which are uncertain by their very nature) were excluded.

Figure 2.6 shows the results of this comparison. The morphologies are in good agreement although Galaxy Zoo shows a tendency towards more early-type classifications. This is likely due to the *gri* composite images used by Galaxy Zoo, which overemphasise the red light dominated by the longer-lived stars. The star-forming regions that trace the arms of spiral galaxies are dominated by the light of the most luminous (but short-lived) blue stars that emit most strongly in passbands blueward of those employed by Galaxy Zoo.

2.6 Final Selection

The original 6dFGS sample was selected to apparent-magnitude limits $(J, H, K) = 13.75, 12.95, 12.65)$ in the near-infrared. This means that any subsequent FP subsample will carry the imprint of these cuts in both surface brightness and size. The mean completeness of the original 6dFGS sample down to these limits is 90 percent, with the majority of missing galaxies coming from those within $\sim$0.5 mag of the survey limit. The usual practice adopted in any statistical analysis is to weight each galaxy by the number of *expected* galaxies (sharing the same selection characteristics) over those *actually observed*. The inverse of this ratio is called the *selection*

probability. In a similar vein, we need to account for the shape of our sample in FP-space due to apparent magnitude selection through appropriate selection weights, as described below.

2.6.1 Incompleteness and Selection Probability

Our sample has slightly brighter flux limits than the original 6dFGS magnitude limits (Jones et al., 2009), reflecting the changes in the 2MASS (and, consequently, 6dFGS) magnitude limits that occurred after the 6dFGS sample was selected. To maintain high completeness in each passband over the whole sample area, we impose our own (slightly modified) magnitude limits of $J \leq 13.65$, $H \leq 12.85$ and $K \leq 12.55$. At fixed luminosity distance, the magnitude limit is a strict cut in the r–i plane; given the distance range of the sample, this flux limit translates into a graduated selection effect in the r–i plane. In fitting the FP distribution we can account for the galaxies excluded by this selection effect by weighting the likelihood of each galaxy with a selection probability as described in §3.5.

Finally, in order to reduce the impact on the fit from a small number of galaxies with extremely low selection probabilities, we impose a minimum selection probability requirement ($S \geq 0.05$).

The selection probability requirement is the only sample selection criterion that induces a significant residual bias, because it is the only one not accounted for in the normalisation of the probability distribution when computing the likelihood. We therefore correct for the (small) residual biases it produces by calibrating its impact using mock FP samples, as described in Section 3.6.2.

We also remove outliers and blunders by requiring $\chi^2 \leq 12$ (i.e. removing galaxies that deviate by more than about 3.5σ from the fitted model; see equation 3.17 and Section 3.5). This limit was chosen after analysing the χ^2 distributions of the samples in each passband with the following procedure.

We plot the χ^2 distribution for each passband sample in Figure 2.7, showing the distribution for the observed FP samples (black) and for mock galaxies samples (red). A χ^2 function was fit to each distribution with the number of degrees of freedom (d.o.f.) as a free parameter. The d.o.f. recovered from fitting to the samples for each passband, was a maximum value of ~ 2.85 for the mock simulations and ~ 2.87 for the observed samples (after the extreme χ^2 outlier were removed).

We expect that the χ^2-d.o.f. for these samples is exactly three (rather than close to it) given the three dimensions of the Fundamental Plane. However, the fitted d.o.f. was always <3 and were a poor fit to the tail of the distribution, even after relaxing or tightening the χ^2 selection limit. We then investigated, using a mock galaxy sample, the effect of removing our most severe limit i.e. from velocity dispersion, and found that this was the dominant cause of the slightly reduced d.o.f.. The χ^2 distribution

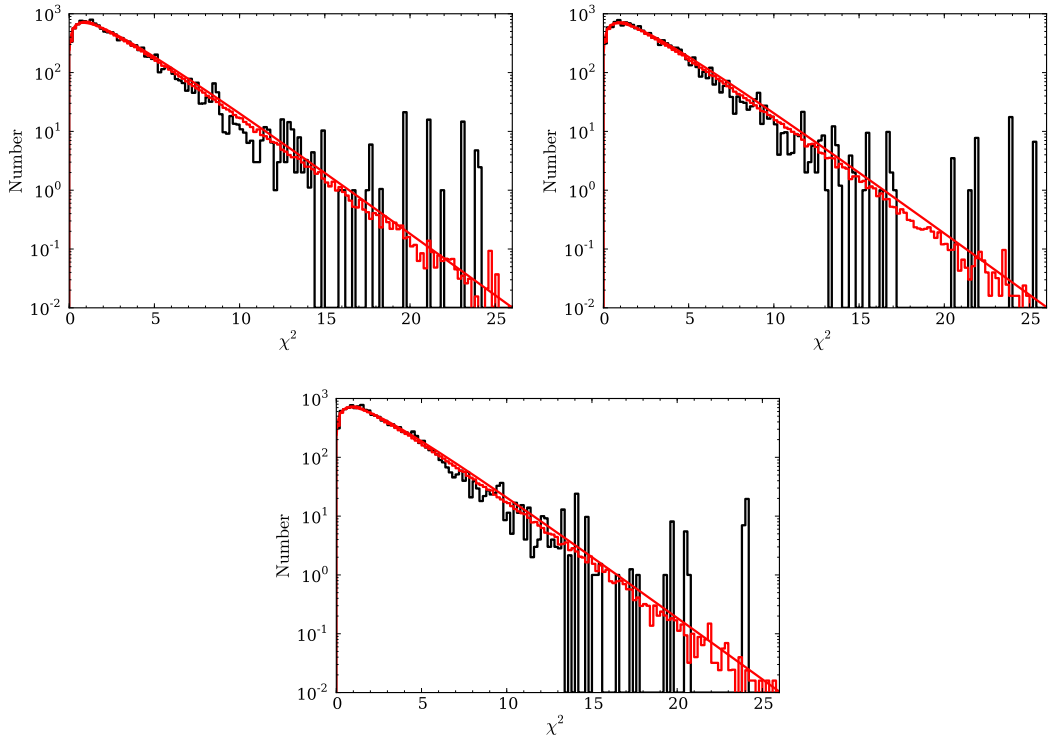

Figure 2.7: The distribution of χ^2 for the J (*top left*), H (*top right*) and K (*bottom*) band observed FP samples (black) and for mock galaxies in a sample drawn from the best-fitting 3D Gaussian model (red). The smooth curve is an analytic χ^2 distribution with 2.83 (J band), 2.85 (H band), and 2.84 (K band) degrees of freedom, derived by fitting to the mock samples (there are fewer than 3 degrees of freedom due to the censoring of the 3D Gaussian by selection effects.)

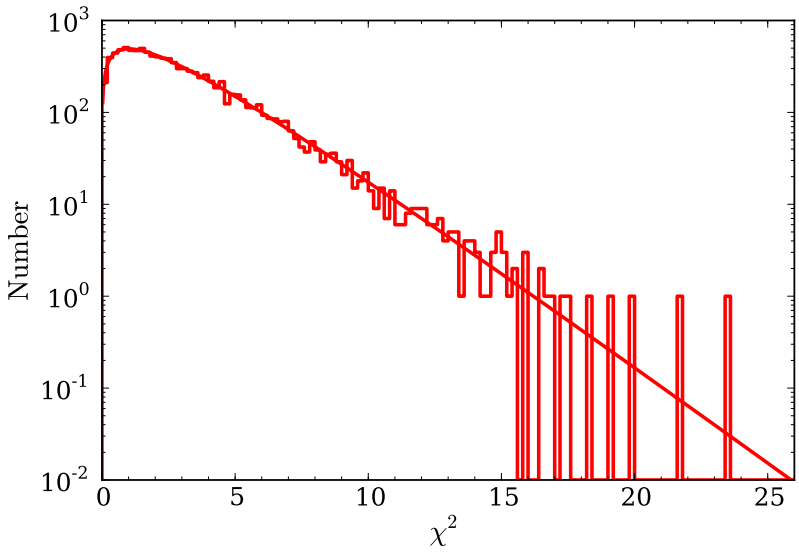

Figure 2.8: The distribution of χ^2 for a J band mock FP simulation, where no velocity dispersion limit has been applied to the sample. The fitted χ^2-distribution is plotted in red with the d.o.f. = 3.

for this mock sample is shown in Figure 2.8 with the fitted d.o.f. equal to three.

2.6.2 Fully-cleaned FP Sample

After applying all these selection criteria to obtain the samples to which we fit the FP, the numbers of galaxies remaining in each of the passbands are 8901 (J band), 8568 (H band) and 8573 (K band). The numbers of galaxies for which we can derive peculiar velocities are somewhat larger, since we can re-instate at least the galaxies excluded by the lower redshift limit.

Table 2.2 summarises each stage of the selections following the initial pre-selection.

2.7 Measurement Errors

Each galaxy in the FP sample has an associated uncertainty from the measurement errors in each of its FP observables: size, velocity dispersion and surface brightness. The treatment of these errors is often simplified or approximated when fitting the FP; e.g. La Barbera et al. (2010a) use mock galaxy samples to approximate errors and correlations. Here we show how the maximum likelihood method that ultimately becomes our tool for fitting, also allows us to to deal with the errors in all the observables (and their correlations) in a straightforward manner.

For galaxy n, the measurement uncertainties are included through the error matrix, $\mathbf{E}_n$, given by

$$\mathbf{E}_n = \begin{pmatrix} \epsilon_{r_n}^2 + \epsilon_{rp_n}^2 & 0 & \rho_{ri}\epsilon_{r_n}\epsilon_{i_n} \\ 0 & \epsilon_{s_n}^2 & 0 \\ \rho_{ri}\epsilon_{r_n}\epsilon_{i_n} & 0 & \epsilon_{i_n}^2 \end{pmatrix} . \tag{2.10}$$

Table 2.2: Summary of the 6dFGS Fundamental Plane sample selection criteria. The criteria apply to central velocity dispersion s, redshift distance cz (upper and lower limits), morphology, apparent magnitude m, selection probability S, and χ^2. The column N_{exc} shows the number of galaxies that would be removed by the specified selection cut *alone*. However, the number in brackets for each subtotal (or total) is the actual number of galaxies excluded when multiple selection limits are *combined* (i.e. without double-counting the galaxies that are eliminated by more than one selection criterion).

Sample	Selection Limit	N_g	N_{exc}	Comments
6dFGSz		124 646		full redshift sample (good quality z)
$6dFGS_{FP}$		11 287		galaxies with derived FP parameters
6dFGSv	$s \geq 2.05$		287	aperture-corrected s cut
	$cz \geq 3000$*		92	lower cz limit
	$cz \leq 16\,120$*		750	upper cz limit
	Morphology		429	flagged classification (§2.5)
	SUBTOTAL:	9794	1558 (1493)	
$6dFGSv_J$	$J \leq 13.65$		1024	
	$S \geq 0.05$		32	
	$\chi^2 \leq 12$		48	
	TOTAL:	8901	1104 (893)	J band FP sample
$6dFGSv_H$	$H \leq 12.85$		1427	
	$S \geq 0.05$		41	
	$\chi^2 \leq 12$		45	
	TOTAL:	8568	1513 (1226)	H band FP sample
$6dFGSv_K$	$K \leq 12.55$		1398	
	$S \geq 0.05$		32	
	$\chi^2 \leq 12$		46	
	TOTAL:	8573	1476 (1221)	K band FP sample

*Note: these galaxies are excluded from the fitting of the FP, but are included when deriving FP distances and peculiar velocities.

The quantities ϵ_r, ϵ_s and ϵ_i are the observational errors on the FP parameters r, s and i, and their estimation is discussed in Campbell (2009). The errors in the velocity dispersions, ϵ_s, are based on the Tonry & Davis (1979) formula derived for the Fourier cross-correlation technique, and are dependent on the measured signal-to-noise in the cross-correlation peak. These error estimates are validated by the large number of repeat velocity dispersion measurements in the 6dFGS sample. The typical error on the velocity dispersions in the 6dFGS FP sample is around 0.054 dex or 12%.

The photometric errors, ϵ_r and ϵ_i, were estimated by studying the scatter when comparing the sizes and surface brightnesses obtained from the three independent 2MASS passbands. We assume that the surface brightness colours (i.e. the values of $i_J - i_H$, $i_J - i_K$, and $i_H - i_K$) are very similar for every galaxy within each narrow range of apparent magnitude, and that the dominant cause of variation from one galaxy to the next is the error in the surface brightness measurements. We then compute the mean square deviation in surface brightness colour for the J and H bands, δ^2_{JH}, over the N galaxies within a specified apparent magnitude bin, given by

$$\delta^2_{JH} = (\Sigma_{n=1,N}[(i_{J,n} - i_{H,n}) - < i_J - i_H >]^2)/N \ . \tag{2.11}$$

If we assume that δ^2_{JH} is the sum of the mean square errors in i_J and i_H, and that δ^2_{JK} and δ^2_{HK} are likewise the sums of the mean square errors in i_J and i_K, and i_H and i_K, respectively, then we can solve for the error in i_J alone, obtaining

$$\epsilon_{i,J} = [0.5(\delta^2_{JH} + \delta^2_{JK} - \delta^2_{HK})]^{1/2} \ . \tag{2.12}$$

This is the error on i_J, which we compute separately in apparent magnitude bins of width 0.2 mag. We similarly compute $\epsilon_{i,H}$ and $\epsilon_{i,K}$, shifting the magnitude bins by the mean color of the galaxies in the sample, to get the surface brightness errors in each band as a function of apparent magnitude.

Figure 2.9 shows the J, H, and K band surface brightness errors as a function of J, H, and K apparent magnitude. We approximate the errors using the following

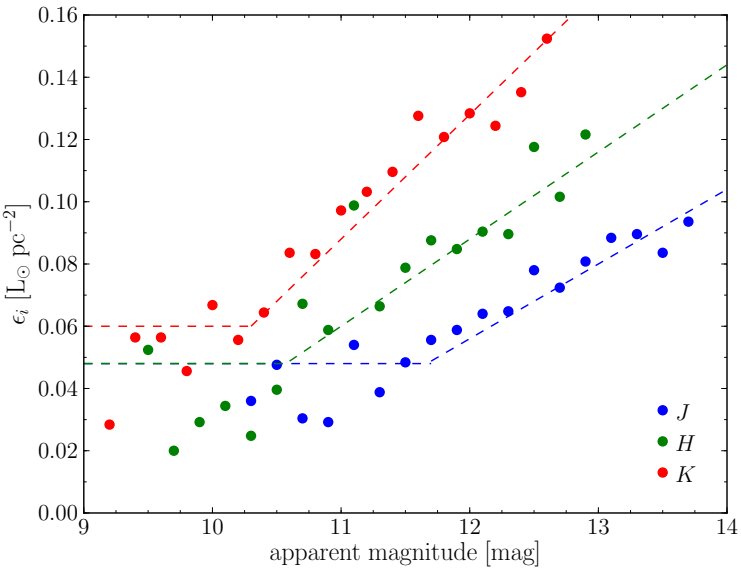

Figure 2.9: The blue (green, red) points show the derived measurement error on i_J (i_H, i_K) as a function of m_J (m_H, m_K). The measurement errors, ϵ_i, are in units of $L_\odot/pc^2$. We approximate these measurement error relations by the dashed lines of the corresponding colours, which are specified by equation 2.13.

relations, which are shown as dashed lines in Figure 2.9:

$$\begin{aligned}
\epsilon_i &= \begin{cases} 0.024\ m_J - 0.232 & m_J \geq 11.7 \\ 0.048 & m_J < 11.7 \end{cases} \\
\epsilon_i &= \begin{cases} 0.028\ m_H - 0.248 & m_H \geq 10.6 \\ 0.048 & m_H < 10.6 \end{cases} \\
\epsilon_i &= \begin{cases} 0.04\ m_K - 0.352 & m_K \geq 10.3 \\ 0.060 & m_K < 10.3\ . \end{cases}
\end{aligned} \tag{2.13}$$

Note that at bright apparent magnitudes we conservatively truncate the J and H band errors at 0.048 mag and the K band error at 0.060 mag.

There is no correlation between the errors in s and those in r or i, but there is a strong correlation between those in r and i. This is quantified by a correlation coefficient that is determined empirically by studying the distribution of the differences in r against the differences in i for pairs of independent passbands. The coefficient is found to be $\rho_{ri} = -0.95$ for all passbands. To preserve this correlation, the error in r is calculated directly from the error in i using $\epsilon_r = 0.68\epsilon_i$. The typical error in the J band on the effective radii is around 0.049 dex or 11% and on surface brightness is around 0.073 dex or 17%. However in the correlated combination in which these quantities appear in the FP, namely $X_{\rm FP} = r - bi$, the typical error on $X_{\rm FP}$ is just

0.016 dex or 4%.

There is an additional error term for effective radius, ϵ_{rp}, which allows for the uncertainty in the conversion of angular to physical units under the assumption that the galaxy is at its redshift distance (i.e. neglecting the unknown peculiar velocity). This error term is approximated as $\epsilon_{rp_n} = \log(1 + 300\,\mathrm{km\,s^{-1}}/cz_n)$, which assumes a typical peculiar velocity of 300 km s^{-1} for the galaxies in the sample (Strauss & Willick, 1995). Because we explicitly exclude galaxies at low redshifts, where the peculiar velocities are potentially large relative to the recession velocities (see §2.6), ϵ_{rp} is typically <3% and contributes less than 10% to the overall error in r.

We note that a similar error on surface brightness exists due to the use of observed redshifts (uncorrected for peculiar velocities) in computing the cosmological dimming. However, we do not include this in our measurement error matrix because it is typically less than 0.4%, which is negligible when added in quadrature to the photometric measurement errors.

2.8 Supplementary Parameters to the FP Catalogue

The final stage in our preparation of the 6dFGSv catalogue is the measurement of supplementary information relevant to the Fundamental Plane and the way in which galaxies fall upon it. Our parameters of interest are those that characterise the local environment of each galaxy, as well as its integrated stellar population (in terms of age and metallicity). We are motivated by the idea that the *intrinsic* scatter in the Fundamental Plane is due to residuals in one or more of these secondary parameters that reflect the formation history of the galaxy in some way.

2.8.1 Local Environment: Groups and Clusters

Groups and clusters in the the 6dFGS sample were identified using a friends-of-friends group-finding algorithm (Merson et al., in prep.). The algorithm follows a similar procedure to the group-finding method used to construct the 2dF Percolation-Inferred Galaxy Groups (2PIGG) Catalogue of the 2dF Galaxy Redshift Survey (Eke et al., 2004), but calibrated to the specifications (redshift depth and sample density) of the 6dFGS.

This group catalogue is used to test the universality of the Fundamental Plane (i.e. whether the FP coefficients vary with galaxy environment) and to derive mean redshifts for groups and thus group distances and peculiar velocities (in addition to distances and peculiar velocities for single galaxies). Combining galaxies into groups is important to our future peculiar velocity analysis for two reasons: (i) it minimises the 'Finger-of-God' distortions of distances and peculiar velocities produced by virialised structures in redshift space; (ii) it allows us to correct any variations in the FP with environment that might bias the distance and peculiar velocity estimates.

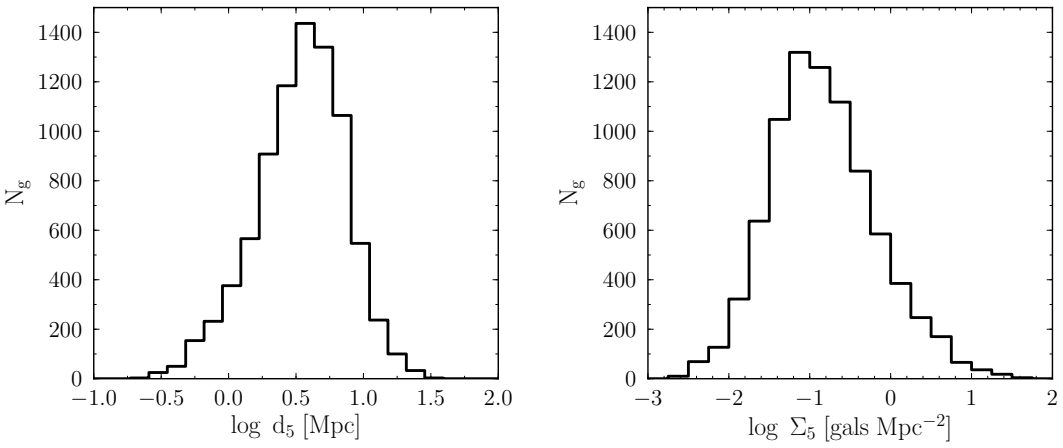

Figure 2.10: Distribution of local environment parameters for 8258 FP galaxies. *Left:* distance to the 5^{th} nearest neighbour, $\log d_5$; *right:* surface density measured to the 5^{th} nearest neighbour, $\log \Sigma_5$.

From the initial 11 287 galaxies in the 6dFGS FP subsample, there were 3186 galaxies found in groups containing at least four members (and so deemed to have reliable group membership status). The flux-limited nature of our survey meant that the faintest members of a group might not have been observed, so the richness of a group (which we use as proxy for global environment) is defined as the number, N_R, of observed galaxies in the group brighter than a specified absolute magnitude, chosen so that galaxies brighter than this would be visible throughout the sample volume. Any galaxy not in a group was given a richness $N_R = 0$, signifying its status as either a field galaxy or a bright member of a poor group.

In addition to this group catalogue, we also determine parameters that define each galaxy's local environment using the method described in Wijesinghe et al. (2012). In this catalogue, local environment is represented by the projected comoving distance, d_5 (in Mpc) to the 5^{th} nearest neighbour and the surface density, Σ_5 (in galaxies Mpc^{-2}), is therefore defined as

$$\Sigma_5 = 5/\pi \cdot d_5^2 \ . \tag{2.14}$$

To exclude contamination from foreground and background galaxies these density measurements are made within a velocity cylinder of $\pm 1000\,\mathrm{km\ s^{-1}}$. In our final FP sample, there are 8258 galaxies for which we can calculate reliable values of these estimators of local environment (see Figure 2.10).

2.8.2 Stellar Population Parameters: Age and Metallicity

To analyse the stellar content of galaxy populations in our sample and their effect on the 6dFGS Fundamental Plane, several stellar population parameters were measured

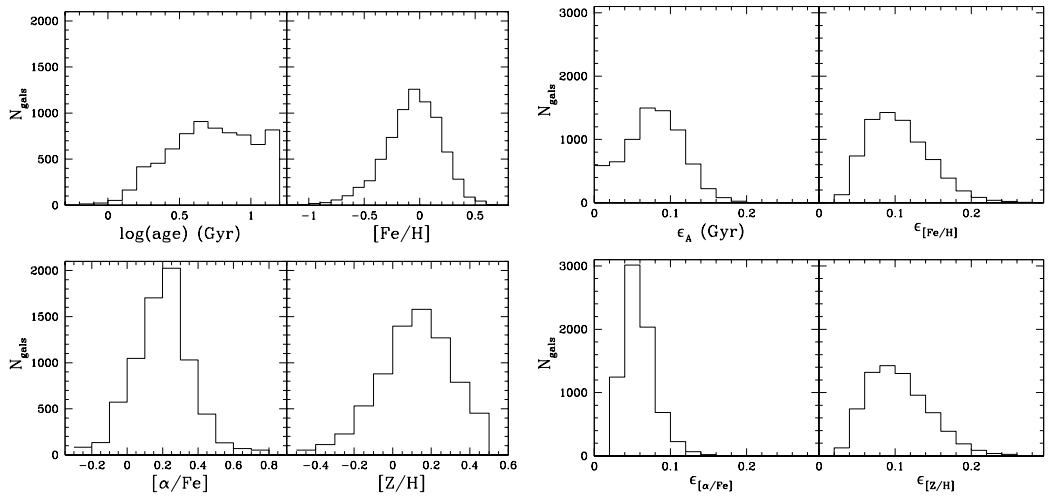

Figure 2.11: Histograms of the four (log age, [Fe/H], [α/Fe] and [Z/H]) stellar population parameters (*left*) and their statistical uncertainties (*right*) for the sub-sample of 7132 galaxies. (Figures 2 and 3 from Springob et al. 2012).

from the 6dF galaxy spectra. The quantities chosen to be representative of the galaxy stellar populations were: the age of the galaxy (log age), the galaxy metallicity (derived for both [Fe/H] and [Z/H]) and the abundance of α elements ([α/Fe] — a parameter indicative of the formation timescale of the galaxy).

These four parameters are derived using the χ^2 fitting procedure of Proctor & Sansom (2002). This technique involves minimising the χ^2 difference between Lick index (absorption-line) measurements of the observed 6dF galaxy spectra and synthetic spectra from the single stellar populations (SSP) models of Korn, Maraston & Thomas (2005). The comparison uses as many Lick indices as possible and is therefore largely insensitive to issues such as poor flux calibration (which is difficult for a such a large sample of galaxy spectra), emission line contamination and error in calibration to the Lick system. This fitting procedure is found to be more robust compared to those that use only a few indices (Proctor, Forbes & Beasley, 2004).

The final sample of stellar population parameters were required to have a quality measurement, Q_{SP} (based on the reduced χ^2 and number of indices fitted) of $Q_{SP} <= 10$, and galaxy spectra with S/N per Å > 9. From our final FP sample, this results in a sample of 7132 galaxies with reliable stellar population measurements.

The distribution for each of the stellar population parameters log age, [Fe/H], [α/Fe], and [Z/H], along with the distribution of their measurement errors is given in Figure 2.11. The values for each parameter for each individual galaxy will be presented in Proctor et. al., (in prep.)

Table 2.3: Summary of the 6dFGS Fundamental Plane sample parameters. For each parameter we list its name, unit and a short description.

Parameter	Units	Description
6dFGSid	-	Source name in the 6dFGS catalogue
R.A.	degrees	Right ascension
Dec.	degrees	Declination
z_{helio}	km s^{-1}	Heliocentric frame galaxy redshift
S/N	Å^{-1}	Signal-to-noise ratio of 6dF spectra
σ_{raw}	km s^{-1}	Raw measured velocity dispersion
2MASSid	-	Source name in the 2MASS XSC catalogue
m	mag	Total apparent JHK magnitude
$\log R_0^{SC}$	arcsec	Seeing corrected effective radius in the JHK band
μ_0^{MSC}	mag arcsec^{-2}	Magnitude and seeing corrected surface brightness in the JHK band
m-type	-	Average morphological type classification
$\epsilon_{m-\mathrm{type}}$	-	Error in m-type
MFLAG	-	Flag of problem morphological classifications
GroupID	-	Group or cluster identification number
N_R	-	Richness of galaxy group or cluster
z_{group}	km s^{-1}	Group or cluster mean redshift
d_5	Mpc	Projected comoving distance to the 5$^{\mathrm{th}}$ nearest neighbour
Σ_5	gals Mpc^{-2}	Surface density measured to the 5$^{\mathrm{th}}$ nearest neighbour
log age	Gyr	Logarithm of galaxy age
[Fe/H]	-	Fe abundance
[α/Fe]	-	α-element abundance ratio
[Z/H]	-	Overall galaxy metallicity
Q_{SP}	-	Quality of the stellar population parameter fits
ϵ_{age}	dex	Error in log age
$\epsilon_{[\mathrm{Fe/H}]}$	dex	Error in [Fe/H]
$\epsilon_{[\alpha/\mathrm{Fe}]}$	dex	Error in [α/Fe]
$\epsilon_{[\mathrm{Z/H}]}$	dex	Error in [Z/H]
M	mag	Absolute magnitude
$\log R_e$	h^{-1} kpc	Logarithm of effective radius in the JHK band (physical units)
$\log \sigma_0$	km s^{-1}	Logarithm of aperture-corrected central velocity dispersion
$\log\langle I_e\rangle$	L$_\odot$ pc^{-2}	Logarithm of mean JHK band surface brightness at R_e
ϵ_r	dex	Error in $\log R_e$
ϵ_{rp}	dex	Error in $\log R_e$ unit conversion
ϵ_s	dex	Error in $\log \sigma_0$
ϵ_i	dex	Error in $\log\langle I_e\rangle$
S	-	Selection probability weighting
cz	km s^{-1}	CMB frame galaxy redshift

2.9 Summary

In this chapter we present the catalogue of 6dFGS Fundamental Plane data used in this thesis for $\sim 10^4$ early-type galaxies reaching out to $cz_{helio} = 16\,500\,\mathrm{km\ s^{-1}}$. By combining the kinematic parameters derived from 6dF spectra (Section 2.3) and photometric parameters from 2MASS JHK band images (Section 2.4) we obtain a sample of 11 287 galaxies with measured Fundamental Plane parameters. To improve the final samples for fitting the Fundamental Plane, we impose the selection criteria outlined in Section 2.6. The final numbers of galaxies in each of the passbands are 8901 (J band), 8568 (H band) and 8573 (K band). The parameters derived for each galaxy in these samples is summarised in Table 2.3. Table 2.3 also includes the supplementary parameters required for our FP analysis of galaxy morphology (as described in Section 2.5) and galaxy environment and stellar populations (outlined in Section 2.8).

The final 6dFGS FP dataset comprises accurate FP parameters for a sample of $\sim 10^4$ galaxies to determine the near-infrared Fundamental Plane. In this thesis will also use these galaxies to measure FP distances and peculiar velocities in the 6dFGS volume and hence compile the largest peculiar velocity survey to date – the 6dFGS peculiar velocity survey (6dFGSv).

Chapter 3

Fitting the Fundamental Plane

3.1 Introduction

The Fundamental Plane relation is defined as

$$\log R_e = a \log \sigma_0 + b \log\langle I_e \rangle + c \tag{3.1}$$

where the coefficients a and b are the *slopes* of the plane and the constant c is the *offset* of the plane. In this study we employ units of h^{-1} kpc for effective radius R_e, km s^{-1} for central velocity dispersion σ_0, and $\mathrm{L}_\odot\,\mathrm{pc}^{-2}$ for mean surface brightness $\langle I_e \rangle$. We prefer to use $\log\langle I_e \rangle$ rather than $\langle \mu_e \rangle$ (which is in units of mag arcsec^{-2}), so that all our FP parameters are unscaled logarithmic quantities; this means that the relative errors and scatter are directly comparable in all axes. Throughout the rest of this thesis we adopt an abbreviated notation for the FP parameters: $r \equiv \log R_e$, $s \equiv \log \sigma_0$ and $i \equiv \log\langle I_e \rangle$. Hence we write the FP relation as

$$r = as + bi + c\ . \tag{3.2}$$

The determination of a Fundamental Plane for a sample of early-type galaxies therefore requires deriving the coefficients (i.e. a, b and c) that define equation 3.2. The standard method for deriving these coefficients is to fit the FP by modelling the distribution as a uniform plane with Gaussian scatter. These coefficients can be equivalently defined with respect to s or i rather than in terms r, as in equation 3.2, and we should note that this definition does not assume that we are necessarily using a regression on r to determine the FP coefficients. However, there is little consensus among the literature as to the best way to fit the FP, and several forms of linear regression have been used to recover the best-fit FP.

Herein lies the difficulty in comparing the results of different FP studies, as physical variations can be mimicked by biases resulting from the interaction of the fitting method with the sample selection criteria or complicated error dependencies in the data. The regression methods typically used to fit the FP broadly fall in the category of linear least squares, minimising the residuals of one of the FP variables or the residuals orthogonal to the plane. The type of least-squares regression chosen

is often determined by the focus of the study (e.g. regression on $\log R_e$ to estimate distances or regression on $\log\langle I_e\rangle$ for a stellar population study), though it is well-known that different regression methods do not necessarily converge on a unique (or even consistent) best fit, particularly if selection effects or correlated measurement errors are not fully accounted for (Saglia et al., 2001; Hogg, Bovy & Lang, 2010). This tendency to use different regression techniques interchangeably has made it challenging to compare the results of different FP studies, and in some cases has led to conclusions that are either incorrect or misleading.

There is also the additional question of whether the traditional FP model of a 2D plane with Gaussian scatter is statistically robust or truly representative of the distribution of galaxies in FP space. Saglia et al. (2001) have shown that a 3D Gaussian model provides a more accurate (and therefore less biased) representation of the galaxy distribution, at least for the large, bright, early-type galaxies in most FP samples. A maximum likelihood Gaussian model is also more versatile in dealing with complex sample selection criteria and correlated measurement errors, more robust against outliers and blunders in the data, and provides unbiased and precise estimates of the FP parameters and their uncertainties.

This chapter is concerned with revealing the inherent bias in linear regression methods used to fit the FP, motivating the development of a new FP fitting procedure. This new method models the FP distribution as a 3D Gaussian that is fit with maximum likelihood, in a similar manner to the procedure used by Saglia et al. (2001) and also Bernardi et al. (2003b). We quantify how well this model fits our 6dFGS data set (as defined in Chapter 2) and describe how mock FP samples (that are used for error analysis and model validation) are generated. The maximum likelihood fit to a 3D Gaussian will be used in subsequent chapters, as we explore the FP as a function of galaxy properties (Chapter 4) and use the FP as a distance indicator (Chapter 5).

3.2 Sources of Fundamental Plane Bias

The method of least-squares is used in FP fitting for its simplicity and relatively fast numerical implementation. However, such regression techniques can be biased by the choice of variable they minimise, the unacknowledged properties of the model they assume, the selection effects they fail to model, and the (possibly correlated) uncertainties they do not include in the fit. Simple regressions are thus likely to result in unreliable and biased fits to the Fundamental Plane.

Specifically, we identify the dominant sources of bias in FP samples, in general, as arising from: (i) the model for the FP distribution and its intrinsic scatter; (ii) selection effects, in the form of both hard and soft censoring of the sample; and (iii) the (often correlated) measurement errors on all three FP variables.

(i) *FP distribution model:* A 3D Gaussian is a simple and convenient model that is empirically found to be a better match to the (censored) observed FP distribution of early-type galaxies (Saglia et al., 2001; Bernardi et al., 2003b) than the standard model of a 2D plane-surface with Gaussian scatter in one direction. The 3D Gaussian naturally accounts not only for the scatter about the plane but also the distribution within the plane—the usual standard model effectively assumes that galaxies uniformly populate the whole plane.

(ii) *Selection effects:* Censoring of the intrinsic FP distribution is always present for observed FP samples, in both obvious and not-so-obvious ways. If the fitting technique is to avoid biased results due to censoring, it must account for all the selection effects. These include both hard selection limits in FP variables (e.g. in velocity dispersion due to the limiting instrumental resolution) or soft (i.e. graduated) selection limits in any other observable (or combination of observables, e.g. the joint selection on size and surface brightness due to the flux limit of a sample). By using maximum likelihood fitting it is straightforward to incorporate these limits (see §3.5); in comparison, for linear regressions it is significantly more difficult to account for selection effects more complex than a hard limit in one variable.

(iii) *Measurement errors:* The modelling of measurement errors in a FP sample is complicated by the fact that galaxies have different errors in all three of their FP parameters, and some of these errors are significantly correlated (notably those in r and i). Standard least-squares regression only accounts for uncorrelated measurement errors (and in naive applications, only measurement errors in one parameter). However, a maximum likelihood approach can account exactly for differing measurements errors and their correlations in a straightforward way.

3.2.1 Least-Squares Regression Bias

As discussed above, a maximum likelihood method is clearly to be preferred in principle; however it does not necessarily follow in practice that the limitations of the linear regression approach result in significant biases when fitting the FP. We therefore illustrate the consequences of using linear regressions to fit mock samples simulated by drawing galaxies from a 3D Gaussian intrinsic FP and applying realistic measurement errors and selection effects. The process of creating these mock samples is outlined in Section 3.6.1.

Three different types of mock samples were fit with each of the standard linear least-squares regressions (i.e. by minimising residuals in the distance-dependent quantity, $X_{\rm FP} \equiv r - bi$, the distance-independent quantity, $\log \sigma_0 \equiv s$, or the residuals orthogonal to the regression line) and compared to a maximum likelihood fit of a 3D Gaussian. The lefthand panels of Figure 3.1 compare the fits to these mocks using the observed effective radius versus the predicted effective radius (calculated from equa-

tion 3.2). The simplest mock sample, panel (a) and panel (e), is just the intrinsic distribution with no observational errors or selection effects applied to it; consequently it is the tightest sample and the best fit has almost no method-dependent bias.

However, when simulated observational error scatter is added to the mock FP parameters, as illustrated by panel (b), the sample is significantly skewed away from the one-to-one line as a result of the systematic variation in the observational errors with velocity dispersion, size and surface brightness, as well as the correlation between the observational errors in size and surface brightness. The skewing effect is exacerbated when censoring is also present in the mock sample; panel (c) shows the situation where the censored data is absent, while panel (d) is the same but with the censored data shown in red. This censoring is the result of observational selection effects operating on both velocity dispersion (due to the instrumental spectral resolution limit) and jointly on size and surface brightness (due to the sample apparent magnitude limit). The consequences of this skewing of the sample distribution are illustrated in panels (a)–(d) by the discrepancy between the 1-1 relation (black line) and the best-fit orthogonal regression (grey line). The overall effect shown in panels (c) and (d) is a sample with a best-fit slope of 0.84 rather than the true value of unity.

This biasing is also seen in the frequently used 2D projection of the FP showing the distance-dependent photometric parameter, $X_{\rm FP} \equiv r - bi$, and distance-independent spectroscopic parameter, $s \equiv \log \sigma_0$. The righthand panels (e)–(h) in Figure 3.1 show this projection for precisely the same mock FP samples as those in the lefthand panels. The most obvious selection effect on the mock sample in the righthand bottom panel is the velocity dispersion limit, which censors the red points to the left of the vertical dashed line at $s \geq 2.05$ (i.e. $\log \sigma_0 \geq 112\,{\rm km\ s^{-1}}$). Galaxies (in red) to the right of this line are those eliminated by the joint selection effect on r and i due to the apparent magnitude limit of the sample, which tends to censor galaxies with smaller sizes and fainter surface brightnesses in a way that depends on the galaxy's redshift.

These simulations show that the combined effect from all the selection criteria and measurement errors skews the best fit when not accounted for correctly (as is the case for least-squares fitting), most noticeably for the regressions on $X_{\rm FP}$ and s. The orthogonal fit (dashed grey line) fits the data well in this projection, but this is a consequence of fixing the value of b, a priori, to approximately the correct value. In this case, b has been fixed to the canonical value of $b = -0.75$; because this differs from the input value of $b = -0.88$ for the mock sample, the fit deviates from the input plane (particularly at the low-σ end). Additionally, Figure 3.1 also illustrates why the maximum likelihood best fit does not appear, by eye, to be a good fit to

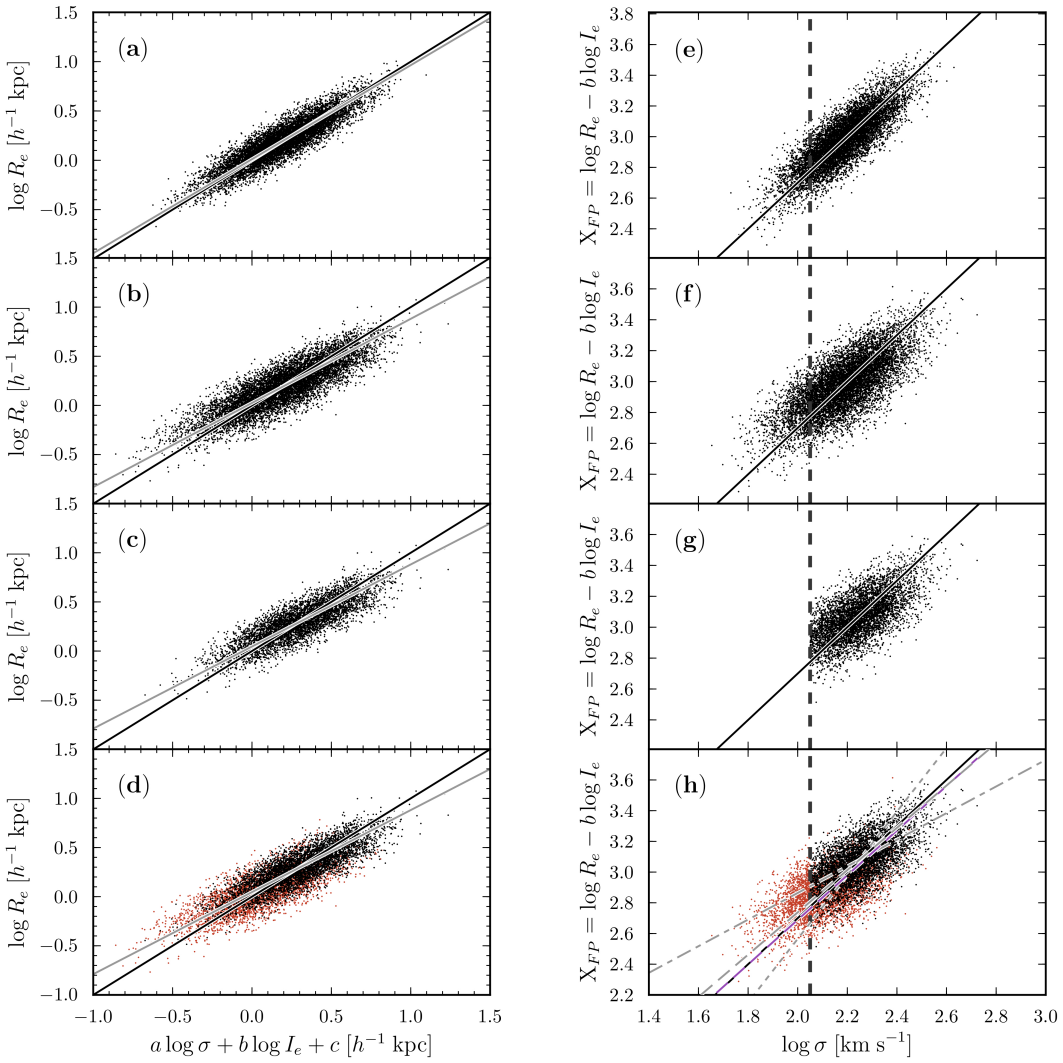

Figure 3.1: *Panels (a)–(d):* Comparison of the observed effective radius against predicted effective radius (calculated from equation 3.2) for mock samples all with the same underlying FP ($r = 1.52s - 0.89i - 0.33$) and intrinsic scatter, but subject to differing levels of measurement errors and sample censoring: (a) no measurement errors or censoring ($N_g = 8901$); (b) measurement errors but no censoring ($N_g = 8901$); (c) both measurement errors and censoring ($N_g = 5139$); (d) as for (c) but with the censored data points shown in red ($N_g = 8901$). Note that the sample is skewed from the one-to-one line (in black) by the measurement errors and the censoring of the sample, as indicated by the best-fit orthogonal regression lines for each sample (in grey). *Panels (e)–(h):* For the same mock samples as in (a)–(d), the correlation between the distance-dependent quantity, $X_{FP} \equiv r - bi$, and the distance-independent quantity, $s \equiv \log \sigma_0$. The vertical dashed black line indicates the hard cut in $\log \sigma_0$ ($s \geq 2.05$) that is applied, along with other selection cuts, in censoring the mock samples in panels (g) and (h). In each panel the solid black line indicates the intrinsic FP that the mock samples were generated from; panel (h) also shows as grey lines the standard least-squares regressions (in 2D) minimising with respect to X_{FP} (dot-dash) and s (short-dashed), and the orthogonal regression (dashed), while the solid magenta line shows the maximum likelihood fit to a 3D Gaussian.

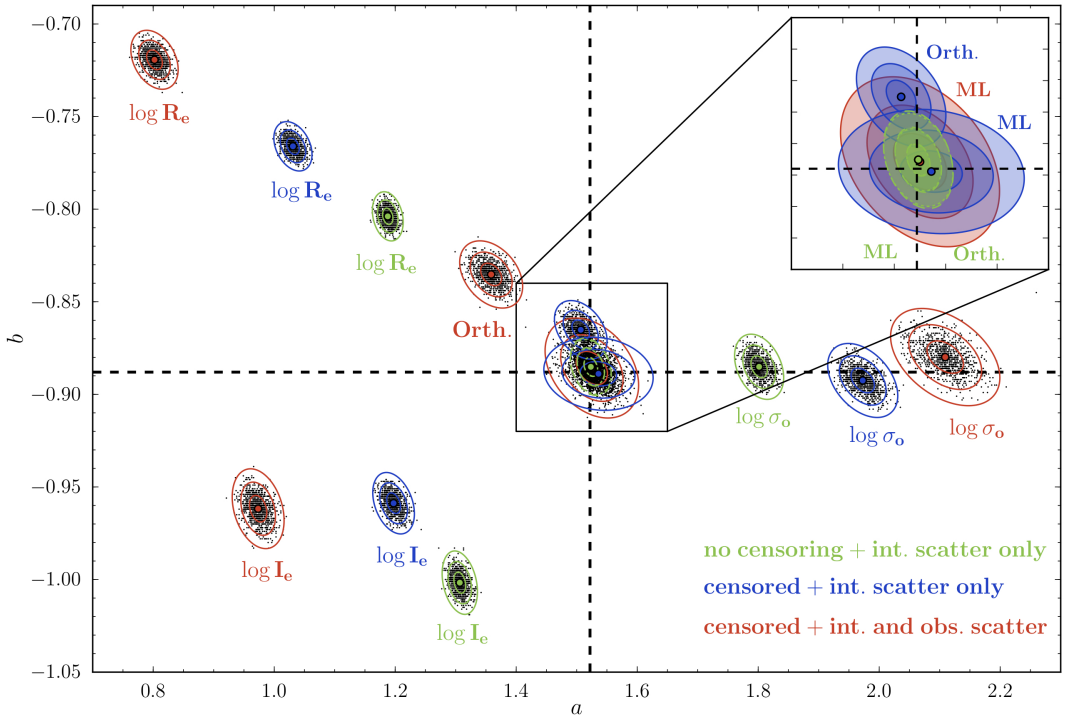

Figure 3.2: Best-fit values for the FP slopes, a and b, for each of 1000 mock FP samples (black dots) fit with least-squares regressions (in 3D) minimising the residuals in each of the three FP variables (i.e. r, s, i) and orthogonal to the plane; also fit with the maximum likelihood 3D Gaussian. The labels on each cluster of black points indicate the fitting method used; the colours indicate whether intrinsic scatter, observational errors and selection effects (censoring) are included in the mock samples, as follows: green indicates the mocks only include the intrinsic scatter of the FP; blue indicates the mocks include intrinsic scatter and censoring; red indicates the mocks include intrinsic scatter, observational scatter and censoring. The mean values of the fitted slopes (coloured dots) and the 1σ, 2σ and 3σ contours (coloured ellipses) are over-plotted in the colour corresponding to the type of mock sample. The dashed lines indicate the input FP coefficients ($a = 1.52$ and $b = -0.89$) from which all the mock samples were drawn.

the observed data—the observational errors and the selection effects systematically skew the observed sample away from the underlying intrinsic distribution.

This exercise demonstrates that, for samples with realistic observational errors and censoring, the input FP is best recovered with the maximum likelihood method. Regressions on $X_{\rm FP}$ or s lead to highly biased results, while the 2D orthogonal regression gives a reasonable fit, at least for this particular combination of observable– but only if b is fixed a priori or close to the true value. However, as shown below, regressions on r, s, i and the orthogonal residuals *all* show significant biases when fitting the FP parameters in 3D, and only the maximum likelihood method accurately recovers the FP.

To illustrate the contrast resulting from different fitting methods in 3D and the impact of various problems with the real data, we fit simulated samples with progres-

sively more realistic properties (just as in Figure 3.1). Figure 3.2 shows the fitted FP slope values (a and b) for 1000 mock samples of various types (each sample containing 8901 galaxies) using least-squares regression in 3D on each of the FP variables (i.e. r, s, i) and orthogonal to the plane, as well as our 3D Gaussian model fitted using a maximum likelihood method. The results, in green, are fits to mocks that only include the intrinsic scatter of the FP; in blue are the fits to mocks with both intrinsic scatter and sample censoring due to the selection criteria; and in red are fully realistic mocks including all the effects of intrinsic scatter, selection criteria and observational error.

The linear regressions on individual FP parameters give biased estimates of a and b, even for the 'ideal' case (green), and become progressively more strongly biased as censoring and observational errors are included (blue and red). The $\log \sigma_0$ slope, a, is biased high, even for the 'ideal' case, when an FP sample is fit by minimising the $\log \sigma_0$ residuals as compared to the other fitting techniques. This is consistent with previous studies (Jorgensen, Franx & Kjaergaard, 1996; La Barbera et al., 2010a) and is a result of the dominant selection limit in $\log \sigma_0$. The sense of the trends in both a and b, for all regression methods, agrees with those found by Saglia et al. (2001), as shown in their Figure 6.

Figure 3.2 also indicates that orthogonal regression (in 3D) is the least biased of the regression methods; however, in the most realistic simulations (red), it nonetheless returns slopes that are biased by many times the nominal precision of the fits (given by the 1σ contour). This is consistent with the fact that, for a sample with no selection criteria, orthogonal regression of a model that accounts for the FP scatter in all three axes is equivalent to a maximum likelihood fit of a Gaussian model. However, this 'ideal' case is not realistic and, in most cases, the ML Gaussian model coefficients a and b are not equivalent to the orthogonal plane-fit coefficients because the ML fit also accounts for the selection effects in the sample. The maximum likelihood fitting method clearly out-performs all the regression methods, recovering the FP slopes without significant bias for *all* types of mock samples (see the inset, which expands the region centred on the input values of the FP slopes).

As might be expected for all fitting methods the error contours on the fitted slopes become larger when censoring and observational errors are applied to the mock samples. Less obviously, the error contours for the most realistic mocks (red) are largest for the maximum likelihood fit and the regression on s; the apparently greater precision of the r, i and orthogonal regressions are obtained at the expense of very substantial biases in the fitted slopes. These regression fits thus give a false sense of precision while at the same time introducing biases that are many times larger than the nominal errors on the fitted slopes.

3.3 3D Gaussian FP Model

The Fundamental Plane is modelled as a three-dimensional Gaussian in a similar fashion to the approach adopted by the EFAR survey (Saglia et al., 2001; Colless et al., 2001b) and subsequently by Bernardi et al. (2003b). This choice of model is justified by the good empirical match it provides to the distribution of galaxies in FP space, at least for samples limited by their selection criteria to larger, brighter galaxies; we discuss the choice of this model further in Section 4.7.

In one dimension, the Gaussian probability distribution for a given galaxy, n, is

$$P(x_n) = \frac{1}{\sqrt{2\pi\sigma^2}} \exp - \frac{(x_n - \bar{x})^2}{2\sigma^2} \tag{3.3}$$

for a variable, x_n, with mean $\bar{x}$ and standard deviation σ. Generalising this to three dimensions, the probability density distribution $P(\boldsymbol{x}_n)$, for a given galaxy, n, occupying the position $\boldsymbol{x}_n = (r - \bar{r}, s - \bar{s}, i - \bar{i})$ in FP space with respect to the mean values $\bar{r}$, $\bar{s}$ and $\bar{i}$ is

$$P(\boldsymbol{x}_n) = \frac{\exp[-\frac{1}{2}\boldsymbol{x}_n^{\mathsf{T}}(\boldsymbol{\Sigma} + \mathbf{E}_n)^{-1}\boldsymbol{x}_n]}{(2\pi)^{\frac{3}{2}}|\boldsymbol{\Sigma} + \mathbf{E}_n|^{\frac{1}{2}} f_n} \tag{3.4}$$

where f_n is the normalisation factor accounting for the fact that, due to selection effects, the galaxies do not fully sample the entire Gaussian distribution. The total 3D scatter in FP space is given by the addition of the FP variance matrix, $\boldsymbol{\Sigma}$ (specifying the intrinsic scatter of the FP distribution in 3D) and the observational error matrix $\mathbf{E}_n$ (specifying the observational errors in r, s and i and their correlations; this is constructed in §2.7).

3.3.1 FP Variance Matrix

The FP variance matrix, $\boldsymbol{\Sigma}$, is defined in the space of the FP distribution with axes that are normal to the plane. $\boldsymbol{\Sigma}$ is a symmetric, positive-definite matrix, and therefore can be calculated by transforming the variance matrix of the FP variables in the native (r, s, i)-space, $\mathbf{V}$, with the normalised eigenvectors of $\boldsymbol{\Sigma}$ (see Section 3.3.3), $\mathbf{T}$, using

$$\boldsymbol{\Sigma} = \mathbf{T}^{\mathsf{T}}\mathbf{V}\mathbf{T} \tag{3.5}$$

where

$$\mathbf{T} = \begin{pmatrix} \frac{1}{\sqrt{1+a^2+b^2}} & \frac{b}{\sqrt{1+b^2}} & \frac{-a}{\sqrt{(1+b^2)(1+a^2+b^2)}} \\ \frac{-a}{\sqrt{1+a^2+b^2}} & 0 & \frac{-(1+b^2)}{\sqrt{(1+b^2)(1+a^2+b^2)}} \\ \frac{-b}{\sqrt{1+a^2+b^2}} & \frac{1}{\sqrt{1+b^2}} & \frac{ab}{\sqrt{(1+b^2)(1+a^2+b^2)}} \end{pmatrix}$$

and

$$\mathbf{V} = \begin{pmatrix} \sigma_1^2 & 0 & 0 \\ 0 & \sigma_2^2 & 0 \\ 0 & 0 & \sigma_3^2 \, . \end{pmatrix}$$

The covariance matrix, $\mathbf{\Sigma}$, is convolved with measurement errors to describe the distribution of galaxies according to our 3D Gaussian model. However the covariance matrix does not account for the effects of sample censoring/selection in FP space and therefore does not fully describe the FP fit coefficients (unless one has a full distribution of galaxies without censoring) when using a 3D Gaussian model. It is possible to use other combinations of the covariance matrix elements to derive the coefficients of FP fits with respect to other FP parameters (e.g. regression on r compared to orthogonal about the plane); but again this assumes the full Gaussian distribution is included in the sample, without censoring/selection. In the ML fit of the 3D Gaussian model, the censoring and selection effects are accounted for in the normalisation of the Gaussian probability distribution.

3.3.2 3D Gaussian Distribution Normalisation

The selection effects due to instrumental resolution of the velocity dispersion measurements are accounted for in the normalisation, f_n, of the distribution. The total volume of the probability density function is normalised to that volume which is accessible after the selection cuts are imposed such that $\int P(\boldsymbol{x}) d\boldsymbol{x} = 1$. For a trivariate Gaussian with lower selection limits of $r_{\rm cut}$, $s_{\rm cut}$ and $i_{\rm cut}$, this normalisation integral is

$$f_n = \int_{r_{\rm cut}}^{\infty} \int_{s_{\rm cut}}^{\infty} \int_{i_{\rm cut}}^{\infty} \frac{\exp[\frac{1}{2}(\boldsymbol{x}_n^{\mathsf{T}}(\mathbf{\Sigma} + \mathbf{E}_n)^{-1}\boldsymbol{x}_n)]}{\sqrt{(2\pi)^3 |\mathbf{\Sigma} + \mathbf{E}_n|}} \, d\boldsymbol{x} \tag{3.6}$$

where $\boldsymbol{x}_n = (r_n, s_n, i_n)$.

To determine f_n equation 3.6 needs to be transformed to an integral that can be evaluated numerically. That is, an integral for which the infinite integration limits have been converted to finite terminals. Hence, we transform the original integral to an integral over a unit hyper-cube using the following method outlined in Genz (1992).

The first step is to use the Cholesky decomposition of the matrix sum $\mathbf{\Sigma} + \mathbf{E}_n = \mathbf{C}$ to make the coordinate transform $\boldsymbol{x} = \mathbf{C}\boldsymbol{y}$. For a positive, definite matrix the Cholesky decomposition is formed from the product of a unique lower triangular matrix, $\mathbf{L}$, and its conjugate transpose such that $\mathbf{C} = \mathbf{L}\mathbf{L}^{\mathsf{T}}$.

Another transformation is then applied using the cumulative distribution function of the standard normal distribution function, $\Phi(y)$, i.e.

$$\Phi(y) = \frac{1}{2\pi} \int_{-\infty}^{y} \exp^{-\frac{1}{2}\theta^2} \, d\theta \, . \tag{3.7}$$

A last substitution was made to perform the integration over a unit hyper-cube, resulting in the integral

$$\begin{aligned} f_n = & \left[1-\Phi\left(\frac{r_{\rm cut}}{C_{00}}\right)\right] \\ & \times \int_0^1 \left[1-\Phi\left\{\frac{s_{\rm cut}}{C_{11}} - \frac{C_{10}}{C_{11}}\Phi^{-1}\left[(1-w_0)\Phi\left(\frac{r_{\rm cut}}{C_{00}}\right)+w_0\right]\right\}\right] \\ & \times \int_0^1 \left[1-\Phi\left\{\frac{i_{\rm cut}}{C_{22}} - \frac{C_{20}}{C_{22}}\Phi^{-1}\left[(1-w_0)\Phi\left(\frac{r_{\rm cut}}{C_{00}}\right)+w_0\right]\right. \right. \\ & - \frac{C_{21}}{C_{22}}\Phi^{-1}\left[(1-w_1)\Phi\left\{\frac{s_{\rm cut}}{C_{11}}\right.\right. \\ & \left.\left.\left. - \frac{C_{10}}{C_{11}}\Phi^{-1}\left[(1-w_0)\Phi\left(\frac{r_{\rm cut}}{C_{00}}\right)+w_0\right]\right\}+w_1\right]\right\}\right] \int_0^1 d\boldsymbol{w} \ . \end{aligned} \tag{3.8}$$

In practice, our model only includes an explicit selection cut in velocity dispersion (i.e. $\sigma \geq \sigma_{\rm cut}$) and hence $r_{\rm cut} = i_{\rm cut} = -\infty$. Equation 3.8 then reduces to

$$f_n = \int_0^1 1-\Phi\left[\frac{s_{\rm cut}}{C_{11}} - \frac{C_{10}}{C_{11}}\Phi^{-1}(w_0)\right]\, dw_0 \ . \tag{3.9}$$

3.3.3 3D Gaussian $\boldsymbol{v}$-space Axes

The Fundamental Plane space can be described either in terms of the observational parameters or in terms of the unit vectors along the principal axes of the 3D Gaussian characterising the galaxy distribution (hereafter, $\boldsymbol{v}$-space). The Fundamental Plane itself is defined by its normal vector, which is the eigenvector of the intrinsic FP variance matrix $\boldsymbol{\Sigma}$ with the smallest eigenvalue. A 3D representation of the $\boldsymbol{v}$-space axes ($\boldsymbol{v}_1$, $\boldsymbol{v}_2$, $\boldsymbol{v}_3$) with respect to the axes of the observational parameters (r, s, i) is shown in Figure 3.3.

The resulting vectors that define the axes of the Gaussian are

$$\begin{aligned} \hat{\boldsymbol{v}}_1 &= (1/\sqrt{1+a^2+b^2}) \cdot \boldsymbol{v}_1 \ , \\ \hat{\boldsymbol{v}}_2 &= (b/\sqrt{1+b^2}) \cdot \boldsymbol{v}_2 \ , \\ \hat{\boldsymbol{v}}_3 &= (ab/\sqrt{(1+b^2)(1+a^2+b^2)}) \cdot \boldsymbol{v}_3 \ , \end{aligned} \tag{3.10}$$

where

$$\begin{aligned} \boldsymbol{v}_1 &= \hat{\boldsymbol{r}} - a\hat{\boldsymbol{s}} - b\hat{\boldsymbol{i}} \ , \\ \boldsymbol{v}_2 &= \hat{\boldsymbol{r}} + \hat{\boldsymbol{i}}/b \ , \\ \boldsymbol{v}_3 &= -\hat{\boldsymbol{r}}/b - (1+b^2)\hat{\boldsymbol{s}}/(ab) + \hat{\boldsymbol{i}} \ , \end{aligned} \tag{3.11}$$

in terms of the FP slopes a and b. Equations 3.10 and 3.11 describe the same

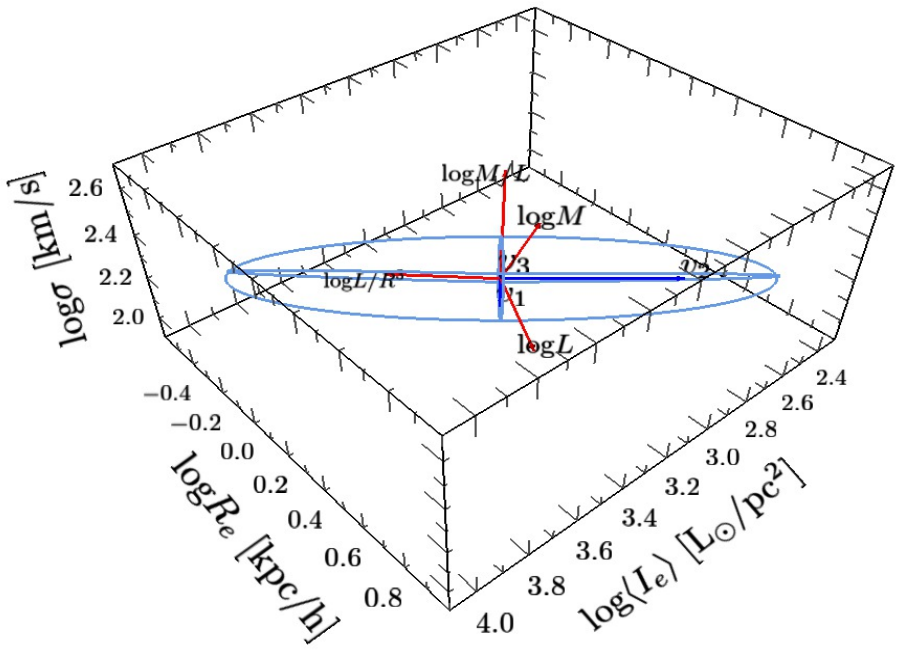

Figure 3.3: A 3D schematic of FP space, showing the vectors $\boldsymbol{v}_1$, $\boldsymbol{v}_2$, $\boldsymbol{v}_3$ (in dark blue) that define the axes (see equation 3.10) of our Gaussian model (3σ Gaussian ellipsoid in cyan) as they are oriented with respect to the three observational parameter axes r, s, i. We also show (in red) the vectors corresponding to the physical quantities $\log M$, $\log L$, $\log M/L$ and $\log L/R^3$ as defined in Section 3.3.3. We note that the angle between the vectors $\log M/L$ and $-\boldsymbol{v}_1$ and also $\log L/R^3$ and $-\boldsymbol{v}_2$ are both within 5° of each other. (Readers viewing the digital version of thesis using Acrobat Reader v8.0 or higher can enable interactive 3D viewing of this schematic by mouse clicking on the figure; see Appendix A for more detailed usage instructions.)

axes defined by Colless et al. (2001b) for the EFAR FP study, with the exception that the value of b quoted in this study is the coefficient of $\log\langle I_e\rangle$ (with units of $\mathrm{L}_\odot\,\mathrm{pc}^{-2}$) rather than the coefficient of $\langle\mu_e\rangle$ (with units of $\mathrm{mag\,arcsec}^{-2}$) used in the EFAR study, so that $b_{\rm 6dF} = -2.5\,b_{\rm EFAR}$. In this definition, as in Colless et al. (2001b), equations 3.10 and 3.11 also assume that the s-component of the $\boldsymbol{v}_2$ vector is zero. We show this simplification does not effect the accuracy of this model in Sections 3.7.1 and 4.2.3.

The direction of the short axis ($\hat{\boldsymbol{v}}_1$), which runs *through* (i.e. normal to) the plane, is fully determined by the fitted slopes a and b. The long axis ($\hat{\boldsymbol{v}}_2$), which runs *along* the plane, is fixed by being orthogonal to $\hat{\boldsymbol{v}}_1$ and having no $\log\sigma_0$ component. Although this is fixed by fiat, in fact (as we show in Section 3.7.1) this is very close to the longest natural axis of the 3D Gaussian if no constraints are placed on its direction. The advantage of this definition of $\hat{\boldsymbol{v}}_2$ lies in its physical interpretation as the direction within the FP that has no dynamical component, connecting only the photometric parameters r and i . The third, intermediate axis ($\hat{\boldsymbol{v}}_3$), which runs *across* the plane, is orthogonal to both $\hat{\boldsymbol{v}}_1$ and $\hat{\boldsymbol{v}}_2$.

Figure 3.3 also shows the relation between the $\boldsymbol{v}$-space axes and the physical quantities of dynamical mass (M), luminosity (L), mass-to-light ratio (M/L) and luminosity density (L/R^3). The logarithm of these quantities can be expressed as a function of the FP parameters, under the assumption of homology, as $m = r + 2s$ and $l = 2r + i$, where $m \equiv \log M$ and $l \equiv \log(L)$. The logarithm of mass-to-light ratio is then simply $m - l = -r + 2s - i$ and the logarithm of luminosity density is $l - 3r = -r + i$. Therefore, in the case of the virial plane, where $a = 2$ and $b = -1$, the principal axes are aligned with these quantities: $\boldsymbol{m} - \boldsymbol{l} = -\boldsymbol{v}_1$ and $\boldsymbol{l} - 3\boldsymbol{r} = -\boldsymbol{v}_2$. Even for the actual *tilted* FP we find the angle between these vectors is small, as our observed FP has $\boldsymbol{v}_1$ offset 5.0° from $\boldsymbol{m} - \boldsymbol{l}$ and $\boldsymbol{v}_2$ offset 3.6° from $\boldsymbol{l} - 3\boldsymbol{r}$. The fact that L/R^3 very nearly matches the $\boldsymbol{v}_2$ direction is a point that we revisit in Chapter 5, when we examine the physical interpretation of the distribution of galaxies in FP space.

Finally, the likelihood function, $\mathcal{L}$, is evaluated from the product of the probability density function (equation 3.4) for each galaxy, n, using

$$\mathcal{L} = \prod_{n=1}^{N_{\rm g}} P(\boldsymbol{x}_n)^{1/S_n} \ . \tag{3.12}$$

The probability density function is weighted by the fraction of the survey volume in which the galaxy could have been observed, which is inversely proportional to the selection probability, S_n, depending on the magnitude and redshift selection criteria imposed on the FP sample (see §3.5). The probability is normalised, as described

in Section 3.3.2, over the region of the FP space allowed by the selection criteria, so that $\int P(\boldsymbol{x})\ \mathrm{d}^3\boldsymbol{x} = 1$.

For convenience, the log-likelihood value ($\ln \mathcal{L}$) is used, so the product in equation 3.12 can be reduced to a summation, and then evaluated for our particular, $\mathrm{P}(\boldsymbol{x}_n)$:

$$\begin{aligned} \ln \mathcal{L} = -\sum_{n=1}^{N_\mathrm{g}} S_n^{-1} \Bigg[& \frac{3}{2}\ln(2\pi) + \ln(f_n) \\ & + \frac{1}{2}\ln(|\boldsymbol{\Sigma} + \mathbf{E}_n|) + \frac{1}{2}\boldsymbol{x}_n^{\mathsf{T}}(\boldsymbol{\Sigma} + \mathbf{E}_n)^{-1}\boldsymbol{x}_n \Bigg] \ . \end{aligned} \tag{3.13}$$

The leading factor in the summation is the weight of the n^{th} galaxy, given by the inverse of its selection probability. Within the square brackets, the first three terms are the normalisation of the probability, and the final term is half the χ^2.

3.4 Maximum Likelihood Method

In Section 3.3 we outlined the features of our 3D Gaussian model for the Fundamental Plane. To find the most probable set of parameters defining this model, Θ, given our FP data, x, we apply Bayes' Theorem

$$\Pr(\Theta|x) = \frac{\Pr(x|\Theta)\Pr(\Theta)}{\Pr(x)} \tag{3.14}$$

where $\Pr(\Theta|x)$ is the conditional probability of the model given the evidence from the data, i.e. the posterior probability distribution, $\Pr(x|\Theta)$ is the probability of the model parameters given the data (i.e. the likelihood function), $\Pr(\Theta)$ is the prior probability distribution before the data is taken into account and $\Pr(x)$ normalises the probability distribution.

Specifically, in our maximum likelihood fitting procedure we assume a constant (non-informative) prior i.e. $\Pr(\Theta) = 1$, $\Pr(x|\Theta)$ is the likelihood function for a 3D Gaussian distribution (as defined in the previous section) and the normalisation, $\Pr(x)$, is encompassed by f_n. Therefore, to estimate the best-fit parameters of our FP model given the observed data, we maximise (or minimise the negative logarithm of) the posterior probability distribution as defined by equation 3.13. In this thesis, we in fact refer to this posterior probability distribution as the *likelihood function* to reinforce the assumption of a constant prior.

The log-likelihood of equation 3.13 is maximised to simultaneously fit for the eight FP parameters that define the 3D Gaussian model discussed in the preceding section. The parameters that are derived from the fit are: the slopes of the plane (a and b, which define the directions of the 3D Gaussian's axes through equation 3.10); the centre of the 3D Gaussian in FP space ($\bar{r}, \bar{s}, \bar{i}$), which can be used to calculate the

Table 3.1: Input coefficients defining the simulated FP galaxy samples in Sections 3.4.1 and 3.4.2. Note: units are based on surface brightness in mag arcsec^{-2}.

a	b	$\bar{r}$	$\bar{s}$	$\bar{u}$	σ_1	σ_2	σ_3
1.225	0.326	0.350	2.376	16.900	0.1755	1.8745	0.7255

offset of the FP ($c = \bar{r} - a\bar{s} - b\bar{i}$); and the dispersion of the Gaussian in each of the three axes ($\sigma_1, \sigma_2, \sigma_3$). The set of parameters $\{a, b, \bar{r}, \bar{s}, \bar{i}, \sigma_1, \sigma_2, \sigma_3\}$ that maximise the log-likelihood of the 3D Gaussian are therefore those that define the best-fit model to the FP data. Note that the offset of the FP, c, is defined in terms of these parameters as $c = \bar{r} - a\bar{s} - b\bar{i}$.

3.4.1 Grid Search

Initially, the likelihood function was maximised using a brute-force grid search where the likelihood was evaluated at each point within a grid of given size and resolution. The size and resolution of the grid was defined by upper and lower bounds, as well as the number of grid points within the specified (independent) search range for each of the fitted parameters. The grid search method was chosen to test the algorithm, as it is robust, straightforward in its implementation, and can be used to map the likelihood surface and obtain error estimates in the fitted algorithm.

The efficiency and accuracy of the grid search algorithm was tested by recovering the likelihood estimates first from a simulated mock galaxy sample. The observable parameter distribution was sampled according to a Gaussian distribution with additional Gaussian measurement noise (see procedure of Section 3.6.1) with a given set of Fundamental Plane parameters chosen to be similar to previous survey fits (Table 3.1). These values reflect the units of previous surveys i.e. surface brightness in units of mag arcsec^{-2}, and are only used in this analysis of minimisation methods (within Section 3.4) - throughout the rest of this thesis, units of surface brightness $\mathrm{L}_\odot$ pc^{-2} are used exclusively.

Maximum likelihood fitting was applied to the simulated data with the grid search algorithm to evaluate the extent of any bias inherent in the algorithm itself. Initially, only five parameters $\{a, b, \sigma_1, \sigma_2, \sigma_3\}$ were fit and the rest were fixed (to the values in Table 3.1), for efficiency in testing. The speed of the grid search was mainly dependent on the size and resolution of the grid, the number of galaxies in each sample (N_g) used to calculate the likelihood function, the number of multiple likelihood fits (N_fits) and evaluation of the normalisation f_n. The grid search algorithm was therefore limited by the significant computational time associated with increasing the size of the parameters, such as N_g and N_fits, to improve the accuracy of the fitting. To resolve this issue, we implemented an optimisation algorithm to

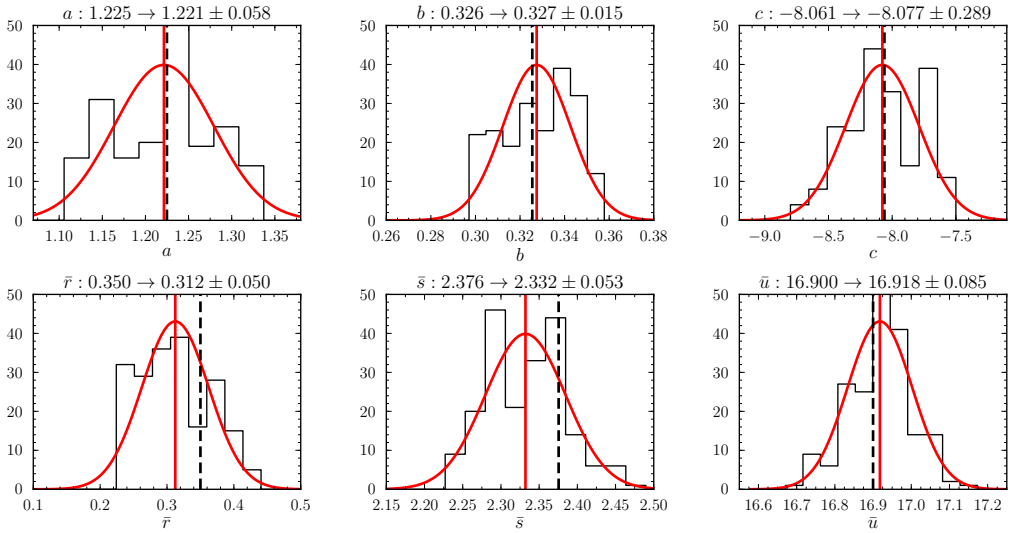

Figure 3.4: Histograms of the maximum likelihood best-fit FP coefficients, $\{a, b, \bar{r}, \bar{s}, \bar{u}\}$ from 200 simulations and $N_{\rm g} = 500$ galaxies per simulation. The likelihood function is normalised using Monte Carlo integration and the number of MC integration points is 10^2. Each panel is labelled at the top with the name of the parameter, the input value of the parameter for the 200 mock samples, and the mean and rms of the best-fit parameters obtained from ML fits to these mocks; a Gaussian with this mean and rms is overplotted on the histograms. The vertical dashed line shows the input value of the parameter and the vertical solid line shows the mean of the best-fit values.

.

calculate the maximum of the likelihood instead (see Section 3.4.2). The numerical integration of the normalisation function, f_n, was also a CPU-intensive element of the algorithm that was investigated in more detail.

In our maximum likelihood method, we account for the reduced volume due to selection cuts in the FP axes through the normalisation, f_n, defined in equation 3.6. The first numerical integration method used to evaluate f_n, was an adaptive Monte Carlo method. To mimic the real data as closely as possible, only one selection cut in the velocity dispersion (due to instrumental limitation) of $s_{\rm cut} < 2.0$ was implemented in the simulated mock sample. After this selection cut (and hence normalisation integration) was included in the fitting routine, the maximum likelihood estimates were found to be biased compared to those used to generate the sample (see Figure 3.4). In these early test simulations, the ML method was used to fit 200 mock samples, with 500 galaxies in each sample. In order for the computational time to be kept to a minimum, the Monte Carlo integration only used 100 points to evaluate f_n, which led to large errors in the derivation of f_n. For this reason, the input FP parameters were not well recovered, as can be see in Figure 3.4. Only two ($\bar{s}$ and $\bar{u}$) out of the five parameters were recovered accurately with a Gaussian distribution.

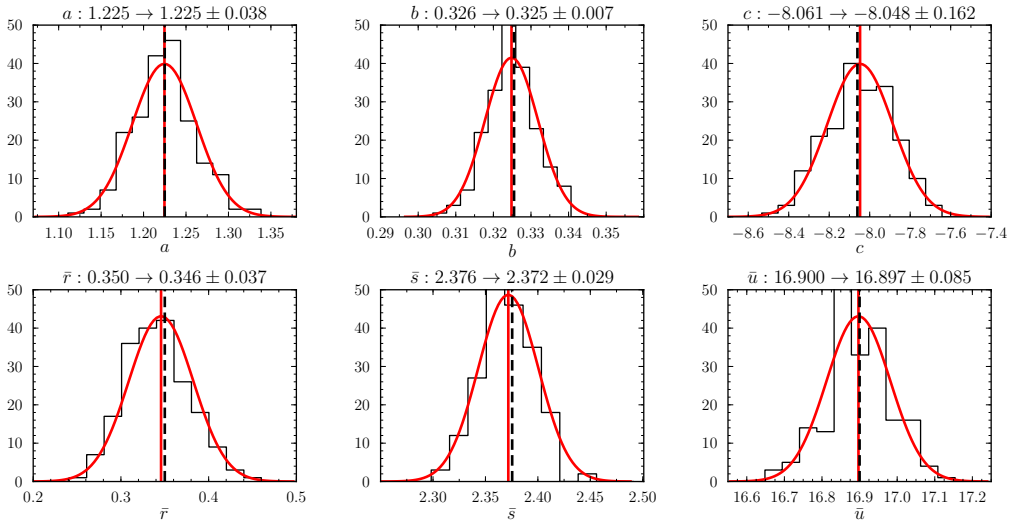

Figure 3.5: As for Figure 3.4 using 200 simulations and $N_g = 500$ galaxies per simulation but the likelihood function is normalised using Monte Carlo integration and the number of MC integration points is increased to 10^5. Each panel is labelled at the top with the name of the parameter, the input value of the parameter for the 500 mock samples, and the mean and rms of the best-fit parameters obtained from ML fits to these mocks; a Gaussian with this mean and rms is overplotted on the histograms. The vertical dashed line shows the input value of the parameter and the vertical solid line shows the mean of the best-fit values.

The fitting algorithm recovered all the parameters correctly once the number of Monte Carlo points was increased to 10^5, as shown in Figure 3.5. However, the increase in accuracy was achieved at the expense of CPU time, and so alternative integration methods were explored. The integration of the normalisation function, f_n, was found to be particularly suited to a numerical method based on adaptive multidimensional integration. The algorithm could then be extended to include all relevant selection cuts in the 6dFGS data sample, including the redshift and magnitude cuts (see Section 3.5).

3.4.2 Simplex Method

Once the grid search algorithm was able to recover the maximum likelihood estimates from a mock sample with sufficient accuracy, the algorithm was modified to find the maximum likelihood using optimisation (rather than a grid search). The method chosen was a general, optimisation algorithm that works efficiently in multiple dimensions known as the Nelder-Mead downhill simplex method (Nelder & Mead, 1965). The so-called simplex, is a geometric object (defined by the dimensions of the function being maximised) that is used to bound the minimum (or equivalently, in our case, the maximum) through reflection, expansion and contraction of its vertices.

The simplex method offers a significant reduction in computational time (from

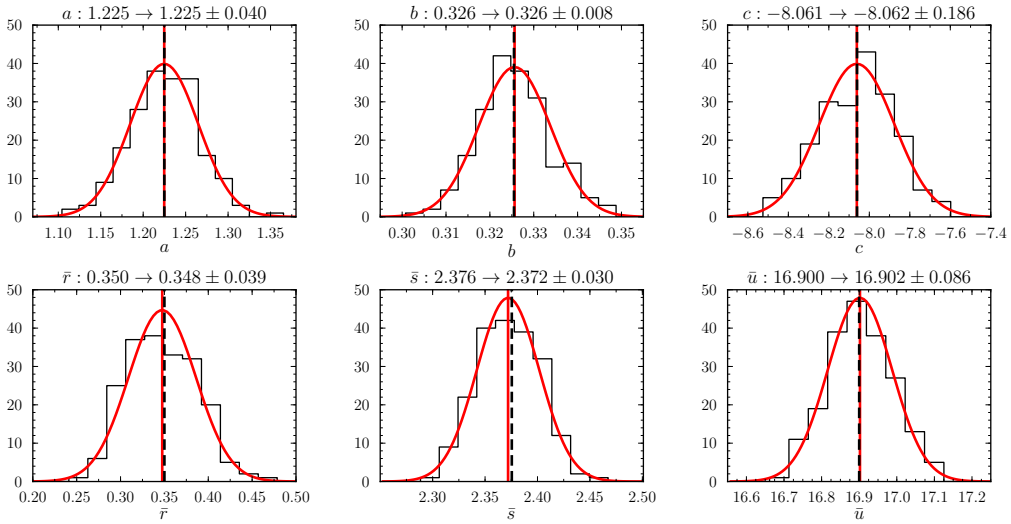

Figure 3.6: As for Figure 3.4 using 200 simulations and $N_{\rm g} = 500$ galaxies per simulation but the best-fit values are recovered using adaptive multidimensional integration and the likelihood function is maximised using simplex optimisation. Each panel is labelled at the top with the name of the parameter, the input value of the parameter for the 500 mock samples, and the mean and rms of the best-fit parameters obtained from ML fits to these mocks; a Gaussian with this mean and rms is overplotted on the histograms. The vertical dashed line shows the input value of the parameter and the vertical solid line shows the mean of the best-fit values.

hours to seconds), compared to a grid search as it samples fewer points (and hence function evaluations) to find the maximum. This speed-up in computational time was critical in being able to scale-up the mock simulations to more realistic sample sizes ($N_{\rm g} \sim 10^4$), closer to that of our sample data. Figure 3.6 shows the results from a simulation using both simplex optimisation and adaptive multidimensional integration.

3.4.3 BOBYQA Optimisation Algorithm

The final optimisation method that was explored is a non-derivative multi-dimensional optimisation algorithm called BOBYQA (Bound Optimisation BY Quadratic Approximation; Powell, 2006). BOBYQA is found to be more robust and efficient than more generic optimisation algorithms such as the Nelder-Mead simplex algorithm. It performs well under the FP fitting demands of high dimensionality (simultaneous optimisation of *eight* parameters) and large sample size ($\sim 10^4$ galaxies). The parameters in the BOBYQA algorithm that can be tuned to suit the particular function being optimised are the initial and final tolerance lengths, $\rho_{\rm beg}$ and $\rho_{\rm end}$, and the number of interpolation points between each iteration, $N_{\rm int}$.

The optimal value for these parameters is dependent on the complex interplay between the function being minimised, the number of dimensions, the number of

Table 3.2: Summary of BOBYQA simulation results. For each simulation we list the BOBYQA parameters, $N_{\rm int}$, $\rho_{\rm beg}$ and $\rho_{\rm end}$, as well as the CPU time, t, and average number of function evaluations per simulation, $\langle N_{\rm evals}\rangle$, for ten independent fits.

$N_{\rm int}$	$\rho_{\rm beg}$	$\rho_{\rm end}$	t (h:m)	$\langle N_{\rm evals}\rangle$
10	10^{-1}	10^{-6}	2:15	1298±393
14	10^{-1}	10^{-6}	1:28	642±104
17	10^{-1}	10^{-6}	1:18	587±102
20	10^{-1}	10^{-6}	1:02	556±102
30	10^{-1}	10^{-6}	0:56	449±52
45	10^{-1}	10^{-6}	1:11	527±65
10	10^{-2}	10^{-6}	2:04	1193±156
10	10^{-1}	10^{-5}	2:08	1008±127
10	10^{-1}	10^{-6}	2:15	1298±393
10	10^{-1}	10^{-7}	2:34	1141±195

fitted variables, the required accuracy of the minimised parameters, and the computation time expended. As such, it is difficult to derive the exact values analytically (Powell, 2006). Therefore these three parameters were chosen after considerable numerical experimentation by fitting to a realistic mock FP sample and varying the parameters independently. Table 3.2 summarises the results of applying our FP fitting method to the same mock sample, generated with the input parameters $\{a = 1.5, b = 0.3, \bar{r} = 0.19, \bar{s} = 2.16, \bar{u} = 17.28, \sigma_1 = 0.058, \sigma_2 = 0.655, \sigma_3 = 0.199\}$, for different BOBYQA parameters.

$\rho_{\rm beg}$ is the initial value of the trust region radius used in the iterative procedure of the function minimisation. Initially we set $\rho_{\rm beg} = 10^{-1}$ as a sensible tolerance value and increase it to 10^{-2}, finding that is does not significantly impact the accuracy or speed of the BOBYQA optimisation (Table 3.2).

$\rho_{\rm end}$ is the final value of the trust region radius used in the iterative procedure of the function minimisation which we initially set to $\rho_{\rm end} = 10^{-6}$ and vary from $10^{-5} - 10^{-7}$. The simulation using $\rho_{\rm end} = 10^{-5}$ gave sufficient final accuracy but not at the expense of computational time (c.f. $\rho_{\rm end} = 10^{-7}$).

$N_{\rm int}$ is an integer in the interval $[n + 2, \frac{1}{2}(n + 1)(n + 2)]$ where n is the number of number of fitted parameters (in this case, $n = 8$). The value of $N_{\rm int} = 2n + 1$ is recommended in Powell (2006) but tested with more sophisticated functions and problems of higher dimensionality. Therefore we tested values in the range $[10, 45]$ and including the recommended value of $N_{\rm int} = 17$ for our case. In practise, we found the case of $N_{\rm int} = 30$ was the most favourable simulation in both computational time and number of function evaluations.

In summary, the values of the optimisation parameters that were found to be

both efficient and giving the required accuracy were $\rho_{\rm beg} = 10^{-1}$, $\rho_{\rm end} = 10^{-5}$ and $N_{\rm int} = 30$. The BOBYQA algorithm with these parameters was used for all the fitting presented in this work.

3.5 Selection Criteria in the FP Model

Fundamental Plane studies must employ some form of model to analyse censored or truncated data resulting from observational selection effects. If these models fail to account for statistical effects that are due to selection, they run the risk of biasing the fitting method being used to recover the FP. We now describe the dominant selection limits—both hard and graduated—that pertain to FP data and how a maximum likelihood fitting method can account for this censoring in a straightforward and transparent manner.

A central velocity dispersion lower limit is typical of FP surveys, which are unable to measure dispersions accurately for galaxies below the instrumental resolution of the spectrograph. Because this limit is applied to just one of the FP parameters (i.e. s), the appropriate 3D Gaussian normalisation is calculated by integrating over the volume of the distribution that remains after the velocity dispersion cut, as outlined in Section 3.3.2. In this way the likelihood is appropriately normalised and the maximum likelihood method correctly accounts for the truncation of the FP in velocity dispersion by this hard selection limit.

Most FP samples are drawn from flux-limited surveys, excluding galaxies fainter than some apparent magnitude limit. This selection effect can be accounted for, as per equations 3.13 and 3.12, by weighting the individual log-likelihood of each galaxy by the inverse of its selection probability S; this is analogous to a $1/V_{max}$ weighting (Schmidt, 1968).

For the case of a FP survey with explicit redshift limits, the selection probability is proportional to the fraction of the survey volume between these limits over which a particular galaxy can be observed given the survey's apparent magnitude limit. This is a function of the limiting distance D_n^{lim} (in $h^{-1}\,$Mpc) out to which the galaxy n, with an absolute magnitude M_n, can be observed given the survey magnitude limit m^{lim} in a given passband, and can be calculated as

$$D_n^{lim} = 10^{0.2(m^{lim} - M_n - 25)} \ . \tag{3.15}$$

If the redshift cz_n^{lim} corresponding to this luminosity distance is larger (smaller) than the high (low) redshift limit of the survey, $cz_{\rm max}$ ($cz_{\rm min}$), then a galaxy with that absolute magnitude will definitely have been observed (or not) and the selection probability is $S = 1$ (0). However, if cz_n^{lim} is between the minimum and maximum survey redshifts, then the selection probability is given by the fractional comoving

volume in which it *could* be observed given the apparent magnitude limit. Therefore the selection probability function is

$$S_n = \begin{cases} 1 & cz_n^{lim} \geq cz_{\max} \\ \frac{V(cz_n^{lim}) - V(cz_{min})}{V(cz_{\max}) - V(cz_{\min})} & cz_{\min} < cz_n^{lim} < cz_{\max} \\ 0 & cz_n^{lim} \leq cz_{\min} \end{cases} \tag{3.16}$$

where $V(cz)$ is the comoving volume of the survey out to redshift cz. This definition of S_n is similar to the selection probability of the EFAR survey, although their selection probability function was based on a size parameter rather than absolute magnitude (Saglia et al., 2001).

In addition to these selection effects, an FP sample may contain spurious outliers whose significance is best characterised by a χ^2 value. The χ^2 for a particular galaxy n can be calculated as

$$\chi_n^2 = \boldsymbol{x}_n^{\mathsf{T}} (\boldsymbol{\Sigma} + \mathbf{E}_n)^{-1} \boldsymbol{x}_n \ . \tag{3.17}$$

Note that this is twice the exponent of the Gaussian probability distribution of equation 3.4 and appears in the final term of equation 3.13. Thus, χ^2 measures the departure of a galaxy in FP-space from a given 3D Gaussian model, and outliers can be identified and removed based on their extreme (and extremely unlikely) values of χ^2. The refined sample, excluding these high-χ^2 outliers, can then be re-fitted to achieve an improved fit that is not biased by outliers.

3.6 Mock Galaxy FP Samples

We now describe the process of generating mock catalogues from a model that reproduces all of the main features of the observed data sample as closely as possible. It is important that the mock samples are robust and well calibrated, as they serve several functions. We use them: to perform comparisons of different fitting methods (§3.2.1); to validate the ML fitting method and the assumption of a 3D Gaussian model for the data (§3.6.1 and §4.2.2); to correct for residual bias effects (§3.6.2); and to determine the accuracy and precision of the fits (§3.8).

3.6.1 Mock Sample Algorithm

We create mock samples from a given set of FP parameters $\{a, b, c, \bar{r}, \bar{s}, \bar{i}, \sigma_1, \sigma_2, \sigma_3\}$ using the following steps to generate each mock galaxy:

1. Draw values for v_1, v_2 and v_3 at random from a 3D Gaussian with corresponding specified variances σ_1, σ_2 and σ_3.

2. Transform these values from the $\boldsymbol{v}$-space (principal axes) coordinate system to the $\{r, s, i\}$-space (observed parameters) coordinate system using the inverse

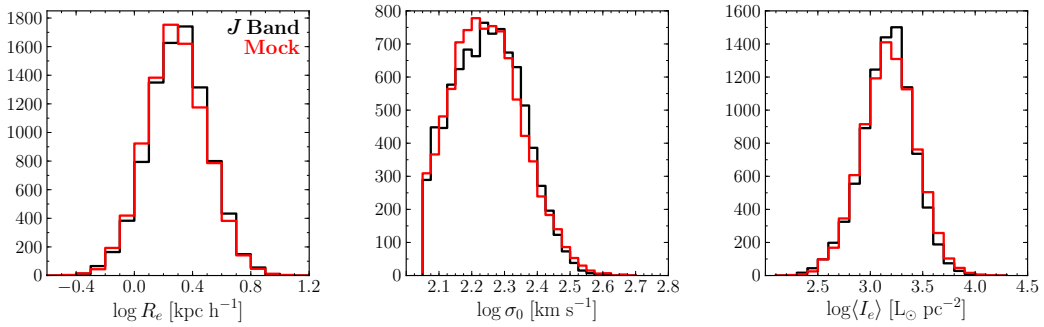

Figure 3.7: The distribution of the observed Fundamental Plane parameters $\log R_e$, $\log \sigma_0$ and $\log\langle I_e \rangle$ for the 6dFGS J band sample (black) and a mock sample (red) of the same size ($N_g = 8901$) and the same selection criteria, with FP coefficients $a = 1.52$ and $b = -0.89$.

of the relations in equation 3.10 with the specified FP slopes (a and b) and FP mean values ($\bar{r}$, $\bar{s}$ and $\bar{i}$).

3. Generate a comoving distance from a random uniform density distribution over the volume out to $cz_{\rm max} = 16\,120\,{\rm km\ s^{-1}}$ using the assumed cosmology. This comoving distance is converted to an angular diameter distance in order to calculate an angular effective radius from a physical effective radius.

4. The redshift of each mock galaxy is also derived from this comoving distance; it must be greater than the lower limit on cz to remain in the mock sample.

5. Derive an apparent magnitude from the surface brightness and effective radius (in angular units) of each galaxy which are obtained at step (2), using $m = \langle \mu_e \rangle - 2.5 \log[2\pi(R_e^\theta)^2]$.

6. Estimate rms measurement uncertainties from this magnitude using equation 2.13, via the prescription given in §2.7, and use these uncertainties to generate Gaussian measurement errors in $\{r, s, i\}$ from the error matrix in equation 2.10 (including the correlation between ϵ_r and ϵ_i).

7. Add these measurement errors to $\{r, s, i\}$ to obtain the observed values of the FP parameters; the velocity dispersion must be greater than the lower selection limit to remain in the mock sample.

8. Compute the observed magnitude using the observed values of r and i (i.e. including measurement errors); it must be brighter than the limiting magnitude for the galaxy to remain in the sample.

9. Compute the selection probability from the observed magnitude and redshift using equations 3.15 and 3.16; it must be greater than the minimum selection probability for the galaxy to remain in the mock sample.

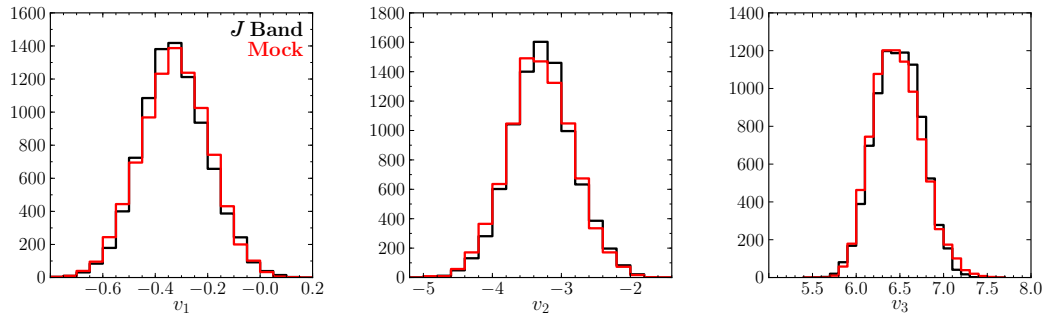

Figure 3.8: The distribution of the natural Fundamental Plane parameters v_1, v_2 and v_3 for the 6dFGS J band sample (black) and a mock sample (red) of the same size ($N_g = 8901$) and the same selection criteria, with FP coefficients $a = 1.52$ and $b = -0.89$.

This process is repeated until the desired number of galaxies is generated for the mock sample.

Figure 3.7 compares the distributions of effective radius, velocity dispersion and surface brightness for the 6dFGS J band FP sample and a mock sample generated from the best-fitting 3D Gaussian model (see below) having the same number of galaxies, the same selection criteria and the same observational errors. The mock sample accurately replicates the distribution of the galaxies in FP space, both for the observed parameters (r, s and i) and the 'natural' parameters (v_1, v_2 and v_3), which are shown in Figure 3.8. This close match between the model and the data justifies our use of a 3D Gaussian model for the distribution of galaxies in FP space.

3.6.2 Residual Bias Corrections

The only effect that is not explicitly corrected for in the maximum likelihood fitting process, and which introduces a (small) bias, is the exclusion of low-selection-probability (i.e. high-weight) galaxies. These galaxies are excluded because: (a) they may be outliers; and (b) they enter the likelihood with high weights and may therefore distort the fits. They cannot be directly accounted for in the ML fit because we do not have an explicit model for the distribution of outliers.

In practice this bias is small because only a small number of galaxies are excluded, and may be quantified under the assumptions of our model using mock samples. By applying the same selection criteria to the mocks as we do to the data, we can recover the correction Δy for the residual bias in parameter y as the difference between the value $y_{\rm obs}$ obtained from fitting the observed data and the value $y_{\rm mock}$ recovered as the average from ML fits to many mock samples:

$$\Delta y = y_{\rm obs} - y_{\rm mock} \tag{3.18}$$

where y can be any of the parameters describing the 3D Gaussian model of the FP,

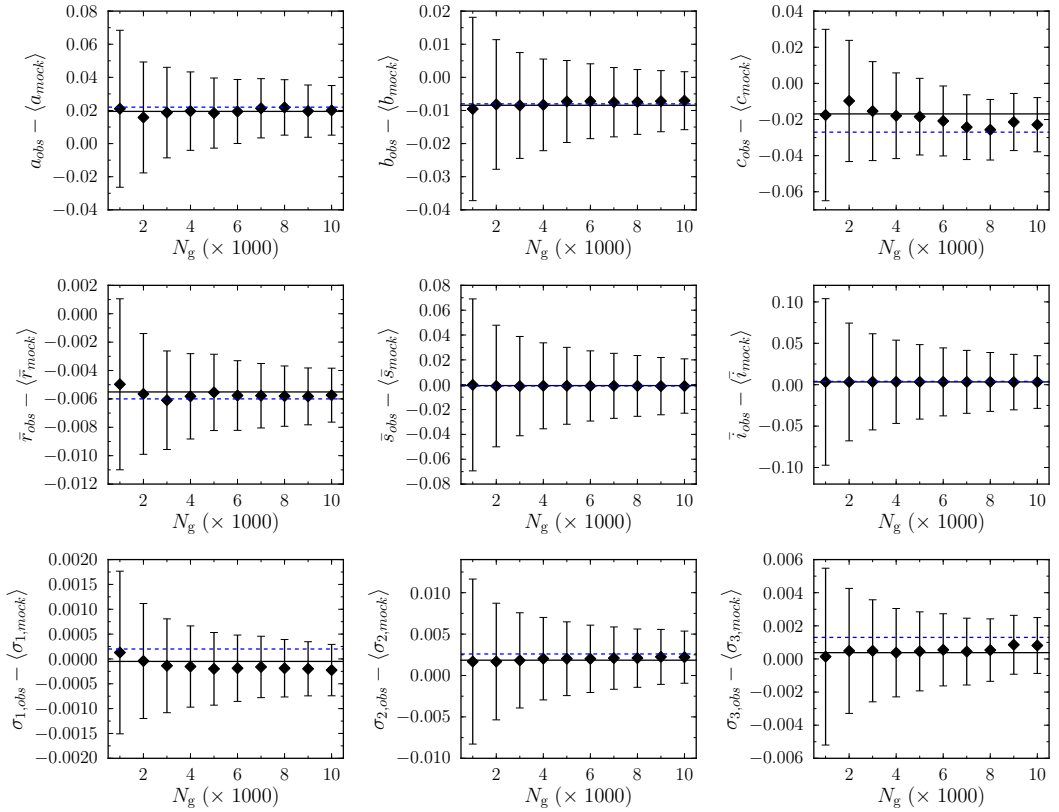

Figure 3.9: Residual bias for each of the fitted FP coefficients $\{a, b, \bar{r}, \bar{s}, \bar{i}, \sigma_1, \sigma_2, \sigma_3\}$ for mock FP samples ranging in sample size from $10^2 - 10^4$. The median from 200 mock simulations for each sample size is plotted along with error bars scaled according to N_g; a constant fit to these points is shown as a solid line. The (blue) dashed line represents the final bias correction derived from mock samples of the best-fit J band FP.

$\{a, b, c, \bar{r}, \bar{s}, \bar{i}, \sigma_1, \sigma_2, \sigma_3\}$. To correct fits to the observed data for residual bias, these corrections should be added to the best-fit FP parameter values to recover the 'true' parameters:

$$y_{\rm cor} = y_{\rm obs} + \Delta y \ . \tag{3.19}$$

These bias corrections were obtained by fitting mock samples of increasing sample size, with N_g ranging from 1000 to 10 000 galaxies (see Figure 3.9). For each sample size, 200 mock simulations were generated and fit with the maximum likelihood fitting method. The trend in bias as a function of sample size was fit with linear regression, which appears as a solid line in Figure 3.9. For all fitted parameters the bias correction was found to be constant for all sample sizes.

It is possible that the fitted parameters are covariant with each other, which could result in a correlated bias between different parameters. However the residual bias corrections are very small, and any covariance between the fitted parameters has a negligible effect (with the exception of c, as it is derived from the other fitted

Table 3.3: Residual bias correction for the best-fit FP coefficients. These corrections are added to the fitted parameters to remove the residual bias. Note that these corrections are small for all parameters.

a	b	c	$\bar{r}$	$\bar{s}$	$\bar{i}$	σ_1	σ_2	σ_3
0.022	-0.008	-0.027	-0.006	-0.001	0.004	0.0002	0.0026	0.0013

parameters).

Once it was established that the bias induced by selection effects was robust against sample size, we derived the final bias corrections from 200 mock samples of the best-fit J band Fundamental Plane. This value was therefore employed as a fixed bias correction for all parameters regardless of sample size. This correction is plotted as a dashed line in Figure 3.9 to demonstrate its consistency and independence of sample size; corrections are listed for each fitted FP parameter in Table 3.3.

3.7 Extending the 3D Gaussian FP Model

In this section, we propose two alternate FP models that extend the existing model (derived in this chapter), with the intent of testing their robustness and efficiency in later chapters. In doing so, we will establish our 3D Gaussian model to be superior in both respects.

3.7.1 Additional σ-component of 3D Gaussian Vectors

Our 3D Gaussian model of the FP assumes that the s-component of the $\boldsymbol{v}_2$ vector is zero; i.e. that the vector representing the longest axis of the 3D Gaussian lies wholly in the r–i plane. This is based in part on previous studies (Saglia et al., 2001; Colless et al., 2001b), and is also assumed for convenience and simplicity.

We can test how accurate this assumption is by extending the vector definitions of equation 3.10 to include this component, with coefficient k, defining the set of axes

$$\begin{aligned}
\boldsymbol{v}_1 &= \hat{\boldsymbol{r}} - a\hat{\boldsymbol{s}} - b\hat{\boldsymbol{i}}, \\
\boldsymbol{v}_2 &= \hat{\boldsymbol{r}} - k\hat{\boldsymbol{s}} + (1-ka)\hat{\boldsymbol{i}}/b, \\
\boldsymbol{v}_3 &= (ka^2 - a + kb^2)\hat{\boldsymbol{r}} + (ka - 1 - b^2)\hat{\boldsymbol{s}} + (kb + ab)\hat{\boldsymbol{i}}
\end{aligned} \tag{3.20}$$

and then including this extra parameter in our fitting algorithm.

3.7.2 Additional Age Component in FP Model

The Fundamental Plane possesses an intrinsic scatter that can not be explained entirely by measurement errors, and the origin of which is still a source of debate in

the literature (see D'Onofrio et al. 2006 for a review). Studies of the Fundamental Plane usually investigate whether galaxy properties correlate with residuals from the plane in order to explain this scatter (e.g. Jorgensen, Franx & Kjaergaard, 1996; Pahre, de Carvalho & Djorgovski, 1998; Bernardi et al., 2003b; Gargiulo et al., 2009; Graves, Faber & Schiavon, 2009b).

In this section we develop the method to incorporate a trend in the direction of the plane with the smallest scatter ($\boldsymbol{v}_1$ in our Gaussian model), as a means to motivate its use in Chapter 5. Here we ascertain whether a trend in stellar content (in particular, we will focus on galaxy age) can be incorporated into the FP model and used to reduce the overall scatter of the FP by exploring a very simple extension of the model that includes a linear trend with age through the FP.

We include an age component in our existing FP model by adding log age as a fourth dimension in FP space along with r, s and i. We assume that age varies almost entirely in the $\boldsymbol{v}_1$ direction (normal to the plane) as suggested by the results of Springob et al. (2012). We therefore assume the $\boldsymbol{v}_2$ and $\boldsymbol{v}_3$ vectors have no age component, and derive a fourth $v-$space vector that is orthogonal to the other three vectors. The resulting vector definition of this new 4D Gaussian model is

$$\begin{aligned}
\boldsymbol{v}_1 &= \hat{\boldsymbol{r}} - a\hat{\boldsymbol{s}} - b\hat{\boldsymbol{i}} - k_A\hat{\boldsymbol{A}},\\
\boldsymbol{v}_2 &= \hat{\boldsymbol{r}} + \hat{\boldsymbol{i}}/b,\\
\boldsymbol{v}_3 &= -\hat{\boldsymbol{r}}/b - (1+b^2)\hat{\boldsymbol{s}}/(ab) + \hat{\boldsymbol{i}}\\
\boldsymbol{v}_4 &= \hat{\boldsymbol{r}} - a\hat{\boldsymbol{s}} - b\hat{\boldsymbol{i}} + (1+a^2+b^2)\hat{\boldsymbol{A}}/k_A
\end{aligned} \tag{3.21}$$

where k_A is the component of $A = \log \text{age}$ in the $\boldsymbol{v}_1$ direction. Additional parameters that need to be fitted along with k_A in this model are the centroid of 4D Gaussian in A ($\bar{A}$) and the intrinsic scatter in the $\boldsymbol{v}_4$ vector (σ_4); this gives a total of 11 free parameters to be fitted.

Both the intrinsic variance matrix, $\boldsymbol{\Sigma}$, and observed measurement error matrix, $\mathbf{E}$ are also extended to four dimensions to include σ_4 and age measurement errors ϵ_A, respectively. If we assume that the age error measurements, ϵ_A, are uncorrelated with errors in the other FP parameters, then for each galaxy, n, the revised error matrix, $\mathbf{E}_n$ is

$$\mathbf{E}_n = \begin{pmatrix}
\epsilon_{r_n}^2 + \epsilon_{rp_n}^2 & 0 & \rho_{ri}\epsilon_{r_n}\epsilon_{i_n} & 0\\
0 & \epsilon_{s_n}^2 & 0 & 0\\
\rho_{ri}\epsilon_{r_n}\epsilon_{i_n} & 0 & \epsilon_{i_n}^2 & 0\\
0 & 0 & 0 & \epsilon_{A_n}^2 \ .
\end{pmatrix} \tag{3.22}$$

Finally, the selection effects from galaxy age are incorporated into the normalised probability density function of the 4D Gaussian model in a similar way to Section 3.3.2. For a 4D Gaussian with lower selection limits of r_{cut}, s_{cut} and i_{cut} and

$A_{\rm cut}$, this normalisation integral is

$$f_n = \int_{r_{\rm cut}}^{\infty}\int_{s_{\rm cut}}^{\infty}\int_{i_{\rm cut}}^{\infty}\int_{-\infty}^{A_{\rm cut}} \frac{\exp[\frac{1}{2}(\boldsymbol{x}_n^{\mathsf{T}}(\boldsymbol{\Sigma}+\mathbf{E}_n)^{-1}\boldsymbol{x}_n)]}{\sqrt{(2\pi)^4|\boldsymbol{\Sigma}+\mathbf{E}_n|}}\,d\boldsymbol{x} \tag{3.23}$$

where $\boldsymbol{x}_n = (r_n, s_n, i_n, A_n)$. This integral is transformed using the same procedure from Section 3.3.2 and again, there are no explicit selection limits in the r and i direction (so $r_{\rm cut} = i_{\rm cut} = -\infty$). Equation 3.23 then reduces to

$$\begin{aligned} f_n = \int_0^1 \left\{1 - \Phi\left[\frac{s_{\rm cut}}{C_{11}} - \frac{C_{10}}{C_{11}}\Phi^{-1}(w_0)\right]\right\}\int_0^1 \left(1 + \Phi\left[\frac{A_{\rm cut}}{C_{33}} - \frac{C_{30}}{C_{33}}\Phi^{-1}(w_0)\right.\right. \\ \left.\left. -\frac{C_{31}}{C_{33}}\Phi^{-1}\left\{(1-w_1)\Phi\left[\frac{s_{\rm cut}}{C_{11}} - \frac{C_{10}}{C_{11}}\Phi^{-1}(w_0)\right] + w_1\right\} - \frac{C_{32}}{C_{33}}\Phi^{-1}(w_2)\right]\right)\int_0^1 d\boldsymbol{w} \end{aligned} \tag{3.24}$$

3.8 Performance of the ML model

The distribution of the parameters derived from ML fits to 1000 mock samples (each sample containing 8901 galaxies, as for the 6dFGS J band sample) are shown in Figure 3.10. Note that the residual bias corrections (the differences between the input parameters and the mean of the fitted parameters) are comparable to or less than the rms scatter in the fits (i.e. comparable to or less than the random errors in the fitted values). This highlights the accuracy with which the ML method recovers the FP parameters even in the presence of significant observational errors and various types of sample censoring.

3.9 Summary

We have demonstrated that significant biasing can occur when deriving a best-fit FP using least-squares regression, the predominant fitting method used in previous studies. Standard regression techniques implicitly assume models that fail to accurately represent the underlying distribution of galaxies in FP space, and moreover do not fully account for observational errors and selection effects that tend to bias the best-fit plane.

We show that a 3D Gaussian provides an excellent empirical match to the distribution of galaxies in FP space for the 6dFGS sample, and we use a maximum likelihood fitting technique to properly account for all the observational errors and selection effects in our well-characterised sample.

After considerable testing of brute force grid-search methods and a generic simplex routine, a more sophisticated optimisation algorithm, BOBYQA, was chosen to maximise the likelihood function of the 3D Gaussian model to accurately recover the best-fit of the FP galaxies.

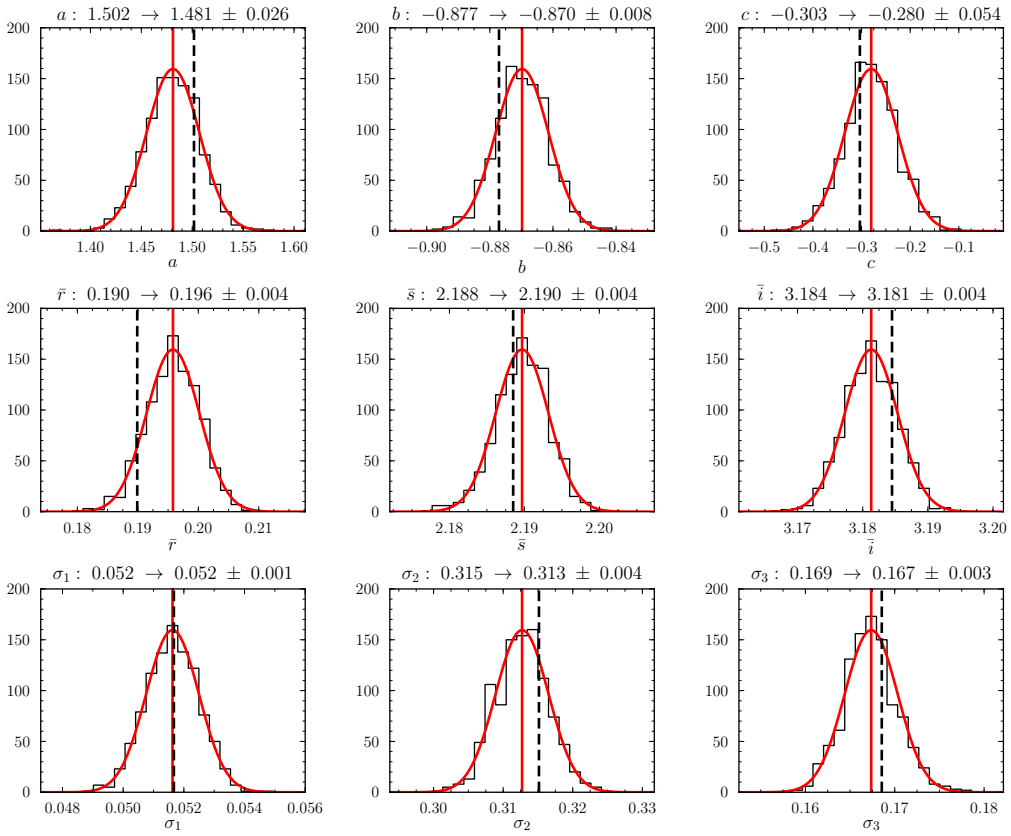

Figure 3.10: Histograms of the maximum-likelihood best-fit values of the J band FP parameters $\{a, b, c, \bar{r}, \bar{s}, \bar{i}, \sigma_1, \sigma_2, \sigma_3\}$ from 1000 simulations. Each panel is labelled at the top with the name of the parameter, the input value of the parameter for the 1000 mock samples, and the mean and rms of the best-fit parameters obtained from ML fits to these mocks; a Gaussian with this mean and rms is overplotted on the histograms. The vertical dashed line shows the input value of the parameter and the vertical solid line shows the mean of the best-fit values. The residual bias correction (see §3.6.2) is the offset between the dashed line and the solid line; in all cases this is comparable to or smaller than the modest rms scatter in the fitted parameter.

Realistic mock FP samples are simulated which closely match the distribution of the galaxies in Fundamental Plane space and exhibit all the dominant selection effects of the actual data. The accuracy of these mock simulations allows us to use them to derive small corrections for any residual bias effects that aren't explicitly modelled in the fitting method.

Finally, a Monte-Carlo analysis using mock simulations was used to confirm that a 3D Gaussian model fit with maximum likelihood gives superior results to regression techniques and to show that all the fitted FP coefficients in the model are consistently recovered with a high level of precision. This accuracy is measured for samples that are subject to censoring in multiple variables and correlated uncertainties in the FP parameters (in a way that simulates the data), demonstrating that the derived maximum likelihood fitting method performs well under these demands and is an unbiased and robust technique for fitting the Fundamental Plane.

Chapter 4

The NIR Fundamental Plane

4.1 Introduction

In this chapter we present the best-fitting Fundamental Plane to the 6dFGS J band sample - the largest homogeneous near-infrared FP sample of early-type galaxies to date. This best-fit plane is an unbiased determination of the FP, as the censoring effects and correlated uncertainties present in the data are accounted for with the robust maximum likelihood fitting algorithm described in the previous chapter.

We discuss the properties of the near-infrared Fundamental Plane (such as *tilt* in the FP slopes) as derived from the 6dFGS data and how it differs from the more prevalent optical FP derivations. A comparison of the 6dFGS FP is made to other FP studies, in general, to investigate whether a coherent understanding of the FP emerges from different observational data sets and different fitting techniques.

Once the global FP for our full sample is established, we then investigate the galaxy populations within the sample and the physical implications of their distribution in FP space. This includes quantifying how the FP varies between the J, H and K near-infrared bands and also with respect to other multi-waveband survey FP results. We determine the environmental dependencies of the FP by using proxies for both local (surface density) and global (richness) galaxy environment. By fitting the FP to galaxies that span a range of environments, we test the universality of the FP and its consistency across galaxies in the field and galaxies in clusters. We also classify the morphological mix of galaxies in our sample and determine whether different types of elliptical and bulge-dominated galaxies lie on the same Fundamental Plane. We also consider if morphological outliers are dominating the scatter in our FP measurements.

Lastly, we analyse scatter about the plane, noting the subtleties in the interpretation of where the most probable position of a galaxy is, with respect to its size, in relation to the Fundamental Plane. This has ramifications for measuring the errors in FP distances that will be derived in Chapter 6, where the errors will be discussed in more detail.

4.2 The 6dFGS J band Fundamental Plane

Fundamental Plane studies in optical passbands are relatively abundant, while studies in near-infrared passbands are less so. It is only recently that large, homogeneous FP data sets across both optical and near-infrared wavelengths have become available (Hyde & Bernardi, 2009; La Barbera et al., 2010b). Using near-infrared photometry in FP analyses is advantageous because in these passbands the lower extinction reduces the variations due to dust and the dominance of older stellar populations reduces the variations due to recent star-formation (at least in the absence of a significant population of intermediate-age AGB stars—cf. Maraston 2005). Comparing optical and near-infrared observations can reveal the effect of variations in the mass-to-light (M/L) ratios on the Fundamental Plane.

4.2.1 Fundamental Plane Parameters and Uncertainties

Figure 4.1 is a 3D visualisation of the 6dFGS J band FP sample. It is important to show the 3D view of the FP, rather than the 2D plots usually found in the literature, because information is lost in projecting the FP onto two dimensions from its native three dimensions, and the true properties of the 3D distribution of the FP are disguised.

Using our maximum likelihood fitting routine we recover the best-fit FP in the J, H and K passbands for samples containing 8901, 8568 and 8573 galaxies respectively. The full details of the FP fits in these bands are given in Table 4.1, including all eight fitted parameters together with the constant of the fit (c), the offset of the plane in the r-direction (r_0; see below), the total rms scatter about the FP in the r-direction (σ_r), and the total rms scatter in distance (σ_d); the difference between these two scatters is discussed in Section 6.3.3.

The errors in the best-fit FP parameters that are given in Table 4.1 are estimated as the rms scatter in fits to multiple mock samples (generated as described in Section 3.6) using the parameters of the best-fit FP as discussed in Section 2.7.

Both the bias corrections and the random errors are small; the fractional errors in the FP slopes (a and b) and dispersions (σ_1, σ_2 and σ_3) are all less than 2%. For the offset of the FP, $c \equiv \bar{r} - a\bar{s} - b\bar{i}$, the uncertainty is 0.054 dex or 12%. However as a measure of the uncertainty in the relative sizes and distances of galaxies due to the fit, this 'intercept' offset is misleading. A better measure is the uncertainty in $\bar{r}$, which is 0.9%; but even this is an over-estimate of the practical impact of the uncertainty in the fit, as the point $(\bar{r}, \bar{s}, \bar{i})$ is at the edge of the observed distribution (i.e. the observed distribution is well-fitted by a Gaussian centred close to the velocity dispersion limit). The most realistic estimate of the uncertainty is the r-axis offset of the fitted FP, as it affects size and distance estimates for 6dFGS galaxies, given by the uncertainty in r_0, the r-value of the fitted FP at a fiducial point in the middle of the

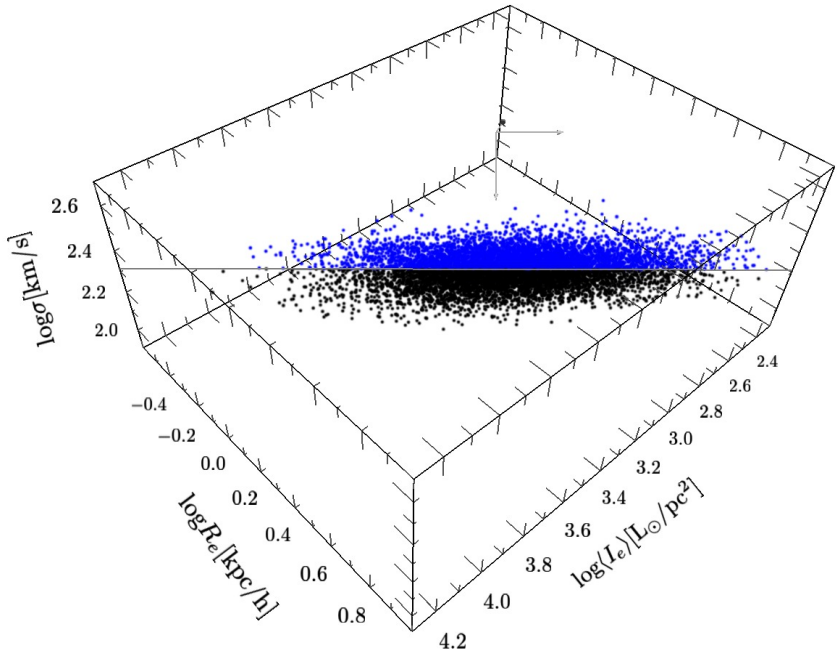

Figure 4.1: 3D visualisation of the 6dFGS J band Fundamental Plane in r, s, i space. The best fitting plane (in grey) has slopes $a = 1.523$ and $b = -0.885$, and an offset $c = -0.330$. The galaxies are colour-coded according to whether they are above (blue) or below (black) the best-fit plane. (Readers viewing the digital version of this thesis using Acrobat Reader v8.0 or higher can enable interactive 3D viewing of this schematic by mouse clicking on the figure; see Appendix A for more detailed usage instructions.)

Table 4.1: Best-fit 6dFGS FP parameters (including bias corrections) and their associated uncertainties for: (i) the full J, H and K samples; (ii) the J band N_R richness subsamples (field, low, medium and high); (iii) the J band Σ_5 local environment subsamples (low, medium and high); and (iv) the J band morphology subsamples (early and late types). As well as the nine FP parameters, the table also lists: $N_{\rm g}$, the number of galaxies in each sample; r_0, the location of the FP at the fiducial point ($s_0 = 2.3, i_0 = 3.2$); σ_r, the scatter about the FP in the r-direction (see §4.8); and σ_d, the scatter in the distance (see §6.3.3).

Sample	$N_{\rm g}$	a	b	c	$\bar{r}$	$\bar{s}$	$\bar{i}$	r_0	σ_1	σ_2	σ_3	σ_r	σ_d
J band	8901	1.523±0.026	-0.885±0.008	-0.330±0.054	0.184±0.004	2.188±0.004	3.188±0.004	0.345±0.002	0.053±0.001	0.318±0.004	0.170±0.003	0.127 (29.7%)	0.097 (22.5%)
H band	8568	1.473±0.024	-0.876±0.008	-0.121±0.051	0.175±0.004	2.190±0.003	3.347±0.004	0.465±0.002	0.051±0.001	0.318±0.004	0.167±0.003	0.123 (28.8%)	0.096 (22.3%)
K band	8573	1.459±0.024	-0.858±0.008	-0.103±0.050	0.153±0.005	2.189±0.003	3.430±0.005	0.511±0.003	0.050±0.001	0.329±0.004	0.166±0.003	0.123 (28.8%)	0.095 (22.1%)
$N_R \leq 1$	6495	1.512±0.030	-0.882±0.010	-0.307±0.063	0.183±0.005	2.187±0.004	3.197±0.005	0.351±0.002	0.053±0.001	0.315±0.005	0.161±0.003	0.127 (29.7%)	0.097 (22.5%)
$2 \leq N_R \leq 5$	1248	1.582±0.058	-0.899±0.021	-0.436±0.122	0.154±0.014	2.170±0.012	3.168±0.012	0.331±0.005	0.051±0.002	0.324±0.011	0.201±0.009	0.126 (29.3%)	0.098 (22.7%)
$6 \leq N_R \leq 9$	546	1.573±0.088	-0.862±0.029	-0.538±0.187	0.220±0.017	2.208±0.012	3.154±0.015	0.327±0.006	0.044±0.003	0.325±0.014	0.181±0.011	0.120 (28.0%)	0.094 (21.8%)
$N_R \geq 10$	612	1.504±0.094	-0.903±0.029	-0.248±0.195	0.228±0.016	2.220±0.012	3.171±0.014	0.324±0.006	0.054±0.003	0.316±0.013	0.173±0.011	0.129 (30.1%)	0.095 (22.1%)
$\Sigma_5 \leq 0.07$	2664	1.486±0.051	-0.848±0.014	-0.354±0.113	0.190±0.008	2.192±0.005	3.203±0.006	0.354±0.004	0.053±0.002	0.314±0.007	0.147±0.004	0.126 (29.3%)	0.095 (21.9%)
$0.07 < \Sigma_5 \leq 0.25$	2812	1.516±0.043	-0.915±0.015	-0.220±0.090	0.175±0.008	2.183±0.007	3.189±0.007	0.343±0.003	0.053±0.002	0.313±0.007	0.173±0.006	0.126 (29.5%)	0.097 (22.5%)
$\Sigma_5 > 0.25$	2782	1.564±0.039	-0.889±0.013	-0.418±0.079	0.188±0.009	2.190±0.007	3.170±0.008	0.335±0.003	0.050±0.001	0.326±0.007	0.185±0.006	0.127 (29.6%)	0.097 (22.5%)
E+E/S0+S0	6956	1.535±0.029	-0.879±0.010	-0.384±0.060	0.156±0.005	2.199±0.004	3.230±0.004	0.339±0.002	0.052±0.001	0.296±0.004	0.170±0.003	0.128 (29.8%)	0.096 (22.3%)
Sp bulges	1945	1.586±0.067	-0.861±0.017	-0.512±0.138	0.305±0.009	2.151±0.008	3.016±0.008	0.384±0.006	0.052±0.002	0.319±0.008	0.157±0.005	0.127 (29.7%)	0.097 (22.6%)

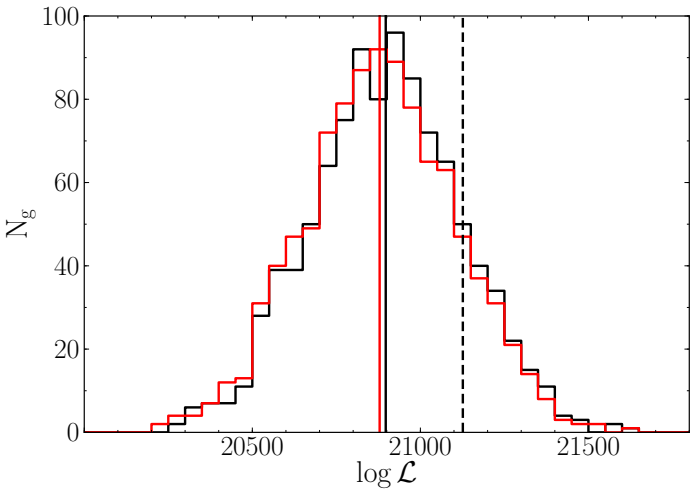

Figure 4.2: Distribution of likelihood values from 1000 mock samples. The FP coefficients used to generate these mock simulations are the same values used to generate the mocks in Figure 3.10. The likelihood values in the red histogram were calculated for each mock sample using these identical input FP values, whereas the likelihood values in the black histogram were calculated using the individual best fit for each mock. The mean likelihoods from these mocks (red: $\ln\mathcal{L} = 20\,878 \pm 225$; black: $\ln\mathcal{L} = 20\,897 \pm 224$) are indicated by the solid lines, and are comparable to but lower than the best-fit likelihood obtained for the actual data ($\ln\mathcal{L} = 21\,126$), shown by the dashed black line.

observed sample: $s_0 \equiv 2.3$ and $i_0 \equiv 3.2$. Using r_0 reduces the covariance between fitted coefficients, as is the case when using mean-subtracted values, although we compare the fits at a *fiducial* point so that the comparison between different FP fits is consistent. The rms scatter in $r_0 \equiv as_0 + bi_0 + c$ is just 0.5%.

4.2.2 Likelihood Model Validation

That our 3D Gaussian model is a good representation of the observed distribution of galaxies in FP space is verified by the remarkable similarities between the mock and data likelihoods. The histogram of log-likelihood values in Figure 4.2 gives the distribution from the same 1000 mock simulations as Figure 3.10, derived in two ways: first by calculating the likelihoods for all the mocks using the best-fit FP of the data (red histogram), and second, by calculating the likelihoods using the best-fit FP values from each individual mock (black histogram). It makes little difference which method is used, as the distribution of likelihoods for these two situations are very similar.

The mean of each histogram (red: $\ln\mathcal{L} = 20\,878 \pm 225$; black: $\ln\mathcal{L} = 20\,897 \pm 224$) is plotted as a solid line. The likelihood of the best fit to the actual data ($\ln\mathcal{L} = 21\,126$) is shown by the dashed vertical line, and is larger than the means of the two mock distributions but still well within the range of likelihoods spanned by the mock samples. The fact that the likelihood recovered from the data is higher than that

from the mocks (i.e. $\ln \mathcal{L}$ is more positive) is a result of excluding the χ^2 outliers from the data, which may also remove the extreme tail of the Gaussian distribution. Genuine outliers do not exist in the mock samples and so no χ^2 clipping is applied, and the lower likelihoods of the mock samples in Figure 4.2 reflect this difference. In summary, the similarity in likelihood values indicates that the fitting algorithm has accurately recovered the input FP and also that the 3D Gaussian model is a suitable representation of the observed FP distribution.

4.2.3 Additional σ-component of 3D Gaussian Vectors

Our 3D Gaussian model of the FP assumes that the s-component of the $\boldsymbol{v}_2$ vector is zero, to simplify the vector definition. In Section 3.7.1 we provided the vector definition of the Gaussian model that includes this extra parameter (k), which we can now use to test the accuracy of this assumption. We perform a nine-parameter maximum likelihood fit with the same J band sample of galaxies, finding a best-fit value $k = 0.09 \pm 0.01$ and a J band FP given by

$$r = (1.51 \pm 0.03)s - (0.86 \pm 0.01)i - (0.39 \pm 0.06) \ . \tag{4.1}$$

Therefore, when there are no constraints placed on the components of $\boldsymbol{v}_2$, the s-component is close to—but slightly larger than—zero. The coefficient of s is much smaller than the coefficients of any of the other vector components, the intrinsic scatter about the plane ($\sigma_1 = 0.052$) is the same to within 0.5%, and the error in distances is 24.3%, slightly larger than for the standard 8-parameter model (due to the additional dependency on s, which has the largest observational errors). Hence, the addition of a ninth parameter provides no practical advantages, and we retain the simplifying approximation of fixing $k \equiv 0$.

4.2.4 Bayesian Model Selection

To justify our choice of the standard 3D Gaussian model, as defined in Section 3.4, over the alternative models we have considered in Sections 3.7.1 and 3.7.2, we compare these models using the Bayes information criterion (Schwarz, 1978).

The Bayes information criterion, or BIC, can be used to objectively choose between different models and determine whether increasing the number of free parameters in the model will result in overfitting. It has the advantages of being easy to compute and independent of the assumed priors for the models, and in the limit of large sample size it approaches $-2\ln(B)$, where B is the the Bayes factor that gives the relative posterior odds of the models under comparison. The BIC depends on the size of the sample (N), the log-likelihood of the best fit ($\ln \mathcal{L}$), and the number

of free parameters in the model (k), and is given by

$$\mathrm{BIC} = -2\ln(\mathcal{L}) + k\ln(N)\ . \tag{4.2}$$

The model with the lowest BIC value is preferred.

For the standard 8-parameter model of Section 3.4, the BIC value is $-42\,075$, as compared to $-42\,287$ for the 9-parameter model including an additional σ component in the $\boldsymbol{v}_2$ vector (Section 3.7.1) and $-31\,833$ for the 11-parameter model including age as an additional parameter (Section 3.7.2). Therefore the BIC indicates that the 11-parameter model including age is not an improvement on the standard model; this will be explored further in Chapter 5. However the 9-parameter model that includes a σ-component in the $\boldsymbol{v}_2$ vector does have a lower BIC value than the standard 8-parameter model, and so is the objectively preferred model. We nonetheless choose to employ the standard 8-parameter 3D Gaussian model because of its simpler physical interpretation, reduced computational burden, and marginally better precision in estimating distances.

4.3 Fundamental Plane Differences between Passband

Table 4.1 gives the best-fit FP parameters for each of the J, H and K bands. The FP slopes a and b are consistent between these passbands at about the joint 1σ and 2σ levels respectively. All three samples also have the same (small) intrinsic scatter orthogonal to the FP, $\sigma_1 = 0.05\,\mathrm{dex}$ (12%). Figure 4.3 illustrates the variation with wavelength of the fitted FP slopes a and b, and also the offset of the FP in the r direction (the latter quantified by r_0). The figure shows the results of fitting FPs to 1000 mock samples in each passband with input parameters given by the best-fit FP for the corresponding observed sample (as per Table 4.1). It also shows the mean values of the fitted parameters for the mock samples, and the 1σ and 2σ contours of their distributions. As expected, the bias-corrected mean coefficients accurately recover the input values; for reference, the coefficients of the best-fit FP for the observed J band sample are marked in each plot as a pair of dashed black lines.

The marginally significant (2σ) difference in the slopes between the J and K bands may be due to the fact that J band mass-to-light ratios are almost independent of metallicity, whereas this is not the case in the K band (Worthey, 1994). In this regard it is worth noting that the J band FP is (marginally) closer to the virial plane than the K band FP.

In the central and right panels, there is a clear offset in r_0 between passbands, with r_0 increasing at longer wavelengths. We expect the differences in r_0 between passbands should be consistent with the mean colours. To quantify the mean difference in r_0 (i.e. Δr_0) as a function of mean colour and surface brightness, we assume

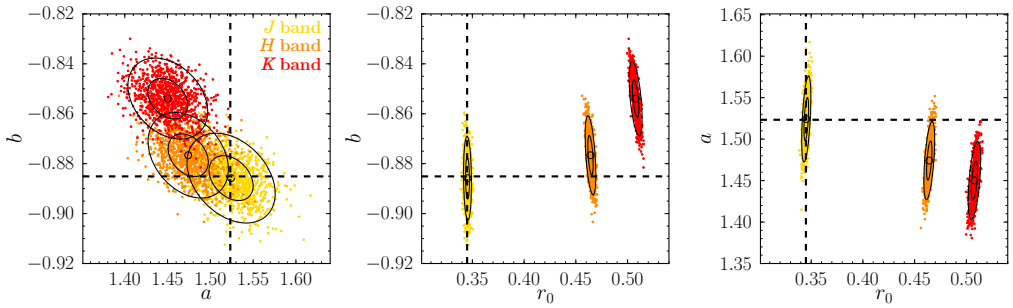

Figure 4.3: Uncertainties on the FP parameters for the 6dFGS J (yellow; $N_g = 8901$), H (orange; $N_g = 8568$) and K (red; $N_g = 8573$) samples. The points show the best-fit FP parameters for each of 1000 mock samples that take as input the best-fit FP parameters for the observed sample in each band. The mean values of the fitted FP parameters from the mocks, and their 1σ and 2σ contours, are also plotted. For reference, the input FP parameters used to generate the samples for the J band are indicated as dotted lines. *Left:* b versus a, showing similar FP coefficients although with a very weak trend of decreasing a and increasing b with increasing wavelength. *Centre:* b versus r_0, showing significant offsets between the FPs in the three passbands. *Right:* a versus r_0, again showing the FP offsets.

that the FP slopes are consistent in each band (a good approximation given the similarity of the coefficients in Table 4.1) and that the galaxies are homologous. These approximations lead to the following relation:

$$\Delta r_0 = b(\Delta i_0 + 0.4\langle J - H\rangle) \tag{4.3}$$

where $\langle J-H\rangle$ is the mean colour in the J and H bands (or similarly $\langle J-K\rangle$ for the J and K bands) and Δi_0 is the mean difference in i_0, the surface brightness offset of the FP at a fiducial point (here taken to be $s_0 = 2.3$ and $r_0 = 0.35$). For $b = -0.88$, the mean offset in r_0 between J and H bands (as calculated from equation 4.3) is -0.14 as compared to the offset of -0.12 observed directly from the fits (see the r_0 values in Table 4.1). Similarly, for the J and K bands, the predicted Δr_0 is -0.19, as compared to the observed offset of -0.17 from the fits.

The predicted values are very close to the offsets observed, so we conclude that the offsets in r_0 between passbands are a consequence of the mean colours, as expected. Equivalently, allowing for the mean colours the FP is consistent between the J, H and K bands.

4.4 Comparison to Literature

A summary of previous FP slope determinations from the literature is given in Table 4.2, along with the passband, sample size and fitting method of each study. Where more than one regression method was employed, the slopes from the orthogonal regression fit are given. The coefficients of surface brightness, b, were converted to the units used in this work (i.e. as the coefficient of $i \equiv \log\langle I_e\rangle$ rather than $\langle\mu_e\rangle$,

Table 4.2: Best-fit FP slopes a and b as reported by previous studies in the literature. Also listed are the passband, sample size and fitting method used in each study. FP fits in optical and near-infrared passbands are shown respectively in the upper and lower halves of the table. Where available, the observed scatter orthogonal to the FP ($\sigma_\perp$) and the scatter about the FP in $\log R_e$ (σ_r) are given.

Survey	Band	N_g	a	b	$\sigma_\perp$	σ_r	Type of fit
Dressler et al. (1987b)	B	97	1.33±0.05	−0.83±0.03	-	20%	inverse regression
Djorgovski & Davis (1987)	r_G	106	1.39±0.14	−0.90±0.09	-	20%	2-step inverse regression
Lucey et al. (1991)	V	66	1.26	−0.82	-	17%	forward regression
Guzman, Lucey & Bower (1993)	V	37	1.14	−0.79	-	17%	forward regression
Jorgensen, Franx & Kjaergaard (1996)	r	226	1.24±0.07	−0.82±0.02	-	17%	orthogonal regression
Hudson et al. (1997)	R	352	1.38±0.04	−0.82±0.03	-	21%	inverse regression
Müller et al. (1998)	R	40	1.25	−0.87	-	19%	orthogonal regression
Gibbons, Fruchter & Bothun (2001)	R	428	1.37±0.05	−0.84±0.03	-	21%	inverse regression
Colless et al. (2001b)	R	255	1.22±0.09	−0.84±0.03	11%	20%	ML Gaussian
Bernardi et al. (2003b)	g	5825	1.45±0.06	−0.74±0.01	13%	25%	ML Gaussian
Bernardi et al. (2003b)	r	8228	1.49±0.05	−0.75±0.01	12%	23%	ML Gaussian
Hudson et al. (2004)	V\R	694	1.43±0.03	−0.84±0.02	-	21%	inverse regression
D'Onofrio et al. (2008)	V	-	1.21±0.05	−0.80±0.01	-	-	orthogonal regression
La Barbera et al. (2008)	r	1430	1.42±0.05	−0.76±0.008	15%	28%	orthogonal regression
Gargiulo et al. (2009)	R	91	1.35±0.11	−0.81±0.03	-	21%	orthogonal regression
Hyde & Bernardi (2009)	g	46410	1.40±0.05	−0.76±0.02	16%	31%	orthogonal regression
Hyde & Bernardi (2009)	r	46410	1.43±0.05	−0.79±0.02	15%	30%	orthogonal regression
La Barbera et al. (2010a)	g	4589	1.38±0.02	−0.79±0.003	-	29%	orthogonal regression
La Barbera et al. (2010a)	r	4589	1.39±0.02	−0.79±0.003	-	26%	orthogonal regression
Scodeggio, Giovanelli & Haynes (1997)	I	109	1.25±0.02	−0.79±0.03	-	20%	mean regression
Pahre, Djorgovski & de Carvalho (1998)	K	251	1.53±0.08	−0.79±0.03	-	21%	orthogonal regression
Bernardi et al. (2003b)	i	8022	1.52±0.05	−0.78±0.01	11%	23%	ML Gaussian
Bernardi et al. (2003b)	z	7914	1.51±0.05	−0.77±0.01	11%	22%	ML Gaussian
La Barbera et al. (2008)	K	1430	1.53±0.04	−0.77±0.008	14%	29%	orthogonal regression
Hyde & Bernardi (2009)	i	46410	1.46±0.05	−0.80±0.02	15%	29%	orthogonal regression
Hyde & Bernardi (2009)	z	46410	1.47±0.05	−0.83±0.02	15%	29%	orthogonal regression
La Barbera et al. (2010a)	J	4589	1.53±0.02	−0.80±0.003	-	26%	orthogonal regression
La Barbera et al. (2010a)	H	4589	1.56±0.02	−0.80±0.005	-	27%	orthogonal regression
La Barbera et al. (2010a)	K	4589	1.55±0.02	−0.79±0.005	-	28%	orthogonal regression
6dFGS (this paper, Table 4.1)	J	8901	1.52±0.03	−0.89±0.008	15%	30%	ML Gaussian
6dFGS (this paper, Table 4.1)	H	8568	1.47±0.02	−0.88±0.008	15%	29%	ML Gaussian
6dFGS (this paper, Table 4.1)	K	8573	1.46±0.02	−0.86±0.008	15%	29%	ML Gaussian

where the conversion is $b_i = -2.5b_\mu$). In those studies where an orthogonal rms scatter about the plane was quoted (based on an orthogonal regression or ML fit), we have listed this value in the $\sigma_\perp$ column and converted it to an rms scatter in the $r \equiv \log R_e$ direction using $\sigma_r = \sigma_\perp(1 + a^2 + b^2)^{1/2}$ (for reference, this scaling factor is 2.0 for $a = 1.5$ and $b = 0.88$). Note that the rms scatter in $r \equiv \log R_e$ in dex, δ_r, is conventionally converted to a fractional scatter in R_e in percent, σ_r, using $\sigma_r \equiv (10^{+\delta_r} - 10^{-\delta_r})/2$.

Table 4.2 shows the increase over time in the size of the samples being studied and also the variety of fitting techniques employed, with the more recent studies generally preferring orthogonal regression or ML fits. The fitted value of the FP coefficient of velocity dispersion, a, is typically found to be 1.2–1.4 at optical wavelengths and 1.4–1.5 in the near-infrared, as found in the most recent FP studies analysing large data sets across multiple passbands (Hyde & Bernardi, 2009; La Barbera et al., 2010a). *Within* individual studies in the optical, a tends to be larger in redder passbands; *between* studies the differences are at least as large as this trend. This trend, however, is observed across optical to near-infrared wavelengths, but (as here) not over the JHK passbands (see Table 4.2). This implies, as expected, that there is relatively little variation with mass or size in the dominant stellar populations (and hence the stellar M/L) across these near-infrared passbands. By contrast, b is generally consistent with being constant across passbands within any individual study, although it varies over the range -0.74 to -0.90 when comparing different studies.

A direct comparison of the 6dFGS FP to the results of other studies is constrained by the fact that only one study uses J and H band samples (La Barbera et al., 2010a), and only two studies use K band samples (Pahre, Djorgovski & de Carvalho, 1998; La Barbera et al., 2010a). Moreover, neither of these studies use a ML fitting technique, so we have chosen to compare with orthogonal regressions, where available, as the next-best fitting method. Our $s \equiv \log \sigma_0$ slope ($a = 1.52$) is consistent with the other near-infrared FP fits in being steeper than is generally found in optical passbands. Our $i \equiv \log\langle I_e \rangle$ slope ($b = -0.89$) is at the upper end of the range of previous results. Due to the large sample and homogeneous data afforded by the 6dFGS, the fractional errors on both slopes (for a less than 2% and for b less than 1%) are significantly smaller than is the case for older FP samples, and comparable to those obtained for the similarly large and homogeneous SDSS and UKIDSS samples (Hyde & Bernardi, 2009; La Barbera et al., 2010a).

The recent SPIDER FP study by La Barbera et al. (2010a) provides the closest match to 6dFGS in both sample size and passbands: we can compare the J, H and K ML Gaussian FP fits for more than 8500 6dGFS galaxies with orthogonal regression FP fits in the same bands for 4589 SPIDER galaxies. The two studies

obtain almost identical values of a in the J band (1.52 and 1.53), but 6dFGS finds a to be significantly smaller in the H and K bands (1.47 and 1.46), while SPIDER finds slightly larger values in these bands (1.56 and 1.55). The differences between the two studies in the H and K band values of a are significant relative to the estimated uncertainties (3.2σ). Within each of the 6dFGS and SPIDER studies the values of b are consistent across the three bands; however 6dFGS finds b in the range -0.89 to -0.86, while SPIDER obtains a higher value, $b = -0.79$. This difference in b is highly significant relative to the estimated uncertainties ($>8\sigma$), but may be at least partly attributed to the fact that orthogonal regression tends to find systematically higher values of b, as shown in Figure 3.2.

As well as comparing the *slopes* of the FP fits, it is interesting to consider the *scatter* about the FP found in different studies. The rms scatter about the FP relation projected in the $\log R_e$ direction (σ_r in Table 4.2) is usually taken as an estimate of the rms uncertainty in distances and peculiar velocities when the FP is used as a distance estimator. This uncertainty is widely quoted as being 20% or even smaller, a figure reflected in Table 4.2 for the older FP samples. However the scatter in $\log R_e$ calculated in this way for the most recent studies (La Barbera et al., 2008; Hyde & Bernardi, 2009; La Barbera et al., 2010a), and for the 6dFGS sample, is in fact almost 30%. This is somewhat surprising, given that these recent samples are large and generally contain good-quality homogeneous measurements of the FP parameters. In part the difference may be due to the fact that these larger samples may contain a more heterogeneous mix of galaxy types than the older 'hand-picked' samples (see Section 4.6 below). However a major source of this discrepancy is that it is *not* correct to interpret the rms scatter about an orthogonal regression or ML fit, projected in $\log R_e$, as the uncertainty in distance. As discussed in detail in Section 6.3.3, if one correctly accounts for the distribution of galaxies in the FP, then the true distance error, σ_d, is significantly smaller than σ_r. For the 6dFGS sample, while the rms scatter about the FP in the $\log R_e$ direction is $\sigma_r = 29\%$, the rms scatter in the distance estimates is in fact $\sigma_d = 23\%$. This difference is discussed in detail in Section 6.3.3.

4.5 Environment and the Fundamental Plane

We investigate possible variations in the FP with *group* environment, characterised by richness, and with *local* environment, characterised by a nearest-neighbour density measure.

4.5.1 Galaxy Richness

First, we consider potential environmental effects that correlate with the scale of the dark matter halos that galaxies inhabit, using the richness estimates from the

group catalogue described in Section 2.8.1, as a proxy for halo mass. We define four subsamples according to richness N_R: galaxies in the field or very low richness groups ($N_R \leq 1$), galaxies in low-richness groups ($2 \leq N_R \leq 5$), galaxies in medium-richness groups ($6 \leq N_R \leq 9$), and those galaxies in high-richness groups and clusters ($N_R \geq 10$). There are 6495 field galaxies, 1248 in low-richness groups, 546 in medium-richness groups, and 612 in high-richness groups and clusters.

The distribution of these richness subsamples in FP space can be viewed in the 3D visualisation of Figure 4.4, where the galaxies in the 6dFGS J band FP sample are colour-coded by the richness of the group environment they inhabit. From examination of these distributions it is apparent that these subsamples tend to populate similar FPs. This is broadly confirmed by the best-fit FP parameters for each of these richness subsamples given in Table 4.1. The FP slopes a and b are similar within 1σ for all four richness subsamples and the full J band sample, and the offset of the FP, given by r_0, is similar for the three subsamples of galaxies in groups. The one significant difference is between the offset for the field galaxy subsample and the group subsamples.

These similarities and differences are clarified in Figure 4.5, which shows the best-fitting parameters of each richness subsample, along with the 1σ and 2σ error contours determined from 200 mock samples. The consistency of the FP slopes is shown in the left panel of this figure, while the difference in FP offsets between the field and group subsamples is shown in the centre and right panels. This offset is $\Delta r_0 \approx 0.02\,\mathrm{dex}$, which is relatively small compared to the total scatter in r of the full sample ($\sigma_r = 0.127\,\mathrm{dex}$). Nonetheless, it corresponds to a systematic size or distance offset of about 4.5%, and is statistically significant at $>3.7\sigma$. Such an offset would have an appreciable impact on estimates of the relative distances of field and group galaxies if it were not accounted for.

4.5.2 Local Galaxy Density

We repeat the above analysis for the sample of 8258 galaxies for which we have local environment estimates, as described in §2.8.1. This sample is divided by local surface density (Σ_5) into three approximately equal-sized subsamples: 2664 galaxies in low-density environments ($\Sigma_5 \leq 0.07$), 2812 galaxies in medium-density environments ($0.07 < \Sigma_5 \leq 0.25$) and 2782 galaxies in high-density environments ($\Sigma_5 > 0.25$). We fit FPs to each of these subsamples individually, deriving the best-fit parameters given in Table 4.1. The coefficient of velocity dispersion, a, is similar across the three subsamples and also with respect to the global sample. There is weak variation (at the 2σ level), in the surface brightness coefficient, b, with galaxies in denser environments tending to have an FP with a shallower b slope; galaxies in the low surface density sample exhibit the largest variation in b from the global FP. However,

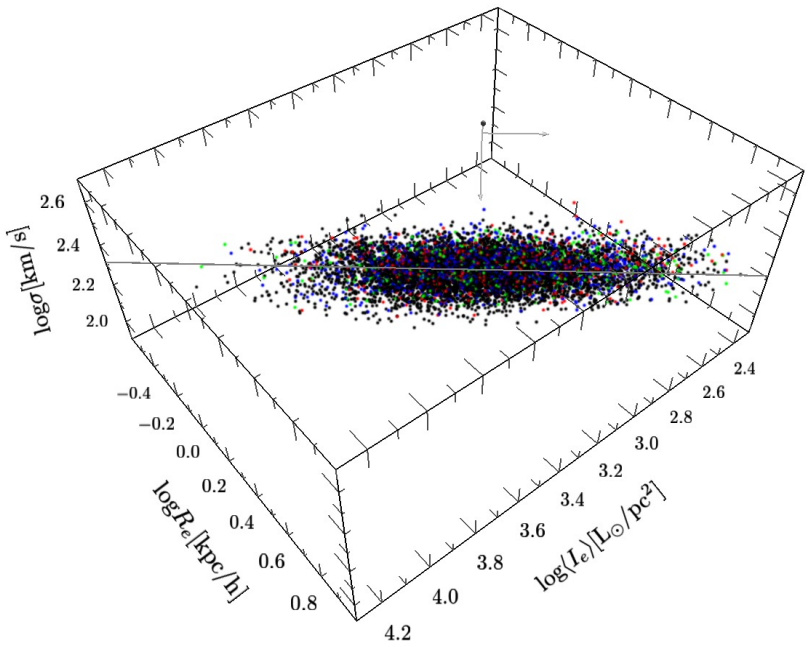

Figure 4.4: 3D visualisation of the 6dFGS J band Fundamental Plane with individual galaxies colour-coded by the richness of the group environment they inhabit: 6495 field galaxies in black; 1248 galaxies in low-richness groups in blue; 546 galaxies in medium-richness groups in green; and 612 galaxies in high-richness groups in red (these richness classes are defined in the text). The best-fitting plane (in grey) for the entire sample (with $a = 1.523$, $b = -0.885$ and $c = -0.330$) is shown for reference. (Readers viewing the digital version of this thesis using Acrobat Reader v8.0 or higher can enable interactive 3D viewing of this schematic by mouse clicking on the figure; see Appendix A for more detailed usage instructions.)

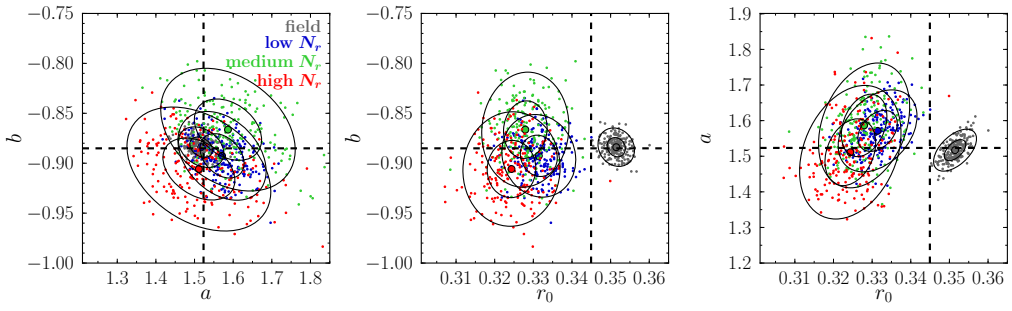

Figure 4.5: As for Figure 4.3, but comparing the FP fits to four richness samples spanning field (grey; $N_g = 6495$), low richness (blue; $N_g = 1248$), medium richness (green; $N_g = 546$) and high richness (red; $N_g = 612$) galaxy samples. The points in each panel are the fits to 200 mocks of each of these four subsamples; the large black circles show the means and the ellipses the 1σ and 2σ contours of the distribution of fitted parameters. The dashed lines show, for reference, the best-fit parameters for the full J band sample.

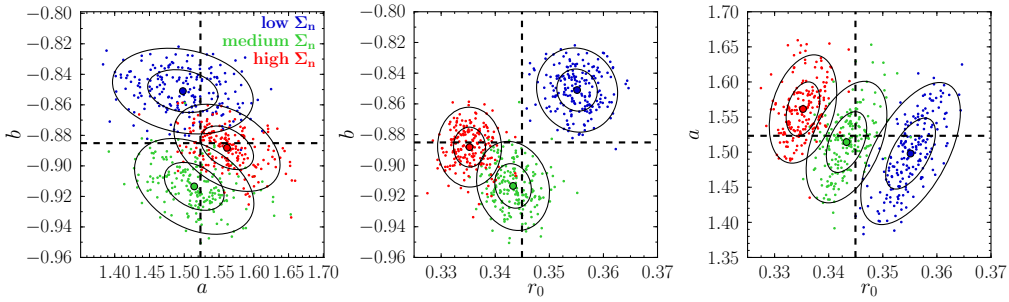

Figure 4.6: As for Figure 4.3, but comparing the FP fits to three local surface density, Σ_5, samples spanning low Σ_5 (blue; $N_g = 2664$), medium Σ_5 (green; $N_g = 2812$) and high Σ_5 (red; $N_g = 2782$) galaxy samples. The points in each panel are the fits to 200 mocks of each of these three subsamples; the large black circles show the means and the ellipses the 1σ and 2σ contours of the distribution of fitted parameters. The dashed lines show, for reference, the best-fit parameters for the full J band sample.

the strongest trend with local environment is in the offset of the FP, where r_0 is systematically smaller for galaxies with higher surface density. The significance of this trend is clearly shown in the centre and right panels of Figure 4.6, where we plot the best-fit FP slopes, a and b, and the r_0 offset from 200 mock simulations of each local surface density subsample.

Comparing the local density FP fits illustrated in Figure 4.6 to those for richness shown in Figure 4.5, we find the same consistency in a and the same trend with environment in r_0. The general, although not monotonic, trend in b as a function of local surface density is not seen for global environment, although this may possibly be because our higher richness subsamples have too few galaxies to recover such a weak trend.

4.5.3 Comparison to Literature

Suggestions of environmental dependence in the FP (or the D_n–σ relation) first emerged in studies where a weak offset between galaxies in clusters (such as Coma and Virgo) and the field was detected (Lucey, Bower & Ellis, 1991; de Carvalho & Djorgovski, 1992). However it was later suggested that these differences could be attributed to errors in measurement, as no such offset in the FP was subsequently found between field and cluster galaxies in other similar studies (Burstein, Faber & Dressler, 1990; Lucey et al., 1991; Jorgensen, Franx & Kjaergaard, 1996). As samples of early-type galaxies increased, and the range covered in environment and mass was extended, trends with environment were found for *local* density indicators such as cluster-centric distance (Bernardi et al., 2003b) and local galaxy density (D'Onofrio et al., 2008). The latter study also found a strong trend in the FP slopes a and b with *local* galaxy density, but no trend with *global* environment parameters such as richness, R_{200} and group velocity dispersion.

More recently, La Barbera et al. (2010c) explored the role of environment in the FP and found a strong trend with local galaxy density (and a weaker trend with normalised cluster-centric distance), independent of passband. Evidence of this trend is indicated by a lower offset of the FP for galaxies in high-density regions compared to low-density regions, consistent with previous results (Bernardi et al., 2003b; D'Onofrio et al., 2008). The slope a was found to decrease in high-density regions (in all passbands), while b tended to weakly increase with local galaxy density (a trend that disappears in the near-infrared). Similar trends in the FP parameters were found for galaxies in groups and the field.

The results obtained for the 6dFGS sample are consistent with other recent studies, in that the variation of the FP is more pronounced for parameters that reflect *local* density or environment than for those that are proxies for *global* environment. Even though we compare the offset between FPs using r_0 rather than c (as La Barbera et al. 2010c do), the trend we find with surface density (i.e. lower r_0 for galaxies in higher-density environments), is at least qualitatively consistent with that of the SPIDER study. However, to anticipate the discussion in Section 5.4, these variations in the FP with environment are smaller than the variation found with age; if the age of the stellar population is indeed the main driver of FP variations, then the environmental variations may be primarily the result of correlations between environment and stellar population.

4.6 Morphology and the Fundamental Plane

We examine the morphological variation of the Fundamental Plane using a visual classification of each galaxy morphology from multiple experienced observers, as described in Section 2.5. The J band FP sample was divided into two morphological subsamples: 6956 elliptical and lenticular galaxies (those classified as E, E/S0 or S0) and 1945 early-type spiral bulges (those classified as S0/Sp or Sp and having bulges filling the 6dF fibre aperture). Note that the initial NIR selection criteria mean there are relatively few of the latter class, and that these may have some degree of bias towards larger $\log R_e$. We do not separate the E and S0 galaxies into separate subsamples since there is significant overlap in our morphological classifications for these two classes. We note that the FP is, in general, found to be consistent between samples of E and S0 galaxies (Jorgensen, Franx & Kjaergaard, 1996; Colless et al., 2001b), and that, in fitting the E and S0 galaxies as one morphological subsample, we find the same scatter about the FP as for the full sample.

Figure 4.7 is a 3D visualisation of the J band FP sample colour-coded by morphology, with the ellipticals and lenticulars in red and the early-type spiral bulges in blue. This figure shows that the two morphological subsamples populate slightly different locations *within* the FP, with the early-type spiral bulges more common at

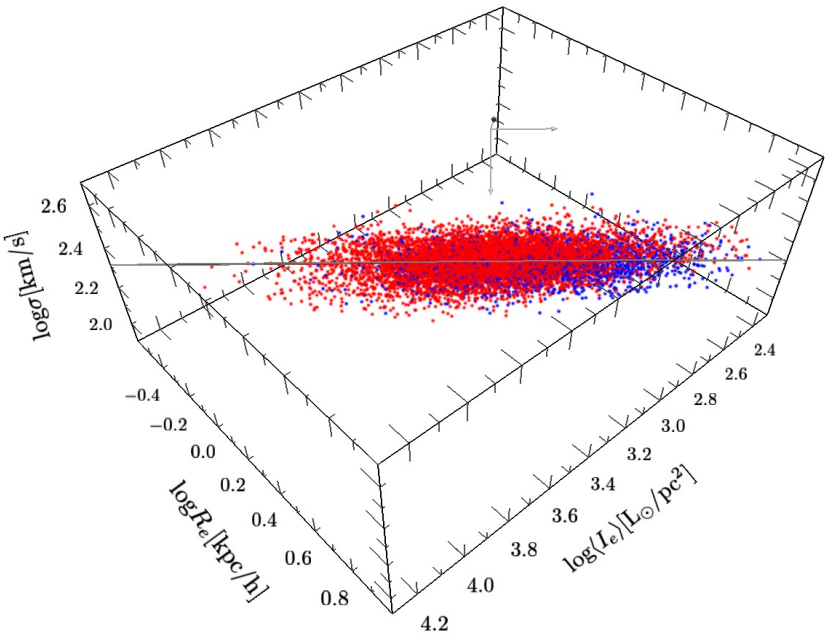

Figure 4.7: 3D visualisation of the 6dFGS J band Fundamental Plane in $\boldsymbol{r}$,$\boldsymbol{s}$,$\boldsymbol{i}$ space. The best-fitting plane (in grey) for the J band (with $a = 1.523$, $b = -0.885$ and $c = -0.330$) is plotted for reference. The galaxies are colour-coded according to morphology: 6956 early types in red and 1945 late types in blue (these morphological classes are defined in the text). The best-fitting plane (in grey) for the entire sample (with $a = 1.523$, $b = -0.885$ and $c = -0.330$) is shown for reference. (Readers viewing the digital version of this thesis using Acrobat Reader v8.0 or higher can enable interactive 3D viewing of this schematic by mouse clicking on the figure; see Appendix A for more detailed usage instructions.)

larger $\log R_e$.

The best-fit FP parameters for these two subsamples are given in Table 4.1, and their relative values and errors are illustrated using mock samples in Figure 4.8. The figure shows that the FP slopes, a and b, are consistent for the different morphological classes but that the offset in $\log R_e$, while small ($\Delta r_0 = 0.045$ dex) relative to the overall scatter in $\log R_e$, is highly significant (7σ) and corresponds to a systematic error of 10% in sizes and distances. An offset of this amplitude would have a substantial impact on estimates of the relative distances of E/S0 galaxies and Sp bulges if it were not accounted for.

4.6.1 Morphological Dependence of Size Offset

In addition to the difference in FP offset, there is a large shift in the centroid of the distribution *within* the FP, with the early-type spiral bulges having $\bar{r} = 0.304$ while the ellipticals and lenticulars have $\bar{r} = 0.155$; i.e. the spiral bulges are typically 35% larger. We speculate that this may be due to the selection criteria imposed, namely

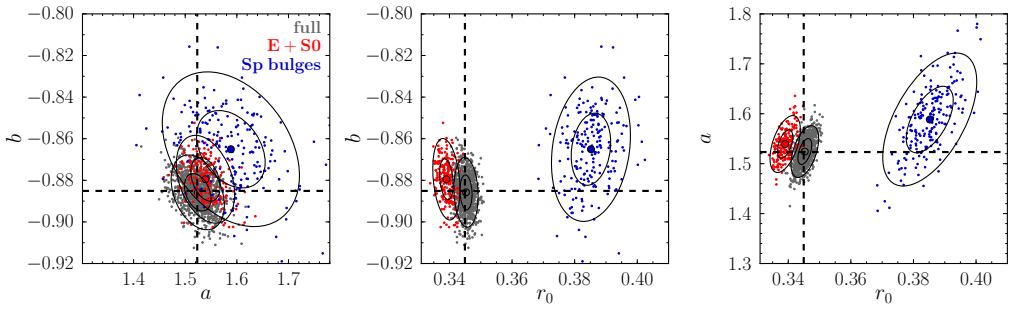

Figure 4.8: As for Figure 4.3 but comparing the FP fits to the two morphological subsamples: 6956 elliptical and lenticular galaxies (E/S0) in red and 1945 early-type spiral bulges (Sp bulges) in blue; the full J band sample of 8901 galaxies is shown in grey. The points in each panel are the fits to 200 mocks of the two morphological subsamples and to 1000 mocks of the full sample; the large black circles show the means of the fitted parameters and the ellipses show the 1σ and 2σ contours of the distribution. The dashed lines show, for reference, the best-fit parameters for the full observed J band sample.

that the spiral bulges had to fill the 6dF fibre apertures.

In fact, this offset is evident in the distribution of apparent angular size ($\log R_0$) for each of these subsamples (see Figure 4.9) where the mean and distribution of the E/S0 galaxies (in red) is more similar to the *global* FP sample (in black). The spiral bulges (in blue), however, have a mean apparent size that is on average larger than the early-types and closer to that of the 6dF fibre aperture size ($R_0 = 6.7$ arcsec).

We therefore re-sampled the elliptical/lenticular sample to have the same apparent size distribution as the spiral bulges (distribution shown in green in Figure 4.9), and re-fit the FP to this subsample; this did not induce an offset in r_0 as observed in the spiral bulges as seen in Figure 4.10. The size-selected subsample has FP slopes and an r_0 offset comparable to the E/S0 subsample. We conclude that this offset is not primarily a selection effect, but rather a real difference between the FPs of the ellipticals/lenticulars and the early-spiral bulges.

4.7 The Fundamental Plane as a 3D Gaussian

Although throughout this thesis we emphasise the value of fitting a 3D Gaussian model to the FP, we emphasise that we are not saying that the intrinsic FP is necessarily Gaussian. That may be the case in some axes, but in others (e.g. in luminosity or velocity dispersion) the intrinsic distribution very likely takes some other form (such as a Schechter function)—a form that is only approximated by a Gaussian over the range of values in our sample (i.e. the bright/large/massive end of the distribution).

We have chosen to use a Gaussian model because it is computationally easy and because empirically it fits the data in our sample (as evidenced by Figure 3.8). In practice the observed FP is consistent with (well modelled by) a Gaussian partly due

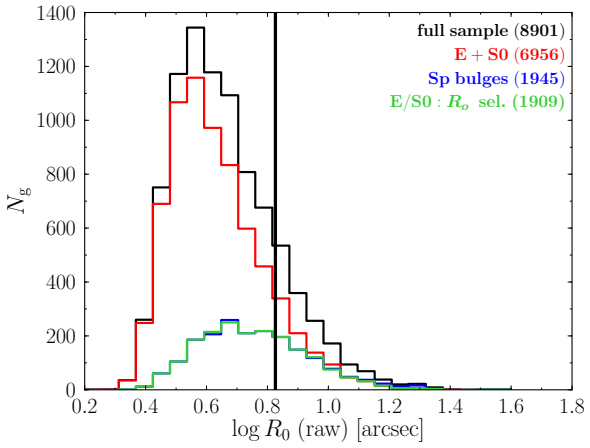

Figure 4.9: Apparent size distribution (raw $\log R_0$ in units of arcseconds) for the full FP sample (black; $N_g = 8901$), E/S0 subsample (red; $N_g = 6956$), spiral bulges subsample (blue; $N_g = 1945$) and size-selected subsample (green; $N_g = 1909$). The 6dF fibre size, i.e. $R_0 = 6.7$ arcsec is plotted for comparison.

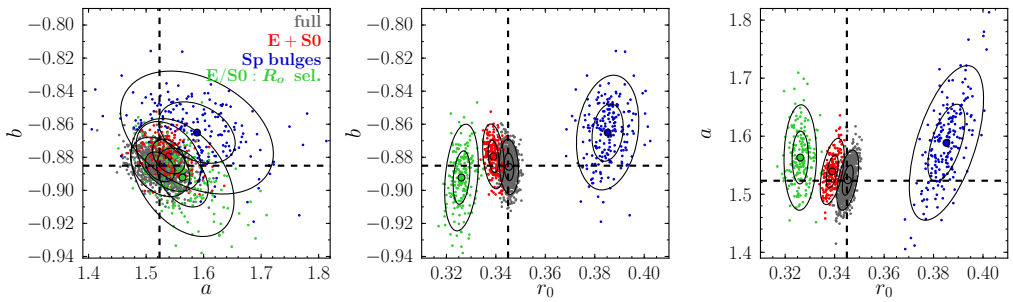

Figure 4.10: As for Figure 4.3 but comparing the FP fits to the two morphological subsamples (same as for Figure 4.8: 6956 elliptical and lenticular galaxies (E/S0) in red and 1945 early-type spiral bulges (Sp bulges) in blue; the size-selected morphology subsample (E+S0:sz) of 1945 galaxies in green; the full J band sample of 8901 galaxies is shown in grey. The points in each panel are the fits to 200 mocks of the three morphological subsamples and to 1000 mocks of the full sample; the large black circles show the means of the fitted parameters and the ellipses show the 1σ and 2σ contours of the distribution. The dashed lines show, for reference, the best-fit parameters for the full observed J band sample.

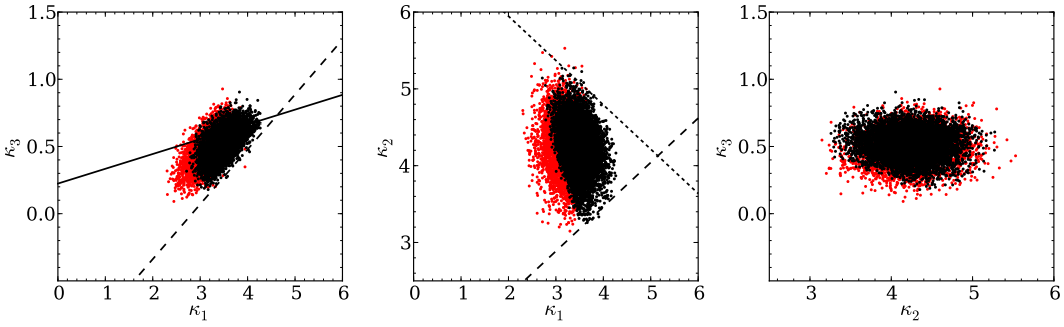

Figure 4.11: The κ-space distribution of the 6dFGS J band FP sample (black) and the galaxies excluded by our selection criteria from a corresponding mock sample (red). *Left:* the κ_3–κ_1 projection of the FP showing the best-fit 6dFGS relation ($\kappa_3 \propto 0.110\kappa_1$, solid line) and the lower limit on M/L as a function of mass ($2\sqrt{3}\kappa_3 - \sqrt{2}\kappa_1 > -4.0$; long-dashed line). *Centre:* the κ_2–κ_1 projection showing the upper limit defining the 'zone of exclusion' for dissipation ($\kappa_1 + \sqrt{3}\kappa_2 < 12.3$; short-dashed line) corresponding to the Bender, Burstein & Faber (1992) B band limit ($\kappa_1 + \kappa_2 < 7.8$); also the apparent lower limit on luminosity density ($\sqrt{3}\kappa_2 - \kappa_1 > 2.0$; long-dashed line). *Right:* the κ_3–κ_2 projection.

to either (or both) the sample selection criteria and the observational errors. The errors are approximately Gaussian and are relatively large in the raw quantities r, s and i (although not in some combined quantities like $r - bi$). Convolved with the intrinsic FP, they give the distribution a more Gaussian form.

This effect is compounded by the selection criteria. For example, the velocity dispersion cut-off truncates the probable Schechter function of the intrinsic distribution in such a way that the the truncated distribution can be fit by a truncated Gaussian (the exponential part of a Schechter function is similar to a Gaussian that is truncated near its peak). This truncated distribution is then blurred and made more Gaussian by the observational errors.

In sum, although a Gaussian intrinsic distribution is statistically a sufficiently good model for the data in the 6dFGS sample (as well as being computationally convenient), the substantial effects due to the sample selection criteria and observational errors mean that we cannot conclude that the underlying physical distribution is Gaussian. While the ML method successfully fits a Gaussian to the intrinsic FP distribution, a more realistic distribution might fit as well or better.

4.7.1 The Fundamental Plane in κ-space

Bender, Burstein & Faber (1992) proposed studying the FP using κ-space, a coordinate system related to key physical parameters such as galaxy mass (M) and luminosity (L). Bender et al. took as their observed parameters $\log \sigma_0^2$, $\log I_e$ and $\log R_e$ (with σ_0 in units of km s^{-1}, R_e in units of kpc and I_e in units of $\mathrm{L}_\odot\,\mathrm{pc}^{-2}$)

and defined κ-space in terms of the orthogonal set of basis vectors given by

$$\begin{aligned}
\kappa_1 &\equiv (\log \sigma_0^2 + \log R_e)/\sqrt{2} = (2s + r)/\sqrt{2}, \\
\kappa_2 &\equiv (\log \sigma_0^2 + 2\log I_e - \log R_e)/\sqrt{6} = (2s + 2i - r)/\sqrt{6}, \\
\kappa_3 &\equiv (\log \sigma_0^2 - \log I_e - \log R_e)/\sqrt{3} = (2s - i - r)/\sqrt{3}.
\end{aligned} \tag{4.4}$$

In this coordinate system, κ_1 is proportional to $\log M$, κ_2 is proportional to $\log(M/L\, I_e^3)$ and κ_3 is proportional to $\log(M/L)$.

FP samples in κ-space (Bernardi et al., 2003b; Burstein et al., 1997; Kourkchi et al., 2012) are often plotted in the κ_3–κ_1 projection (to show an almost edge-on view of the FP) and the κ_2–κ_1 projection (to show an almost face-on view of the FP). Figure 4.11 shows the κ-space distribution for the J band 6dFGS FP sample (black points) in all three 2D projections of κ-space. The galaxies rejected from a mock set of galaxies by the 6dFGS sample selection criteria are also shown (in red) to illustrate the effects of censoring on the observed κ-space distribution.

We can compute the principal axes of the FP distribution in (r, s, i)-space, (v_1, v_2, v_3), in terms of $(\kappa_1, \kappa_2, \kappa_3)$ using the inverse of the transform defined by equation 4.4 to map from κ-space to (r, s, i)-space followed by the transform defined by equations 3.10 & 3.11 to then map to (v_1, v_2, v_3). Inserting the values of a and b for the best-fit J band FP given in Table 4.1, we obtain

$$\begin{aligned}
v_1 &= +0.083\kappa_1 + 0.002\kappa_2 - 0.754\kappa_3 \ , \\
v_2 &= -0.469\kappa_1 + 0.882\kappa_2 - 0.050\kappa_3 \ , \\
v_3 &= -0.631\kappa_1 - 0.312\kappa_2 + 0.422\kappa_3 \ .
\end{aligned} \tag{4.5}$$

As expected, v_1 (the direction normal to the FP) is very close to κ_3, which is proportional to $\log M/L$. However, because the transformation from (r, s, i)-space to κ-space is non-orthogonal, there is significant mixing in κ-space between v_1 and v_3, with $v_1 \cdot v_3 = -0.6$.

In κ-space the best-fit J band FP derived in (r, s, i)-space is given by

$$\kappa_3 = 0.110\kappa_1 + 0.002\kappa_2 + 0.216 \ . \tag{4.6}$$

This is significantly shallower than the relation found by Bender, Burstein & Faber (1992), which was $\kappa_3 \propto 0.15\kappa_1$ (although the difference is in part due to the fact that Bender et al. were working in the B band and the 6dFGS result is for the J band). Because the coefficient of κ_2 is so small, equation 4.6 is essentially a relation between $\kappa_3 \propto \log M/L$ and $\kappa_1 \propto \log M$. Neglecting the κ_2 term and using the definitions of

κ_1 and κ_3 given in equation 4.4 yields

$$\frac{\log M/L}{\sqrt{3}} = 0.110\frac{\log M}{\sqrt{2}} + constant\ , \tag{4.7}$$

which corresponds to $M/L \propto M^{0.135}$.

It is illuminating to derive this same relationship starting from the *assumption* that mass-to-light ratio has a simple power-law dependency on mass. Letting $m = \log M$ and $l = \log L$, and assuming that (ignoring constants) $m = 2s + r$ and $l = 2r + i$, if the mass-to-light ratio is a power of mass, $m - l = \alpha m$, then we can write the FP as

$$r = 2\left(\frac{1-\alpha}{1+\alpha}\right)s - \left(\frac{1}{1+\alpha}\right)i + constant\ . \tag{4.8}$$

By equating FP coefficients with equation 3.2 we get two relations for α, namely $\alpha = (2 - a)/(2 + a)$ and $\alpha = -(1 + b)/b$. For an arbitrary FP relation there is no requirement that these two relations give consistent values for α. However, as it happens, for the particular values $a \approx 1.52$ and $b \approx -0.88$ that are very close to the best-fit J band FP for the 6dFGS sample, these relations give consistent values of $\alpha \approx 0.136$. Hence our best-fit FP is consistent with (but does not require) a simple scenario in which mass-to-light ratio is a power of mass, namely $M/L \propto M^{0.136}$ (or, equivalently, $M/L \propto L^{0.157}$).

This relation (strictly, the relation given by equation 4.6) is shown as the solid line in Figure 4.11. Because the transformation from $(\kappa_1, \kappa_2, \kappa_3)$ is, by definition, orthogonal to $(r, 2s, i)$ but *not* orthogonal to (r, s, i), the transformation from (r, s, i)-space to κ-space does not preserve the shape of the 3D Gaussian and consequently this relation is not a particularly compelling description of the κ-space distribution.

The 6dFGS galaxies respect the zone of exclusion in the κ_1–κ_2 plane noted by Bender, Burstein & Faber (1992), corresponding to an upper limit on the amount of dissipation that a hot stellar system of a given mass undergoes. This limit is indicated by the short-dashed line in the centre panel of Figure 4.11, given by $\kappa_1 + \sqrt{3}\kappa_2 < 12.3$. The long-dashed line in the same panel provides another limit, $\sqrt{3}\kappa_2 - \kappa_1 > 2.0$, corresponding to a lower bound on the luminosity density, L/R^3 of an early-type galaxy of a given mass. However this requires further investigation, as more compact galaxies may be catalogued in the 2MASS database as stars and consequently would be excluded from our study. The sharpest and most striking limit is that indicated by the long-dashed line in the left panel of Figure 4.11, $2\sqrt{3}\kappa_3 - \sqrt{2}\kappa_1 > -4.0$. This implies that for these early-type galaxies there is a minimum mass-to-light ratio that increases with increasing mass as $(M/L)_{min} \propto M^{1/2}$. Since these galaxies all have similar stellar populations, this suggests that more massive galaxies have a maximum stellar-to-total mass ratio that decreases as $M^{-1/2}$.

4.8 Fundamental Plane Scatter

In general, the total scatter in r that we recover for the 6dFGS FP ($\sigma_r \approx 29\%$) is comparable to that found in other recent studies (Gargiulo et al., 2009; Hyde & Bernardi, 2009; La Barbera et al., 2010a), but larger than the value typically quoted as the FP distance error ($\sigma_r \sim 20\%$) found in earlier studies (see Table 4.2). However, it is important to note that the larger value of σ_r found in recent studies (and here) is the rms scatter, projected along the r-direction, about the best-fitting orthogonal or maximum-likelihood FP. In §6.3.3, we show that this over-estimates the actual FP distance errors.

Here we examine the individual components contributing to the overall scatter about the FP. This scatter results from a combination of intrinsic scatter in the FP relation (the physical origins of which are subject to investigation), observational errors and contamination from outliers (such as non-early-type galaxies or merging objects). To understand how each of these contribute to the total rms scatter in r, we split σ_r into the quadrature sum of these components:

$$\sigma_r^2 = (a\epsilon_s)^2 + \epsilon_X^2 + \sigma_{r,int}^2 \ . \tag{4.9}$$

The first term represents the effect of the rms observational scatter in velocity dispersion, ϵ_s, on the overall scatter in r. Because ϵ_s is scaled by a, the FP coefficient of s, this term is larger for samples with larger FP slopes. Since a tends to increase with wavelength ($a \approx 1.2$–1.4 in optical passbands and $a \approx 1.4$–1.5 in near-infrared passbands), this term is generally larger for near-infrared selected samples (such as 6dFGS) than for optically selected samples (such as SDSS). The rms velocity dispersion error of the 6dFGS sample is $\epsilon_s = 0.054\,\mathrm{dex}$ (i.e. 12%, comparable to other large survey samples; see Campbell, 2009). So, given our J band slope of $a = 1.52$, this term amounts to a contribution to the overall scatter of about 18%. To more directly determine the effect of the errors in s on the FP fits, we have fitted subsamples restricted to smaller ϵ_s values (see Table 4.3). While we find no change in the FP slopes (at the 1σ level), there is a small but significant change in the offset, and a modest reduction (at most 5%) in the overall scatter in $\log R_e$, consistent with that expected from the smaller value of ϵ_s and the above formula for the total scatter.

The second term in equation 4.9 is the rms observational scatter in the combined photometric quantity $X_{\rm FP} \equiv r - bi$, which accounts for the high degree of correlation between the measurement errors in r and i (see §2.7). This correlation conspires to make the value of this term negligible in comparison to the other terms; for all the 6dFGS passbands, $\epsilon_X \leq 4\%$.

The final term represents the intrinsic scatter of the FP relation in the r direction. For a pure 3D Gaussian distribution the intrinsic scatter in r would be given by

Table 4.3: Best-fit FP dependence on velocity dispersion error, ϵ_s. As well as the ϵ_s selection criteria for each subsample we list the number of galaxies, $N_{\rm g}$, maximum likelihood fitted FP slopes, a and b, r_0 offset and rms scatter about the r-direction, σ_r (in dex).

ϵ_s	$N_{\rm g}$	a	b	r_0	σ_r
no limit	8901	1.523±0.026	-0.885±0.008	0.345±0.002	0.127 (30%)
≤0.07	7913	1.523±0.026	-0.896±0.009	0.346±0.002	0.124 (29%)
≤0.06	6694	1.529±0.029	-0.903±0.010	0.349±0.002	0.122 (28%)
≤0.05	4692	1.528±0.032	-0.909±0.011	0.356±0.003	0.118 (27%)
≤0.03	1855	1.558±0.053	-0.894±0.018	0.376±0.005	0.108 (25%)

$\sigma_r = \sigma_1(1 + a^2 + b^2)^{1/2}$, which, for our typical values of $a = 1.5$ and $b = -0.88$, yields $\sigma_r \approx 2.0\,\sigma_1$. However, because our observed distribution is heavily censored by our selection criteria, the actual distribution of galaxies in FP space is a truncated 3D Gaussian, and so we cannot apply this formula. Instead we must calculate σ_r either from equation 4.9, taking the difference between the total scatter and the rms measurement errors, or as the rms scatter in $r - as - bi$ for mock samples drawn from the same intrinsic 3D Gaussian and the same selection criteria, but with no measurement errors. Both these approaches yield the same estimate for the intrinsic scatter in r for our J band sample: $\sigma_{r,int} \approx 23\%$. The intrinsic scatter is therefore the single largest contributor to the overall scatter about the 6dFGS FP.

Thus we have our total scatter in r of 29% being the quadrature sum of 18% scatter from the measurement errors in velocity dispersion, 4% scatter from the measurement errors in the photometric quantities, and 23% scatter from the intrinsic dispersion of the FP distribution.

4.9 Summary

With the maximum likelihood approach from Chapter 3 we obtain a best-fit FP in the 2MASS J band of $R_e \propto \sigma_0^{1.52\pm0.03} I_e^{-0.89\pm0.01}$. Fits in the H and K bands are consistent with this at the 1σ level once allowance is made for differences in mean colour, implying that M/L variations along the FP are consistent among these near-infrared passbands.

We investigate possible changes in the FP with environment, looking for variations with both global environment (quantified by group or cluster richness) and local environment (quantified by the surface density to the fifth-nearest neighbour). We find little variation of the 6dFGS FP slopes (i.e. the coefficients of velocity dispersion and surface brightness) with either of these measures of environment. However there is a statistically and physically significant offset of the FP with environment in the sense that, at fixed velocity dispersion and surface brightness, galaxies in the field and low-density regions are on average about 5% larger than those in groups and

higher-density regions.

Morphological classification of our FP sample allows us to separate the galaxies into two broad types: elliptical (E) and lenticular (S0) galaxies are combined into one subsample and early-type spiral (Sp) galaxies define the other type. For the latter, the construction of our sample means that we are effectively determining the FP parameters for the bulges of these galaxies. We find that this sample of early-type Sp bulges has FP slopes and scatter consistent with the E/S0 galaxy sample, although the FPs are offset in the sense that, at fixed velocity dispersion and surface brightness, early-type Sp bulges are on average about 10% larger than E/S0 galaxies. Contrary to our expectations, this does not appear to be a selection effect. Since the 6dFGS FP sample is dominated by E/S0 galaxies (6956 E/S0's and 1945 Sp bulges), the additional scatter in the overall FP from the offset in the FPs of the two types of galaxies is negligible.

Lastly, we deconstruct the scatter in r about the FP, σ_r, into contributions from observational errors and intrinsic scatter, and find that the overall scatter of 29% is the quadrature combination of an 18% observational contribution and a 23% intrinsic contribution. The observational contribution is strongly dominated by the velocity dispersion errors, and compounded by the fact that the FP slope is steeper in near-infrared passbands than in optical passbands—the FP coefficient of σ_0 is $a \approx 1.5$ for J, H and K and $a \approx 1.2$–1.4 for B, V and R, so the same error on σ_0 contributes 15–50% more scatter to σ_r for the near-infrared FP than the optical FP.

The overall scatter in R_e about the 6dFGS FP is larger than the widely-quoted value of 20%, but in fact is consistent with virtually all recent studies of large samples of galaxies (see Table 4.2). Moreover, the actual scatter in distance estimates is *not* the same as the scatter in R_e about the best-fit maximum-likelihood FP; the implications of which will be discussed later in Chapter 6.

Chapter 5

Stellar Populations and the Fundamental Plane

5.1 Introduction

The Fundamental Plane is found to be tilted with respect to the FP that one would expect if galaxies were homologous virialised systems with a constant mass-to-light ratio. The observed tilt and finite thickness of the FP are usually attributed to departures from the assumption of a constant M/L ratio which can be driven by variations in stellar content within the plane (see, e.g., Ciotti, Lanzoni & Renzini, 1996; Busarello et al., 1997; Graham & Colless, 1997; Trujillo, Burkert & Bell, 2004; D'Onofrio et al., 2006; Cappellari et al., 2006). By studying the stellar populations of early-type galaxies and their correlations with FP parameters, we can understand the galaxy formation and evolution processes that lead to the formulation of the Fundamental Plane itself.

Variation due to different stellar populations in the Fundamental Plane can also induce a source of scatter in the distances and peculiar velocities which are derived from the FP. Hence, if the effects of stellar population variation can be quantified and accounted for, they can potentially be used to reduce the scatter about the relation and increase the accuracy of the measured FP distances.

In Section 5.2 we determine the global trends of stellar population parameters with the Fundamental Plane in two ways; first using binned stellar population measurements in FP space and then by deriving the partial derivatives of the stellar population parameters (as well as physically relevant parameters such as mass, luminosity and mass-to-light ratio). These results are compared to the most recent FP studies (e.g. Graves, Faber & Schiavon, 2009a,b) in Section 5.3 where we postulate a formation scenario to explain the observed trends.

We consider trends with the residuals orthogonal to the plane in Section 5.4, establishing whether FP trends with stellar populations can be used to reduce the scatter about the plane. Finally, in Section 5.5 we examine the implications of using these trends to reduce the scatter in distance specifically, by developing a Fundamental Plane model which accounts for the trend in an additional parameter and then fitting the FP to subsamples segregated by stellar population parameters.

5.2 Variation of Stellar Populations through the Fundamental Plane

We analyse the stellar population trends within the Fundamental Plane by binning the 7132 galaxies (for which we have measured stellar population parameters) with respect to the $\boldsymbol{v}$-space axes defining the 3D Gaussian model of the Fundamental Plane (see Section 3.3.3). The $\boldsymbol{v}$-space vectors are defined by the global best-fit FP in Table 4.1. We bin along each $\boldsymbol{v}$-space vector with a width of 0.1 dex along the $\boldsymbol{v}_1$ direction, and 0.2 dex in both the $\boldsymbol{v}_2$ and $\boldsymbol{v}_3$ direction, so that each direction contains an approximately equal number of bins. We remove bins containing less than 5 galaxies from further analysis, which results in a total of 92 bins in FP space.

The median value for all stellar population parameters is then measured for each bin. Using these binned stellar population parameters, we analyse the FP trends in two different ways. The first approach involves plotting individual stellar population parameters against each FP parameter (§5.2.1) while the second utilises partial derivatives and the full 3D distribution (§5.2.2).

5.2.1 Global Trends with Stellar Population Parameters

We quantify the global variation of the stellar population parameters in FP space by examining their correlations with the Fundamental Plane parameters. In Figure 5.1, we plot the median values for each bin (in $\boldsymbol{v}$-space) of the stellar population parameters (i.e. log age, [Fe/H], [α/Fe] and [Z/H]) against the FP values (i.e. $r \equiv \log R_e$, $s \equiv \log \sigma_0$ and $i \equiv \log\langle I_e \rangle$). The trends with each of these parameters are determined by a least squares regression to the binned data, shown as a solid line in Figure 5.1, which we compare with Graves, Faber & Schiavon (2009b). The linear regression on velocity dispersion (centre panel) indicates that it is positively correlated with all the stellar population parameters, a trend also found by Graves, Faber & Schiavon (2009b). Effective radius (left panel) is found to be weakly correlated with [Fe/H] and [Z/H] (equivalent to [Mg/H] measured by Graves et. al.) consistent with the Graves, Faber & Schiavon (2009b) results. However the weak anti-correlation between r and galaxy age in Graves, Faber & Schiavon (2009b), is not apparent in our sample and unlike Graves et. al., we do not observe any stellar population variation with surface brightness (right panel).

However, the interpretation of these global correlations is obscured by the fact that the Fundamental Plane parameters are correlated with each other. Hence, it is difficult to disentangle the trends of stellar population and FP parameters with those of the FP parameters themselves. An alternative approach outlined in the next section, which does not suffer from this effect, is to calculate the partial derivatives of these correlations.

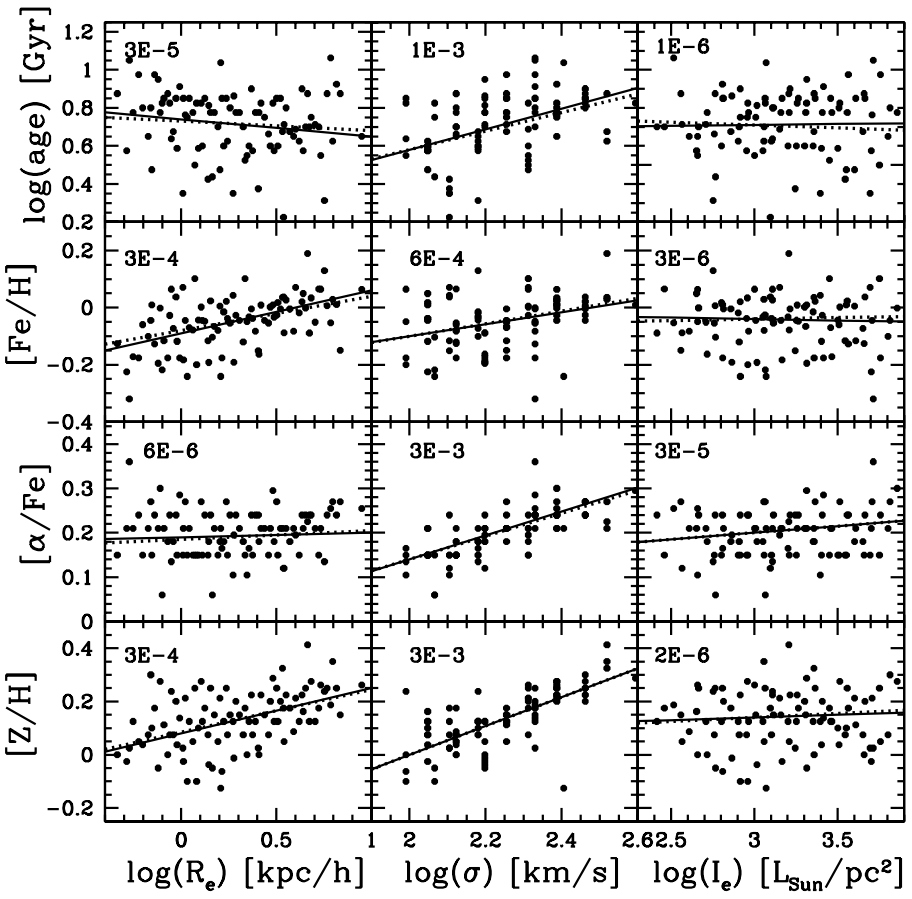

Figure 5.1: Global correlations between stellar population parameters (log age, [Fe/H], [α/Fe] and [Z/H]) with FP space parameters ($r \equiv \log R_e$, $s \equiv \log \sigma_0$ and $i \equiv \log\langle I_e \rangle$). Each point is the median value of one of the stellar population parameters in a bin in FP space, plotted against the corresponding r, s or i value at the centre of that bin. We also superimpose the best fit regression line to the plotted points (solid line) and a best-fitting line to a set of directional derivatives for r, s and i (dashed line, see Section 5.2.2). The R^2 correlation coefficient is given in the upper left-hand corner of each plot. (Figure 4 from Springob et al. 2012)

5.2.2 Variations along the 3D Gaussian Axes

To visualise the extent and direction of the stellar population trends in the Fundamental Plane, we need to view the full 3D distribution of galaxies in Fundamental Plane space, as in Figure 5.2. Figure 5.2 provides an unencumbered view of the trends in log age, [Fe/H], [α/Fe] and [Z/H] where each point represents a bin in FP space whose size is scaled by the number of galaxies in that bin. The points are also coloured by the median value of the stellar population parameter for each of log age, [Fe/H], [α/Fe] and [Z/H], in each bin.

To interpret these trends, we need to characterise the stellar population variation for each Fundamental Plane parameter while keeping the other two FP parameters fixed. This allows us to derive individual stellar population trends without introducing correlations between FP parameters in contrast to the simplistic global trends calculated in Section 5.2.1. Therefore, this method requires the calculation of partial derivatives, $\partial\mathcal{S}/\partial\mathcal{F}$, for each of the four stellar population parameters (indicated by $\mathcal{S}$) with respect to each of the three FP parameters (indicated by $\mathcal{F}$). Here we summarise the details of the method as given in Springob et al. (2012).

The partial derivatives are calculated by performing a linear regression to the median values in each bin along each of the $\boldsymbol{v}$-space vectors (i.e. $\boldsymbol{v}_1$, $\boldsymbol{v}_2$ and $\boldsymbol{v}_3$) for each stellar population parameter. The partial derivatives in this context, represent the *gradient* of each stellar population parameter, i.e. $\nabla\mathcal{S}$, in the direction of the $\boldsymbol{v}$-space vectors. However, we can also generalise the derivation of partial derivatives of the stellar population parameters to the FP space parameters (r, s and i) and also the logarithm of physical quantities such as dynamical mass ($m = \log M$), luminosity ($l = \log L$) and mass-to-light ratio ($m - l = \log M/L$). Therefore, strictly speaking we cannot refer to these as partial derivatives, instead they are directional derivatives. For example, the directional derivative of $\nabla_{\hat{r}}$[Fe/H] is the change in [Fe/H] per unit r and $\nabla_{\hat{m}}$[Fe/H] the change in [Fe/H] per unit m.

The directional derivatives ($\nabla_{\hat{\mathcal{F}}}\mathcal{S}$) for all four stellar population parameters (log age, [Fe/H], [α/Fe] and [Z/H]) and their statistical error (ϵ) are summarised in Table 5.1. We compare the significance of these derivatives (defined as χ) using the ratio of the absolute value of each directional derivative to its statistical error, i.e. $\chi = |\nabla\mathcal{S}|/\epsilon$, highlighting the most significant trends (with $\chi > 3$) in Table 5.1.

In $\boldsymbol{v}$-space the stellar population parameters are found to vary with $\boldsymbol{v}_1$ and $\boldsymbol{v}_3$, but not with $\boldsymbol{v}_2$. The physical interpretation of the complete lack of any stellar population variation with $\boldsymbol{v}_2$ will be discussed further in Section 5.3. The strongest trends observed in $\boldsymbol{v}$-space are with age through the plane (i.e. in $\boldsymbol{v}_1$) and metallicity (Z/H) across the plane (i.e. in $\boldsymbol{v}_3$) whilst [Fe/H] and [α/Fe] vary along a superposition of both $\boldsymbol{v}_1$ and $\boldsymbol{v}_3$.

The stellar population trends with FP parameters in Table 5.1 vary between the

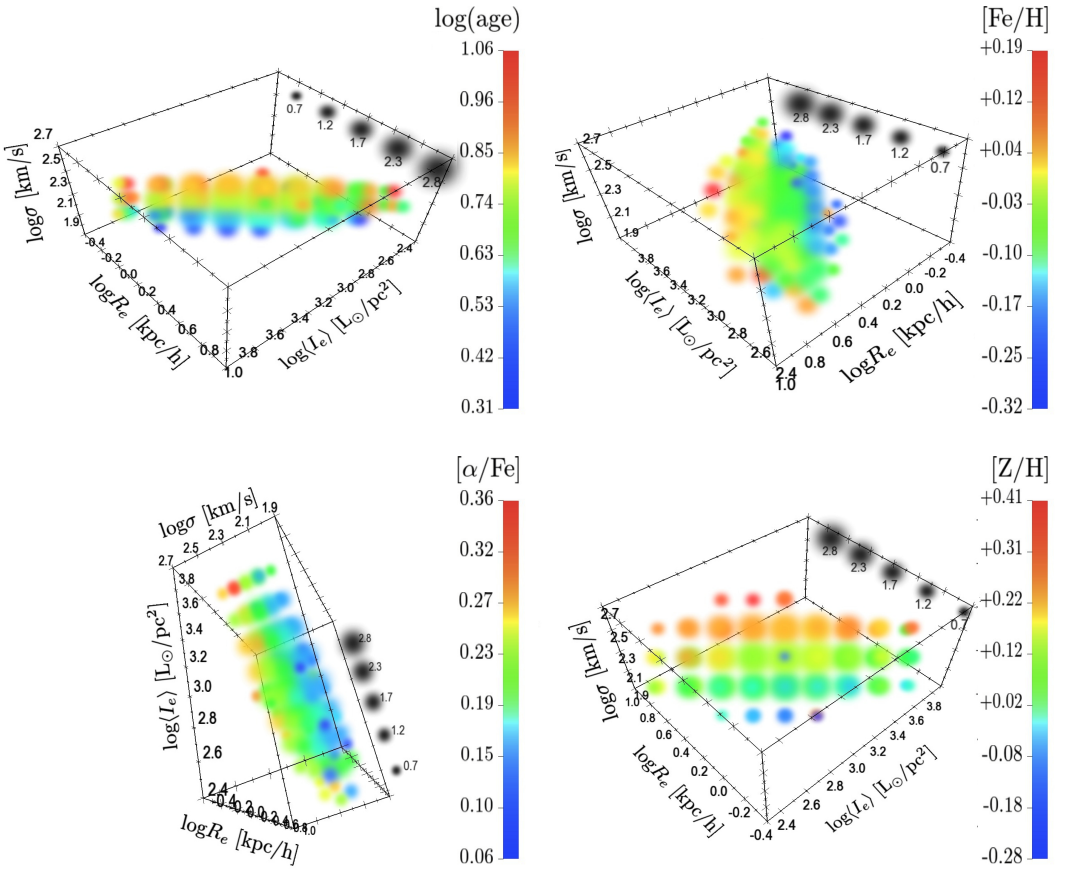

Figure 5.2: 3D visualisation of stellar population variation across the 6dFGS J band Fundamental Plane. Each sphere represents a bin in FP space, including 5 or more galaxies. The sphere is placed at the midpoint of the bin's (r, s, i) coordinates, colour-coded so that redder colours represent (a) older ages, (b) higher values of [Fe/H], (c) higher values of [α/Fe], and (d) higher values of [Z/H], as given by the colour scale on the right of each plot. The size of the sphere scales with the logarithm of the number of galaxies in the bin, as given by the scale established by the black spheres on the side of the plot. The number labelling each of the black spheres is the logarithm of the number of galaxies in a bin represented by a sphere of that size. (Readers viewing the digital version of this thesis using Acrobat Reader v8.0 or higher can enable interactive 3D viewing of this schematic by mouse clicking on the figure; see Appendix A for more detailed usage instructions.) Figures 5-8 from Springob et al. (2012).

different parameters. All the stellar population parameters are positively correlated with velocity dispersion except [Fe/H], even though it does exhibit a global trend (as found in Section 5.2.1). The trends with r and i differ between stellar population parameters as follows: age increases with decreasing r and i, [Fe/H] and [Z/H] increase with increasing r and i and [α/Fe] shows no correlation with r and i.

We have also determined the stellar population variation in FP space by combining the directional derivatives of $\nabla_{\hat{r}}\mathcal{S}$, $\nabla_{\hat{s}}\mathcal{S}$ and $\nabla_{\hat{i}}\mathcal{S}$ to form global trends. The best-fit linear regression of these 'total' observed trends are shown as dashed lines in Figure 5.1. The total fits indicate agreement with the global trends even when derived without assuming variation is along one axis.

We define the log quantities of dynamical mass, luminosity and mass-to-light, under the assumption of homology, as a function of the FP parameters (in the same way as for Section 3.3.3) such that $m = r+2s$, $l = 2r+i$ and hence $m-l = r+2s-i$. The vectors corresponding to the directions of $\boldsymbol{m}$, $\boldsymbol{l}$ and $\boldsymbol{m}-\boldsymbol{l}$ are shown in Figure 3.3, indicating close correspondence of $\boldsymbol{m}-\boldsymbol{l}$ with $-\boldsymbol{v}_1$ and $\boldsymbol{l}-3\boldsymbol{r}$ or luminosity density with $-\boldsymbol{v}_2$. From Table 5.1, we show the stellar population trends with m, l and $m-l$ are not as significant as those with the FP or $\boldsymbol{v}$-space vectors.

In summary, we find that age varies most strongly with v_1, [Fe/H] varies most strongly with v_1 and r, [α/Fe] most strongly with s, and [Z/H] most strongly with v_3.

5.3 Comparison to Graves et. al.

Previous studies, such as Nelan et al. (2005) and Thomas et al. (2005) focused on studying stellar population trends in the context of a 1D mass sequence, in particular the relations with velocity dispersion as a proxy for galaxy mass. Graves, Faber & Schiavon (2009a), however, extend upon and improve this analysis by examining the '2D family of early-type galaxy stellar populations and their structural properties' and in doing so include variations with residuals from the FP i.e. through the plane. While the evolution of stellar populations i.e. mass-to-light variation through the plane, does contribute to the thickness of the plane, Graves, Faber & Schiavon (2010) speculate its origin could be due to genuine structural differences.

The correlations between stellar population and FP parameters that Graves, Faber & Schiavon (2010) determine, are summarised in their Table 3. To compare the trends in our dataset found in Table 5.1 to theirs, we note that their vector definitions in FP space (which we call $\boldsymbol{r'}$, $\boldsymbol{s'}$ and $\Delta\boldsymbol{i}$) are not orthogonal and possess the following differences to our $\boldsymbol{v}$-space. $\boldsymbol{r'}$ and $\boldsymbol{s'}$ are the direction within the plane along which r increases but s remains constant and the direction within the plane along which s increases but r remains constant respectively. $\Delta\boldsymbol{i}$ is the residual from the plane along the i direction. They are related to our $\boldsymbol{v}$-space in the following way;

Table 5.1: Summary of stellar population trends in FP space. For each stellar population parameter, $\mathcal{S}$ (log age, [Fe/H], [α/Fe] and [Z/H]) the trends are quantified by the directional derivative ($\nabla_{\hat{\mathcal{F}}}\mathcal{S}$) for a number of galaxy parameters; the vectors defining the Fundamental Plane i.e. $\boldsymbol{v}_1$, $\boldsymbol{v}_2$ and $\boldsymbol{v}_3$, the FP parameters i.e. r, s and i, log mass (m), log luminosity (l) and log mass-to-light ratio ($m-l$). We also list the statistical error (ϵ) and χ value ($=|\nabla_{\hat{\mathcal{F}}}\mathcal{S}|/\epsilon$) for each directional derivative. The most significant trends with $\chi^2 > 3$ are highlighted. (Table 2 from Springob et al. 2012.)

FP parameter	$\nabla_{\hat{\mathcal{F}}}$ age	ϵ	χ	$\nabla_{\hat{\mathcal{F}}}$[Fe/H]	ϵ	χ	$\nabla_{\hat{\mathcal{F}}}$[$\alpha$/Fe]	ϵ	χ	$\nabla_{\hat{\mathcal{F}}}$[Z/H]	ϵ	χ
v_1	**-1.47**	**0.12**	**12.25**	**0.37**	**0.10**	**3.70**	**-0.24**	**0.05**	**4.80**	0.07	0.13	0.54
v_2	-0.04	0.04	1.00	0.05	0.02	2.50	-0.01	0.01	1.00	0.05	0.03	1.67
v_3	0.08	0.09	0.89	**0.26**	**0.04**	**6.50**	**0.16**	**0.02**	**8.00**	**0.46**	**0.04**	**11.50**
r	**-0.70**	**0.08**	**8.75**	**0.37**	**0.06**	**6.17**	-0.03	0.03	1.00	**0.32**	**0.07**	**4.57**
s	**1.16**	**0.11**	**10.55**	-0.11	0.08	1.38	**0.29**	**0.04**	**7.25**	0.25	0.10	2.50
i	**-0.57**	**0.08**	**7.13**	**0.25**	**0.05**	**5.00**	-0.02	0.03	0.67	**0.22**	**0.06**	**3.67**
m	**0.32**	**0.05**	**6.92**	0.03	0.03	0.88	**0.11**	**0.02**	**6.44**	**0.16**	**0.04**	**3.87**
l	**-0.39**	**0.04**	**11.01**	**0.20**	**0.03**	**7.62**	-0.02	0.01	1.19	**0.17**	**0.03**	**5.65**
$m-l$	**0.60**	**0.04**	**14.51**	**-0.14**	**0.03**	**4.72**	**0.11**	**0.02**	**6.96**	-0.01	0.04	0.18

$\boldsymbol{r}'$ is the same as $\boldsymbol{v}_2$, $\Delta\boldsymbol{i}$ is equivalent to our $\boldsymbol{v}_1$ to within a scale factor (although it is defined differently) and finally $\boldsymbol{s}'$ is the vector defined most differently with respect to $\boldsymbol{v}$-space as it includes both a strong component in $\boldsymbol{v}_3$ and a $\boldsymbol{v}_2$ component. In the absence of stellar population trends with $\boldsymbol{v}_2$ (as we find), $\boldsymbol{s}'$ should be equivalent to $\boldsymbol{v}_3$. If we replace $\Delta\boldsymbol{i}$ for $\boldsymbol{v}_1$, $\boldsymbol{r}'$ for $\boldsymbol{v}_2$, $\boldsymbol{s}'$ for $\boldsymbol{v}_3$, [α/Fe] for [Mg/Fe] and [Z/H] for [Mg/H] we find good agreement with Table 3 from Graves, Faber & Schiavon (2010). We can also compare the least significant stellar population trends (less than 3σ) in Table 5.1 with the observed 'null' trends of Graves, Faber & Schiavon (2010), and find the only differences are that we do not observe a trend of age with $\boldsymbol{v}_3$, or [Z/H] with $\boldsymbol{v}_1$. Therefore, we find very consistent trends with all the stellar population parameters even though the methods of binning the data differ and Graves, Faber & Schiavon (2010) measure stellar population parameters from stacked spectra in each bin, whereas we measure individual stellar population parameters for each galaxy.

Other studies have also investigated stellar population trends with respect to the residuals from the FP. Gargiulo et al. (2009) find an anti-correlation between the FP residuals in the r-direction and age and also a stronger anti-correlation between the residuals in r and [α/Fe]. These results are consistent with the same trends we measure with residuals along the $\boldsymbol{v}_1$ direction, given that the residuals in $\boldsymbol{v}_1$ are proportional to the residuals with r (i.e. an increase in $\boldsymbol{v}_1$ is proportional to an increase in r). However, we find the correlation with age is more significant than that in [α/Fe], unlike Gargiulo et al. (2009).

It remains that the most significant result from Table 5.1 is that there is no stellar population variation along the $\boldsymbol{v}_2$ direction. This result is interesting because there was no physical motivation for defining the $\boldsymbol{v}$-space vectors, instead the axes are determined by fitting the 3D Gaussian to our data. However, these vectors are observed to align with stellar population parameters, suggesting some physical motivation for their orientation in FP space; a possible hypothesis for the distribution of galaxies along these axes in FP space is the subject of the next section.

5.3.1 $\boldsymbol{v}_2$ and Merging History

Graves, Faber & Schiavon (2009b) attempt to explain the variation of stellar population parameters with velocity dispersion but not effective radius, by postulating that the variation is a consequence of galaxies following different merger histories. They suggest velocity dispersion is independent of merger history as has been shown through N-body simulations (Robertson et al., 2006) and that galaxies with different merger histories (but similar mass and hence, velocity dispersion) have varying radii and surface brightness, while keeping their velocity dispersion in tact.

In the context of our results from Sections 5.2.1 and 5.2.2 where we *do* observe correlations between stellar population trends and r, we need only modify the above

scenario from Graves, Faber & Schiavon (2009b) to explain these results; varying merger histories could serve to induce more scatter in the relations between r and the stellar population parameters while still retaining the overall trend. Correlations between velocity dispersion and other galaxy parameters are found to be relatively independent of merger history as shown in the simulations by Kobayashi (2005). The variation of merger history, however, does have the effect of increasing the scatter of, but still retaining, the correlations with effective radius.

If we apply the same reasoning to the stellar population variations with effective radius, we offer the following explanation of our results. In terms of the Fundamental Plane, along the $\boldsymbol{v}_3$ axis, galaxies with increasing r, s and i will also have increasing m, l and [Z/H] consistent with increasing the total mass of the system or mass of the dark matter halo. Along the $\boldsymbol{v}_2$ axis galaxies with increasing r will have a decreasing i both of which depend upon the merger history of the galaxy. Therefore, as $\boldsymbol{v}_2$ is aligned closely with luminosity density (i.e. L/R^3), we suggest that luminosity density is significantly dependent upon merger history which is largely independent of stellar population (as shown in Figure 14 of Springob et al. 2012). This hypothesis would then infer that the distribution of galaxies in FP space are physically driven by two *different* (and unrelated) processes along the $\boldsymbol{v}_2$ and $\boldsymbol{v}_3$ axes.

5.4 Fundamental Plane Residual Trends

In §4.5 and §4.6 we examined the dependence of the 6dFGS FP on environment and morphology by comparing the FP fits for appropriate subsamples of galaxies. Here we take an alternative approach by looking at the trends of the orthogonal residuals (defined as $r-(as+bi+c)/\sqrt{1+a^2+b^2}$) from the FP with various galaxy properties. As well as morphology, group richness (N_R) and local density (Σ_5), we also consider three stellar population parameters discussed in the previous sections: log age, metallicity ([Z/H]) and alpha-enhancement ([α/Fe]). For this particular purpose we convert our morphological classifications to the discrete m-type scheme (defined in Section 2.5) where E = 0, S0 = 2, Sp = 4 and 1, 3 and 5 are the respective transition classes.

Figure 5.3 shows the mean residuals orthogonal to the best-fit global J band FP (with $a = 1.52$ and $b = -0.89$) as a function of these properties. The mean orthogonal residuals are computed in bins of $\log \Sigma_5$ (for 8258 galaxies), morphological type and $\log N_R$ (for 8901 galaxies), and log age, [Z/H] and [α/Fe] (for 6679 galaxies). A weighted least-squares regression is performed to quantify the significance of the linear trend in the binned data. The slope and offset of the linear fit for each galaxy property (and associated error) are given at the top of each panel, along with the reduced χ^2 of the fit.

The strongest trend of the FP residuals is clearly with the age of the stellar popu-

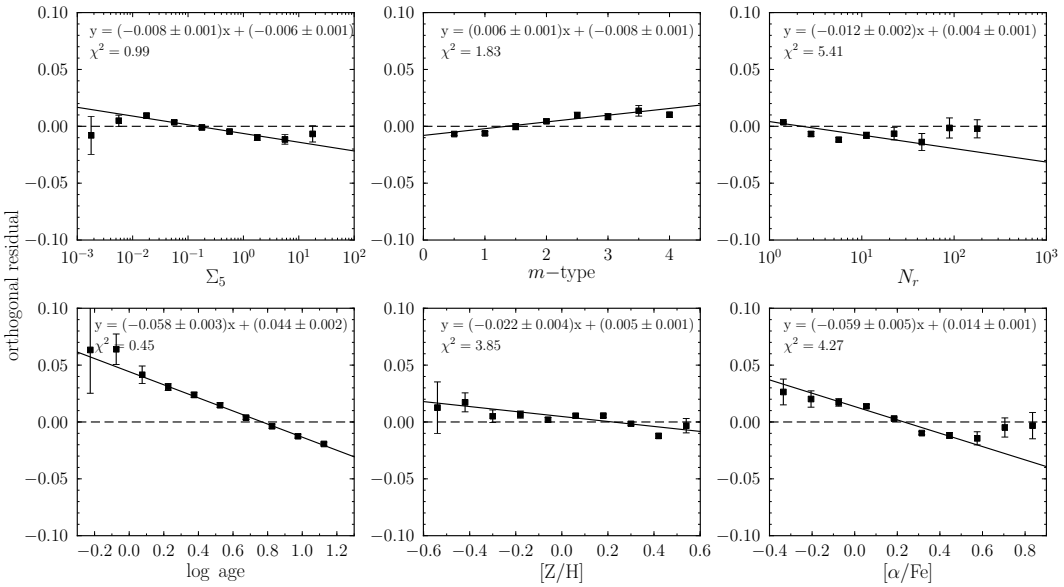

Figure 5.3: Correlation of orthogonal residuals relative to the best-fit FP ($a = 1.52$ and $b = -0.89$) with various galaxy properties: local density (Σ_5), morphological type (m-type) and group richness (N_R), and log age, [Z/H] and [α/Fe]. In each panel the best-fitting line for the binned residuals is given along with the corresponding reduced χ^2 value.

lation, and amounts to ∼0.08 dex over the full range in age; the next strongest trend is with [α/Fe], amounting to ∼0.05 dex over the observed range. Both these trends are highly statistically significant, although a line is not a good fit to the relation in the case of [α/Fe]. The residuals from the FP show relatively weaker (although still statistically significant) trends with morphological type, local density, group richness and metallicity. These results are consistent with our fits to subsamples defined on the basis of these properties, and confirm the equivalent analysis in the preceding sections of this chapter.

5.4.1 Scatter in the FP Age Trend

We identify galaxy age as the stellar population parameter that will have the most significant effect on FP distances as the direction it varies in most is *through* the plane. We observe that v_1 and log age are mildly anti-correlated (as expected from Table 5.1) from the contour plot (Figure 5.4) of v_1 vs log age for all galaxies with reliable stellar populations parameters ($N_g = 7132$; left) and for galaxies in a narrow slice of v_2 ($-0.05 < v_2 < 0.05$) and v_3 ($-0.05 < v_3 < 0.05$; right). The contours correspond to the number of galaxies found within a single smoothing length (0.075 for log age and 0.025 in v_1) with more galaxies found in the areas of redder colour. In these plots, the trend in age is visible but with large scatter.

In the right panel, we superimpose error bars (in the lower left) that indicate the average measurement error on both log age and v_1 where the v_1 measurement errors

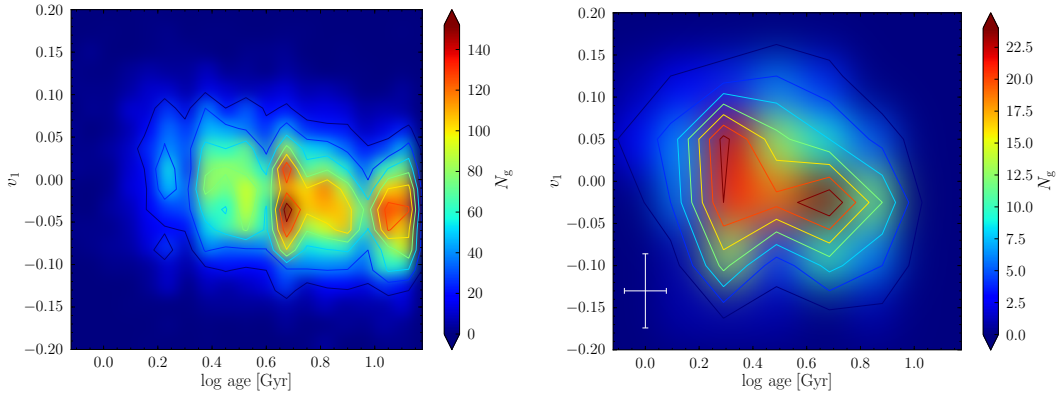

Figure 5.4: Contour plot of v_1 vs log age for all galaxies with stellar population parameters ($N_g = 7143$), showing the mild but statistically significant anti-correlation (See Table 5.1). The colour scale given on the right shows the number of galaxies found within a single smoothing length, which is 0.075 in log age (*left*) and 0.025 in v_1 (*right*); redder colours correspond to areas in v_1-age space with more galaxies. In the right panel, we only include galaxies along a narrow range of v_2 and v_3: $-0.05 < v_2 < 0.05$, and $-0.05 < v_3 < 0.05$. In the lower left of this plot, we show the size of the error bars corresponding to the average statistical error on log age (0.078 dex), and the average measurement error on v_1 (0.044 dex) in this subsample.

have been derived by projecting the measurement errors on r, s, and i along the v_1 direction. Most of the total scatter in the v_1 direction is due to these large measurement errors, suggesting minimal gain in using individual galaxy ages to reduce the scatter in the FP. However, if galaxy ages could be precisely determined, then these results imply that it would be possible to reduce the intrinsic scatter about the FP by a few percent.

5.5 Stellar Population Trends and FP Distances

We have now established that galaxy age is the parameter that varies most directly through the FP. We find that the strongest trend with the FP residuals is with age, and we therefore explore whether it is possible to reduce the intrinsic scatter about the FP using this age variation.

To this end, we first outline a procedure for incorporating stellar population effects in our Gaussian model of the Fundamental Plane and then fit the FP to individual subsamples of age and metallicity to assess the impact these trends will have on the scatter in the FP.

5.5.1 Adding Age to the Fundamental Plane Model

In the previous sections it was found that there is a clear trend of galaxy age through the FP (i.e. along the $\boldsymbol{v}_1$ direction), as expected from models of the effect of stellar populations on mass-to-light ratios (e.g. Bruzual & Charlot, 2003; Korn, Maraston & Thomas, 2005). The variation of age through the FP is shown in Figure 5.5,

a 3D visualisation of the FP-space distribution of the subsample of 6679 galaxies with stellar population parameters, with colour encoding log age. Here we ascertain whether this trend in age can be incorporated into the FP model and used to reduce the overall scatter of the FP by exploring a very simple extension of the model that includes a linear trend with age through the FP.

We include an age component in our existing FP model by adding log age as a fourth dimension in FP space along with r, s, and i as described in Section 3.7.2. The 4D Gaussian model including age is then fit to this subsample resulting in an FP (after bias correction) of

$$r = (1.56 \pm 0.03)s - (0.89 \pm 0.01)i + (0.13 \pm 0.01)A - 0.43 \pm 0.06 \tag{5.1}$$

with $\sigma_1 = 0.048 \pm 0.001$ and $\sigma_4 = 0.40 \pm 0.01$. Although the intrinsic scatter through the FP (σ_1) is reduced from its value in the standard 3D Gaussian model (where $\sigma_1 = 0.053$), the large scatter in σ_4 and steeper slope in $\log \sigma_0$ suggest that the scatter in distance has not been reduced by including an age component. In fact, the scatter in distance (see Section 6.3.3) is slightly larger, at $\sigma_d = 0.100$ dex (23.3%), than for the standard 3D Gaussian model, where $\sigma_d = 0.097$ dex (22.5%).

5.5.2 Correcting the FP for Stellar Population Trends

In the previous section, the addition of age as a fourth parameter in our Gaussian FP model did not significantly improve the scatter about the FP, due to the substantial uncertainty in estimating ages of stellar populations. Therefore we attempt to reduce the scatter instead by fitting to FP subsamples defined by age.

We divide the galaxies with reliable age measurements which are not excluded by our FP redshift cuts (i.e. $N_g = 6679$ galaxies in total) into large age bins (to reduce the scatter of individual galaxies), and use our maximum likelihood model to fit the Fundamental Plane to each of the subsamples and determine any offsets between them. From the *full* sample of 8901 J band galaxies, there are 2222 galaxies which do not have stellar population measurements either due to poor S/N or a high χ^2 value in Lick-index fitting; we refer to these galaxies as belonging to the *unknown* age subsample. For the remaining 6679 galaxies we define three subsamples divided in age: young galaxies (age ≤ 3 Gyr), intermediate age galaxies ($3 <$ age ≤ 8 Gyr) and old galaxies (age > 8 Gyr). There are 1419 young galaxies, 3181 intermediate age galaxies, and 2079 old galaxies. For comparison, for the same set of 6679 galaxies, we also define three equal-sized subsamples according to metallicity, [Z/H]: galaxies that are metal-poor ($[Z/H] \leq 0.05$), galaxies of intermediate metallicity ($0.05 < [Z/H] \leq 0.2$), and those that are metal-rich ($[Z/H] > 0.2$). There are 2231 metal-poor galaxies, 2144 intermediate metallicity galaxies and 2304 metal-rich galaxies.

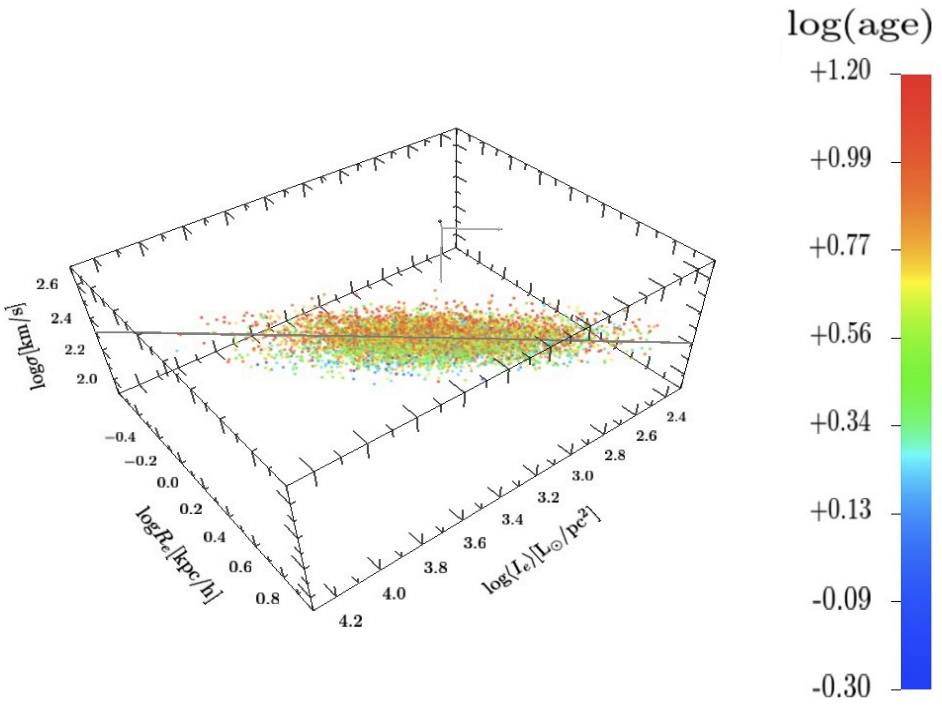

Figure 5.5: 3D visualisation of the 6dFGS J band Fundamental Plane with individual galaxies colour-coded by log age. The best-fitting plane (in grey) for the entire sample (with $a = 1.523$, $b = -0.885$ and $c = -0.330$) is shown for reference. (Readers viewing the digital version of this thesis using Acrobat Reader v8.0 or higher can enable interactive 3D viewing of this schematic by mouse clicking on the figure).

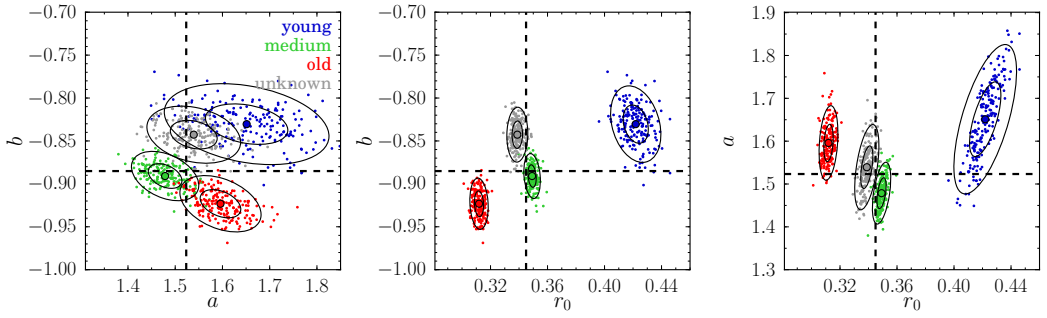

Figure 5.6: As for Figure 4.3, but comparing the FP fits to three age samples spanning young age (blue; $N_g = 1419$), medium age (green; $N_g = 3181$) and old age (red; $N_g = 2079$) galaxy samples as well as those galaxies with unknown age (grey; $N_g = 2222$). The points in each panel are the fits to 200 mocks of each of these four subsamples; the large black circles show the means and the ellipses the 1σ and 2σ contours of the distribution of fitted parameters. The dashed lines show, for reference, the best-fit parameters for the full J band sample.

The best-fit FP values of the individual stellar population subsamples are summarised in Table 5.2 using the same notation as in Section 4.2.1. The uncertainties in Table 5.2 are estimated (in the same way as for Table 4.1) as the rms scatter in each FP coefficient from fits to 200 mock simulations (or 1000 mock simulation in the case of the *full* sample). The FP slopes, a and b, are similar to within 1–2σ for all age subsamples (as well as the unknown subsample) and consistent with the full FP sample. A statistically significant trend in r_0, the FP offset at a fiducial point, is observed such that younger galaxies tend to have a larger r_0 and the r_0 offset of the intermediate age galaxies (i.e. $r_0 = 0.348 \pm 0.003$) is within 1σ of the full sample $r_0 = 0.345 \pm 0.002$. The same trends are observed for the metallicity subsamples such the FP slopes are consistent with each other and the full sample, and the r_0 offset is smaller ($r_0 = 0.333 \pm 0.003$) for the metal-rich galaxies as compared to the metal-poor galaxies ($r_0 = 0.368 \pm 0.006$).

These trends are clearly shown in Figure 5.6 (and also Figure 5.7 but for metallicity) where we compare the best-fitting parameters of a, b and r_0 against each other, from 200 mock simulations of the three age (and unknown) subsamples. We plot the best-fit values as well as the 1σ and 2σ error contours, highlighting the significance of the r_0 variation which is also consistent with the variation of effective radius found in Table 5.1. This suggests that while the age subsamples share the same Fundamental Plane (as they have consistent slope values), the individual planes for each stellar population are in fact offset to one another.

In addition, the intrinsic thickness or scatter in the plane, as quantified by σ_1, is reduced from $\sigma_1 = 0.056 \pm 0.002$ dex (12.9%) for the young galaxies down to $\sigma_1 = 0.043 \pm 0.002$ dex (9.9%) for the oldest galaxies. However, because these subsamples are smaller than the full sample and the observational error in the FP is large for all

Table 5.2: Best-fit 6dFGS FP parameters (including bias corrections) and their associated uncertainties for: (i) the full J band sample; (ii) the J band subsample with unknown stellar population parameters; (iii) the J band log age subsamples (young, medium and old); and (iv) the J band metallicity subsamples (metal-poor, medium and metal-rich). As well as the nine FP parameters, the table also lists: $N_{\rm g}$, the number of galaxies in each sample; r_0, the location of the FP at the fiducial point ($s_0 = 2.3, i_0 = 3.2$); and σ_r, the scatter about the FP in the r-direction (see §4.8).

Subsample	$N_{\rm g}$	a	b	c	$\bar{r}$	$\bar{s}$	$\bar{i}$	r_0	σ_1	σ_2	σ_3	σ_r
Full Sample	8901	1.524±0.026	-0.885±0.008	-0.329±0.054	0.183±0.004	2.188±0.004	3.188±0.004	0.345±0.002	0.052±0.001	0.318±0.004	0.167±0.003	0.127 (29.7%)
$\mathcal{S}$ Unknown	2222	1.529±0.050	-0.840±0.016	-0.495±0.110	0.213±0.008	2.194±0.006	3.154±0.008	0.338±0.004	0.053±0.002	0.316±0.007	0.164±0.005	0.134 (31.5%)
age $\leq$ 3 Gyr	1419	1.651±0.087	-0.828±0.022	-0.729±0.185	0.189±0.012	2.145±0.010	3.171±0.010	0.421±0.008	0.056±0.002	0.322±0.010	0.165±0.007	0.135 (31.5%)
3 $<$ age $\leq$ 8 Gyr	3181	1.472±0.036	-0.889±0.013	-0.195±0.074	0.183±0.008	2.186±0.006	3.195±0.007	0.348±0.003	0.049±0.001	0.309±0.007	0.174±0.005	0.116 (27.1%)
age $>$ 8 Gyr	2079	1.599±0.043	-0.927±0.015	-0.401±0.089	0.151±0.008	2.213±0.006	3.223±0.008	0.311±0.003	0.043±0.002	0.323±0.008	0.168±0.005	0.117 (27.2%)
$[Z/H] \leq 0.05$	2231	1.632±0.065	-0.872±0.017	-0.599±0.130	0.100±0.010	2.130±0.008	3.189±0.009	0.368±0.006	0.055±0.002	0.315±0.007	0.165±0.006	0.134 (31.4%)
$0.05 < [Z/H] \leq 0.2$	2144	1.548±0.056	-0.908±0.015	-0.303±0.118	0.195±0.009	2.205±0.005	3.212±0.008	0.354±0.004	0.051±0.002	0.318±0.007	0.147±0.005	0.125 (29.3%)
$[Z/H] > 0.2$	2304	1.403±0.044	-0.907±0.014	0.009±0.094	0.268±0.007	2.261±0.004	3.210±0.006	0.333±0.003	0.045±0.001	0.311±0.006	0.144±0.004	0.111 (25.8%)

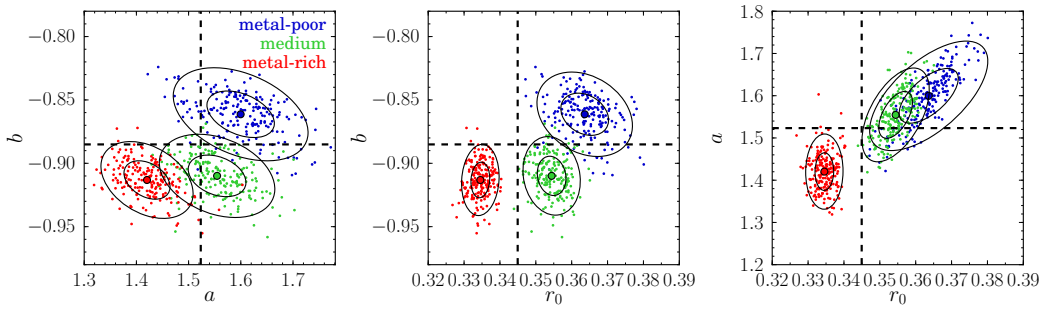

Figure 5.7: As for Figure 4.3 but comparing the FP fits to three metallicity sample spanning metal-poor (blue; $N_g = 2231$), medium metallicity (green; $N_g = 2144$) and metal-rich (red; $N_g = 2304$) galaxy samples. The points in each panel are the fits to 200 mocks of the three metallicity subsamples the large black circles show the means of the fitted parameters and the ellipses show the 1σ and 2σ contours of the distribution. The dashed lines show, for reference, the best-fit parameters for the full observed J band sample.

the subsamples, the *total* scatter (including measurement error) about the plane is decreased by <3% for the older age subsamples as compared to the full sample with $\sigma_r = 0.127$ dex (29.7%). From Table 5.2, we estimate that segregating the galaxies by age reduces the scatter in r by ∼2.5% for 60% of the sample (i.e. medium and old age galaxies) but increases the scatter by ∼1.8% for the remaining 40% (i.e. young and unknown age galaxies). If we divide by metallicity instead, we find a larger reduction in scatter (∼3.9%) for the metal-rich galaxies but for only 26% of the sample, leading to only a slight improvement to the overall scatter.

We find only a modest gain in the distance scatter when segregating our FP sample by age but we defer further analysis of this approach until Chapter 6 where we incorporate the age variation with FP distances and peculiar velocities.

5.6 Summary

Global stellar population trends within the Fundamental Plane were derived by binning individual galaxy measurements of the stellar population parameters in FP space. We confirmed previous correlations of stellar population parameters with velocity dispersion, and discovered new correlations with effective radius and surface brightness.

Using our 3D Gaussian model of the FP we determined the vector directions of the stellar population trends, finding the strongest variation to be age through the plane (i.e. in the $\boldsymbol{v}_1$ direction) and no stellar parameters to vary along the $\boldsymbol{v}_2$ direction. We propose that the significant lack of stellar population variation with $\boldsymbol{v}_2$ (and close alignment with luminosity density) suggests that the $\boldsymbol{v}_2$ vector represents a dependence on galaxy merger history and hence independent of stellar content.

We find that the strongest trend is with age, and we speculate that, of the galaxy properties considered in this thesis, age is the most important systematic source of

offsets from the FP, and drives (through the correlations of age with environment, morphology and metallicity) most of the variations with the other galaxy properties.

Therefore, we investigated two different approaches using the strong age variation to improve the scatter on FP distance measurements. First, we developed a FP model that incorporates the age trend though the plane. From this analysis, we conclude that: (i) there is a statistically significant contribution from age variations to the scatter through the FP, which is slightly reduced by including age in the FP model; and (ii) the combination of large measurement errors on individual galaxy ages, intrinsic scatter in age about the FP, and the tilt of the FP (specifically, the angle between $\boldsymbol{v}_1$ and r), means that—for the 6dFGS sample—including age in this method does not significantly improve the distance estimates obtained from the FP. This might change, however, if more precise age measurements were available.

The second method involved fitting the FP to subsamples divided by age, which shows some marginal improvement in the scatter about the plane. However, we need to perform this same segregation in the peculiar velocity analysis (Chapter 6) in order to determine the actual gain in the distance (hence peculiar velocity) estimates.

Chapter 6

Peculiar Velocities

6.1 Introduction

The 'cosmic web' of large-scale structure in galaxies is formed through the gravitational collapse of density fluctuations in the early-universe. The overdensities in the distribution of matter induce *peculiar* motions that arise from the gravitational effects of neighbouring galaxies, in excess of the Hubble flow associated with the expansion of the universe. The redshift of a galaxy, cz, alone recovers the total motion of a galaxy, including the radial components from both the Hubble flow and its peculiar velocity. Disentangling the peculiar velocity of a galaxy from its recessional velocity requires the measurement of a redshift-independent distance in addition to the redshift. In this chapter we will measure galaxy peculiar velocities using distances determined from the Fundamental Plane relation as derived in Chapter 4.

In the linear regime we can relate the peculiar velocity field, $\boldsymbol{v}(\boldsymbol{r})$, to the matter density field, $\delta_m(\boldsymbol{r})$ via gravitational instability (Peebles, 1993), using

$$\boldsymbol{v}(\boldsymbol{r}) = \frac{f}{4\pi} \int d^3\boldsymbol{r}' \frac{\boldsymbol{r}' - \boldsymbol{r}}{|\boldsymbol{r}' - \boldsymbol{r}|^3} \delta_m(\boldsymbol{r}') \ , \tag{6.1}$$

where f describes the rate of growth of structure and is approximately equal to $\Omega_m^{0.6}$ (Peebles, 1980); Ω_m is the matter density parameter. Therefore, peculiar velocities are a direct probe of the underlying matter distribution, providing additional information to redshift surveys.

Peculiar velocities distort the galaxy distribution in redshift-space from the distribution in real-space, affecting the determination of distance estimates. On small scales, random motions cause galaxy structure to be elongated along the line of sight, an effect known as the 'Finger of God'. On large scales, the clustering of matter is amplified by the coherent infall of galaxies towards overdense regions. In linear theory, the effects of the latter type of distortion can be characterised by the linear redshift-space distortion parameter, β, defined by $\beta = \Omega_m^{0.55}/b$ (using $f \sim \Omega_m^{0.55}$, updated by Linder 2005) assuming galaxy fluctuations are biased with respect to mass fluctuations by $\delta_g = b\delta_m$ where b is the linear bias parameter. Equation 6.1

can therefore be expressed as

$$\boldsymbol{v}(\boldsymbol{r}) = \frac{\beta}{4\pi} \int d^3\boldsymbol{r}' \frac{\boldsymbol{r}' - \boldsymbol{r}}{|\boldsymbol{r}' - \boldsymbol{r}|^3} \delta_g(\boldsymbol{r}') \ , \tag{6.2}$$

We can derive β from the comparison of the matter and velocity fields from the observed peculiar velocities (using distance indicators such as the FP) to those from the predictions of redshift surveys. One of the largest and most detailed density and velocity field reconstructions, from Erdoğdu et al. (2012, submitted; updated from Erdoğdu et al. 2006), is derived from the Two-Micron All-Sky Redshift Survey (2MRS; Huchra et al., 2012). We use the 2MRS velocity field model from this analysis to compare with the measured peculiar velocities of the galaxies in the 6dFGS FP sample.

Peculiar velocities are also used to study the coherent peculiar motion, or bulk flow, in a volume with respect to the CMB rest frame. From the peculiar velocity field derived from the 6dFGS FP sample, we will determine the total bulk flow motion, $\boldsymbol{u}_{\rm tot}$, and the residual bulk flow (after subtracting the 2MRS prediction), $\boldsymbol{u}_{\rm res}$.

The structure of this chapter is as follows: in Section 6.2 we outline the features of the 2MRS reconstructed density and peculiar velocity field, the model used throughout this chapter. We introduce the 6dFGSv sample of ∼9000 FP distances and peculiar velocities in Section 6.3, where we also describe the implementation of peculiar velocity probability distributions and calibration of the peculiar velocity zeropoint.

In Section 6.4 we develop a maximum likelihood model for fitting parameters defining the peculiar velocity field (such as β and $\boldsymbol{u}$). This model incorporates the 2MRS model predictions and the 3D Gaussian FP model of Chapter 3. We use this maximum likelihood method to fit three types of peculiar velocity (v_p) models:

1. The v_p field assuming that the matter follows the galaxy distribution of 2MRS, with β as the free parameter.

2. The v_p field assuming that the matter follows the galaxy distribution of 2MRS, with β and a residual bulk flow $\boldsymbol{u}_{\rm res}$ as free parameters.

3. The v_p field assuming that it can only be modelled by a total bulk flow $\boldsymbol{u}_{\rm tot}$.

In Section 6.5 we test the robustness of this new likelihood model using mock simulations for a range of mock peculiar velocity distributions. We extend this model to include a bulk flow in Section 6.6. The best-fit values of β and $\boldsymbol{u}$ are derived by comparing the peculiar velocity model to the 6dFGSv data in Section 6.7. We then investigate whether introducing an age trend into the peculiar velocity model can achieve tighter constraints on these parameters (Section 6.8) and also quantify the

additional uncertainty in the calibration of $\bar{r}$ (Section 6.9). Finally we discuss the implications of these results in Section 6.10.

6.2 The 2MRS Reconstructed Velocity Field

Density and velocity fields that are reconstructed from redshift surveys can provide a cosmographic description of the universe and are also used to investigate the processes that govern structure formation on the largest scales. By comparing the observed peculiar velocity field to a reconstructed prediction of the velocity field, we can determine $\beta = \Omega^{0.55}/b$, linking the total mass density and the bias in the distribution of galaxies relative to the underlying distribution of mass.

One of the largest, most complete reconstructed velocity fields at present is derived from galaxies in the Two-Micron All-Sky Redshift Survey (2MRS). In the final data release (Huchra et al., 2012), the 2MRS consists of measured redshifts for 44 699 galaxies with a magnitude limit of $K_s = 11.75$. The dense, all-sky sampling of 2MRS provides an ideal counterpart for comparison of the predicted velocity field with the dense, homogenous sampling of the observed 6dFGS galaxies, given the significant overlap in the southern hemisphere.

Hence, we choose the 2MRS reconstructed density and velocity fields of Erdoğdu et al. (2012, submitted; updated from Erdoğdu et al. 2006) which uses the 2MRS redshift sample to recover the linear theory predictions for density and velocity. We summarise here the methods of reconstruction that are outlined in Erdoğdu et al. (2006, which closely follows the method of Fisher et al. 1995), where it was applied to a smaller 2MRS sample of $N_{\rm g} = 20\,860$ galaxies with a brighter magnitude limit of $K_s = 11.25$ and a median redshift of $z \simeq 0.02$ or $6000\,{\rm km\ s^{-1}}$.

The first step in the reconstruction process is to make an assumption about how the galaxy density in redshift-space (observed from a redshift survey) traces the mass distribution such that on the largest scales the two are linearly related with some constant of proportionality, b, called the linear bias parameter. The density and velocity fields in redshift-space are decomposed into spherical harmonics and Bessel functions (or Fourier-Bessel functions). In redshift-space, spherical harmonics and Fourier-Bessel functions are a convenient representation of these fields as they separate out the line-of-sight effects of redshift-space distortions from the transverse distribution on the sky. The velocity field is similarly expanded using spherical harmonics and Fourier-Bessel series and is defined by a transverse and radial component. However, we can only observed peculiar velocities in the radial direction therefore we only need to couple the radial modes to derive the velocity field from the real-space density field.

Similarly, the redshift-space distortions induced by peculiar velocities are only prevalent in the radial direction and couple only to the radial modes in the con-

version from redshift to real-space. These linear redshift distortions are therefore encompassed in the coupling matrix (defined in Fisher et al. 1995) given a value for the β parameter ($\beta \equiv \Omega^{0.55}/b$), which is assumed by Erdoğdu et al. (2006, 2012 submitted) to be β=0.4.

To determine the real-space density field (from redshift space) the effects of Poisson 'shot noise' error due to the finite sampling of the observed galaxies needs to be accounted for. The method employed in Erdoğdu et al. (2006) to minimise this effect uses Wiener filtering to smooth the data. This type of filtering smooths the field by using the ratio of the signal variance over the variance from both the signal and noise, thereby using the distribution of the galaxies in the data as a prior to minimise the overall statistical noise.

Finally the reconstructed peculiar velocity field is derived from the Wiener-filtered real-space density field by relating the harmonics of the gravity field to those of the density field (in linear theory). In Figure 6.1, we show the reconstructed density field (as smooth coloured contours) and predicted velocity field (as a vector field in black) of 2MRS (Erdoğdu et al. 2012, submitted) in a slice through the Supergalactic plane at SGZ = $4.0\,h^{-1}$ Mpc (i.e. closest to the plane at SGZ = $0\,h^{-1}$ Mpc given the resolution of the reconstruction). The largest local structures are present as overdensities in Figure 6.1 including the Shapley Concentration (upper left), Coma Cluster (upper middle) and Hydra-Centaurus (centre left).

The final reconstruction we use assumes $\beta = 0.4$ and is arranged on a regular grid in Supergalactic coordinates extending over $\pm 196\,h^{-1}$ Mpc in all three Cartesian dimensions. The predicted density and peculiar velocity field is calculated for gridpoints within $196\,h^{-1}$ Mpc of the origin, with spacing of $8\,h^{-1}$ Mpc in real-space. This was resampled in redshift-space to achieve a higher resolution grid (using interpolation) with $4\,h^{-1}$ Mpc spacing. For this model, the conversion to redshift-space does not generate any 'triple-valued' zones (where one redshift corresponds to three different distances), as the grid-spacing in the model is sufficiently coarse to smooth out the effects of 'triple-valued' regions. We make use of both these peculiar velocity reconstructions to simulate mock peculiar velocities and assign predicted peculiar velocities to the 6dFGSv sample of galaxies.

6.3 6dFGSv FP Distances and Peculiar Velocities

In this section, we introduce the 6dFGSv sample of galaxies which form the basis of the 6dFGS local peculiar velocity field. For each galaxy we calculate a distribution of distance/peculiar velocities rather than a single velocity value. We also outline the correct Bayesian approach for measuring the error in distance for our 3D Gaussian FP model and the procedure for calibrating the zeropoint of the 6dFGSv FP distances and peculiar velocities.

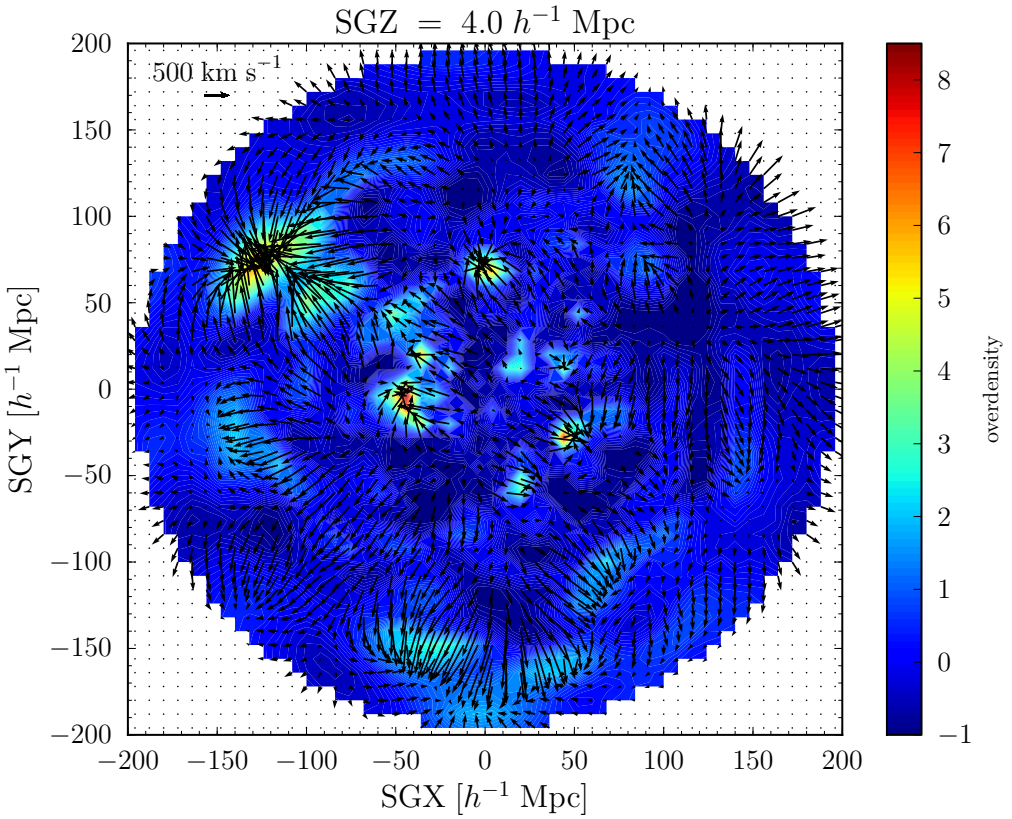

Figure 6.1: The reconstructed density and velocity fields from the 2MRS model of Erdoğdu et al. (2012, submitted), in a slice through the Supergalactic plane (SGZ = $4.0\,h^{-1}$ Mpc). The contour levels of the density field, as denoted by the colour bar, have a spacing of 0.1. The arrows overplotted in black, represent the predicted velocity field in the CMB frame. The scale of the velocity vectors is indicated by the arrow with 500 km s^{-1} in the upper lefthand corner. The red, overdense features represent the largest structures in the 2MRS volume including the Shapley Concentration at (SGX,SGY) = $(-130, +70)$, Coma at (SGX,SGY) = $(+10, +70)$, Hydra-Centaurus at (SGX,SGY) = $(-40, -10)$ and Perseus-Pisces at (SGX,SGY) = $(+50, -30)$.

6.3.1 Bayesian Peculiar Velocities

The 6dFGS Fundamental Plane is modelled as a 3D Gaussian defined by a likelihood function that is maximised to determine the best-fitting FP. It is therefore a natural extension of this Bayesian formalism, to similarly treat the distances and peculiar velocities, determined by this Fundamental Plane, as probability distribution of values instead of point-like single measurements.

More precisely, for each galaxy we calculate $P(v_p|r_\theta, s, i, cz)$, the posterior probability of a peculiar velocity, v_p, given the measured FP values of r_θ, s, i and cz. The angular size, r_θ, is used in the expression for $P(v_p|r_\theta, s, i, cz)$, as it is the observable quantity that is related to the distance of a galaxy, rather than the physical size, r, which is calculated assuming the galaxy is at its redshift distance (without allowing for peculiar velocities which is the parameter being measures). The posterior probability distribution for a peculiar velocity, v_p, is defined as

$$P(v_p|r_\theta, s, i, cz) = \frac{P(r_\theta, s, i, cz|v_p)\, P(v_p)}{P(r_\theta, s, i, cz)} \tag{6.3}$$

given $P(r_\theta, s, i, cz|v_p)$, the likelihood of observing a galaxy with r_θ, s, i and cz (according to the 3D Gaussian model of the FP) for a given v_p and a prior $P(v_p)$, which are both normalised by $P(r_\theta, s, i, cz)$.

To compute the posterior probability distribution of v_p from equation 6.3, the FP parameters need to be specified. To calculate the likelihood, $P(r_\theta, s, i, cz|v_p)$ we therefore use the best-fit FP values to the final J band FP sample from Table 4.1 where $a = 1.52$, $b = -0.89$, $\bar{r} = 0.18$, $\bar{s} = 2.19$, $\bar{i} = 3.19$, $\sigma_1 = 0.053$, $\sigma_2 = 0.318$, $\sigma_3 = 0.170$. We then consider a range of values for v_p between $-25\,000$ to $+25\,000$ km s^{-1}, evenly sampled in intervals of 100 km s^{-1}. This range is sufficiently large to encompass the peculiar velocities that may be observed, including the large errors (with an rms of $\sim$23% in distance, which at $cz \sim 16\,000$ km s^{-1} corresponds to $\sim$4000 km s^{-1} error in velocity). The likelihood corresponding to each v_p value is then evaluated and multiplied by a flat prior (for simplicity, although a more complicated prior could be assumed) and then normalised to calculate the posterior probability distribution. The subject of normalisation in this model will be discussed in Section 6.4.2.

An example of the probability distribution of velocities for one galaxy is shown in Figure 6.2. The asymmetry of this distribution is caused by that fact that galaxy distance is derived as a logarithmic quantity in FP space (i.e. $\log R_e$) which is then converted to a linear peculiar velocity resulting in a log-normal distribution. For individual galaxies, the peak of the probability distributions tend to have an amplitude of thousands of km s^{-1}, as in this case. This is usually an over-estimate of the typical amplitude of galaxy peculiar velocities, driven by the large distance errors.

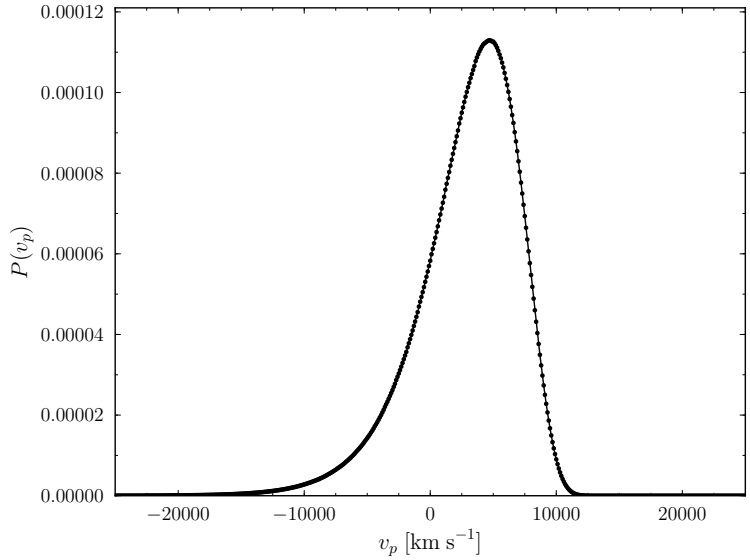

Figure 6.2: Posterior probability distribution of peculiar velocities for a typical galaxy in the 6dFGSv sample, which is log-normal but is sampled evenly in linear units.

6.3.2 6dFGSv Sample

The 6dFGSv provides the largest sample of galaxy peculiar velocity measurements to date and is also a more homogeneous sample than most previous large velocity samples. It consists of the galaxies in 6dFGS for which we have Fundamental Plane data, a sample of 11 287 galaxies. We impose the same selection criteria (in s, cz, morphology, apparent magnitude, χ^2) as the final J Band FP sample, with the exception that we reinstate galaxies with low selection probability (i.e. $S < 0.05$) and those below the lower redshift limit (i.e. $cz < 3000\,\mathrm{km\ s^{-1}}$). These galaxies were excluded from the sample used to fit the FP as potential sources of scatter, however we can measure the peculiar velocity of these galaxies. Therefore, in total there are 8989 galaxies with peculiar velocity measurements that comprise the 6dFGSv.

Galaxy distance and peculiar velocity measurements are potentially affected by several sources of bias, which therefore must be taken into account. In the case of a magnitude-limited sample only the brightest galaxies at the largest distances are observed, leading to homogeneous Malmquist bias. The bias induced by the spatial distribution of galaxies is known as inhomogeneous Malmquist bias and can be corrected for using the reconstructed density distribution from redshift surveys as a prior. We discuss the Malmquist bias corrections we apply to this sample in Section 6.4.

The distribution on the sky of the 6dFGSv galaxies is shown in Figure 6.3, illustrating the dense and homogeneous coverage of 6dFGS in the Southern Hemisphere. Each point represents a galaxy in the 6dFGSv and is colour-coded by their predicted peculiar velocities as derived from the 2MRS density field of Erdoğdu et al. (2012,

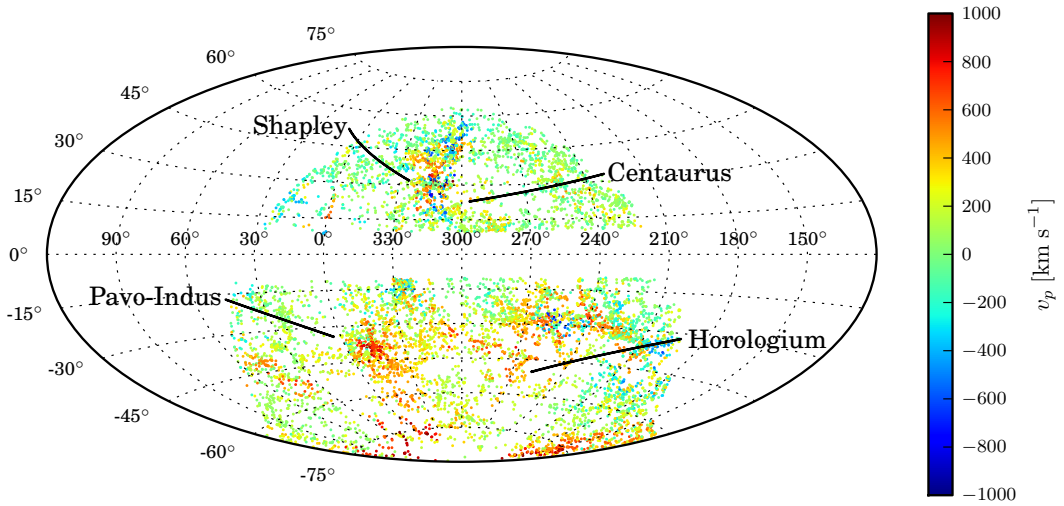

Figure 6.3: Distribution of 6dFGSv galaxies (N_g = 8989) in Galactic latitude (l) and longitude (b), shown in an equal-area Aitoff projection. Individual galaxies are colour-coded by their *predicted* peculiar velocities (in km s^{-1}) from the 2MRS density field of Erdoğdu et al. (2012, submitted). The 6dFGSv galaxies are located in the central region of this projection (with the absence around the edges due to the lack of 6dFGS galaxies in the Northern Hemisphere). Some of the large structures in the 6dFGSv volume are also indicated including the Shapley Supercluster and the Pavo-Indus Supercluster.

submitted), highlighting areas of positive (in red) and negative (in blue) peculiar velocities.

Figures 6.4 and 6.5 show a comparison, on a galaxy-by-galaxy basis, for the 6dFGSv of the predicted (left) peculiar velocities from the 2MRS velocity field reconstruction, and the observed (right) peculiar velocities i.e. the expectation value of the individual posterior probability distributions. Each set of plots shows the SGX versus SGY coordinates of galaxies divided into four SGZ slices (in h^{-1} Mpc) and colour-coded by peculiar velocity (defined as $\log[cz/H_0 D]$). The four slices do not span the same range in SGZ coordinates and are chosen so that they cover the Southern Hemisphere to emphasise the sampling of the 6dFGSv galaxies. Galaxies are divided into the following SGZ ranges: SGZ $< -70\,h^{-1}$ Mpc, $-70 <$ SGZ $< -20\,h^{-1}$ Mpc, $-20 <$ SGZ $< +20\,h^{-1}$ Mpc and SGZ $> +20\,h^{-1}$ Mpc.

There is some similarity between the global features in Figures 6.4 and 6.5, e.g. a prominence of blue/red or negative/positive velocities in certain regions but any visible correlations are obscured by the scatter in the individual peculiar velocity measurements compared to the predicted one.

A direct comparison of the observed peculiar velocities of the 6dFGSv sample with the 2MRS predicted velocities is given in Figure 6.6. Again, it is difficult to see any correlation between them through the noise in the individual measurements, although there is a weak trend (in red; from a weighted least-squares regression) with

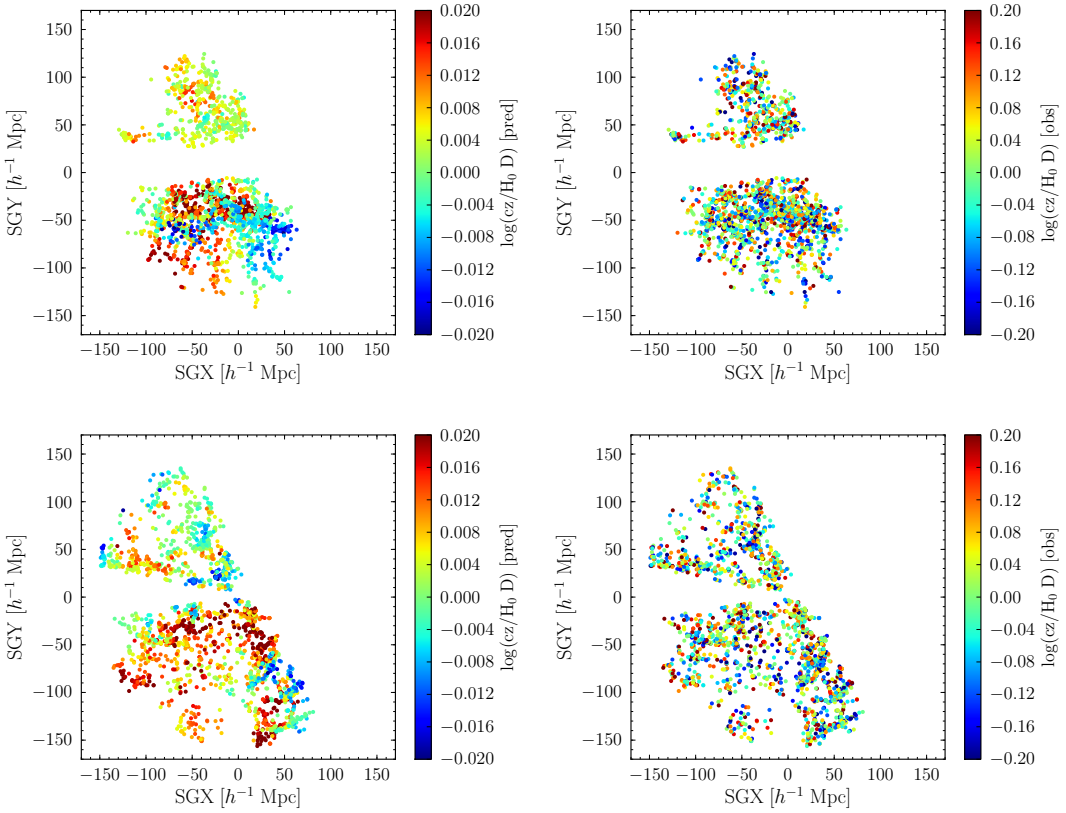

Figure 6.4: Comparison of predicted (*left*) peculiar velocities from the 2MRS velocity field and observed (*right*) peculiar velocities from the expectation value of posterior probability distributions in the 6dFGSv sample. Galaxies are plotted in Supergalactic coordinates SGX versus SGY colour-coded by peculiar velocity (defined as $\log[cz/H_0 D]$). Each plot represents a subsample of galaxies divided by SGZ into the following slices: SGZ $< -70\,h^{-1}$ Mpc (*top panel*; 2224 galaxies) and $-70 <$ SGZ $< -20\,h^{-1}$ Mpc (*bottom panel*; 2062 galaxies)

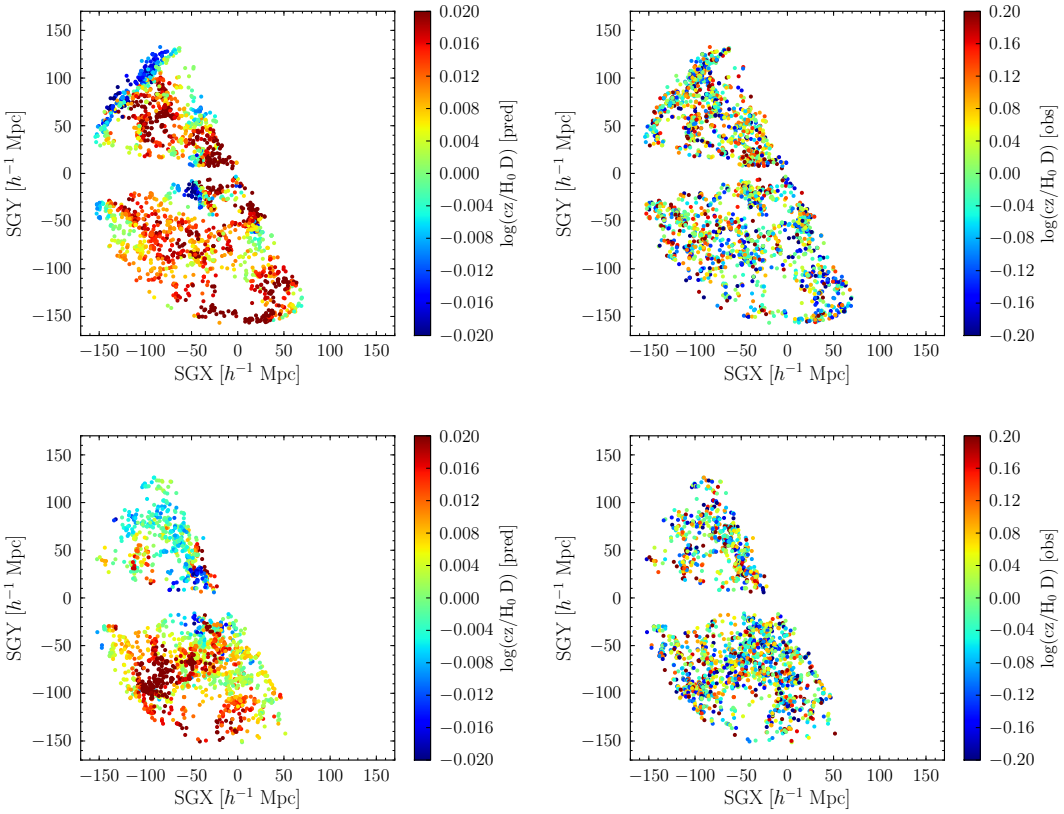

Figure 6.5: As for Figure 6.4, but for galaxies divided by SGZ into the following slices: $-20 <$ SGZ $< +20\,h^{-1}$ Mpc (*top panel*; 2645 galaxies) and SGZ $> +20\,h^{-1}$ Mpc (*bottom panel*; 2059 galaxies).

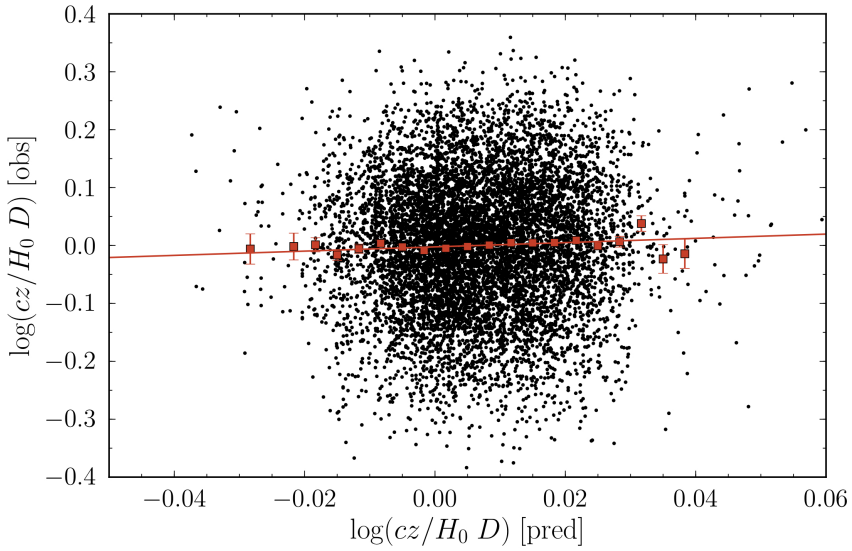

Figure 6.6: Observed (6dFGSv) versus predicted (2MRS model) peculiar velocities for all the galaxies ($N_g = 8989$) in the 6dFGSv sample. A weighted least-squares regression is shown (in red) with a slope of 0.37 ± 0.11, offset of 0.0 ± 0.01 and a correlation coefficient of 0.04.

a slope of 0.37 ± 0.11 and a correlation coefficient of 0.04.

6.3.3 Distance Errors

In Chapter 4 we found that the scatter about the 6dFGS FP in r is 29%. However, this does *not* mean that, when we use this FP fit to measure distances, we will only measure them to this precision. To understand why this is the case, we must consider the procedure used to measure distances and peculiar velocities from the FP.

In the most naive approach, one would convert the observed angular radius of a galaxy to a physical radius assuming that the distance to the galaxy is given by its redshift distance. The peculiar velocity of the galaxy would then be approximated by the offset of this galaxy from the FP in r. Since the peculiar velocity is measured from the offset along the r-direction, the average scatter from the FP in r then represents the total error in galaxy distances and peculiar velocities (from the combination of measurement errors and intrinsic scatter).

However there is a more general (and precise) way to estimate the peculiar velocity. The peculiar velocity of a galaxy, n, is given by its offset along the r-direction from a particular value, r_n^*. This r_n^* is the most likely radius for galaxy n, given a particular set of observed values of the velocity dispersion and surface brightness, s_n and i_n. In the preceding paragraph, we assumed that r_n^* is a point on the FP, given by $r_n^* = as_n + bi_n + c$. This assumption is valid if the FP is best modelled as an infinite plane with uniform scatter. However, the assumption is *not* valid if the distribution of galaxies in FP space is best modelled by a 3D Gaussian, and the

minor axis of this Gaussian is not aligned with the r-axis.

In equation 3.4, we show the expression for the probability density distribution of a single galaxy n. In equation 3.13 , we give the sum of the log of such probability densities for all galaxies in our sample. For a particular galaxy with known observational errors, each of the terms in equation 3.13, is fixed except the final χ^2 term, which is a quadratic function of the physical parameters r, s and i.

Since we directly observe s and i, we can fix them at the observed values s_n and i_n. We can then use this equation to give us the probability density distribution of r for fixed $s = s_n$ and $i = i_n$ (i.e. $P(r|s,i)$). This is a quadratic function of the form

$$\ln(P(r|s,i)) = k_0 + k_1(r - \bar{r}) + k_2(r - \bar{r})^2 \tag{6.4}$$

where k_0, k_1 and k_2 are functions of s_n, i_n, the observational errors for the galaxy, and the FP fit parameters (a, b, $\bar{r}$, $\bar{s}$, $\bar{i}$, σ_1, σ_2, and σ_3). They can thus be obtained by expanding the matrix multiplication terms in the preceding equations. The effective expectation value for galaxy distances and peculiar velocities occurs at the maximum likelihood—i.e. the maximum of this quadratic function,

$$r^* - \bar{r} = -k_1/(2k_2) \ . \tag{6.5}$$

This value varies from galaxy to galaxy, depending both on the galaxy's position in FP space and its observational errors. If we evaluate this in the case of no errors, and insert the values of the FP fit parameters given in Table 4.1 for the J band sample, we find that the effective expectation value for distances is given by the plane $r^* = 1.18s - 0.80i + 0.152$; this relation differs quite markedly from the underlying Fundamental Plane. However, since we do in fact have observational errors, and they vary from galaxy to galaxy, the peculiar velocity expectation values for individual galaxies will *not* be confined to a plane. As noted in Section 3.2.1, it is for this reason (as well as the censoring of the distribution) that a simple regression (whether orthogonal or in the r-direction) of an infinite plane is *not* equivalent to our ML fit of a 3D Gaussian model and therefore the above relation is, similar to, but not the same as the coefficients derived from a direct fit of the plane about the r-direction.

We have evaluated this J band expectation value distance (i.e. the maximum likelihood distance) for every galaxy in our sample, and find that the scatter about this value is 23%. This, then, is the distance error in the J band assuming no Malmquist bias corrections. If we include Malmquist bias corrections by simply calculating the f_n normalisation term in the likelihood (equation 3.13) of an individual galaxy, for the magnitude limit that is appropriate for that galaxy's distance, the scatter increases to 27%.

This 23% scatter (before Malmquist bias correction) in distance is significantly

smaller than the 29% that is naively obtained by calculating the scatter in r about the best-fit FP. The difference is purely a consequence of the fact that, in our empirically well-justified 3D Gaussian model for the distribution in FP space, galaxies are not symmetrically distributed about the FP in the r direction. Thus, for fixed s and i, the probability density of galaxies in r is not maximised on the FP, the expectation value for the observed distance is not the redshift distance, the expectation value of the peculiar velocity is not zero, and the scatter in distance and peculiar velocity relative to this expectation value is less than the scatter relative to the FP.

6.3.4 Calibrating the FP Zeropoint

The relative galaxy distances and peculiar velocities measured from the Fundamental Plane must be calibrated with respect to some zeropoint. Calibrations that are commonly applied include forcing the sum of the peculiar velocities in the sample to be zero or fixing the peculiar velocity of a well-know cluster (e.g. Coma) to be zero.

We derive peculiar velocity measurements for a 6dFGS galaxy sample that extends across the entire southern sky but includes very few galaxies in the Northern Hemisphere. The lack of galaxies in the north means the measurement of the bulk flow (and β) is therefore susceptible to a systematic deviation in the FP zeropoint if calibrated by fixing the mean peculiar velocity in our sample to zero. If there is a significant bulk flow towards the north (or south) celestial pole, this would result in a average negative (or positive) peculiar velocity which would make the former assumption invalid.

To avoid this potential problem, we instead calibrate the zeropoint using only those galaxies near the celestial equator, roughly approximating a great circle region in our hemispherical sample that will remain largely unaffected by a polar bulk flow. We define this subsample as the $N_{\rm g} = 3828$ galaxies north of $\delta = -20^\circ$ and fit the $\bar{r}$ value after fixing the other coefficients that define the FP (i.e. a, b, $\bar{s}$, $\bar{i}$, σ_1, σ_2, σ_3) to the bias-corrected best fit values of the *global* plane. The best-fit value (after bias correction) of the mean effective radius for this subsample is $\bar{r} = 0.177 \pm 0.007$ which is consistent with, but slightly smaller than the global FP value of $\bar{r} = 0.184 \pm 0.004$. Note that if this difference in $\bar{r}$ were due to a real distance offset rather than a statistical fluctuation, it would correspond to relative distance error of 1.6%, or a velocity error of 160 km s^{-1} at a distance of 10 000 km s^{-1} (i.e. we would have underestimated the bulk flow in the direction of the south celestial pole by of order this amount).

In order to use this $\bar{r}$ value in our FP zeropoint calibration, we need to ensure that this declination-limited subsample of galaxies has a similar FP (offset only in $\bar{r}$) to the global FP and is consistent within errors, given that we are using a reduced number of galaxies. We generate 200 mock simulations (with $N_{\rm g} = 3828$ galaxies

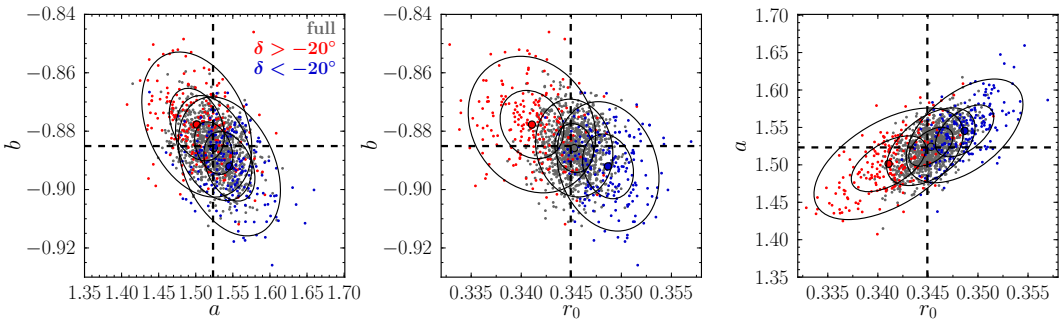

Figure 6.7: Uncertainties on the FP parameters for subsamples selected with declination, comparing subsamples with $\delta > -20°$ (red; $N_g = 3828$), and $\delta < -20$ (blue; $N_g = 5073$) and the full sample (green; $N_g = 8901$). The points show the best-fit FP parameters for each of 200 mock samples of the declination-selected subsamples and 1000 mocks of the full sample. The mean values of the fitted FP parameters from the mocks, and their 1σ and 2σ contours, are also plotted. For reference, the input FP parameters used to generate the samples for the J band are indicated as dotted lines. *Left:* b versus a, showing similar FP coefficients. *Centre:* b versus r_0, showing weak trend of larger r_0 with decreasing b. *Right:* a versus r_0, showing same weak trend but with increasing a.

per simulation) using the best-fit plane to the $\delta > -20°$ subsample (and also to the $\delta < -20°$ subsample with $N_g = 5073$ galaxies, as a consistency check) and fit the FP to each simulation using the maximum likelihood procedure of Chapter 3. The resulting mean best-fit values (and their 1σ and 2σ error contours) are plotted in Figure 6.7 and compared to 1000 mock simulations of the global J band FP (as done in Chapter 4). Both declination-limited subsamples have FP slopes that are consistent with each other and the global FP within the 1σ errors. They are slightly offset in r_0, corresponding to their offsets in $\bar{r}$, although the differences are within the 2σ joint errors.

6.4 Peculiar Velocity Likelihood Model

To measure the parameters defining the local peculiar velocity field including β and the bulk flow motion of the sample, we develop and extend the maximum likelihood method used to fit the Fundamental Plane coefficients to include galaxy peculiar velocity measurements (as outlined in Section 6.2). The likelihood function of this new velocity field model incorporates the probability distribution of the 3D Gaussian model that defines the FP likelihood function (equation 3.13). The revised likelihood function is defined as

$$\ln \mathcal{L} = -\sum_{n=1}^{N_g} \frac{3}{2}\ln(2\pi) + \ln(x_n) + \frac{1}{2}\ln(|\mathbf{\Sigma} + \mathbf{E}_n|) + \frac{1}{2}\boldsymbol{x}_n^{\mathsf{T}}(\mathbf{\Sigma} + \mathbf{E}_n)^{-1}\boldsymbol{x}_n \ . \qquad (6.6)$$

in a similar manner to equation 3.13 but with two notable differences. The first is that the likelihood function for the velocity model is not weighted by any selection

probability because we can't assume a galaxy is at its redshift distance in order to account for the magnitude selection in our sample. Instead we make this correction in the likelihood normalisation (f_n) which also accounts for Malmquist bias, as described in Section 6.4.2. The second major difference is that the FP coefficients are not free parameters in this case and are *fixed* to those of the global J band bias-corrected best-fit plane (see Table 4.1) except for the FP offset in effective radius, $\bar{r}$, which is derived from a declination-limited subsample in Section 6.3.4. In this model, adopted throughout this chapter, we treat the galaxies as test particles which are used as a measure of the peculiar velocity field at a given point in redshift-space. Because the peculiar velocities in our model are exclusively in redshift-space, inhomogeneous Malmquist bias is insignificant.

Additionally, the effective radius of each galaxy is now dependent on the redshift distance modified by the galaxy peculiar velocity, based on the following procedure. For a given galaxy with predicted peculiar velocity, v_n, we define the components of the model peculiar velocity, v_{model}, as

$$v_{model} = v_n \left(\frac{\beta}{\beta_{\rm fid}} \right) + \boldsymbol{u} \cdot \hat{\boldsymbol{r}} \tag{6.7}$$

where $\hat{\boldsymbol{r}}$ is the unit direction vector of the galaxy in Supergalactic coordinates (in $h^{-1}\,$Mpc) and $\boldsymbol{u}$ is a dipole flow (to be fit) also with respect to Supergalactic coordinates (in km s^{-1}). In practice, we fit for the β parameter scaled by a fiducial β parameter (i.e. $\beta_{\rm fid} = 0.4$) corresponding to the 2MRS field input value in the form $M_\beta = \beta/0.4$, which we hereafter refer to as the β multiplier. In equation 6.7 we define a model where M_β and $\boldsymbol{u}$ are fit simultaneously, however we can similarly derive models where we fit for β only, i.e.

$$v_{model} = v_n \left(\frac{\beta}{\beta_{\rm fid}} \right) \tag{6.8}$$

and also, fit for a dipole only

$$v_{model} = \boldsymbol{u} \cdot \hat{\boldsymbol{r}} \ . \tag{6.9}$$

The best-fit values of M_β and/or $\boldsymbol{u}$ are those for which the likelihood function of equation 6.6 is maximised.

6.4.1 Hubble Redshift and Fundamental Plane Distance

Using the observed redshift (z_{obs}) and the model peculiar velocity calculated by equation 6.7 (or 6.8 or 6.9) for given values of M_β and $\boldsymbol{u}$, we calculate the Hubble redshift (z_H) for each galaxy, corresponding to its distance in the absence of any

peculiar motions, from the redshift relation

$$(1 + z_H) = (1 + z_{obs})/(1 + z_p) \tag{6.10}$$

where z_p is the redshift corresponding to the peculiar velocity, which for this case is $v_{model} = cz_p$.

The observable quantity from the FP is actually the ratio of the log effective radius at the Hubble redshift defined by equation 6.10 ($\log R_H$) and at the observed redshift ($\log R_{obs}$), which are related to the corresponding angular diameter distances, $D_A(z_H)$ and $D_A(z_{obs})$ respectively, by

$$\log \frac{R_H}{R_{obs}} = \log \frac{D_A(z_H)}{D_A(z_{obs})} \ . \tag{6.11}$$

Hence we use equations 6.10 and 6.11 to map back and forth between peculiar velocities and relative distances

6.4.2 Normalisation of the v_p Likelihood Model

In our Fundamental Plane model, we multiply the FP likelihood function by a selection probability weighting to account for the effects of censoring in our magnitude-limited sample and at the same time correct for Malmquist bias. This weighting assumes that the redshift of each galaxy corresponds to its redshift distance neglecting the effect of its peculiar velocity. This approximation may bias the likelihood function for our peculiar velocity model (equation 6.6), as the galaxy distance is now dependent on the value of the free parameters M_β and $\boldsymbol{u}$.

Instead the magnitude selection of our sample is accounted for in the new model by including in the normalisation factor, f_n of equation 6.6, an additional term that corresponds to the magnitude limit appropriate for the distance of each galaxy (inclusive of peculiar velocity).

There is no simple analytic expression for this correction factor, hence f_n is determined using a large ($N_{\rm g} = 100\,000$) Monte Carlo simulation of a FP galaxy sample drawn from the best-fit J band FP values and a selection function that mimics the data. The entire mock sample is used to calculate the value of f_n for distances out to $200\,h^{-1}\,$Mpc (well past the limiting redshift of our sample). The accuracy of f_n derived in this way is sufficient given the large number of mock galaxies in the sample and the close correspondence of the simulations to the data.

The f_n normalisation is used to correct the individual likelihood (in the v_p model) for each galaxy given the survey magnitude limit and assuming a global (best-fit) Fundamental Plane. Hence this method can't be used in fitting the FP itself because f_n depends on the FP parameters. The new f_n is evaluated for each galaxy depending

on the comoving distance corresponding to its Hubble redshift given the trial values for M_β and/or the dipole flow $\boldsymbol{u}$ that is being maximised.

6.4.3 Mock Peculiar Velocity Distributions

The simulate a mock peculiar velocity field that closely matches the observed sample of 6dFGS galaxy velocities, we use the predicted peculiar velocity field reconstructed from the 2MRS density field of Erdoğdu et al. (2012, submitted). The predicted peculiar velocity field is evaluated on a cubical grid in real-space, calculated for grid points within $\pm 196\,h^{-1}$ Mpc of the origin, with spacing of $8\,h^{-1}$ Mpc (as described in Section 6.2). Mock peculiar velocities are generated using the following procedure:

1. Choose a sky position for each mock galaxy randomly from the set of (R.A., Dec.) positions that exist in the actual galaxy sample.
2. Generate a mock comoving distance uniformly distributed in volume.
3. Convert R.A. and Dec. (both in degrees) to Supergalactic (here and throughout) Cartesian coordinates i.e. SGX, SGY and SGZ.
4. Calculate the peculiar velocity (in km s^{-1}) for the mock galaxy at that position by trilinear interpolation of the surrounding peculiar velocity grid points and multiply by the input M_β value.

To calculate the observed redshift, z_0, of each mock galaxy, we use this mock peculiar velocity to correct the galaxy's Hubble redshift, z_H, by inverting the redshift relation of equation 6.10 (where z_p is the redshift corresponding to the peculiar velocity, i.e. $v_p = cz_p$).

6.4.4 Adding a Bulk Flow to the Mock Galaxy Samples

To simulate mock peculiar velocities, v_p, that include a bulk flow component, we use the same procedure outlined in Section 6.4.3 to generate an initial mock peculiar velocity, v_{mock} but extend step 4 to include a bulk flow ($\boldsymbol{u}_{\rm input}$) given the mock galaxy position in normalised Supergalactic coordinates ($\boldsymbol{r}_{\rm mock}$)

$$v_p = v_{mock} + \boldsymbol{u}_{\rm input} \cdot \boldsymbol{r}_{\rm mock} \ . \tag{6.12}$$

These input mock peculiar velocities are derived using the real-space comoving distances but the final predicted peculiar velocities are calculated by a further interpolation of the 2MRS reconstructed peculiar velocities with Supergalactic coordinates given a redshift-space distance, as for the data.

The final stage in generating mock peculiar velocities involves replacing the redshift and peculiar velocity of the galaxies in the richest groups of the sample by the

mean redshift and peculiar velocity of the groups they reside in. We perform this grouping so that the mock simulations emulate the group structure in the data (as described in Section 2.8.1 using the 6dFGS groups and clusters catalogue) as closely as possible.

We assign group redshifts and velocities only to simulated galaxies whose mock distance (in Supergalactic coordinates) is within $1\,h^{-1}$ Mpc of one the largest groups in the 6dFGS group catalogue of Section 2.8.1, given that $1\,h^{-1}$ Mpc is approximately the typical scale of the clusters in our sample. We then treat this mock galaxy as a member of the nearest group, and replace the mock redshift and v_p of this galaxy by the mean redshift and peculiar velocity of the galaxies that are members of that group.

6.5 Testing the Model Galaxy Sample Fits

In this section we test, using mock samples, the robustness of the linear flow model defined by the beta parameter (corresponding to the model of equation 6.8) using mock galaxy samples. We use mock galaxies that are perturbed by peculiar velocities drawn from a range of distributions to quantify any systematic bias associated with this model.

The peculiar velocity distribution models considered here include those based directly on the 2MRS reconstructed velocity field (§6.5.1) which are compared to velocities modelled from a random Gaussian distribution with the same scatter (§6.5.2). We explore the impact of a positive or negative offset in the 2MRS peculiar velocity distribution in §6.5.3 as well as the size of the scatter in the Gaussian distribution in §6.5.4. For completeness we test mock simulations with variable (instead of fixed) errors assigned to each mock galaxy (§6.5.5).

6.5.1 Fitting β to Mock v_p from the 2MRS Velocity Field

The most physically realistic model for the peculiar velocity distribution of our mock galaxies comes from the predicted peculiar velocities derived from the 2MRS density field of Erdoğdu et al. (2012, submitted). For simplicity, we initially assign fixed measurement errors to the FP parameters, using the same average error for each mock galaxy ($\langle\epsilon_r\rangle = 0.049$, $\langle\epsilon_s\rangle = 0.053$, $\langle\epsilon_i\rangle = 0.073$); this change is also reflected in the normalisation of the FP. The effect of using individual measurement errors on each mock galaxy sample will be explored in a later section.

An example of the distribution of peculiar velocities for a mock sample (with $N_{\rm g} = 8989$ galaxies) generated from the 2MRS predicted velocity field is shown in the left panel of Figure 6.8. On average, a mock velocity distribution derived from 2MRS will have a small positive average velocity ($\bar{v}_p \sim 120\,{\rm km\ s^{-1}}$) which is the mean motion in the predicted 2MRS velocity field at the positions of the galaxies in

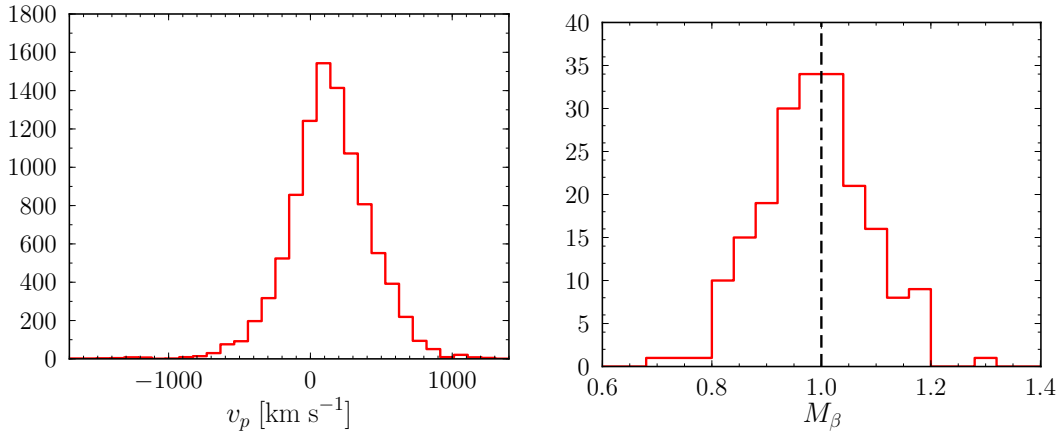

Figure 6.8: *Left:* Peculiar velocity distribution for a mock sample ($N_g = 8989$) where v_p is sampled from the 2MRS reconstructed peculiar velocity field. *Right:* Histogram of best-fit M_β for 200 mock simulations with this v_p distribution. The mean M_β and rms from 200 fits is $\langle M_\beta \rangle = 0.98 \pm 0.10$, indicated by the solid red line, compared to the input value used to generate the mock simulations (i.e. $M_\beta = 1.0$) shown by the dashed black line.

the 6dFGS sample. The mock distribution in Figure 6.8 shows this positive skew as well as a scatter of $\sigma_v \sim 300\,\mathrm{km\ s^{-1}}$.

Using the maximum likelihood method of Section 6.4 and the model of equation 6.8, we can recover the β multiplier (M_β) for 200 mock galaxy samples drawn from this distribution. The distribution of best-fit values of M_β is shown in the right panel of Figure 6.8 with an a mean (indicated by the solid red line) and rms of $\langle M_\beta \rangle = 0.98 \pm 0.10$, which is consistent within the errors with the input value of $M_\beta = 1.0$ (indicated by the dashed black line). The best-fit M_β values for the mock simulations in this section are summarised in Table 6.1. Our likelihood model for the peculiar velocity field therefore performs well when fitting to mock galaxy samples with peculiar velocities simulated from the 2MRS reconstruction, recovering the input value of M_β with an accuracy of 10%.

6.5.2 Mock v_p from 2MRS and Gaussian Distributions

We now compare the distribution of 2MRS predicted velocities to a more simplistic model where the mock peculiar velocities are randomly drawn from a Gaussian of a given width (σ_v). To match the distribution of 2MRS-sampled velocities, we simulate peculiar velocities from a Gaussian of a given mean offset ($v_{\rm off}$) and width $\sigma_v = 300\,\mathrm{km\ s^{-1}}$ which is offset by $v_{\rm off} = +120\,\mathrm{km\ s^{-1}}$ (therefore the average v_p for each mock sample is also $120\,\mathrm{km\ s^{-1}}$). The Gaussian-distributed v_p distribution is not as sharply peaked and the negative tail is not as asymmetric as the velocities sampled from 2MRS, as shown in left panel of Figure 6.9. However, as a toy model distribution it is sufficiently representative of the physical distribution of velocities to use for testing our fitting procedure.

Table 6.1: Summary of the mean best-fit M_β values for mock simulations generated with different v_p distributions. For each case 200 mock galaxy samples are fit using a maximum likelihood procedure. We list the source of the mock peculiar velocities (either from 2MRS reconstructed velocities or a Gaussian distribution), the input velocity offset ($v_{\rm off}$), the *total* average velocity for each sample ($\bar{v}_p$), the input scatter of the distribution (σ_v), how the observational FP errors were generated (either fixed or variable) the mean best-fit $\langle M_\beta \rangle$ and rms scatter, and standard error of the mean (σ_M) of 200 fits to M_β.

mock	v_p model	$v_{\rm off}$ [km s^{-1}]	$\bar{v}_p$ [km s^{-1}]	σ_v [km s^{-1}]	obs. error	$\langle M_\beta \rangle \pm$ RMS [-]	σ_M
(i)	2MRS	-	+120	-	fixed	0.98±0.10	0.007
(ii)	Gaussian	+120	+120	300	fixed	0.99±0.08	0.006
(iii)	2MRS	+120	+240	-	fixed	1.00±0.08	0.006
(iv)	2MRS	−120	0	-	fixed	0.91±0.12	0.008
(v)	Gaussian	-	0	200	fixed	0.95±0.13	0.009
(vi)	Gaussian	-	0	300	fixed	0.95±0.09	0.006
(vii)	Gaussian	-	0	400	fixed	0.95±0.06	0.004
(viii)	2MRS	-	+120	-	variable	1.02±0.10	0.007

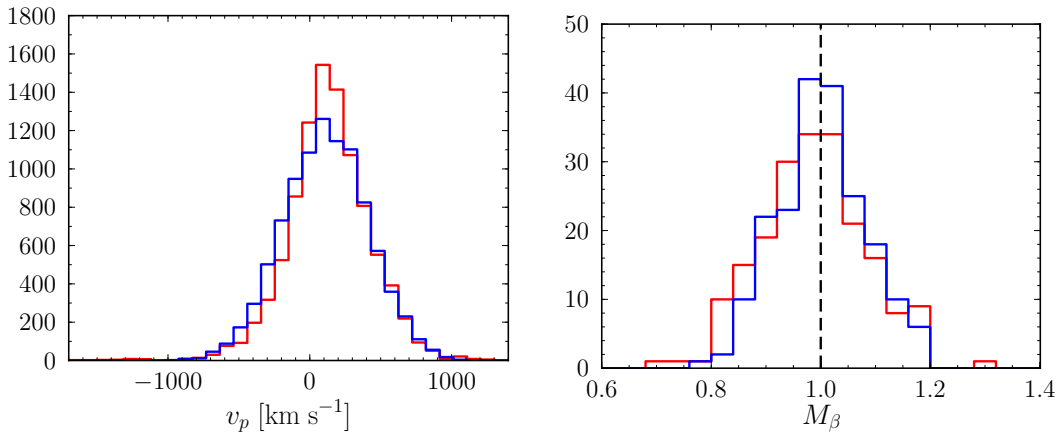

Figure 6.9: As for Figure 6.8, but comparing mock galaxy samples with v_p sampled from the 2MRS velocity field (red, the same as those in Figure 6.8) and a Gaussian distribution of width $\sigma_v = 300\,{\rm km\ s^{-1}}$, offset by $v_{\rm off} = +120\,{\rm km\ s^{-1}}$ (in blue).

In the right panel of Figure 6.9, we compare the best-fit values of M_β for 200 simulations of mock samples with peculiar velocities sampled from the 2MRS reconstructed velocities (red) and those sampled from a Gaussian distribution of width $\sigma_v = 300\,\mathrm{km\ s^{-1}}$ with an input offset of $v_{\rm off} = +120\,\mathrm{km\ s^{-1}}$ (blue). For the 200 mock simulations of Gaussian-sampled peculiar velocities, the best-fitting mean and rms are $\langle M_\beta \rangle = 0.99 \pm 0.08$. This is consistent with the corresponding mock simulations of 2MRS-sampled velocities (i.e. $\langle M_\beta \rangle = 0.98 \pm 0.10$) as shown in Table 6.1.

Our likelihood model is robust to both representations of the mock peculiar velocities (i.e. sampled from the 2MRS peculiar velocity field or a Gaussian distribution of matching width and mean) and for each type correctly fits the input value for M_β.

6.5.3 Mock v_p from 2MRS Distributions with Differing Average Offsets

We investigate the effect of different non-zero average velocity in the mock peculiar velocity distributions. To this end, we generate mock galaxy samples to which we add both a positive and negative offset (i.e. $v_{\rm off}$), of the same magnitude as the mock v_p distributions drawn from 2MRS predicted velocities. The velocity distributions of each type of mock sample are given in the left panel of Figure 6.10 for the mock samples where zero offset is applied (red; total average velocity for each sample is, $\bar{v}_p \sim 120\,\mathrm{km\ s^{-1}}$), a positive offset of $+120\,\mathrm{km\ s^{-1}}$ is applied (green; $\bar{v}_p \sim 240\,\mathrm{km\ s^{-1}}$), and a negative offset of $-120\,\mathrm{km\ s^{-1}}$ is applied (blue; $\bar{v}_p \sim 0\,\mathrm{km\ s^{-1}}$).

The right panel of Figure 6.10 shows the best-fit M_β values for 200 mock simulations of these three types of mocks. The histograms indicate that a tighter constraint on M_β is found when the distribution of peculiar velocities has a higher average peculiar velocity i.e. when $\bar{v}_p \sim +240\,\mathrm{km\ s^{-1}}$. If the v_p distribution has a high average peculiar velocity, then by construction it will sample more galaxies with positive peculiar velocities, hence those galaxies which are systematically closer to us than implied by their redshift distance. Therefore, this effect can be understood as a result of sampling more nearby galaxies which have smaller errors in distance (and hence smaller errors in v_p).

In summary, the broadening of the M_β distribution for more negative $\bar{v}_p$ is accompanied by a trend to lower mean values of $\langle M_\beta \rangle$; e.g. $\langle M_\beta \rangle = 1.00 \pm 0.08$ for $\bar{v}_p \sim 240\,\mathrm{km\ s^{-1}}$ but $\langle M_\beta \rangle = 0.91 \pm 0.12$ for $\bar{v}_p \sim 0\,\mathrm{km\ s^{-1}}$ (see Table 6.1).

6.5.4 Mock v_p from Gaussian Distributions with Differing Widths

Thus far we have only fit mock v_p distributions of a certain width (i.e. $300\,\mathrm{km\ s^{-1}}$). However, to test how robust our fitting method is to the size of the scatter in the velocity distribution, we can generate mock simulations where velocities are drawn from a Gaussian with varying input widths of $\sigma_v = 200, 300$ and $400\,\mathrm{km\ s^{-1}}$ (and in

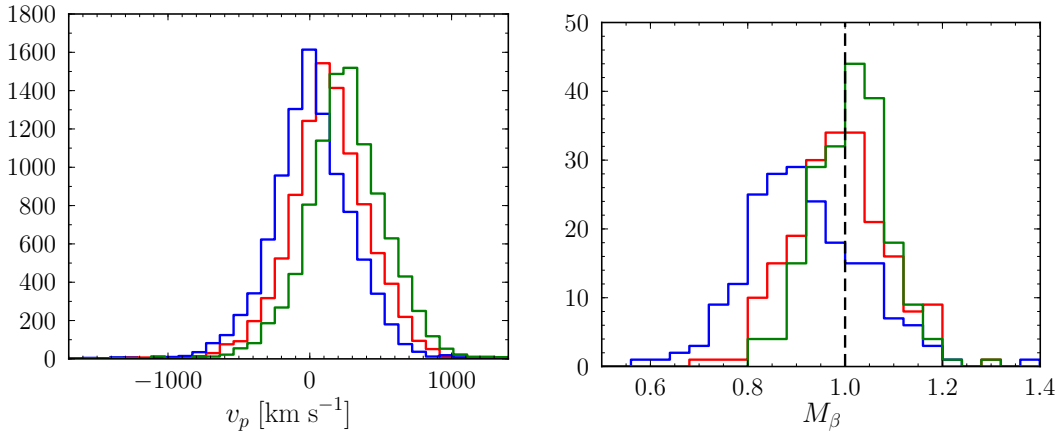

Figure 6.10: As for Figure 6.8, but comparing mock galaxy samples with v_p sampled from the 2MRS velocity field but with a total average v_p offset of 0 km s^{-1} (blue), +120 km s^{-1} (red, the same as those in Figure 6.8), and +240 km s^{-1} (green).

this case, zero mean v_p).

The best-fit M_β values for 200 simulations of each of these mock are given in Figure 6.11 for mocks with v_p distribution of width $\sigma_v = 200$ km s^{-1} (red), $\sigma_v = 300$ km s^{-1} (blue) and $\sigma_v = 400$ km s^{-1} (green). As expected, the mean best-fit $\langle M_\beta \rangle$ values (see Table 6.1) are the same for all three types of mocks i.e. $\langle M_\beta \rangle = 0.95$, but are recovered with better precision when the sample of peculiar velocities has a larger scatter.

Therefore, the peculiar velocity model is sensitive to the scatter in the distribution of mock velocities as reflected in the rms error in fitting to M_β, but maintains the correct best-fit value for M_β regardless of the v_p distribution width.

6.5.5 Mock v_p Distributions with Variable FP Measurement Error

We add an additional layer of complexity to our mock galaxy samples in order to emulate our data sample more closely, by simulating individual measurement errors for the FP parameters of each galaxy (in the same procedure we use for the Fundamental Plane mock samples). Again we fit 200 mock simulations where the peculiar velocities are selected from 2MRS and now include variable measurement errors for r, s and i (and the normalisation of the Fundamental Plane is appropriately altered to incorporate variable errors).

The fitting procedure is still able to recover M_β accurately, as seen in Figure 6.12, with a best fit (see Table 6.1) of $\langle M_\beta \rangle = 1.02 \pm 0.10$ which compares favourably with mock simulations using fixed measurement errors. We will include individual measurement errors on all mock galaxies throughout the rest of this analysis.

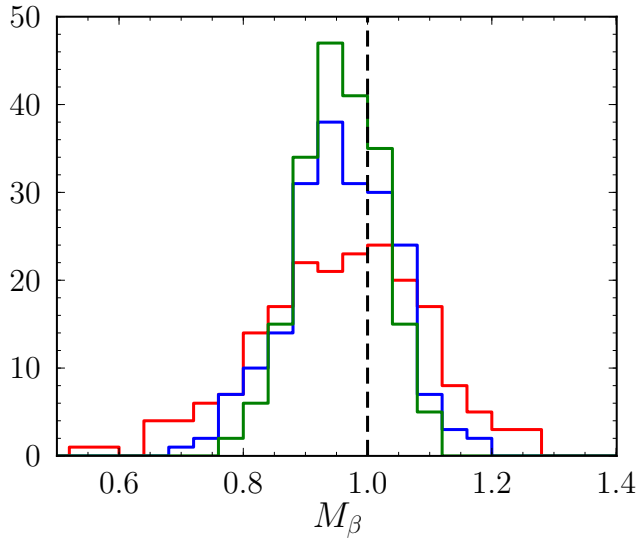

Figure 6.11: Histogram of best-fit M_β values for three types of mocks simulations with 200 samples per simulation ($N_\mathrm{g} = 8989$ galaxies in each sample) where the input v_p is sampled from a Gaussian distribution of width $\sigma_v = 200\,\mathrm{km\ s^{-1}}$ (red), $\sigma_v = 300\,\mathrm{km\ s^{-1}}$ (blue) and $\sigma_v = 400\,\mathrm{km\ s^{-1}}$ (green).

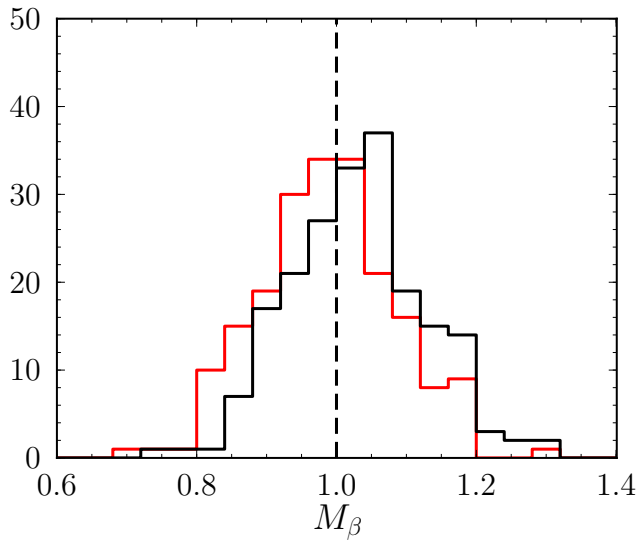

Figure 6.12: Histogram of best-fit M_β value for 200 mock simulations ($N_\mathrm{g} = 8989$ galaxies in each sample) in which the input v_p is sampled from a 2MRS reconstructed velocity distribution where measurement errors were fixed for all galaxies (red, the same as those in Figure 6.8) as compared to the mock simulations where galaxies have individual measurement errors (black).

Table 6.2: Best-fit values to 1000 mock simulations ($N_g = 8989$ galaxies in each sample), fitting (1) M_β only to a model with input $M_\beta = 1$ and $\boldsymbol{u} = 0$, (2) $\boldsymbol{u}_{tot}$ only, to a model with input $M_\beta = 0$ and $\boldsymbol{u} = 0$; and (3) both M_β and $\boldsymbol{u}_{res}$, to a model with input $M_\beta = 1$ and $\boldsymbol{u} = 0$. We list the input values as well as the mean best-fit values (and rms scatter) of M_β and $\boldsymbol{u}$ for each set of mock simulations.

Model	Input		Best-fit			
	M_β [-]	$\boldsymbol{u}$ [km s^{-1}]	$\langle M_\beta \rangle$ [-]	$\langle u_x \rangle$ [km s^{-1}]	$\langle u_y \rangle$ [km s^{-1}]	$\langle u_z \rangle$ [km s^{-1}]
(1) M_β	1.0	-	1.0±0.10	-	-	-
(2) $\boldsymbol{u}_{tot}$	-	(0,0,0)	-	-42.7±41.2	-19.0±34.0	-16.8±38.6
(3) M_β, $\boldsymbol{u}_{res}$	1.0	(0,0,0)	0.89±0.11	-70.2±48.4	-26.7±39.4	-34.0±42.1

6.6 Testing the Model Fits of β and $\boldsymbol{u}$

In this section we extend the peculiar velocity model of the previous section, by introducing a dipole term (i.e. $\boldsymbol{u}$, in addition to M_β) in the peculiar velocity field model that we fit with our maximum likelihood fitting method. In the case where we fit only a dipole term (i.e. fix M_β to zero - corresponding to the model of equation 6.9), we refer to this as the total bulk flow ($\boldsymbol{u}_{tot}$) in the sample.

We also extend this model and fit for both M_β and $\boldsymbol{u}$ simultaneously (corresponding to the model of equation 6.7); in this case the dipole term is the residual bulk flow ($\boldsymbol{u}_{res}$) of motions unaccounted for by the 2MRS predicted velocity field (notably the mass distribution outside the 2MRS volume). Henceforth we refer to the Supergalactic Cartesian components (i.e. with respect to SGX, SGY and SGZ) of the dipole vector, $\boldsymbol{u}$, as simply u_x, u_y and u_z, respectively.

6.6.1 Calibrating Bias Corrections of the Fitting Method

We determine the uncertainties and residual bias corrections on each of the parameters defining the three models using Monte Carlo simulations of galaxy samples (including mock peculiar velocities generated using the method of Section 6.4.4), in a similar manner to the Fundamental Plane coefficient errors in Chapter 4.

To quantify the residual bias in our maximum likelihood fitting, we generate 1000 mock simulations with an input value of $M_\beta = 1.0$ and $\boldsymbol{u} = 0$, and fit just M_β and no induced dipole. Similarly, we generate 1000 simulations with $M_\beta = 0$ and $\boldsymbol{u}$, and fit only the total dipole $\boldsymbol{u}_{tot}$. Finally we generate 1000 mock simulations with $M_\beta = 1$ and $\boldsymbol{u} = 0$, and fit both M_β and the residual dipole $\boldsymbol{u}_{res}$. Table 6.2 summarises the mean best-fit values after fitting to these mock samples.

The distribution of the maximum-likelihood best-fit values to these mock samples is shown in Figure 6.13. For each of the parameters in the three models, the mean of the best-fit values (solid red line) is compared to the input value of the mock

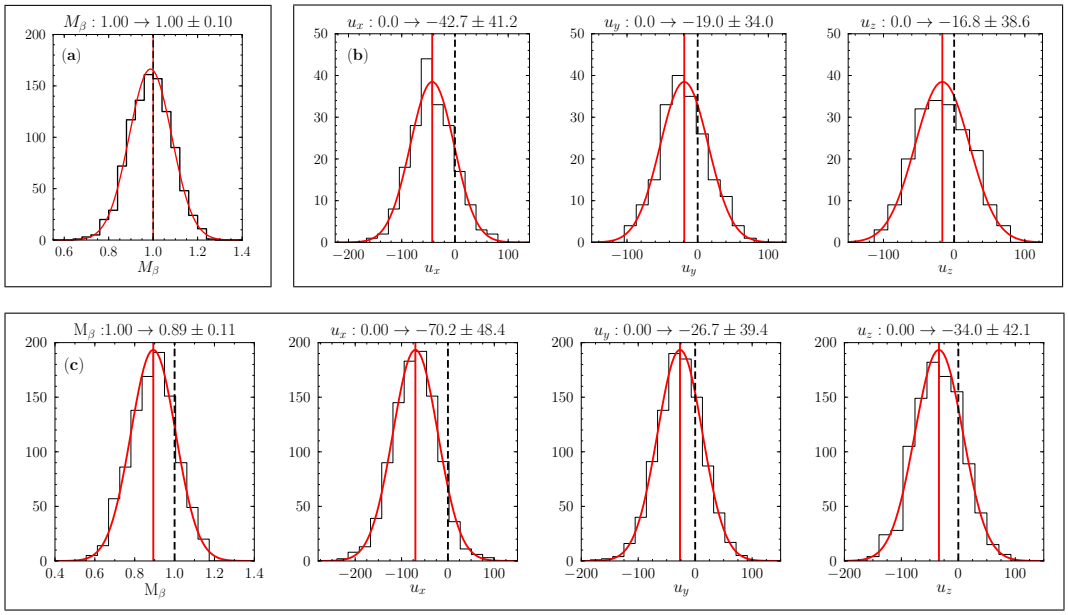

Figure 6.13: Histograms of the maximum-likelihood best-fit values to M_β only (*panel a*), components of the total dipole, $\boldsymbol{u}_{\rm tot}$, only in km s^{-1} (*panel b*) and M_β and components of the residual dipole $\boldsymbol{u}_{\rm res}$ in km s^{-1} (*panel c*). Each histogram is labelled at the top with the name of the parameter, the input value of the parameter for 1000 mock simulations, and the mean and rms of the best-fit parameters obtained from ML fits to these mocks; a Gaussian with this mean and rms is overplotted on the histogram. The vertical dashed line shows the input value of the parameter and the vertical solid line shows the mean of the best-fit values (see Table 6.2). The residual bias correction is the offset between the dashed and solid line.

samples (dashed black line). The offset between the dashed line and the solid line is the residual bias correction (see equations 6.13 and 6.14 below).

Fitting M_β alone (equation 6.8) to 1000 mock simulations, we recover the input value exactly with 10% rms error ($\langle M_\beta \rangle = 1.0 \pm 0.10$). In the model where we fit for a dipole component only (equation 6.8), the best-fit values are systematically lower than the input values of the dipole components. For the total dipole, $\boldsymbol{u}_{\rm tot}$ we therefore determine a bias correction for each component of

$$\Delta u_x = +42.7,\ \Delta u_y = +19.0 \text{ and } \Delta u_z = +16.8\ . \tag{6.13}$$

The best-fit values for 1000 mock simulations when fitting both M_β and the components of a residual velocity dipole (equation 6.7) are also given in Table 6.2. In this model where M_β and $\boldsymbol{u}$ are fit simultaneously, we find a slightly larger offset between the input and mean best-fit parameters. From the mock simulations, we derive a residual bias correction in this model of

$$\Delta M_\beta = 0.11,\ \Delta u_x = +70.2,\ \Delta u_y = +26.7 \text{ and } \Delta u_z = +34.0\ . \tag{6.14}$$

Table 6.3: Best-fit values to the 6dFGSv sample ($N_{\rm g} = 8989$ galaxies) after bias correction, fitting (1) M_β only, (2) $\boldsymbol{u}_{\rm tot}$ only and (3) both M_β and $\boldsymbol{u}_{\rm res}$. We list the best-fit values and rms scatter (derived from the mock simulations in Table 6.4) of M_β and $\boldsymbol{u}$ for each model.

Model	M_β [-]	u_x [km s^{-1}]	u_y [km s^{-1}]	u_z [km s^{-1}]
(1) M_β	0.73 ± 0.10	-	-	-
(2) $\boldsymbol{u}_{\rm tot}$	-	-331.1 ± 43.3	$+82.5 \pm 36.6$	-19.2 ± 37.9
(3) M_β, $\boldsymbol{u}_{\rm res}$	0.72 ± 0.11	-205.7 ± 46.3	$+162.4 \pm 35.0$	$+45.8 \pm 41.6$

This larger offset and the slightly larger uncertainties are presumably due to coupling (i.e. degeneracy) between M_β and $\boldsymbol{u}$ in the fits. We speculate that this is in part due to the limited sky coverage of the peculiar velocity measurements; we address this issue in Section 6.7.2.

6.7 Fitting M_β and $\boldsymbol{u}$ to the Data

We have determined the uncertainties and residual bias inherent in the fitting models of Section 6.4 using well-calibrated mock simulations. Therefore, we now use the maximum-likelihood fitting routines of Section 6.4 to recover the best-fit beta multiplier, total and residual dipole values for the 6dFGSv data sample of $N_{\rm g} = 8989$ galaxies (see Section 6.3).

The best-fitting values (after bias correction) for this sample are summarised in Table 6.3, which includes the mean best-fit value for each parameters in our three v_p models as well as the rms scatter from 200 mock simulations generated using the values from Table 6.3 as input.

6.7.1 Fitting to Mock Simulations Corrected for Bias

We confirm that the bias corrections derived for the fitting models are an accurate representation of the residual bias in the fitting model by generating 200 mock simulations with the bias-corrected values of the best-fit to the data (Table 6.3) as *input* to the mocks. If the bias corrections are accurate, then the mean of the best-fit values will match the best-fit to the data before bias correction, indicating that the input to the mocks is in fact the true best-fit value.

The maximum likelihood models perform remarkably well in recovering the fitted values with the appropriate bias as shown in Figure 6.14. Figure 6.14 includes the distribution of best-fitting values for 200 mock simulations (in each case) when fitting M_β alone (panel a), $\boldsymbol{u}_{\rm tot}$ only (panel b) and M_β and $\boldsymbol{u}_{\rm res}$ (panel c). The difference between the input and best-fit values and standard error of the mean for these mock simulations are also given in Table 6.2. The best-fit M_β value differs from the input by $\delta\langle M_\beta \rangle < 0.02$ with a standard error of the mean as small as $\sigma_M = 0.01$ in both

Table 6.4: Best-fit values to 200 mock simulations ($N_g = 8989$ galaxies in each sample), fitting (1) M_β only to a model with input $M_\beta = 0.73$ and $\boldsymbol{u} = 0$, (2) $\boldsymbol{u}_{tot}$ only, to a model with input $M_\beta = 0$ and $\boldsymbol{u} = (-331.1, +82.5, -19.2)$; and (3) both M_β and $\boldsymbol{u}_{res}$, to a model with input $M_\beta = 0.72$ and $\boldsymbol{u} = (-205.7, +162.4, +45.8)$. We list the input values as well as the difference mean best-fit and input values (and the standard error of the mean, σ_M) of M_β and $\boldsymbol{u}$ for each set of mock simulations.

Model	Input		Difference between best-fit and input			
	M_β [-]	$\boldsymbol{u}$ [km s^{-1}]	$\delta\langle M_\beta\rangle$ [-]	$\delta\langle u_x\rangle$ [km s^{-1}]	$\delta\langle u_y\rangle$ [km s^{-1}]	$\delta\langle u_z\rangle$ [km s^{-1}]
(1) M_β	0.73	-	0.0±0.01	-	-	-
(2) $\boldsymbol{u}_{tot}$	-	(-331.1,+82.5,-19.2)	-	11.8±3.1	3.8±2.6	1.3±2.7
(3) M_β, $\boldsymbol{u}_{res}$	0.72	(-205.7,+162.4,+45.8)	0.02±0.01	10.8±3.3	2.9±2.5	5.8±2.9

models 1 and 2. For models 2 and 3, the difference in the x, y and z-components of $\boldsymbol{u}$ (for both $\boldsymbol{u}_{tot}$ and $\boldsymbol{u}_{res}$) is at most $\sim$12 km s^{-1} for $\delta\langle u_x\rangle$ but as small as $\sim$1 km s^{-1} for $\delta\langle u_z\rangle$, with a consistent, and small, standard error of the mean of $\sim$3 km s^{-1}.

6.7.2 Fitting M_β and $\boldsymbol{u}$ to All-Sky Simulations

In the previous sections, we discovered a systematic offset in the fitted values for M_β and $\boldsymbol{u}$ (i.e. a residual bias), in the sense that the fitted values are lower compared to the input values of the mock simulation. The origin of this offset may be due to the fact that our galaxy sample is restricted to observations in the Southern Hemisphere only. We calculate the size of this effect using 200 mock simulations for the simple case where input $M_\beta = 1.0$ and $\boldsymbol{u} = 0$. We wish to simulate all-sky coverage with these mocks, so we randomly select half of the mock galaxies, and invert the sign of their declinations, while rotating their right ascension by 180 degrees. The best-fit values of M_β and the residual dipole term for these mocks are shown in Figure 6.15 indicating that the maximum likelihood fitting model recovers M_β exactly (rms error of 11%) and a residual dipole consistent with zero (with an rms error < 47 km s^{-1}). Therefore, the source of the residual bias (and the degeneracy between M_β and $\boldsymbol{u}$) is indeed due to having only hemispheric coverage in the 6dFGS, and hence can be accounted for using the mock simulations as discussed above.

6.8 Correcting v_p for Age Variation in the FP

In the previous chapter, the strongest trend in the Fundamental Plane was found to be with galaxy age, predominantly in the $\boldsymbol{v}_1$ direction. Up to this point we have not accounted for the effects of age on the FP in fitting the peculiar velocity field. Here we investigate the result of incorporating age into the maximum likelihood v_p models developed in the previous sections, with the aim of achieving tighter constraints on the beta multiplier and bulk flow.

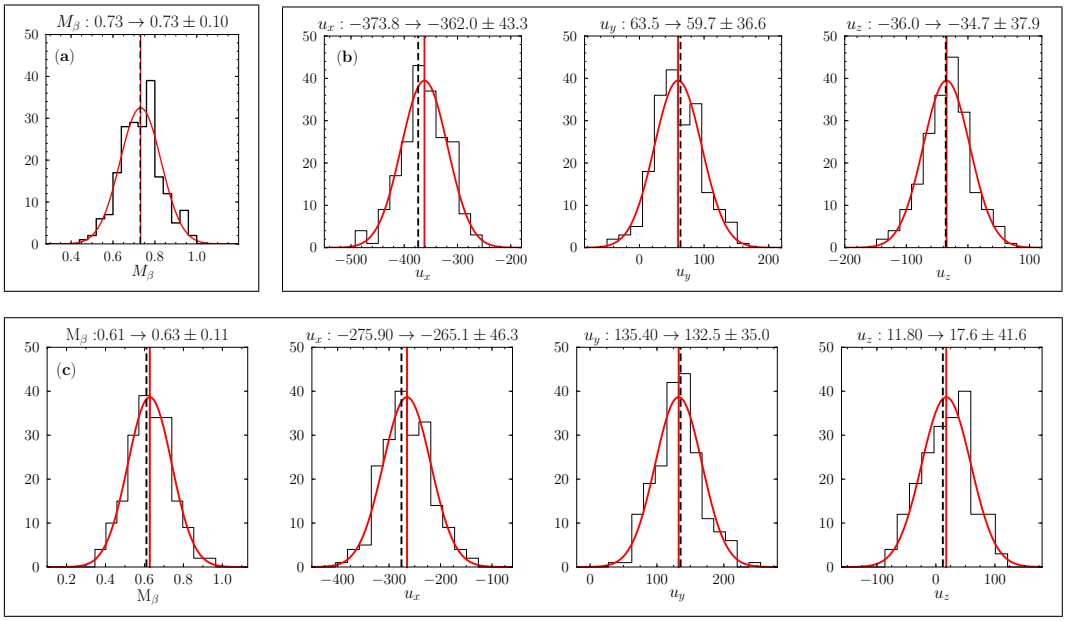

Figure 6.14: As for Figure 6.13 but mock samples are generated with input values of M_β and $\boldsymbol{u}$ derived from fits to data. In this plot, the dashed line is *not* the (bias-corrected) input value of the mocks but instead the best-fit (solid red line) is compared to the input values before bias correction (dashed black line). The small difference between the best-fit and input (before bias correction) indicates that the initial bias corrections applied to the mock simulations are appropriate for each of the models. The best-fit values for these simulations are summarised in Table 6.4.

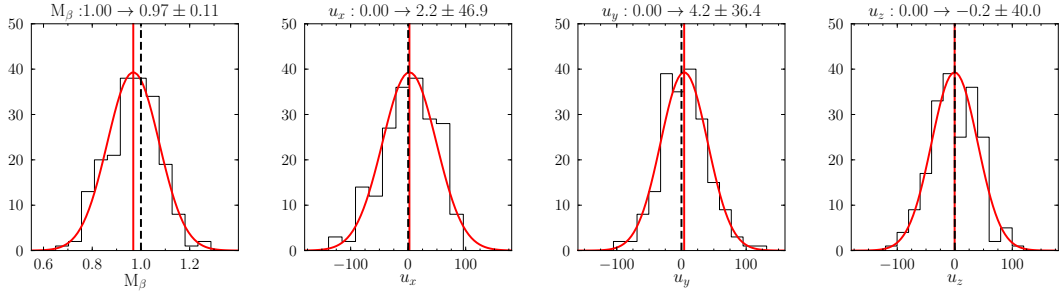

Figure 6.15: As for panel (c) in Figure 6.13, but for 200 mock simulations with simulated sky positions that span both northern and southern hemispheres. The input values of $M_\beta = 1.0$ and $\boldsymbol{u}_{\rm res} = 0.0$ are recovered accurately and therefore no residual bias correction is required in this case.

Table 6.5: Best-fit values to 200 mock simulations (N_g = 8989 galaxies in each sample) where each mock galaxy is corrected for the age trend in $\boldsymbol{v}_1$ through the Fundamental Plane, fitting (1) M_β only to a model with input $M_\beta = 1$ and $\boldsymbol{u} = 0$, (2) $\boldsymbol{u}_{\rm tot}$ only, to a model with input $M_\beta = 0$ and $\boldsymbol{u} = 0$; and (3) both M_β and $\boldsymbol{u}_{\rm res}$, to a model with input $M_\beta = 1$ and $\boldsymbol{u} = 0$. We list the input values as well as the mean best-fit values (and rms scatter) of M_β and $\boldsymbol{u}$ for each set of mock simulations.

Model	Input		Best-fit			
	M_β [-]	$\boldsymbol{u}$ [km s^{-1}]	$\langle M_\beta \rangle$ [-]	$\langle u_x \rangle$ [km s^{-1}]	$\langle u_y \rangle$ [km s^{-1}]	$\langle u_z \rangle$ [km s^{-1}]
(1) M_β	1.0	-	1.0±0.09	-	-	-
(2) $\boldsymbol{u}_{\rm tot}$	-	(0,0,0)	-	-42.3±41.7	-23.5±36.8	-18.9±41.8
(3) M_β, $\boldsymbol{u}_{\rm res}$	1.0	(0,0,0)	0.90±0.11	-70.2±47.4	-26.6±36.5	-30.5±43.9

We couple the sample of galaxies with v_p measurements (N_g = 8989), with the relevant stellar population information by dividing the galaxies into the four age bins defined in Chapter 5; young (age $\leq$ 3 Gyr), intermediate (3 $<$ age $\leq$ 8 Gyr), old (age $>$ 8 Gyr) and unknown (for those galaxies without an age measurement). To simulate this same division in the mock galaxy samples, the mock ages are randomly drawn from the actual observed galaxy ages, so that the ratio of galaxies in each age bin (for a given sample) is preserved.

The maximum likelihood function of the v_p models is then modified so that the eight parameters defining the 3D Gaussian Fundamental Plane model are dependent on which age bin each galaxy is in. The bias-corrected Fundamental Plane coefficients used in this analysis for each of the four age bins are given in Table 5.2.

We follow the method of Section 6.6.1 by deriving bias corrections for each of the three v_p models (now correcting for age) using 200 mock simulations generated from the following input values for model 1 ($M_\beta = 1.0$), model 2 ($\boldsymbol{u}_{\rm tot} = 0.0$) and model 3 ($M_\beta = 1.0$ and $\boldsymbol{u}_{\rm res} = 0.0$). The mean best-fit values from fitting the 200 mocks samples, as shown in Table 6.5, are similar to the corresponding best-fit without correcting for age (in Table 6.2); there is no discernible improvement from accounting for age.

We then apply the age-corrected models to the 6dFGSv sample of galaxies. The best-fit values for each model are reported in Table 6.6 *after* bias correction, using the residual bias derived from the mock simulations in Table 6.5.

Table 6.6 can be directly compared to the models where the age trend is *not* accounted for in Table 6.3. In fitting M_β, the age-corrected model finds a best-fitting value of $\langle M_\beta \rangle = 0.74 \pm 0.10$ similar to the value from the standard model of $\langle M_\beta \rangle = 0.74 \pm 0.10$, and with the same error. The difference between the standard and age-corrected model is larger when fitting $\boldsymbol{u}_{\rm tot}$ only and M_β and $\boldsymbol{u}_{\rm res}$, however

Table 6.6: Best-fit values to the 6dFGSv sample ($N_{\rm g} = 8989$ galaxies) after bias correction, where each galaxy is corrected for the age trend in $\boldsymbol{v}_1$ through the Fundamental Plane, fitting (1) M_β only, (2) $\boldsymbol{u}_{\rm tot}$ only and (3) both M_β and $\boldsymbol{u}_{\rm res}$. We list the best-fit values and rms scatter (derived from the mock simulations in Table 6.4) of M_β and $\boldsymbol{u}$ for each model.

Model	M_β [-]	u_x [km s^{-1}]	u_y [km s^{-1}]	u_z [km s^{-1}]
(1) M_β	0.74 ± 0.10	-	-	-
(2) $\boldsymbol{u}_{\rm tot}$	-	-357.3 ± 40.6	$+101.6 \pm 35.5$	-25.4 ± 39.4
(3) M_β, $\boldsymbol{u}_{\rm res}$	0.70 ± 0.12	-233.1 ± 44.4	$+176.1 \pm 38.1$	$+29.2 \pm 41.8$

the scatter between both models remains the same to within 1-3 km s^{-1} at most. Therefore the inclusion of age as a fourth parameters in our v_p models does not decrease the overall error in the peculiar velocities.

While in principle removing the age trend should reduce the scatter in the FP and, by the same token, the errors in FP distances and peculiar velocities, in practice the variation is not strong enough for individual galaxies trends to impact the fitting of M_β and $\boldsymbol{u}$.

6.9 Additional Uncertainty in $\bar{r}$

In calibrating the zeropoint of the Fundamental Plane (see Section 6.3.4), we derive the offset of the plane in effective radius (i.e. $\bar{r}$) from a subsample of galaxies around the great circle close to the celestial equator to avoid spurious bulk motions along the poles. The re-calibrated value for $\bar{r}$ is then used when fixing the eight parameters defining the global FP in the likelihood function that models the peculiar velocity field. The subsample from which $\bar{r}$ is measured has fewer galaxies in it than the full sample of 8901 galaxies (used to fix the *other* best-fit FP parameters) which may induce additional scatter when fitting the parameters associated with the peculiar velocity model.

To measure the extent of this effect we use the same mock simulations as in Sections 6.6.1 and 6.7.1. We model the uncertainty associated with deriving $\bar{r}$ from a small subsample as a random Gaussian distribution with a width of $\sigma_{\bar{r}} = 0.003$ (i.e. the rms error in $\bar{r}$ from mock simulations of the subsample). Then we use values drawn from this distribution (rather than a *fixed* $\bar{r}$) to define the FP in the likelihood function defining the v_p model parameters.

To determine the bias corrections for the three v_p models we use mocks with input values of $M_\beta = 1.0$, $\boldsymbol{u}_{\rm tot} = 0.0$ and $M_\beta = 1.0$ and $\boldsymbol{u}_{\rm res} = 0.0$. For the model fitting M_β only, there is no bias correction. For the total dipole, $\boldsymbol{u}_{\rm tot}$ we assume a

Table 6.7: Best-fit values to 200 mock simulations ($N_{\rm g}$ = 8989 galaxies in each sample) using variable $\bar{r}$, fitting (1) M_β only to a model with input $M_\beta = 0.73$ and $\boldsymbol{u} = 0$, (2) $\boldsymbol{u}_{\rm tot}$ only, to a model with input $M_\beta = 0$ and $\boldsymbol{u} = (-331.1, +82.5, -19.2)$; and (3) both M_β and $\boldsymbol{u}_{\rm res}$, to a model with input $M_\beta = 0.72$ and $\boldsymbol{u} = (-205.7, +162.1, +45.8)$. We list the input values as well as the mean best-fit values (and rms scatter) of M_β and $\boldsymbol{u}$ for each set of mock simulations.

Model	Input		Best-fit			
	M_β [-]	$\boldsymbol{u}$ [km s^{-1}]	$\langle M_\beta \rangle$ [-]	u_x [km s^{-1}]	u_y [km s^{-1}]	u_z [km s^{-1}]
(1) M_β	0.73	-	0.74±0.16	-	-	-
(2) $\boldsymbol{u}_{\rm tot}$	-	(-331.1,+82.5,-19.2)	-	-368.3±74.2	+57.0±45.0	-37.5±46.5
(3) M_β, $\boldsymbol{u}_{\rm res}$	0.72	(-205.7,+162.1,+45.8)	0.64±0.12	-272.2±73.1	+128.1±45.4	+13.8±46.1

bias correction for each component of

$$\Delta u_x = +49.7,\ \Delta u_y = +21.7 \text{ and } \Delta u_z = +18.8\ . \tag{6.15}$$

From the mock simulations, we derive a residual bias correction for the model fitting M_β and $\boldsymbol{u}_{\rm res}$ of

$$\Delta M_\beta = 0.10,\ \Delta u_x = +70.9,\ \Delta u_y = +26.9 \text{ and } \Delta u_z = +34.1\ . \tag{6.16}$$

These corrections are very similar to those in equations 6.13 and 6.14 from the model where $\bar{r}$ is fixed, indicating that both methods have a similar amount of bias.

The rms scatter, resulting from a variable $\bar{r}$ value, in the best-fitting parameters of each fitting method is measured using the same mock samples in Section 6.7.1 which are generated from input values derived from the bias-corrected best-fit to the data. These input values and recovered best-fit values (to 200 mock simulations) are summarised in Table 6.7 and their distributions are plotted in Figure 6.16. The mean best-fit value for all three v_p models compare favourably with the values from fitting the same mock simulations (but using fixed $\bar{r}$) in Table 6.4 (and Figure 6.14).

However, the rms scatter in each of the best-fit parameters in this model is larger (i.e. $\langle M_\beta \rangle = 0.74 \pm 0.16$) than for the model where $\bar{r}$ is fixed (i.e. $\langle M_\beta \rangle = 0.73 \pm 0.10$). In particular, the rms scatter in u_x in both the model for $\boldsymbol{u}_{\rm tot}$ (i.e. $\langle u_x \rangle = -368.3 \pm 74.2\,{\rm km\ s^{-1}}$) and $\boldsymbol{u}_{\rm res}$ (i.e. $\langle u_x \rangle = -272.2 \pm 73.1\,{\rm km\ s^{-1}}$) is also substantially larger than the rms scatter in the y- and z-components of the dipole (see Table 6.7). Also it is almost 1.5 times larger than the rms error in the corresponding best-fit values in the model where $\bar{r}$ is fixed, in both $\boldsymbol{u}_{\rm tot}$ ($\langle u_x \rangle = -362 \pm 43.3$) and $\boldsymbol{u}_{\rm res}$ ($\langle u_x \rangle = -265.1 \pm 46.3$). We expect the dipole flow in the x-direction (u_x) to contain the largest scatter and hence be affected most strongly by changes in $\bar{r}$, as the x-component of the bulk flow is dominant in the polar region.

The magnitude of the bulk flow ($|\boldsymbol{u}|$) is derived from the quadrature sum of

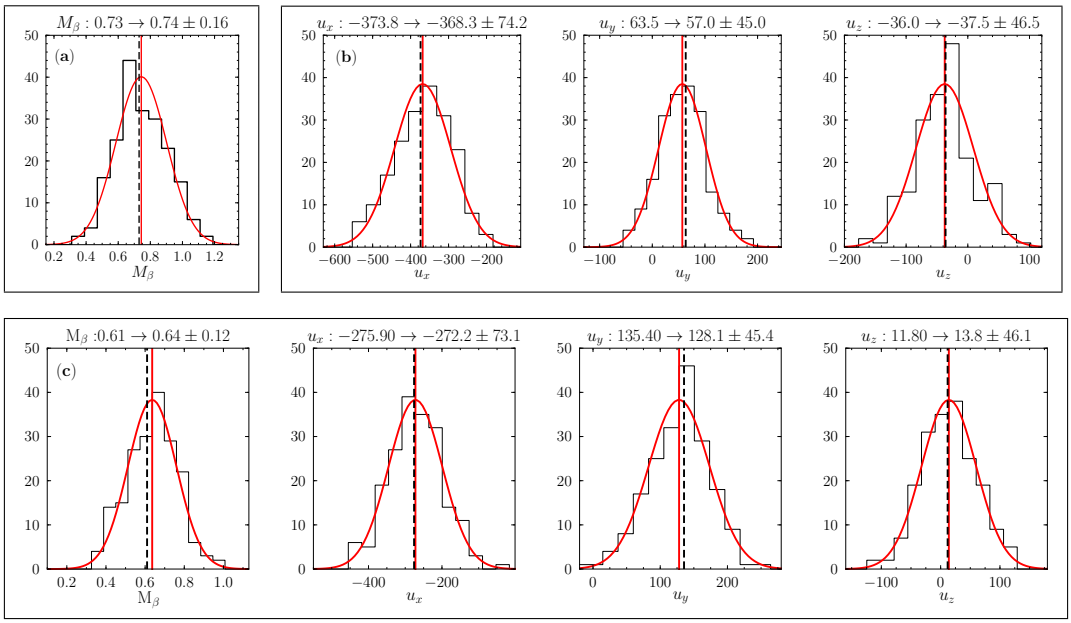

Figure 6.16: As for Figure 6.14, for the same 200 mock simulations but fitted with variable $\bar{r}$ for each simulations, drawn from a Gaussian of width $\sigma_{\bar{r}} = 0.003$. The best-fit values for these simulations are summarised in Table 6.7.

Table 6.8: Best-fit values to the 6dFGSv sample ($N_g = 8989$ galaxies) after bias correction, using variable $\bar{r}$, fitting (1) M_β only, (2) $\boldsymbol{u}_{tot}$ only; and (3) both M_β and $\boldsymbol{u}_{res}$. We list the mean best-fit values and rms scatter (derived from mock simulations in Table 6.7) of M_β and $\boldsymbol{u}$ for each model. For the total and residual bulk flow we also include the calculated values for the magnitude of the bulk flow ($|\boldsymbol{u}|$) in km s^{-1} and the bulk flow direction in Supergalactic (SGL, SGB) coordinates in degrees.

Model	$\langle M_\beta \rangle$ [-]	u_x [km s^{-1}]	u_y [km s^{-1}]	u_z [km s^{-1}]	$\lvert\boldsymbol{u}\rvert$ [km s^{-1}]	SGL °	SGB °
(1) M_β	0.73 ± 0.16	-	-	-	-	-	-
(2) $\boldsymbol{u}_{tot}$	-	-324.1 ± 77.3	$+85.2 \pm 45.5$	-17.2 ± 45.7	336.7±66.3	164.9±10.1	-2.6±8.3
(3) M_β, $\boldsymbol{u}_{res}$	0.71 ± 0.12	-205.0 ± 72.6	$+162.3 \pm 47.9$	$+45.9 \pm 48.9$	272.7±45.0	140.7±16.0	10.8±10.6

the x, y and z dipole components. The direction of this dipole is calculated (in Supergalactic coordinates) with the following relations for latitude, SGB:

$$SGB = \arcsin\left(\frac{u_z}{|u|}\right) \tag{6.17}$$

and for longitude, SGL

$$SGL = \begin{cases} \arccos\left(\frac{u_x}{|u|\cos(SGB)}\right) & u_y > 0.0 \\ 360^\circ - \arccos\left(\frac{u_x}{|u|\cos(SGB)}\right) & u_y < 0.0\ . \end{cases} \tag{6.18}$$

For the 6dFGSv sample, we determine a best-fit β value (from $\beta = M_\beta \times 0.4$) of 0.29 ± 0.06. We measure a total bulk flow amplitude of $|u_{\rm tot}| = 337 \pm 66\,{\rm km\ s^{-1}}$ in the direction of $(SGL, SGB) = (165^\circ \pm 10^\circ, -3^\circ \pm 8^\circ)$ and a residual bulk flow amplitude of $|u_{\rm res}| = 273 \pm 45\,{\rm km\ s^{-1}}$ in the direction of $(SGL, SGB) = (141^\circ \pm 16^\circ, 11^\circ \pm 11^\circ)$.

Therefore, our final best-fit values and rms scatter for the three v_p models (fitting M_β and $\boldsymbol{u}$) are given in Table 6.8 including the bias corrections of equation 6.15 and 6.16 aswell as the magnitude for the residual and total bulk flows (and their (SGL, SGB) coordinates).

6.10 Discussion

6.10.1 Comparison of the β Parameter

By comparing the predicted 2MRS velocities with the observed peculiar velocities from our 6dFGSv survey, we measured a best-fit value for the linear redshift-space distortion parameter of $\beta = 0.29 \pm 0.06$. This is in good agreement with Davis et al. (2011) who find $\beta = 0.33 \pm 0.04$ from a comparison of their own reconstruction of the 2MRS survey with a subsample of ∼3000 measured peculiar velocities from the SFI++ survey (Springob et al., 2007) based on Tully-Fisher distances. The error on the measurement of β is highly dependent on the size of the samples and typical uncertainties on the velocities used to constrain β. The error on β derived from 6dFGSv compares well with the value from Davis et al. (2011) if we account for the fact our sample is approximately three times larger but the individual velocity errors are twice as large, relative to theirs. We gain a factor of $\sqrt{3}$ in precision from the sample size but lose a factor 2 from errors, and so expect this uncertainty to be larger by a factor $\sim 2/\sqrt{3}$ than the value of 0.04 obtained by Davis et. al. We thus might predict an uncertainty of ∼0.05, whereas in fact our uncertainty is 0.06 due to the additional error flowing from our zeropoint calibration (see Section 6.9).

Another recent measurement of β was made by studying the clustering dipole of all galaxies in the 2MASS XSC (and therefore out to a large depth of $\sim 300\,h^{-1}\,{\rm Mpc}$; Bilicki et al., 2011). They measured a value of β from a comparison of the observed

and ΛCDM prediction of the growth of the clustering dipole as a function of the limiting flux of the survey and found $\beta = 0.38 \pm 0.04$ (Bilicki et al., 2011), within $\sim 1.5\sigma$ of our value.

A substantially larger value ($\sim 2.8\sigma$ level) for β of 0.49 ± 0.04 was derived by Pike & Hudson (2005) from a reconstruction of the 2MRS peculiar velocity field but compared to a compilation of three surveys with observed velocities derived from Tully-Fisher distances, surface brightness fluctuations and a compilation of Type Ia Supernovae respectively. Lavaux et al. (2010) used a similar iterative technique to generate a non-linear MAK reconstruction of the 2MRS velocity field which is compared with another compiled catalogue of ∼2000 velocity measurements. Their comparison yielded a value of $\beta \sim 0.52$ from their estimate of $\Omega_m = 0.31 \pm 0.05$.

However, such discrepancies between the comparison of β values may result from their sensitivity to the assumed value of linear bias, b between distributions. The process of Wiener filtering by construction smooths the density field in noisy regions and consequently reduces the density contrast. It therefore tends to lower the estimated value of β, as discussed by Zaroubi (2002). This bias will need to be accounted for in developing this analysis further. Alternatively, it may result from details such as the sample selection limits or differences in fitting methods. Even so, the 6dFGSv value for β agrees, in general, with other recent determinations on similar scales.

Our measurement of β depends only on the 6dFGS and 2MRS datasets, but if we combine our results with measurements of other cosmological parameters from the literature, then we can estimate a value for the amplitude of mass fluctuations on a scale of $8\,h^{-1}$ Mpc (known as σ_8). First, we need to estimate a value for the linear bias parameter, b, using the fact that $b = \Omega^{0.55}/\beta$. Assuming $\Omega_m = 0.274 \pm 0.027$ from the latest WMAP7 constraints (Larson et al., 2011), we calculate a value of $b = 1.69 \pm 0.36$, in agreement with $b = 1.52 \pm 0.29$ derived from the full 6dFGS redshift (6dFGSz) sample (Beutler et al., 2012).

This value of b can in turn be used to infer a value of $f\sigma_8$, given that the amplitude of the mass (σ_8) and galaxy ($\sigma_{8,g}$) fluctuations on scales of $8\,h^{-1}$ Mpc are related by $\sigma_{8,g} = b\sigma_8$. If we adopt a value of $\sigma_{8,g} = 0.97 \pm 0.05$ appropriate to the whole 2MRS sample of galaxies (Westover, 2007), we obtain a value for $f\sigma_8 = \beta\sigma_{8,g} = 0.28 \pm 0.06$. This value is comparable to $f\sigma_8 = 0.31 \pm 0.05$ from Davis et al. (2011) but smaller than $f\sigma_8 = 0.42 \pm 0.07$ as found by Turnbull et al. (2012) and $f\sigma_8 = 0.42 \pm 0.06$ derived from the growth of structure in 6dFGSz (Beutler et al., 2012). Our slightly lower value of $f\sigma_8$ follows from the fact that our value for β is also lower. However, if we use our value of $b = 1.69 \pm 0.36$ and the WMAP7 value of σ_8 ($=0.81 \pm 0.03$), we find $\sigma_{8,g} = 1.37 \pm 0.30$, rather higher than the 0.97 value based on Westover (2007). Westover's value reflects the bias corresponding to $L \sim L^*$, since it applies to the magnitude-limited 2MRS sample. Our $\sigma_{8,g}$ value, on the other hand, is relevant for

the sample selection criteria of the 6dFGSv, and (according to Westover's estimate of the luminosity-dependent bias) corresponds to $L \sim 2.5L^*$. This is larger than the effective luminosity of $L \sim L^*$ that we calculate by assuming galaxies in our sample contribute to our estimate of β in proportion to the volume they independently sample. Therefore the lower value of β derived for our sample does not appear to be driven by the luminosity dependence of bias.

If we assume a value of $f \sim \Omega_m^{0.55} = 0.483 \pm 0.026$ then our estimate of σ_8 is 0.58 ± 0.13. This value of σ_8 agrees with that found by Davis et al. (2011) of $\sigma_8 = 0.65 \pm 0.11$ and is also within 2σ of the WMAP7 result, $\sigma_8 = 0.81 \pm 0.03$ (Larson et al., 2011).

6.10.2 The Local Bulk Flow Motion

In Table 6.9, we provide a comparison of our best-fit total bulk flow for the 6dFGSv sample with a selection of the most relevant bulk flow measurements in the literature. Recently, there have been two conflicting measurements of the bulk flow in the local volume within a radius of $\sim 50\,h^{-1}$ Mpc: a large bulk flow that disagrees with the predictions of ΛCDM (Watkins, Feldman & Hudson, 2009; Feldman, Watkins & Hudson, 2010) and a smaller bulk flow consistent with ΛCDM (Nusser & Davis, 2011, hereafter ND11).

In an effort to construct a large enough sample to measure the convergence of the local dipole, Watkins, Feldman & Hudson (2009) combined peculiar velocity measurements from multiple surveys, with distances from the Fundamental Plane, Tully-Fisher relation, surface brightness fluctuations, and Type Ia supernovae. The bulk flow was measured, using a minimum-variance weighting scheme, to each individual peculiar velocity sample as well as the COMPOSITE survey including all the samples (in total, 4481 peculiar velocity measurements). From the COMPOSITE survey, a bulk flow of 407 ± 81 km s^{-1} towards $l = 287° \pm 9°$ and $b = 8° \pm 6°$ was derived within a Gaussian sphere of radius $50\,h^{-1}$ Mpc, which disagrees with ΛCDM predictions at the 98 per cent confidence level.

However, the bulk flow measurement from the largest survey in the COMPOSITE sample, the Tully-Fisher sample of SFI++ (Springob et al., 2007), was reanalysed using a different method by ND11. In contrast to Watkins et. al., ND11 recover a bulk flow from this sample of 333 ± 38 km s^{-1} in the direction of $l = 276° \pm 3°$ and $b = 14° \pm 3°$ out to $40\,h^{-1}$ Mpc. This value is not at odds with ΛCDM and cosmological constraints from WMAP7 (Larson et al., 2011), and may be a consequence of the differences in the way that ND11 account for the sampling in the volume in question (as compared to Watkins, Feldman & Hudson 2009).

The characteristic depth, defined as the error-weighted mean redshift, of these two samples is $\sim 33\,h^{-1}$ Mpc for COMPOSITE and $\sim 40\,h^{-1}$ Mpc for SFI++ (as analysed

by ND11) whereas the characteristic depth of the 6dFGSv survey is $\sim 73\,h^{-1}\,\mathrm{Mpc}$. Therefore we should also compare our bulk flow results with surveys that are deeper (although limited in sample size) that use SNeIa as tracers of peculiar velocity (e.g. Colin et al., 2011; Dai, Kinney & Stojkovic, 2011, and also Turnbull et al. 2012 with a characteristic depth of $\sim 58\,h^{-1}\,\mathrm{Mpc}$). However we note that as well as their differing radial weighting, the differing sky coverage of the peculiar velocity surveys (the 6dFGSv volume is confined to the Southern Hemisphere only) makes a direct comparison of bulk flow results difficult.

To measure the bulk motion of the local volume, Colin et al. (2011, hereafter CMSS11) analysed a sample of peculiar velocities from the Union2 catalogue of 557 Type Ia Supernovae (Amanullah et al., 2010). The SNe were binned in redshift, and a bulk flow was fit with a maximum likelihood method in cumulative volumes defined by these redshift slices. CMSS11 found that a bulk flow with an amplitude of $\sim 260\,\mathrm{km\ s^{-1}}$ persisted out to $z \sim 0.06$, which they claim is inconsistent at this redshift with ΛCDM at the 1–2σ level.

Another bulk flow measurement was made from the Union2 catalogue using a Bayesian Monte Carlo Markov Chain approach (Dai, Kinney & Stojkovic, 2011, hereafter DKS11). Unlike CMSS11, DKS11 detected a small bulk flow within $z < 0.05$ of $188^{+199}_{-103}\,\mathrm{km\ s^{-1}}$ towards $l = 290^{+39}_{-31}{}^{\circ}$ and $b = 20^{+32}_{-32}{}^{\circ}$ at the 68% confidence level, in agreement with ΛCDM. For the sample beyond $z > 0.05$ they found a bulk flow consistent with zero suggesting a convergence of the bulk flow at that distance. However the sample of SNeIa is too sparse at these redshift to determine this conclusively.

More recently, Turnbull et al. (2012) determined the bulk flow from a sample based on 254 peculiar velocities from three different SNeIa surveys. The bulk flow for the combined 'First Amendment' sample (hereafter 'A1') was recovered using both a maximum likelihood (ML) and a minimum variance (MV) method (similar to Watkins, Feldman & Hudson 2009). The results from their preferred method of minimum variance weighting yield a bulk flow of $249 \pm 76\,\mathrm{km\ s^{-1}}$ in the direction $l = 319^{\circ}\pm18^{\circ}$, $b = 7^{\circ}\pm14^{\circ}$ and is not inconsistent with the predictions of ΛCDM and WMAP7 results (Larson et al., 2011).

Turnbull et al. (2012) also perform a similar maximum likelihood analysis to ours to determine the residual bulk flow of their sample compared to the reconstructed density and peculiar field from the PSCz survey (Branchini et al., 1999). They find a residual bulk flow of $150 \pm 43\,\mathrm{km\ s^{-1}}$ in the direction of $l = 345^{\circ}\pm20^{\circ}$ and $b = 8^{\circ}\pm13^{\circ}$. Even though the amplitude of the residual bulk flow is smaller than the 6dFGSv residual dipole ($273 \pm 45\,\mathrm{km\ s^{-1}}$), both these results suggest there is structure influencing the local dynamics which is either outside of the survey volume or is under-sampled in the reconstructed density and velocity fields.

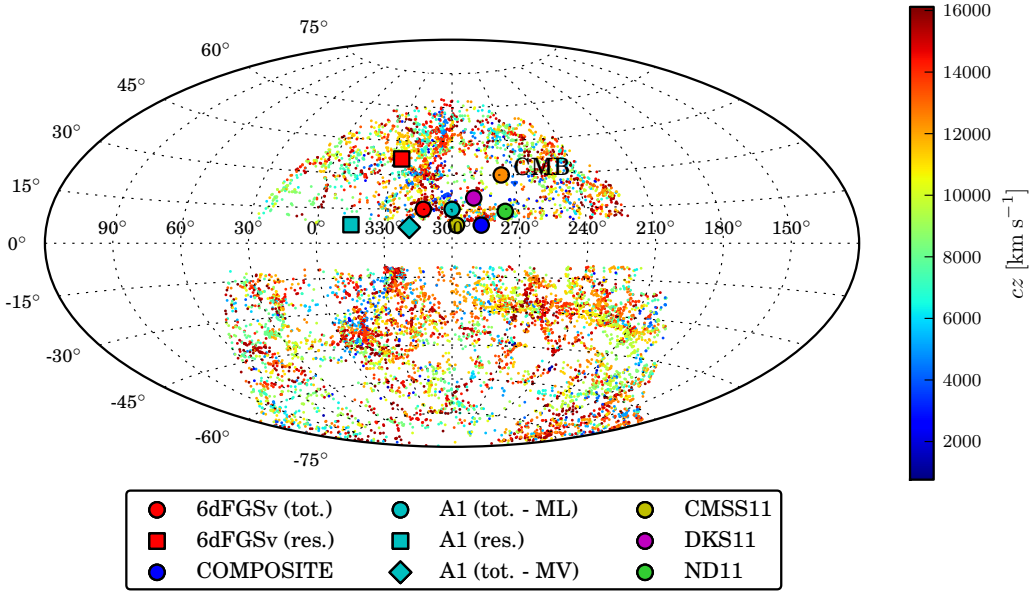

Figure 6.17: Distribution of 6dFGSv galaxies ($N_{\rm g} = 8989$) in Galactic longitude (b) and latitude (l), shown in an equal-area Aitoff projection. Individual galaxies are colour-coded by their CMB frame redshift (in km s^{-1}). The 6dFGSv bulk flow measurements are indicated in red for the total bulk flow of 337 ± 66 km s^{-1} (circle) towards (313°±9°,15°±10°) and the residual bulk flow of 272 ± 45 km s^{-1} (square) in the direction of (326°±13°,37°±14°). The bulk flow measurements from various studies (summarised in Table 6.9) are shown for COMPOSITE (Watkins, Feldman & Hudson, 2009), A1 (Turnbull et al., 2012, including measurements from the maximum likelihood and minimum variance method), CMS11 (Colin et al., 2011), DKS11 (Dai, Kinney & Stojkovic, 2011) and ND11 (Nusser & Davis, 2011). Each point is coloured according to the legend. For reference we also show the direction of the Local Group motion with respect to the CMB (Kogut et al., 1993) in orange.

Table 6.9: Summary of bulk flow measurements from previous studies in the literature. For each study, we list the relevant distance indicator used (DI, with the exception of the combined v_p catalogue of Watkins, Feldman & Hudson 2009), the limiting radius (or the error-weighted radius of a Gaussian sphere is provided, in parentheses, when appropriate) of each sample (R in h^{-1} Mpc), the number of peculiar velocity measurements in the sample (N), the magnitude of the measured total bulk flow, ($|v_{tot}|$ in km s^{-1}) and the direction of the bulk flow in Galactic longitude (l in degrees) and latitude (b in degrees).

	DI	R h^{-1} Mpc	N	$\|v_{tot}\|$ [km s^{-1}]	l [°]	b [°]
6dFGSv (this thesis)	FP	160	8989	337±66	313±9	15±10
COMPOSITE[1]	-	(50)	4481	407±81	287±9	8±6
ND11[2]	TF	(40)	2859	333±38	276±3	14±3
CMSS11[3]	SNe	160	142	260±150	298^{+62}_{-48}	8^{+34}_{-52}
DKS11[4]	SNe	150	132	188^{+199}_{-103}	290^{+39}_{-31}	20^{+32}_{-32}
A1[5]	SNe	(50)	254	249±76	319±18	7±14

[1] The COMPOSITE survey of Watkins, Feldman & Hudson (2009) is a compilation of v_p measurements from SBF, FP, SNe and TF surveys
[2] Nusser & Davis (2011)
[3] Colin et al. (2011)
[4] Dai, Kinney & Stojkovic (2011)
[5] Turnbull et al. (2012)

Our measured total bulk flow of 337 ± 66 km s^{-1} towards $l = 313° \pm 9°$ and $b = 15° \pm 10°$ is therefore comparable with previous measurements and in marginal agreement with each of these surveys. The magnitude is similar to the largest dipole measurements (Watkins, Feldman & Hudson, 2009; Nusser & Davis, 2011), although the 6dFGSv measurement is on a larger scale ($\sim 160\, h^{-1}$ Mpc). The direction of the 6dFGSv bulk flow is also generally consistent with previous determinations.

Figure 6.17 is an all-sky projection of the 6dFGSv sample, colour-coded by the CMB frame redshift of each galaxy. The bulk flow estimates of the most recent surveys (summarised in Table 6.9) are overplotted in Figure 6.17 as large coloured circles (or squares) indicated by the legend. The direction of the bulk flow derived in each study is, in general, located in a narrow 10°-wide strip in b parallel to the Zone of Avoidance. However we would not expect the bulk flow measurement from different surveys to be exactly the same, as they probe different volumes and hence sample the local structures influencing the bulk motion in different ways. For example, we expect the bulk flow from shallower surveys (such as ND11 and Watkins, Feldman & Hudson 2009), indicated by the green and blue points in Figure 6.17 to be closer to the Local Group motion with respect to the CMB. Conversely, we expect the bulk flow of deeper surveys (such as 6dFGSv, CMSS11 and DKS11) to point towards the most massive structures influencing the dynamics of the survey volume. In this case, the bulk flow of 6dFGSv towards (l,b)=(313°±9°, 15°±10°) tends to point in the direction of the Shapley supercluster at (312°, 31°), suggesting Shapley is playing a dominant role in the motions of the 6dFGSv volume. The 6dFGSv residual bulk

flow (red square) is also within 14° in l and 6° in b of the direction of Shapley and is a significant proportion of the total bulk flow, suggesting the supercluster might be underestimated in 2MRS volume, either because it is under-sampled at the edge of the survey or because it extends further out. The dominant effect of Shapley on the Local Group's motion has also been established in the recent reconstruction of the density field by Lavaux & Hudson (2011).

We compare the amplitude of the 6dFGSv bulk flow to other measurements at different scales in Figure 6.18. The bulk flow measurement from previous studies are shown at the effective scale of the samples from which they were derived (approximately at the limiting radius of the sample or the error-weighted radius of a Gaussian window; although the comparison is complicated for the reasons discussed above). The top panel of Figure 6.18 includes both the studies that appear in Figure 14 of Colless et al. (2001b) and Table 6.9, whilst the bottom panel has just the more recent measurements of Table 6.9. The 6dFGSv bulk flow is represented by the red shaded rectangle bounded by the effective sample limits (as described below). We also plot the theoretical prediction of the rms bulk flow calculated in a flat ΛCDM model defined by the WMAP7 results of $\Omega_m = 0.274$, $h = 0.704$ and $\sigma_8 = 0.811$ (Larson et al., 2011), as a solid line for a top-hat window function (both panels) and a dashed line for a Gaussian window function. The 90% error contours for the theoretical prediction corresponding to cosmic variance are shown in light blue (for the top-hat function) and light green (for the Gaussian function).

In general, the measured bulk motions of most studies, shown in in Figure 6.18, are within the 90% range of theoretical expectations and are consistent with a general trend of decreasing bulk flow amplitude at large radii. However, we point out that this type of a comparison is limited by the fact the not all the observed samples are well-described by a top-hat window function; for example, the COMPOSITE (Watkins, Feldman & Hudson, 2009) and A1 (Turnbull et al., 2012) bulk flow measurements are measured within a Gaussian sphere and are therefore best compared to the dotted line and green error contours. Furthermore, the observational errors on each measurement are estimated using different methods between studies and may under (or over) estimate the true uncertainty.

The survey volume and sky coverage of peculiar velocity samples can also affect the bulk flow estimate (as discussed in Section 6.7.2). Hence, we should also take into account the fact that 6dFGSv only covers the Southern Hemisphere when comparing to bulk flow measurements derived from all-sky surveys. The 6dFGSv samples the Southern Hemisphere out to $161\,h^{-1}$ Mpc ($16\,120$ km s^{-1}), and has the same volume as a sphere of radius $129\,h^{-1}$ Mpc ($12\,900$ km s^{-1}); these distances form the upper and lower limit of the effective range, appropriate for the bulk flow measurement in the 6dFGSv volume, as shown in Figure 6.18. The characteristic depth of 6dFGSv

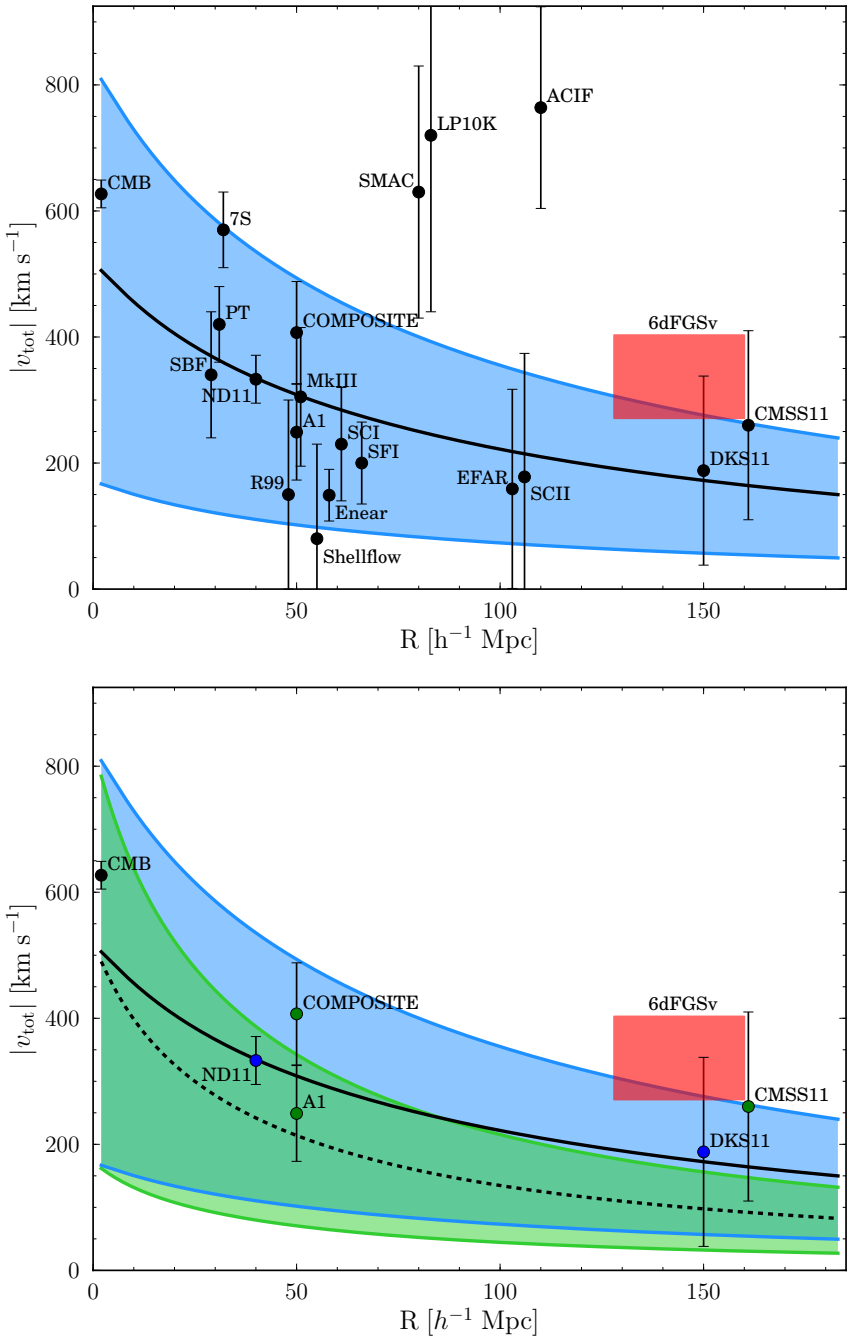

Figure 6.18: The bulk flow amplitude as a function of scale. The 6dFGSv bulk flow measurement is indicated by a red rectangle whose height is the $\pm 1\sigma$ uncertainty in the fitted motion and whose width runs from the outer limit of the survey at $161\,h^{-1}$ Mpc to $129\,h^{-1}$ Mpc, which is the radius of a sphere having the same volume as the hemispherical 6dFGSv survey. The predicted rms bulk flow in a flat ΛCDM model ($\Omega_m = 0.274$, $h = 0.704$ and $\sigma_8 = 0.811$) is shown as the solid black line for a top-hat window function (both panels) and as the dashed black line for a Gaussian window function (lower panel). The light blue and light green shadings around these lines are the 90% range of scatter from cosmic variance. *Top*: Bulk flow measurements from the studies listed in Colless et al. (2001b) and Table 6.9. *Bottom*: Bulk flow measurements from recent studies given in Table 6.9, coloured according to the most appropriate window function (blue for top-hat, green for Gaussian).

($\sim 73\,h^{-1}$ Mpc) is equivalent to a uniformly-sampled spherical (top-hat) volume of radius $\sim 145\,h^{-1}$ Mpc (assuming fixed relative errors). This radius lies within our defined effective range and is therefore an appropriate scale for comparison. However, this is still an over-simplification, and to properly account for the radial distribution of the sample and the variable errors in distance requires a more sophisticated radial weighting scheme, such as that provided by Watkins, Feldman & Hudson (2009) and Turnbull et al. (2012). The ΛCDM prediction for the rms bulk flow amplitude in a sphere of radius 12 900 km s^{-1} is 185 km s^{-1}, and 169 km s^{-1} in a sphere of radius 16 120 km s^{-1}. Our value of $|u_{\rm tot}| = 337$ km s^{-1} lies higher than the ΛCDM prediction at the 2.3–2.5σ level; we discuss the significance of this result in the following section.

6.10.3 Cosmological Implications of a Large Bulk Flow

If the bulk flow of the local volume is observed to differ significantly from the theoretical expectations from ΛCDM cosmology and the latest WMAP7 constraints, this could indicate a departure from standard cosmological models. Watkins, Feldman & Hudson (2009) suggest that the WMAP7 value of σ_8 is lower than observed in their own analysis and some other studies (e.g. Pike & Hudson, 2005; Bond et al., 2005), although the discrepancy in σ_8 is not large enough to account for the amplitude difference of the bulk flow. This is not supported by our 6dFGSv measurement of β which is lower than that found by Pike & Hudson (2005), and indeed somewhat lower than the WMAP7 estimate (albeit consistent at the 2σ level).

An alternative explanation for the divergence in the bulk flow is that the interpretation of the origin of the CMB dipole motion may be incorrect. In a 'tilted' universe model (Turner, 1991; Kashlinsky et al., 2008), some fraction of the CMB dipole is due to fluctuations from the pre-inflationary universe, rather than the Local Group's motion with respect to the background, resulting in an intrinsic bulk flow that does not converge and continues beyond the local volume. A more extreme proposal by Wiltshire et al. (2012) suggests that the CMB dipole is partially induced by differential expansion histories in different directions on the sky, undermining the assumption of a CMB rest frame. However, further observation and theoretical investigation is required to establish the validity of both these models.

There also appears to be some inconsistency in the amplitude of the CMB dipole predicted from reconstructions of the local density and velocity field. As shown by Erdoğdu et al. (2006), the 2MRS velocity field reconstruction only accounts for two-thirds of the $\sim$600 km s^{-1} CMB dipole motion assuming $\beta = 0.4$. The 6dFGSv-derived value of $\beta = 0.3$ leads to a *greater* divergence in the dipole alignment, and does not explain the CMB dipole vector. The Lavaux et al. (2010) reconstruction of the 2MRS velocity field (out to $150\,h^{-1}$ Mpc) also makes a prediction at variance with observation. Therefore more detailed analysis of these reconstructed models is

needed to explain this mismatch and to generate models that can account for the amplitude of the CMB dipole vector.

6.11 Summary

We have measured FP distances and peculiar velocities for ∼9000 galaxies in the 6dFGSv - the largest, and most homogeneous peculiar velocity survey to date. A robust Bayesian procedure was developed to model the peculiar velocity field of this sample, using a maximum likelihood approach and incorporating the 3D Gaussian FP model of Chapter 3. This model was found to perform well under the demands of fitting to multiple types of mock galaxy samples designed to emulate the selection effects and distribution of the real 6dFGSv data. We explicitly model the effects induced by the form of the peculiar velocity distribution (either from a Gaussian or more realistic distribution derived from the 2MRS velocity field), the overall mean offset in the velocity distribution and variation in the width of the distribution. A comprehensive regime of testing with mock galaxy samples demonstrated that out Bayesian fitting procedure was robust with respect to these effects.

We established the bias in the best-fit parameters defining the velocity field that result from the fact that the 6dFGSv sample is restricted to the Southern Hemisphere. We also determined that the addition of an age parameter in our peculiar velocity model to account for the strong age trend in the Fundamental Plane did not tighten the constraints fit by the model, as a result of the scatter in the individual errors in the age measurements for this sample.

We measured a value of the β parameter from a comparison of the 6dFGSv observed velocities to the predicted peculiar velocities of the 2MRS reconstructed density and velocity field. The best-fit value for 6dFGSv was $\beta = 0.29 \pm 0.06$, slightly lower than the value found by other studies (although consistent at the 1.5σ level). We recover a total bulk flow within $\sim 160\,h^{-1}$ Mpc of $|u_{\rm tot}| = 337 \pm 66$ km s^{-1} towards $l = 313° \pm 9°$ and $b = 15° \pm 10°$, suggesting coherent motion in the direction of the Shapley Supercluster. If we account for the fact that our survey volume is limited to the Southern Hemisphere we find the 6dFGSv bulk flow is not consistent with the predictions of ΛCDM at greater than 2σ. The residual bulk flow (after subtracting the 2MRS prediction) of 6dFGSv is $|u_{\rm res}| = 273 \pm 45$ km s^{-1} accounting for most of this motion and is in the direction of $l = 326° \pm 13°$ and $b = 37° \pm 14°$, very close to Shapley. The large amplitude of the residual dipole suggests that the bulk flow motion of 6dFGSv is dominated by mass distributions unaccounted for by the 2MRS volume or that the contribution of the Shapley supercluster is underrepresented in the 2MRS reconstruction.

Chapter 7

Conclusion

7.1 Summary of Conclusions

In this thesis we present the the largest homogeneous sample to date used to determine the NIR Fundamental Plane derived from the 6dF Galaxy Survey. This sample comprises $\sim 10^4$ early-type galaxies from the 6dFGS, extending across the southern sky. We measure the Fundamental Plane distances and peculiar velocities of these galaxies, which form the basis of 6dFGSv - the largest and most uniform galaxy peculiar velocity sample to date. We map the velocity field in the local universe and compare to the density field derived from redshift surveys. This leads to new constraints on the beta parameter linking mass density and galaxy bias as well as the cosmological bulk flow in the 6dFGSv volume.

7.1.1 The 6dFGS Fundamental Plane

We provide the Fundamental Plane parameters for the entire sample of galaxies in the 6dFGS FP survey in Chapter 2. We report homogeneous spectroscopic measurements from 6dF spectra as well as the robust near-infrared photometry (and size information) from 2MASS images for a sample of 11 287 galaxies. Further selection criteria, such as redshift and magnitude, were applied to this sample to remove outliers and improve the quality and usefulness of the final FP sample of $\sim$9000 galaxies in each of the JHK bands. Additional galaxy properties used in the FP study were derived pertaining to galaxy environment (group and clusters catalogue), morphology (visual inspection and classification) and stellar populations (Lick index fitting of galaxy spectra).

In Chapter 3, we demonstrate that the standard regression techniques commonly used to derive a best-fit FP are inherently biased. We develop a robust maximum-likelihood based fitting method which takes into account the selection effects, correlated observational errors and other sources of potential bias present in a FP sample. We show that a 3D Gaussian model of the FP is a less-biased representation (and excellent empirical match) to the distribution of galaxies in FP space, as evidenced through extensive testing with mock FP samples.

In Chapter 4 we apply the robust FP fitting method outlined in Chapter 3, and determine the best-fit FP for the 6dFGS Fundamental Plane sample of early-type

galaxies. We find the best-fit FP for the J band sample is $R_e \propto \sigma_0^{1.52\pm0.03} I_e^{-0.89\pm0.01}$, which is similar to previous NIR FP fits in the literature; the passband variation in the H and K bands is consistent with mean colour variation. The overall scatter in R_e of the 6dFGS FP (and indeed most recent FP studies) is larger than the 20% usually quoted, and is a result of interpreting the rms scatter projected in R_e as the uncertainty in distance. However, for a 3D Gaussian distribution, the true distance uncertainty (23%) is smaller than the scatter in R_e (29%) once the distribution of galaxies in FP space is accounted for.

Galaxies in the 6dFGS FP sample that reside in different environments are found to have the same FP slopes. However the FP does exhibit an offset in size with environment, in the sense that galaxies in high-density regions (or in groups and clusters) have smaller sizes than galaxies in low-density (or in the field) regions. A similar offset is found with morphology, where early-type spiral bulges are on average about 10% larger than elliptical and lenticular galaxies with the same velocity dispersion and surface brightness, even though the scatter in the FP for the two morphological types is similar.

The Fundamental Plane results of Chapter 4 are supplemented by an investigation of the variation of the FP with stellar populations of the 6dFGS galaxies. In Chapter 5, we measure the trends of stellar population parameters in the FP both globally and as linear combinations of partial derivates. We find the strongest trend normal to the FP (i.e. along the $\boldsymbol{v}_1$ axis) is with age, and that there is essentially no stellar population variation along the long ($\boldsymbol{v}_2$) axis of the FP. As $\boldsymbol{v}_2$ is aligned with luminosity density, we suggest that the distribution in this axis of the FP is related to the history of dry mergers (which has no impact on stellar population). The natural axes of the FP are therefore driven by different physical processes. Finally, we determine that age is also the strongest trend with residual orthogonal to the plane and we speculate that this drives (through the correlations of age with environment, morphology and metallicity) most of the variations with the other galaxy properties. The results of Chapters 4 and 5, therefore provide a consistent picture of early-type galaxy formation as observed in the near-infrared.

7.1.2 Peculiar Velocities and Cosmological Parameters

We derive peculiar velocities for the 6dFGS sample in Chapter 6 using our FP relation. We measure FP distances and peculiar velocities for ∼9000 galaxies reaching out to 16 120 km s^{-1}. As an innovation with regard to earlier work, we obtain the Bayesian posterior probability distribution for each galaxy's peculiar velocity. To model the local peculiar velocity field, we apply a maximum likelihood method to determine the parameters defining the velocity field (such as the redshift-space distortion parameter β and the bulk flow $\boldsymbol{u}_{\rm tot}$). A variety of mock peculiar velocity

samples are used to test the accuracy and determine the precision of the ML method, showing that we can properly account for biases and obtain reliable uncertainties for the parameters of the velocity field model.

Comparison of the observed 6dFGS peculiar velocity field and the predicted 2MRS velocity field yields $\beta = 0.29 \pm 0.06$. We measure the bulk flow amplitude within $\sim 160\,h^{-1}\,\mathrm{Mpc}$ to be $|u_{tot}| = 337 \pm 66\,\mathrm{km\ s^{-1}}$ towards $l = 313° \pm 9°$ and $b = 15° \pm 10°$, consistent with most of the recent peculiar velocity samples (e.g. Dai, Kinney & Stojkovic, 2011; Colin et al., 2011; Turnbull et al., 2012) and larger than predicted from ΛCDM expectations at the 2.5σ level.

Most of the bulk flow appears to be in the direction of the Shapley supercluster, confirming that it is an important structure affecting the dynamics in our sample. This is consistent with the fact that Shapley is at the edge of the volume probed by 6dFGSv and, as the largest local structure in our sample, we might expect it to be the dominant cause of the bulk motion *within* the 6dFGSv volume. However there is also a component of the dipole flow, the external field, generated from the matter distribution outside of the surveyed volume. To calculate the relative contributions from the internal and external field in the 6dFGSv sample, we can compare the observed field with the predictions from the reconstructed 2MRS density and peculiar velocity fields. The 2MRS reconstructed velocity field is based on a density distribution that is only slightly larger than the 6dFGSv volume, so it might be expected to under-estimate the impact of external structures on the velocity field. In fact for 6dFGSv we observe a residual bulk flow, after subtraction of the 2MRS model prediction, with a large amplitude ($|u_{\mathrm{res}}| = 273 \pm 45$) which suggests that there are indeed contributions to the external field from mass distributions that are unaccounted for by the 2MRS model.

7.2 Future Work

The 6dFGS peculiar velocity survey presented in this thesis, has a range of scientific applications beyond those investigated here. This section explores a few suggestions for future work including further analysis of the existing 6dFGSv sample, extending the Fundamental Plane and peculiar velocity surveys with supplementary datasets and the way forward with the next generation of peculiar velocity surveys.

7.2.1 The Fundamental Plane

Our stellar population analysis of the FP revealed a significant contribution from age variations in the scatter through the Fundamental Plane, suggesting this scatter could be reduced by accounting for this trend. The large individual errors on the age measurements meant that any improvement in the total FP scatter (and also in the distance errors) when correcting for the age trend was modest, at best. However, the

observed errors associated with metallicity (∼16%) are noticeably smaller, compared with the uncertainties in age (∼20%). These smaller errors, and the correlation between metallicity and age, may mean that metallicity (or some combination of age and metallicity) is a more effective parameter to use than age in reducing the age-related FP scatter.

Furthermore, the results of Chapter 5 suggest a number of important observations with implications for the connection between the stellar population histories of galaxies and their distribution in Fundamental Plane. The most intriguing suggestion is that the $\boldsymbol{v}_2$ direction in the FP represents a variation in luminosity density due to differences in merger history and is thus independent of stellar population effects. To investigate these observations further requires comparison with predictions from the results of N-body simulations coupled with semi-analytic models (SAMs), such as those in the recent analysis of Porter et al. (2012, submitted). These SAMs aim to produce realistic simulations of galaxy formation to predict the structural and stellar population properties of galaxies in the FP which are used to constrain the origin of such observed trends.

The slope of the FP (in $\log \sigma_0$) is usually observed to be steeper in near-infrared passbands as compared to optical passbands (e.g. B,V, or R). A steeper FP (as observed in this research) contributes more scatter (by up to 50%) to the FP distance measurements. One way to reduce this scatter would be to combine the 6dFGS velocity dispersions with effective radius and surface brightness measurements derived from optical photometry, for example in the r band, that has the same or better precision as the 2MASS JHK photometry.

In terms of the photometric measurements, there are several digital photometric surveys which will, between them, provide increasingly deep images of the entire sky over the next five years; the Panoramic Survey Telescope & Rapid Response System (Pan-STARRS[1]) survey in the Northern Hemisphere (Tonry et al., 2012) and the SkyMapper[2] survey in the Southern Hemisphere (Keller et al., 2007). In addition, the AAVSO Photometric All-Sky Survey all-sky photometric survey (APASS[3]) will provide accurate photometry for stars between 10th and 17th magnitude over the whole sky (Henden et al., 2009). It should be possible to achieve a reduction in the systematics in the 2MASS photometry by linking 2MASS to Pan-STARRS and SkyMapper (and the stellar photometry from APASS) from the 0.04 mag (i.e. ∼160 km s^{-1} at a distance of 10 000 km s^{-1}) to the 0.01 mag level.

The 6dFGS Fundamental Plane survey (as described in Chapter 2) presents a significant increase in the number of galaxies and hence FP measurements in the

[1] http://pan-starrs.ifa.hawaii.edu/public
[2] http://www.mso.anu.edu.au/skymapper
[3] http://www.aavso.org/apass

near-infrared. To reduce the overall scatter about the FP, one would need to improve the precision of parameter estimates; this would lead to a better understanding of the properties of early-type galaxies and their formation from the FP and also provide tighter distance measurements. There are various ways in which the uncertainties associated with velocity dispersion measurements can be improved. Recently, the advantages of measuring velocity dispersion within an effective radius (i.e. in larger apertures) rather than a central velocity dispersion have been studied using kinematic information from IFU spectroscopy (Scott et al., 2012; Falcón-Barroso et al., 2011), and it has been claimed that these yield tighter FP constraints. Further improvement may be gained from IFU spectroscopy by measuring both velocity dispersion and rotational velocity which can be combined to provide additional kinematic information. These possibilities can be explored with the planned Sydney-AAO Multi-object IFU (SAMI) survey[4], which will include spatially resolved spectroscopy for hundreds of early-type galaxies.

7.2.2 Cosmological Applications of the 6dFGS Peculiar Velocity Field

The preliminary investigations of the 6dFGSv presented in this thesis can be developed further by studying the origin of the observed large bulk flow measured for our sample towards the Shapley supercluster. To determine the range and influence of this bulk flow we can measure the large-scale flow in concentric spherical shells within our sample volume. In doing so, the relative contributions to this total bulk flow from known structures in the local volume (such as the Great Attractor) can be better understood and ultimately used to determine how much of this flow contributes to the Local Group dipole motion.

The 6dFGSv is a unique probe of cosmology at the largest scales and is intended to provide constraints on a number cosmological parameters. For example, the cosmological parameters relating to the velocity and galaxy power spectra can be derived from the Fisher information matrix both independent of and in conjunction with the 6dFGS redshift survey. A prediction by Burkey & Taylor (2004) of the resulting cosmological constraints from such an analysis is shown in Figure 7.1. It shows the 1σ contours on pairs of parameters including: the amplitude of galaxy power spectrum A_g, the redshift-space distortion parameter β, the power spectrum shape parameter Γ and the matter-galaxy correlation coefficient, r_g (which encompasses the bias between the galaxy and matter fields). From the redshift data alone (black contours), Burkey & Taylor (2004) found the constraints on these cosmological parameters are accurate at the 5% level. However, the addition of peculiar velocity survey data (red contours) allows the degeneracies between the galaxy and matter power spectra to

[4] http://sami-survey.org/

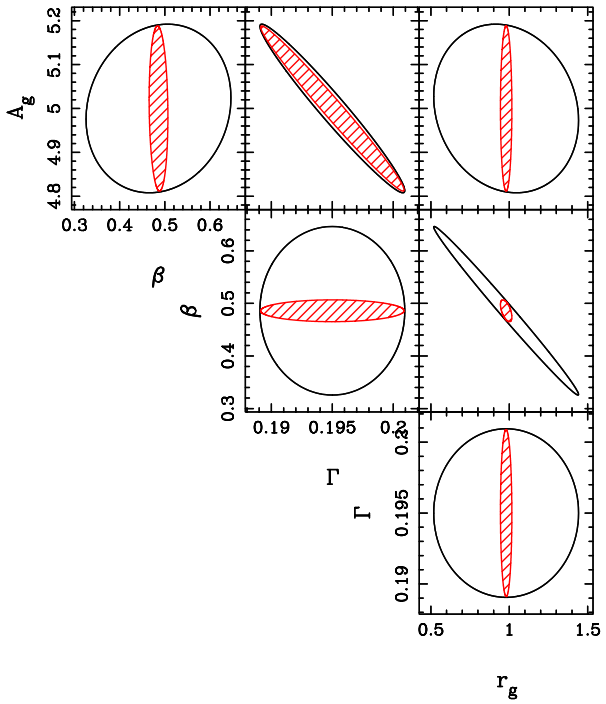

Figure 7.1: 1σ likelihood contours for parameter pairs of $\{A_g, \beta, \Gamma, r_g\}$ for 6dFGS, using a Fisher matrix analysis of the galaxy power spectrum alone (in black) and with both the galaxy and peculiar velocity power spectrum (in red). (Figure 13 from Burkey & Taylor 2004).

be broken and yields the best constraints on these cosmological parameters. In particular, the strong degeneracy between β and r_g found for the redshift survey data is broken by the addition of the peculiar velocities, resulting in substantially smaller joint errors (around 2%). We note these predictions are based on assumptions that are optimistic compared to the actual observations.

A common limitation of peculiar velocity survey data is the sparse and sometimes inhomogeneous sampling of velocity measurements in the survey volume and small-scale aliasing which can bias the measurement of the bulk flow. A more sophisticated analysis of the bulk flow could therefore be applied to the 6dFGSv sample which accounts for this sparse sampling following the method of Watkins, Feldman & Hudson (2009). This minimum-variance weighting scheme determines the optimal weights with respect to an ideal, densely sampled survey to estimate the bulk flow. It can be used to test the convergence between different peculiar velocity samples and also to improve the estimates of cosmological parameters (and their uncertainties).

The predicted peculiar velocity model of Erdoğdu et al. (2012, submitted), based on the 2MRS, is well matched to the specifications of the observed 6dFGSv observed field. However, it is useful to compare the Erdoğdu et al. (2012, submitted) model

(derived from linear perturbation theory) to alternative reconstructions of the density and peculiar velocity fields. One such model is the Monge–Ampère–Kantorovitch (MAK) reconstruction of the peculiar velocity field based on the Lagrangian method of reconstructing galaxy orbits (Lavaux, 2008; Lavaux et al., 2010). Kitaura et al. (2012) provide a more complex peculiar velocity field model which includes non-linear and non-local effects using second order Lagrangian perturbation theory. They simulate an ensemble of reconstructed density and peculiar velocity fields using a Bayesian Networks Machine Learning approach. Both the Lavaux et al. (2010) and Kitaura et al. (2012) reconstructions are also derived from the 2MRS dataset and therefore, the 6dFGSv is an ideal sample to test the predictions from all these models. As it stands, there appears to be some unresolved disparity between the Lavaux et al. (2010) and Erdoğdu et al. (2012, submitted) models (Lavaux, G. 2012, private communication) which should be addressed in the near future.

7.2.3 Extending the 6dFGSv Sample with other Datasets

In Chapter 6 we note that our peculiar velocity field results contain a well-understood bias caused by the fact that the peculiar velocities are derived from measurements (albeit in large volume) mainly in the southern sky. The most obvious way to alleviate this bias is to couple the 6dFGSv data in the Southern Hemisphere with velocity dispersion measurements from SDSS spectra and 2MASS photometry in the Northern Hemisphere. The challenge with combining these datasets is to ensure the systematics between the different samples were small or at least well-characterised; one advantage of using 2MASS images is the all-sky coverage, thereby preserving the homogeneity of the FP photometric measurements . This would create the largest 'all-sky' sample with quality FP distances and peculiar velocity measurements, covering 17 000 square degrees in the south and 8000 square degrees in the north, or almost two thirds of the whole sky. This would provide the best dataset for studying the bulk flow in the local universe and deriving even better cosmological constraints.

7.2.4 Current and Future Peculiar Velocity Surveys

The current status of galaxy peculiar velocity surveys will give us a detailed understanding of the density and velocity field in the local volume (in the region within $cz < 10\,000\,\mathrm{km\ s^{-1}}$). The two main surveys similar in scope to 6dFGSv but using the Tully-Fisher relation as their distance indicator are the 2MASS Tully-Fisher Survey (2MTF) which has measured TF distances for ∼5000 bright edge-on spirals in 2MRS out to $cz \sim 10\,000\,\mathrm{km\ s^{-1}}$ (Masters, Springob & Huchra, 2008) and the 'Cosmic Flows' project[5] in the process of measuring TF distances of spiral galaxies

[5] http://ifa.hawaii.edu/cosmicflows/

over the entire sky (out to $cz < 12\,000\,\mathrm{km\ s^{-1}}$) with the Green Bank Telescope and Parkes radio telescope (Courtois et al., 2011).

In conjunction with these new datasets, there has been an advance in the compilation of previous peculiar velocity datasets with the Extragalactic Distance Database[6] (EDD). The EDD integrates archived datasets specifically for distances derived from the Cepheid period-luminosity relation, surface brightness fluctuations, Type Ia supernovae, the Fundamental Plane and Tully-Fisher relation and also new HI data (of which 'Cosmic Flows' is a large contribution; Tully et al., 2009). 6dFGSv has the advantage of greater depth and sample size than the current surveys discussed here, however each survey is important as an independent measurement of the local velocity field.

In the future, the survey depth of 6dFGSv could potentially be extended even further as part of a proposed survey called TAIPAN i.e. Transforming Astronomical Imaging-surveys through Polychromatic Analysis of Nebulae, using an upgraded version of the 6dF spectrograph. TAIPAN aims to provide an all southern sky survey of up to ∼500 000 galaxies extending out to a redshift of $z \simeq 0.08$. Using the all-southern-sky imaging from SkyMapper, TAIPAN would offer a substantial improvement in the sampling and number of galaxies over 6dFGSv, leading to better determinations of FP distances and peculiar velocity measurements.

Another exciting southern-sky survey on the horizon is the Wide-field ASKAP L-band Legacy All-sky Blind surveY (WALLABY)[7], a blind HI survey for the Australian SKA Pathfinder telescope (ASKAP). WALLABY will comprise ∼500 000 to 600 000 galaxies with a mean redshift of $z \simeq 0.04$ from which Tully-Fisher distances and peculiar velocities can be derived (see Duffy, Moss & Staveley-Smith, 2012). The Northern Hemisphere counterpart to WALLABY is the Westerbork Northern Sky HI Survey (WNSHS)[8] - a prospective HI survey of the northern sky with the Dutch Westerbork Radio Synthesis Telescope (WSRT).

7.3 Concluding Remarks

After the discovery in the late 80's of the Fundamental Plane, it and the Tully-Fisher relation provided a major improvement in measuring galaxy distances at larger distances. Such studies initially provided new insights into the velocity field of the local universe, but towards the end of the 1990s the field suffered stagnation due to the limits of the observational samples. This was due in part to large errors experienced at greater distances as well as the apparent disagreement with other cosmological probes and their convergence on parameter constraints (most notably

[6] http://edd.ifa.hawaii.edu
[7] http://www.atnf.csiro.au/research/WALLABY
[8] http://www.astron.nl/~jozsa/wnshs/index.html

with σ_8). However, in recent years the field has experienced a resurgence due to the arrival of large, homogeneous surveys and better quality measurements driven by technological advances as well as a better understanding of the systematics provided by more sophisticated predictions of the density and velocity field from theoretical models.

With major developments in the field of galaxy peculiar velocities through surveys such as 6dFGSv (enhanced by our greater understanding of galaxy formation and evolution provided by relations such as the Fundamental Plane), we now enter an exciting phase where our observations are reaching the requisite scale and precision to sharpen our understanding of the distribution and motions of matter in the nearby universe, and so test aspects of cosmological models that are not readily accessible using other methods. Peculiar velocities remain one of most value probes of cosmology in the nearby universe and will play a key role in answering the outstanding cosmological questions posed in this thesis, with the wealth of data generated by future surveys such WALLABY and TAIPAN.

Appendix A

3D Visualisation with S2PLOT

An important feature of the Fundamental Plane results within this thesis, is our ability to visualise the 6dFGS FP distribution in its native three-dimensional $r-s-i$ space. As stated already, it is important to show the FP in 3D so as to have an unrestricted view of all dimensions of FP space. Three-dimensional visualisation is made possible due to advances in software, making it more accessible and easier to generate and manipulate 3D plots. Specifically, all 3D plots in this thesis are created using custom C-code and the S2PLOT graphics library (Barnes et al., 2006).

In the digital version of this thesis and in research papers associated with this work (Magoulas et al., 2012; Springob et al., 2012), we are able to include *interactive* 3D figures, which can be accessed by viewing the PDF file of these papers in Adobe Reader Version 8.0 or higher. Interactive 3D-PDF figures were directly embedded using the approach described in Barnes & Fluke (2008) requiring only Adobe Acrobat Professional with a 3D plugin. Therefore, the process of creating and embedding 3D-PDF figures has been made readily accessible by the fact that it uses only open-source programs and industry standard commercial software.

A.1 Interactive 3D Figures

Several of the figures presented here (namely Figures 3.3, 4.1, 4.4, 4.7 and Figure 5.5) can be accessed as 3D interactive visualisations when viewing the digital version of this thesis in Acrobat Reader v8.0 or higher. Once 3D viewing is enabled by clicking on the figure, the 3D mode allows the reader to rotate, pan and zoom the view using the mouse.

The toolbar on each 3D figure contains a host of interactive elements which can help in exploring the 3D visualisation. We particularly direct the reader's attention to the following toolbar features: (i) you can restore the initial default view at any time using the home button; (ii) you can rotate to any orientation you prefer and, where relevant, to special, author-selected 3D views (e.g. the edge-on view of the FP); these can be selected from the Views drop-down menu; (iii) you can toggle the model tree, which allows individual plot elements (e.g. points, planes, vectors) of the 3D figure to be turned on and off, giving the viewer greater control of the interactive figure.

Suggested interactions with particular 3D figures include:

(a) In Figure 3.3, use the model tree to toggle the $\boldsymbol{v}$-space vectors and mass/luminosity vectors one at a time to see how they compare in our 3D Gaussian model. Also, rotate the figure to view the small angle between $\boldsymbol{v}_1$ and $\boldsymbol{m} - \boldsymbol{l}$ and also $\boldsymbol{v}_2$ and $\boldsymbol{l} - 3\boldsymbol{r}$

(b) Figure 4.1 not only contains the J band FP sample of galaxies, but also the H band and K band samples. They can be enabled in the model tree by selecting 'H Band' or 'K Band' respectively. For an unimpeded view of the individual galaxies, toggle the best-fit plane (called 'Fundamental Plane' in the model tree); this also applies to Figures 4.4 and 4.7. In the Views drop-down menu, select 'Edge-on' to view the Fundamental Plane in the projection with the smallest scatter.

(c) In Figure 4.4, rotate and pan across the FP galaxies to explore where the richness subsamples lie.

(d) In Figure 4.7, toggle the individual points of each morphology subsample to see the differences in the way their distributions populate FP space.

(e) In Figure 5.2, view the direction of the stellar population trends in the full three dimensional FP space; in 3D the complexity of these trends can be realised as it is not limited to the 2D projection of Figure 5.1.

Bibliography

Abate A., Erdoğdu P., 2009, MNRAS, 400, 1541

Abazajian K. N. et al., 2009, ApJS, 182, 543

Amanullah R., Lidman C., Rubin D., Aldering G., Astier P., Barbary K., Burns M. S., et al., 2010, ApJ, 716, 712

Barnes D. G., Fluke C. J., 2008, in Astronomical Society of the Pacific Conference Series, Vol. 394, Astronomical Data Analysis Software and Systems XVII, R. W. Argyle, P. S. Bunclark, & J. R. Lewis, ed., pp. 149–+

Barnes D. G., Fluke C. J., Bourke P. D., Parry O. T., 2006, PASA, 23, 82

Bender R., Burstein D., Faber S. M., 1992, ApJ, 399, 462

Bennett C. L. et al., 2003, ApJS, 148, 1

Bernardi M. et al., 2003a, AJ, 125, 1849

Bernardi M. et al., 2003b, AJ, 125, 1866

Bertin G., Ciotti L., Del Principe M., 2002, A&A, 386, 149

Beutler F. et al., 2012, MNRAS, 423, 3430

Bilicki M., Chodorowski M., Jarrett T., Mamon G. A., 2011, ApJ, 741, 31

Blakeslee J. P., Davis M., Tonry J. L., Dressler A., Ajhar E. A., 1999, ApJL, 527, L73

Bolton A. S., Burles S., Treu T., Koopmans L. V. E., Moustakas L. A., 2007, ApJL, 665, L105

Bond J. R. et al., 2005, ApJ, 626, 12

Branchini E. et al., 1999, MNRAS, 308, 1

Bruzual G., Charlot S., 2003, MNRAS, 344, 1000

Burkey D., Taylor A. N., 2004, MNRAS, 347, 255

Burstein D., Bender R., Faber S., Nolthenius R., 1997, AJ, 114, 1365

Burstein D., Davies R. L., Dressler A., Faber S. M., Lynden-Bell D., 1986, in NATO ASIC Proc. 180: Galaxy Distances and Deviations from Universal Expansion, Madore B. F., Tully R. B., eds., pp. 123–130

Burstein D., Faber S. M., Dressler A., 1990, ApJ, 354, 18

Busarello G., Capaccioli M., Capozziello S., Longo G., Puddu E., 1997, A&A, 320, 415

Campbell L., 2009, PhD thesis, Australian National University

Cappellari M. et al., 2006, MNRAS, 366, 1126

Ciotti L., Lanzoni B., Renzini A., 1996, MNRAS, 282, 1

Colin J., Mohayaee R., Sarkar S., Shafieloo A., 2011, MNRAS, 414, 264

Colless M. et al., 2001a, MNRAS, 328, 1039

Colless M., Jones H., Campbell L., Burkey D., Taylor A., Saunders W., 2005, in IAU Symposium, Vol. 216, Maps of the Cosmos, M. Colless, L. Staveley-Smith, & R. A. Stathakis, ed., pp. 180–189

Colless M., Saglia R. P., Burstein D., Davies R. L., McMahan R. K., Wegner G., 2001b, MNRAS, 321, 277

Courtois H. M., Tully R. B., Makarov D. I., Mitronova S., Koribalski B., Karachentsev I. D., Fisher J. R., 2011, MNRAS, 414, 2005

da Costa L. N., Bernardi M., Alonso M. V., Wegner G., Willmer C. N. A., Pellegrini P. S., Maia M. A. G., Zaroubi S., 2000a, ApJL, 537, L81

da Costa L. N., Bernardi M., Alonso M. V., Wegner G., Willmer C. N. A., Pellegrini P. S., Rité C., Maia M. A. G., 2000b, AJ, 120, 95

Dai D.-C., Kinney W. H., Stojkovic D., 2011, JCAP, 4, 15

Davis M., Nusser A., Masters K. L., Springob C., Huchra J. P., Lemson G., 2011, MNRAS, 413, 2906

de Carvalho R. R., Djorgovski S., 1992, ApJL, 389, L49

de Vaucouleurs G., 1948, Annales d'Astrophysique, 11, 247

Desroches L.-B., Quataert E., Ma C.-P., West A. A., 2007, MNRAS, 377, 402

Djorgovski S., Davis M., 1987, ApJ, 313, 59

D'Onofrio M. et al., 2008, ApJ, 685, 875

D'Onofrio M., Valentinuzzi T., Secco L., Caimmi R., Bindoni D., 2006, New Astronomy Reviews, 50, 447

Dressler A., Faber S. M., Burstein D., Davies R. L., Lynden-Bell D., Terlevich R. J., Wegner G., 1987a, ApJL, 313, L37

Dressler A., Lynden-Bell D., Burstein D., Davies R. L., Faber S. M., Terlevich R., Wegner G., 1987b, ApJ, 313, 42

Duffy A. R., Moss A., Staveley-Smith L., 2012, PASA, 29, 202

Dunkley J. et al., 2009, ApJS, 180, 306

Eke V. R., Baugh C. M., Cole S., et al., 2004, MNRAS, 348, 866

Erdoğdu P. et al., 2006, MNRAS, 373, 45

Faber S. M., Jackson R. E., 1976, ApJ, 204, 668

Falcón-Barroso J., Peletier R. F., Balcells M., 2002, MNRAS, 335, 741

Falcón-Barroso J. et al., 2011, MNRAS, 417, 1787

Feldman H. A., Watkins R., Hudson M. J., 2010, MNRAS, 407, 2328

Fisher K. B., Lahav O., Hoffman Y., Lynden-Bell D., Zaroubi S., 1995, MNRAS, 272, 885

Forbes D. A., Ponman T. J., Brown R. J. N., 1998, ApJL, 508, L43

Gargiulo A. et al., 2009, MNRAS, 397, 75

Genz A., 1992, J. Comp. Graph. Stat., 1, 141

Gibbons R. A., Fruchter A. S., Bothun G. D., 2001, AJ, 121, 649

Giovanelli R., Haynes M. P., Freudling W., da Costa L. N., Salzer J. J., Wegner G., 1998, ApJL, 505, L91

Graham A., Colless M., 1997, MNRAS, 287, 221

Graves G. J., Faber S. M., 2010, ApJ, 717, 803

Graves G. J., Faber S. M., Schiavon R. P., 2009a, ApJ, 693, 486

Graves G. J., Faber S. M., Schiavon R. P., 2009b, ApJ, 698, 1590

Graves G. J., Faber S. M., Schiavon R. P., 2010, ApJ, 721, 278

Guzman R., Lucey J. R., Bower R. G., 1993, MNRAS, 265, 731

Hambly N. C. et al., 2001, MNRAS, 326, 1279

Han M., Mould J., 1990, ApJ, 360, 448

Henden A. A., Welch D. L., Terrell D., Levine S. E., 2009, in American Astronomical Society Meeting Abstracts, Vol. 214, American Astronomical Society Meeting Abstracts #214, p. #407.02

Hogg D. W., Bovy J., Lang D., 2010, ArXiv Astrophysics e-prints, arXiv:1008.4686

Hubble E. P., 1926, ApJ, 64, 321

Huchra J. P. et al., 2012, ApJS, 199, 26

Hudson M. J., Lucey J. R., Smith R. J., Steel J., 1997, MNRAS, 291, 488

Hudson M. J., Smith R. J., Lucey J. R., Branchini E., 2004, MNRAS, 352, 61

Hyde J. B., Bernardi M., 2009, MNRAS, 396, 1171

Jarrett T. H., Chester T., Cutri R., Schneider S., Skrutskie M., Huchra J. P., 2000, AJ, 119, 2498

Jones D. H. et al., 2009, MNRAS, 399, 683

Jones D. H. et al., 2004, MNRAS, 355, 747

Jones D. H., Saunders W., Read M., Colless M., 2005, PASA, 22, 277

Jorgensen I., Franx M., Kjaergaard P., 1993, ApJ, 411, 34

Jorgensen I., Franx M., Kjaergaard P., 1995, MNRAS, 276, 1341

Jorgensen I., Franx M., Kjaergaard P., 1996, MNRAS, 280, 167

Jun H. D., Im M., 2008, ApJL, 678, L97

Kashlinsky A., Atrio-Barandela F., Kocevski D., Ebeling H., 2008, ApJL, 686, L49

Keller S. C. et al., 2007, PASA, 24, 1

Kitaura F.-S., Erdoğdu P., Nuza S. E., Khalatyan A., Angulo R. E., Hoffman Y., Gottlöber S., 2012, MNRAS, L528

Kobayashi C., 2005, MNRAS, 361, 1216

Kochanek C. S. et al., 2000, ApJ, 543, 131

Kogut A. et al., 1993, ApJ, 419, 1

Kormendy J., 1977, ApJ, 218, 333

Kormendy J., Fisher D. B., Cornell M. E., Bender R., 2009, ApJS, 182, 216

Korn A. J., Maraston C., Thomas D., 2005, A&A, 438, 685

Kourkchi E., Khosroshahi H. G., Carter D., Mobasher B., 2012, MNRAS, 420, 2835

La Barbera F., Busarello G., Merluzzi P., de la Rosa I. G., Coppola G., Haines C. P., 2008, ApJ, 689, 913

La Barbera F., de Carvalho R. R., de La Rosa I. G., Lopes P. A. A., 2010a, MNRAS, 408, 1335

La Barbera F., de Carvalho R. R., de La Rosa I. G., Lopes P. A. A., Kohl-Moreira J. L., Capelato H. V., 2010b, MNRAS, 408, 1313

La Barbera F., Lopes P. A. A., de Carvalho R. R., de La Rosa I. G., Berlind A. A., 2010c, MNRAS, 408, 1361

Larson D. et al., 2011, ApJS, 192, 16

Lauer T. R., Postman M., 1994, ApJ, 425, 418

Lavaux G., 2008, Physica D Nonlinear Phenomena, 237, 2139

Lavaux G., Hudson M. J., 2011, MNRAS, 416, 2840

Lavaux G., Tully R. B., Mohayaee R., Colombi S., 2010, ApJ, 709, 483

Linder E. V., 2005, Phys. Rev. D, 72, 043529

Lintott C. et al., 2011, MNRAS, 410, 166

Lucey J. R., Bower R. G., Ellis R. S., 1991, MNRAS, 249, 755

Lucey J. R., Guzman R., Carter D., Terlevich R. J., 1991, MNRAS, 253, 584

Lynden-Bell D., Faber S. M., Burstein D., Davies R. L., Dressler A., Terlevich R. J., Wegner G., 1988, ApJ, 326, 19

Magoulas C. et al., 2012, MNRAS, 427, 245

Maraston C., 2005, MNRAS, 362, 799

Masters K. L., Springob C. M., Haynes M. P., Giovanelli R., 2006, ApJ, 653, 861

Masters K. L., Springob C. M., Huchra J. P., 2008, AJ, 135, 1738

McLeod K. K., Rieke G. H., 1995, ApJ, 441, 96

Müller K. R., Freudling W., Watkins R., Wegner G., 1998, ApJL, 507, L105

Nelan J. E., Smith R. J., Hudson M. J., Wegner G. A., Lucey J. R., Moore S. A. W., Quinney S. J., Suntzeff N. B., 2005, ApJ, 632, 137

Nelder J., Mead R., 1965, The Computer Journal, 7, 308

Nigoche-Netro A., Aguerri J. A. L., Lagos P., Ruelas-Mayorga A., Sánchez L. J., Machado A., 2010, A&A, 516, A96+

Nigoche-Netro A., Ruelas-Mayorga A., Franco-Balderas A., 2008, A&A, 491, 731

Nusser A., Davis M., 2011, ApJ, 736, 93

Pahre M. A., de Carvalho R. R., Djorgovski S. G., 1998, AJ, 116, 1606

Pahre M. A., Djorgovski S. G., de Carvalho R. R., 1998, AJ, 116, 1591

Peebles P. J. E., 1980, The large-scale structure of the universe. Princeton, New Jersey: Princeton University Press, 1980

Peebles P. J. E., 1993, Principles of Physical Cosmology. Princeton, New Jersey : Princeton University Press, 1993

Peng C. Y., Ho L. C., Impey C. D., Rix H.-W., 2002, AJ, 124, 266

Perlmutter S. et al., 1999, ApJ, 517, 565

Pike R. W., Hudson M. J., 2005, ApJ, 635, 11

Powell M. J. D., 2006, in "Large-Scale Nonlinear Optimization", Roma, M. and Di Pillo, G., ed., Springer, New York, pp. 2l55–297

Proctor R. N., Forbes D. A., Beasley M. A., 2004, MNRAS, 355, 1327

Proctor R. N., Lah P., Forbes D. A., Colless M., Couch W., 2008, MNRAS, 386, 1781

Proctor R. N., Sansom A. E., 2002, MNRAS, 333, 517

Prugniel P., Simien F., 1997, A&A, 321, 111

Reda F. M., Forbes D. A., Hau G. K. T., 2005, MNRAS, 360, 693

Riess A. G., Davis M., Baker J., Kirshner R. P., 1997, ApJL, 488, L1

Riess A. G. et al., 1998, AJ, 116, 1009

Robertson B., Bullock J. S., Cox T. J., Di Matteo T., Hernquist L., Springel V., Yoshida N., 2006, ApJ, 645, 986

Saglia R. P., Bender R., Dressler A., 1993, A&A, 279, 75

Saglia R. P., Colless M., Burstein D., Davies R. L., McMahan R. K., Wegner G., 2001, MNRAS, 324, 389

Schlegel D. J., Finkbeiner D. P., Davis M., 1998, ApJ, 500, 525

Schmidt M., 1968, ApJ, 151, 393

Schwarz G., 1978, Ann. Statist., 6, 461

Scodeggio M., Gavazzi G., Belsole E., Pierini D., Boselli A., 1998, MNRAS, 301, 1001

Scodeggio M., Giovanelli R., Haynes M. P., 1997, AJ, 113, 101

Scott N., Houghton R. C. W., Davies R. L., Cappellari M., Thatte N., Clarke F. J., Tecza M., 2012, MNRAS, 425, 1521

Sérsic J. L., 1963, Boletin de la Asociacion Argentina de Astronomia La Plata Argentina, 6, 41

Smith R. J., Lucey J. R., Hudson M. J., 2007, MNRAS, 381, 1035

Smoot G. F. et al., 1992, ApJL, 396, L1

Springob C. M. et al., 2012, MNRAS, 420, 2773

Springob C. M., Masters K. L., Haynes M. P., Giovanelli R., Marinoni C., 2007, ApJS, 172, 599

Strauss M. A., Willick J. A., 1995, Phys. Rep., 261, 271

Thomas D., Maraston C., Bender R., Mendes de Oliveira C., 2005, ApJ, 621, 673

Tonry J., Davis M., 1979, AJ, 84, 1511

Tonry J. L. et al., 2012, ApJ, 750, 99

Trujillo I., Burkert A., Bell E. F., 2004, ApJL, 600, L39

Tully R. B., Fisher J. R., 1977, A&A, 54, 661

Tully R. B., Rizzi L., Shaya E. J., Courtois H. M., Makarov D. I., Jacobs B. A., 2009, AJ, 138, 323

Turnbull S. J., Hudson M. J., Feldman H. A., Hicken M., Kirshner R. P., Watkins R., 2012, MNRAS, 420, 447

Turner M. S., 1991, Phys. Rev. D, 44, 3737

Watkins R., Feldman H. A., Hudson M. J., 2009, MNRAS, 392, 743

Watson F. G., Parker Q. A., Miziarski S., 1998, in Society of Photo-Optical Instrumentation Engineers (SPIE) Conference Series, Vol. 3355, Society of Photo-Optical Instrumentation Engineers (SPIE) Conference Series, D'Odorico S., ed., pp. 834–843

Westover M., 2007, PhD thesis, Harvard University

Wijesinghe D. B., et al., 2012, MNRAS, 423, 3679

Wiltshire D. L., Smale P. R., Mattsson T., Watkins R., 2012, ArXiv Astrophysics e-prints, arXiv:1201.5371

Worthey G., 1994, ApJS, 95, 107

York D. G., et al., 2000, AJ, 120, 1579

Zaritsky D., Zabludoff A. I., Willick J. A., 1995, AJ, 110, 1602

Zaroubi S., 2002, MNRAS, 331, 901